DOI: 10.1070/RCR4754

Transient structures and chemical reaction dynamics †

Anatoly A.Ischenko,[a] Peter M.Weber,[b] R.J.Dwayne Miller [c, d]

[a] Moscow Technological University, Institute of Fine Chemical Technologies named after M.V.Lomonosov prosp. Vernadskogo 86, 119571 Moscow, Russian Federation
[b] Department of Chemistry, Brown University
324 Brook Street, 02912 Providence, Rhode Island, US
[c] The Max Planck Institute for the Structure and Dynamics of Matter
Hamburg Centre for Ultrafast Imaging
Luruper Chaussee 149, 22761 Hamburg, Germany
[d] Departments of Chemistry and Physics, University of Toronto
M5S 3H6 Toronto, Canada

To study transition structures that are formed in real time during a chemical reaction process, it is necessary to use ultrafast methods to follow the structural dynamics of molecular systems. For many decades, optical methods have been used to study the electronic states and time course giving rise to structural intermediates of chemical reactions with an ever higher time resolution. Although in some cases optical methods show many details, ultimately the results of these observations give only indirect information about the structure of the chemical reaction intermediates. Experimental observation of the behaviour of matter in the space-time continuum on ultrashort time scale is the necessary first step to explain and, subsequently, to control the nonequilibrium processes and functionality of the systems under study, to trace the relationship between the elements of the triad 'Structure – Dynamics – Function' to fully understand material properties. The results of these studies provide the necessary new information for testing theoretical approaches to the description of nonequilibrium chemical dynamics of molecular systems. The study of the time sequence of ultrafast processes occurring during the evolution of intermediate structures in the course of chemical reactions requires the integration of information that can be obtained by using complementary diffraction and spectroscopic methods based on various physical phenomena. Integration of data from ultrafast diffraction and spectroscopy makes it possible to investigate timescales prior to the onset of dissipation in which the coherent dynamics of matter can be observed. The use of quantum chemical calculations has reached a level of sophistication that makes it possible to explain the results of these experimental studies, the features of nonadiabatic behaviour of intermediate structures, and transition states of chemical reactions of molecular systems. This review analyzes the achievements of this rapidly developing field of modern chemistry, femtochemistry, to observe the primary events directing chemistry.
The bibliography includes 580 references.

Contents

† Dedicated to the memory of Professor Ahmed H.Zewail (26.02.1946 – 02.08.2016).

I. Introduction 1174
II. Transition state and femtosecond transition state spectroscopy 1175
III. Chemical dynamics *via* conical intersection between electronic states 1177
IV. Theory elements of time-resolved electron diffraction 1179
V. The dynamics of wave packets 1186
VI. The diffraction signatures of excited molecules 1191
VII. Imaging the electrocyclic ring-opening reaction of 1,3-cyclohexadiene 1197
VIII. The dynamics of spectrally invisible structures 1204
IX. Photodissociation and ultrafast relaxation of iron pentacarbonyl 1207
X. The structure and nuclear dynamics in free radicals: the Jahn – Teller effect and pseudorotation in cyclopentadienyl radicals 1217
XI. Unimolecular photodissociation of 1,2-diiodotetrafluoroethane 1221
XII. Laser-induced electron diffraction 1224
XIII. Atom-resolved reaction dynamics: realization of the chemists' Gedankenexperiment 1231
XIV. Complementarity of spectroscopy and diffraction for studying structural dynamics 1239
XV. Theory: closing the loop 1241
XVI. Conclusions and future outlook 1243

© 2017 Russian Academy of Sciences and Turpion Ltd.

'*The direct observation of the 'transition state' for chemical reactions clearly merits a place in this series devoted to the 'Holy Grails' of chemistry. The transition state is neither one thing, namely, chemical reagents, nor the other, reaction products. Instead it illustrates the mystical event of transsubstantiation.*' [1]

I. Introduction

Our most basic understanding of material properties is well described by the electrons and atoms comprising the material in a state of equilibrium, where the behaviour changes slowly over time. Chemical reactions, in contrast, are dynamic in nature, occurring on very fast time scales. The fleeting moments of chemical reactions have been studied using optical techniques for decades, with ever higher time resolution. While in some cases, optical techniques reveal much detail, ultimately these observations are indirect probes of the chemical dynamics. The direct probing and understanding of the dynamics of biological, chemical processes, and processes occurring in solids (*e.g.*, transport in metals, their alloys, rectification effects in semiconductors, magnetoresistance *etc.*), which are amenable to study in real time, is still in the early stages. Progress in this field has been pushed by the development of methods for the study of the structural dynamics of matter in a state far from equilibrium, including extreme states. The forthcoming information serves as the basis for testing new theoretical approaches to the description of substances using the 'Structure – Dynamics – Function' triad. Observation of the dynamical behaviour of matter in the space-time continuum on ultrashort time scales is a necessary first step in the explanation and, ultimately, control of the far-from-equilibrium processes and functionality of the systems studied.

The natural time scale of dynamical processes depends on the energy and length scales of the phenomenon of interest. For example, molecular electronic processes occur on timescales from attoseconds to femtoseconds; the atomic and molecular dynamics relevant to chemistry are typically on femtosecond to picosecond time scales; in the range of picoseconds to nanoseconds are ferroelectric, magnetic diffusion, and polarization processes; and time scales of nanoseconds and longer are typical of nucleation, cellular functions, and crystal growth. The corresponding natural length scale for these dynamical processes are in the range of atomic and molecular scales: 0.01 – 10 nm for chemistry and biology, and up to the micrometre scale for interactions between biological cells in grains and metal alloys.

A full description of the time sequence and interaction of dynamical characteristics requires the integration of information from different instrumental methods based on different physical phenomena, first and foremost, diffraction and spectroscopic methods with a time resolution and spatial resolution allowing the study at the limit of the coherent dynamics of matter.

The quest to observe transient molecular structures and the chemical dynamics of molecules during reactions is greatly aided by employing two vantage points: the traditional spectroscopic view, which relies on the observation of energy levels and their populations, and a diffraction view, which directly images molecular structure (please, see more detailed discussion of this issue in Refs 2 – 10). Already in the 1980s, the diffraction paradigm was formulated: implementing electron diffraction with time resolution adds a temporal coordinate to determine the molecular structure dynamics.[11 – 14] Time-resolved electron diffraction (TRED) rests on the concept of flash photolysis originally proposed by Norrish and Porter in 1949.[15] Very recent advances in the generation of X-ray pulses have made possible the closely related time-resolved X-ray diffraction (TRXD). In both methods, short laser pulses create the transient structures and induce chemical dynamics that are subsequently imaged by diffraction at specific 'points' in time. The sequence of stroboscopic diffraction patterns allows the capture of 'molecular movies'.

TRED and TRXD, as methods for structural and dynamical studies of fundamental properties of matter, differ from traditional diffraction methods in both experimental implementation and theoretical approaches used to interpret the diffraction data.[7, 8, 16, 17] Transition to the picosecond and femtosecond time scales raises numerous important issues related to the physical essence of the dynamical parameters of the systems studied by analyzing time-dependent scattering intensities. There is a particularly pronounced need of corresponding theoretical basis for the processing of the diffraction data and the results of spectral investigations of the coherent dynamics of molecules in the field of intense ultrashort laser radiation. Such a unified and integrated approach can be formulated using the adiabatic potential energy surfaces (APES) of the ground and excited states of the molecular systems under study [5, 7, 18] to depict the dynamics.

To understand the forces acting on molecular systems within the complex APES landscapes, it is necessary to explore them in the associated 4D space-time continuum. The introduction of time into diffraction methods and the

A.A.Ischenko. Doctor of Chemical Sciences, Professor, Head of the Department of Analytical Chemistry at the Institute of Fine Chemical Technologies named after M.V.Lomonosov of Moscow Technological University.
Telephone: +7(495)936 – 8894, e-mail: aischenko@yasenevo.ru
Current research interests: structural studies of laser-excited molecules by time-resolved electron diffraction: coherent nuclear dynamics; tomography of molecular quantum states; analytical chemistry (chemical sensors); nanomaterials and related technologies.
P.M.Weber. Professor of Chemistry at the Department of Chemistry, Brown University.
Telephone: +1(401)863 – 3767, e-mail: peter_weber@brown.edu
Current research interests: ultrafast time-resolved studies of chemical reactions using spectroscopic and diffraction methods, molecular beam methods and photoionization/photoelectron spectroscopy, multiphoton processes.
R.J.Dwayne Miller. Director, Max Planck Institute for the Structure and Dynamics of Matter, Hamburg, Germany, and Professor of Chemistry and Physics, University of Toronto, Distinguished Faculty Research Chair in Chemical and Biological Physics, University Professor, Fellow of the Royal Society of Canada, Fellow of the Royal Society of Chemistry.
Telephone: +49(0)40 8998 – 6200, e-mail: dwayne.miller@mpsd.mpg.de
Current research interests: application of ultrashort nonlinear laser and electron spectroscopies to probe various aspects of chemical reaction dynamics and molecular photophysics in biological systems and at interfaces; development of femtosecond electron pulse sources to give a real-time view of atomic motions during chemical reactions and structural transitions.

Received 30 May 2017

development of foundational principles of their analysis opens up new methodologies to study transition states of the reaction centres, and short-lived intermediates in gaseous and condensed media.

The use of pico- or femtosecond bunches of electrons as probes, synchronized with the exciting ultrashort laser pulses, led to the development of ultrafast electron crystallography and nanocrystallographic techniques,[19] dynamic transmission electron microscopy,[2–4, 20, 21] femtosecond electron diffraction of structural transitions [22] and of molecular quantum state tomography.[23] One of the promising applications developed by the electron diffraction methods is their use for the characterization and 'visualization' of processes occurring in the photo-excitation of free molecules and biological objects for the analysis of different surfaces, thin films, and nanostructures (see recent review articles [7, 10, 24–39]). The combination of the state-of-the-art optical techniques and diffraction methods using different physical phenomena but complementing each other opens up new possibilities for structural research at ultrashort time sequences. It provides the required integration of the 'Structure – Dynamics – Function' triad in chemistry, biology, and materials science.[2, 3, 6, 7, 9, 10, 40–42]

Since the 1980s, scientific laboratories around the world have begun to develop a new field of the research aimed at this goal. 'Atom-resolved-molecular movies' have allowed visualization of coherent dynamics of the nuclei in the molecules and fast processes in chemical reactions in real time. Modern femtosecond laser sources have made it possible to significantly change the traditional approaches using continuous electron beams, to create ultrabright pulsed photoelectron sources, to catch ultrafast processes in matter initiated by ultrashort laser pulses and to achieve high space-time resolution to imaging molecular processes. Ultrafast laser spectrocsopic and electron diffraction methods complement each other and open up new possibilities in chemistry and physics to light up atomic and molecular motions involved in the primary processes governing structural transitions and the dynamics of chemical reactions.

II. Transition state and femtosecond transition state spectroscopy

Equilibrium geometries, transition states (TSs) and reaction paths are central to the study of chemical reactions.[18–30, 40–45] A TS or first-order saddle point on the APES is a stationary point that is an energy maximum in one direction and a minimum in all others (Fig. 1).

When excited directly, complexes in TSs undergo nuclear motions characteristic of bound, quasi-bound, or unbound dynamics. In elementary reactions, the motions are on the femtosecond time scale and depend on the dimensionality of the potential.[10, 43–45] For example, in the reaction $[ABA]^{\dagger} \rightarrow A + BA$ there are two relevant coordinates that describe the motion of the triatomic TS species, $[ABA]^{\dagger}$, *viz.*, the symmetric and antisymmetric stretch modes, in addition to the bend. Near the saddle point, the motion is bound in the symmetric stretch and unbound in the antisymmetric stretch (reaction coordinate), and the complex can exhibit vibrational motion along the symmetric coordinate perpendicular to the reaction coordinate.[46] This quantized and bound motion is expected to remain at infinity (*i.e.*, final products) with well-defined coherence, as observed experimentally and studied theoretically.[45] The behaviour perpendicular to the reaction coordinate is different from the Feshbach-type resonance along the reaction coordinate. For this type of resonance, popular in reactive scattering (cross-section *vs.* energy), the motion is quasi-bound along the reaction coordinate and the complex is trapped (finite lifetime), but has no bound motion at infinity.[47] Transition state vibrational dynamics, which are important to the understanding of the nature of the potential in the TS region, are particularly relevant to studies that directly or indirectly probe the TS. These include emission [48] and Raman scattering during dissociation,[49] temporal dynamics,[45] photodetachment spectra,[50] peaks in the continuum spectra of dissociation reactions [51] and structure (steps) in the rate constants plotted *vs.* energy.[52] For systems with a large number of degrees of freedom (N),

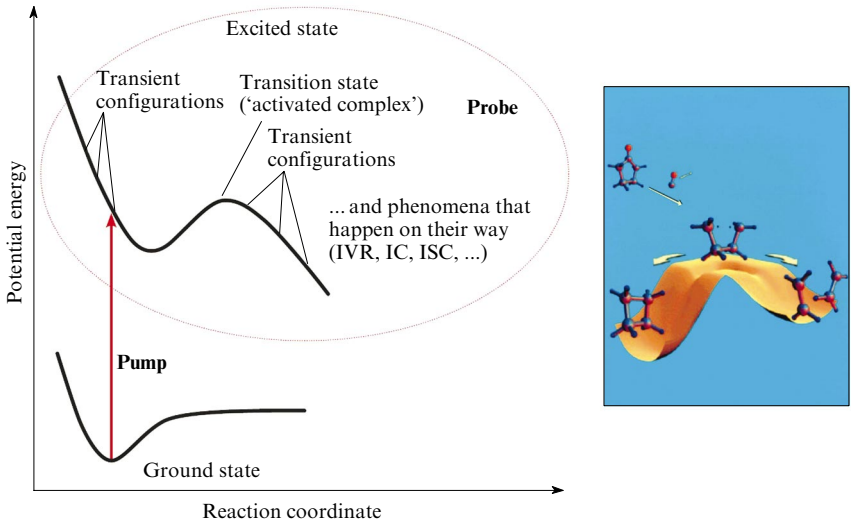


Figure 1. Reaction intermediates. Left: Transition state (activated complex) and transient configurations. IVR — intramolecular vibrational redistribution, IC — internal crossing, ISC — intersystem crossing. Right: 2,3-dimethyl-butene-2 (tetramethylene), bridged tetramethylene are examples of species isolated on the femtosecond time scale.

the situation is more complex. First, the single coordinate perpendicular to the reaction coordinate is now replaced by the $(N-1)$ coordinates of TS theory.[53–57] Second, the wave packet motion may suffer fast spreading as its structure is now comprised of a large number of modes. The isomerization of diphenylethylene (stilbene) is an example of such a complex reaction with 72 modes; the progress along the reaction coordinate can be described by a single motion about the double bond (torsion angle θ),[58,59] with the understanding that this motion requires coupling to the bond elongation along the double bond (as well as some out of plane motion — in all cases a small subset of the full set of vibrational modes). The molecule at the *cis*-configuration is unbound (or quasi-bound) in eight coordinates, but, in principle, is bound along all the other coordinates: a saddle point TS in its strict definition.[46,60]

Transition states of chemical reactions are fundamental in defining the region(s) of internuclear separation (R^*) on the potential energy surface (PES) at which the reagent molecule is 'passing on' to products.[61–63] In contrast to the many successes in applying spectroscopies to the characterization of stable reagents and stable products, TS spectroscopy has been very limited, because of the TS ultrashort lifetime (few vibrational periods) and the very low density of TS molecules that can be probed at R^*.[45] Elegant ideas of time-integrated emission,[64,65] absorption,[66–68] and scattering[49] spectroscopy have been developed to infer the dynamics of the TS.

In 1987 Zewail and co-workers[69] described the technique of femtosecond transition-state spectroscopy (FTS) and its first application to the reaction

$$(I-CN)^* \rightarrow [I\cdots CN]^{\dagger} \rightarrow I + CN + E_{tr}$$

where E_{tr} is the translational energy. The TS, $[I\cdots CN]^{\dagger}$ in this case refers to the range of R (from 2.7 Å to many Å) for the unbound molecule on the excited surface. Zewail and co-workers[69] offered a real-time technique that, because of its time resolution (~40 fs), promises to provide direct information concerning the TS and the spectroscopy of reaction intermediates in the process of falling apart (dissociation) or forming a chemical bond (association).

In Zewail's FTS experiment, a femtosecond pulse excites the bound ICN molecules to a repulsive (C–I) surface, $V_I(R)$. This creates a packet on the APES at time zero.

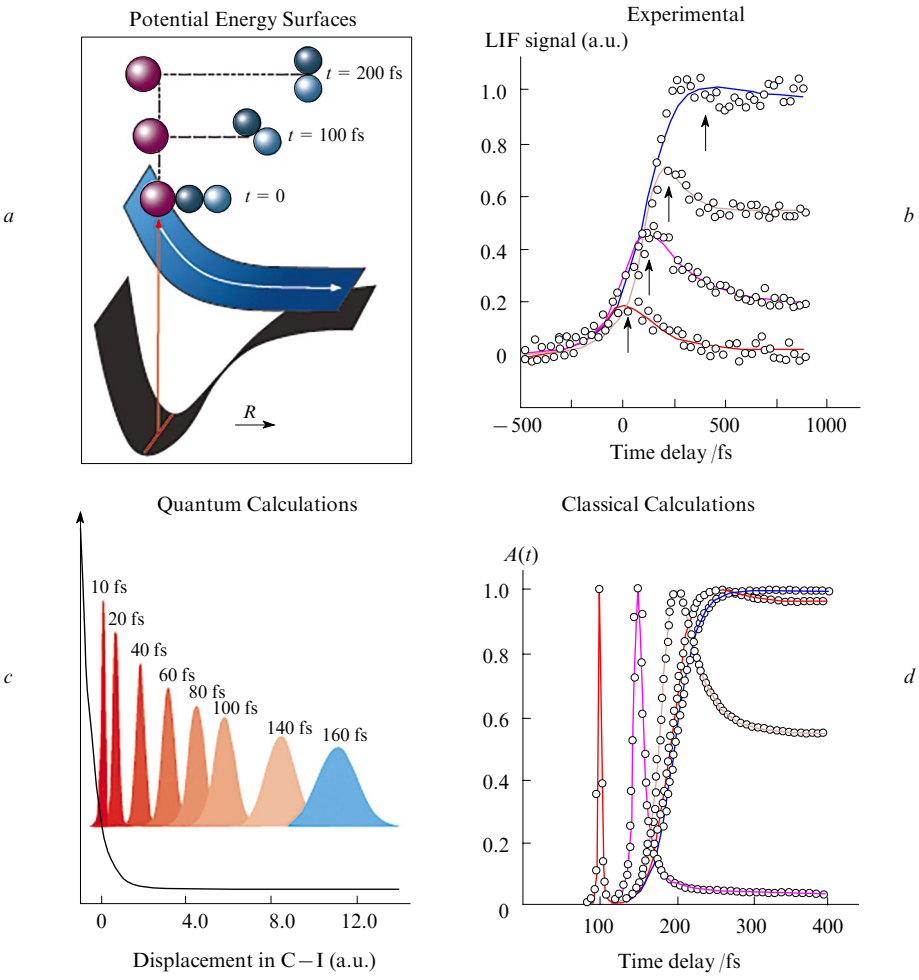


Figure 2. Illustration of FTS using the dissociation of ICN as an example.[70–72] A cartoon of the experiment is shown in (*a*). LIF: laser-induced fluorescence signal. The reaction takes place on the dissociative surface and is followed by the rise and decay of the CN fragment. By recording the CN signal as a function of time, for different probe laser wavelengths, the reaction process is clocked. The solid lines and arrows are guides to the eye and show the approximate peak positions for each data set (*b*). The lower panels show the results of quantum (*c*) and classical (*d*) calculations. $A(t)$ is the FTS signal defined in Ref. 70.

Another femtosecond pulse, the probe pulse, is used to record the CN fragment population as a function of time. Varying the wavelength allows to probe CN fragments at different R (Fig. 2). For this to work, the APES for fragment separation must be different in the ground and excited electronic states. Fortunately, such differences are expected to be general and account for the red wings in spectra involving dissociation and collision.[73] Consequently, the time scale for dissociation might also be inferred from an analysis of line shapes. But the challenge at hand is to record the temporal changes in the spectra and connect them to the shape of the APES on which the dissociation takes place. This requires a theoretical treatment that connects the time-resolved spectroscopic data to spatial positions on the PES ($V(R)$).[74, 75]

The 'two-dimensional' spectroscopic information (t, λ) offered by the pump-probe femtosecond photofragment method[73] enables the extraction of the TS dynamics on the dissociative APES. The important theoretical work of Heller[76] and a review by Polanyi and co-workers[48] offer further important details.

Real-time investigations of the rearrangement of bonds during chemical transformations require femtosecond time resolution, so that the atomic vibrations within the reacting molecules can be observed. Following the development of lasers capable of producing ultrashort laser pulses on this timescale, chemical reactions involving relatively simple molecules have been monitored in detail, revealing the transient existence of intermediate species as reactants are transformed into products.[77–80] The challenge remains how the photochemistry might change with increasing molecular complexity. In relatively simple molecules like ICN, by necessity only a few vibrational modes are involved. (In ICN, in fact, given the strength of the CN bond, there is only one labile coordinate). How does a photochemical reaction occur when there are numerous nonreactive modes for distributing the excited state energy?

III. Chemical dynamics *via* conical intersection between electronic states

The molecular time scales of chemistry require ultrafast optical methods to initiate the reactions. This explicitly limits the studies to photochemical processes. The hope is that the insights so gleamed can be generalized to different reaction mechanisms. In principle, one could try to catch the fleeting moment of a thermally heated sample. However, the statistics for a thermally sampled barrier crossing are such that at any instant, only one molecule in 10^8 is undergoing a barrier-crossing event for barrier heights of the order of 1 eV. In any experiment the background from nonreacting molecules completely obscures the observation of such rare events. Moreover, there is no means to synchronize thermal reactions, as the initial random thermal sampling to the critical point would be a highly distributed function. It is therefore not possible to atomically resolve thermally driven reactions on ground state surfaces. Perturbative methods using pump-probe protocols are needed in which a femtosecond laser excitation pulse is used to prepare the system on a reactive excited state surface. The ensuing photochemistry must occur under barrierless conditions to isolate the correlated motions leading the system through a barrier-crossing region. If there is an excited state barrier to the reaction of interest, one again is confronted with uncorrelated events involving a very small fraction of the system undergoing barrier crossing within the relevant barrier crossing time. The problem is not so different than the thermally sampled ground state problem, in which the crossing time is much shorter than the buildup of the transient intermediates to the final product ground state.[81]

The assumption here is that the excited state surface crosses through the same point in nuclear configurations, *i.e.*, there is a common crossing point for the thermal and the photoexcited reaction involving the formation of the same final product state. This assumption holds in most cases, except when the photoexcited surface lies energetically above multiple barriers to competing processes and relaxes to a distribution of photoproducts. In this case, the reaction dynamics needs to be treated as a uniquely excited state process. The information content is still rigorous with respect to comparing to time-dependent *ab initio* theory as part of the overall goal to develop the toolset to understand chemistry up to arbitrarily large complexity. Indeed, if the separation of the different reaction channels can be made, even in this limit, it should be possible to connect to the reaction modes involved in the thermally sampled region with sufficiently robust theoretical methods.[74, 75, 81, 82]

Conical intersections (CIs), also called 'photochemical funnels', provide the needed barrierless pathways for reactive crossings that occur on femtosecond timescales (see, *e.g.*, Ref. 83). At the intersections, the Born – Oppenheimer approximation breaks down, leading to dynamical processes that can be observed spectroscopically[84–86] and by TRED.[6, 8, 18, 87] This breakdown is particularly common in the photochemistry of polyatomic molecules with a large number of energetically close-lying electronic states and many nuclear degrees of freedom (Fig. 3).

Conical intersections have been found to be crucial in the mechanistic explanation of the photochemical behaviour of a variety of different organic and inorganic systems. Occurring whenever there is an electronic degeneracy, CIs were originally predicted on a mathematical basis by von Neumann and Wigner in 1929.[89] They found that two independent parameters need to be varied to achieve a degeneracy of eigenvalues of a real symmetric matrix (such as a real Hamiltonian matrix). The key idea was that the parameters were independent: if one thinks of them as geometrical parameters then one arrives at the noncrossing rule for diatomics. This rule states that with only one vibrational degree of freedom (the internuclear distance) two electronic states cannot cross if they are of the same symmetry. Teller realized that this does not hold for polyatomic molecules and consequently the PESs of polyatomic molecules may cross in a space of dimension $(n-2)$,[90] where n is the number of vibrational degrees of freedom ($(3N-6)$ for nonlinear polyatomic molecules composed of N atoms). Following von Neumann and Wigner, the two degrees of freedom that need to be independently varied to achieve a degeneracy are conventionally called the gradient difference vector ($\mathbf{X_1}$) and the derivative coupling vector ($\mathbf{X_2}$):[91, 92]

$$\mathbf{X_1} = \frac{\partial(\mathbf{E}_1 - \mathbf{E_2})}{\partial \mathbf{R}}$$

$$\mathbf{X_2} = \left\langle \psi_2(\mathbf{R}) \left| \frac{\partial \mathbf{H}_e}{\partial \mathbf{R}} \right| \psi_1(\mathbf{R}) \right\rangle$$

where $\mathbf{E}_1$ and $\mathbf{E}_2$ are the two electronic eigenvalues, $\mathbf{H}_e$ is defined as the electronic Hamiltonian, $\mathbf{R}$ is the vector of nuclear Cartesian displacements, and ψ_1 and ψ_2 are the

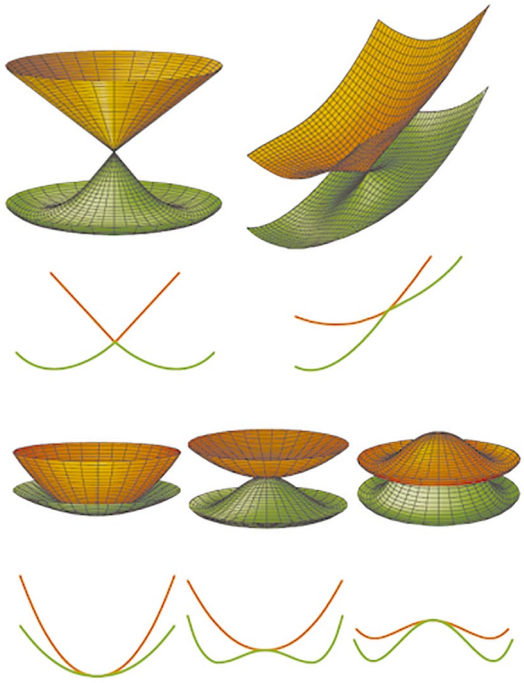


Figure 3. Topologies of conical intersection surfaces (top), and Renner – Teller surfaces (bottom). The top left shows a generic circular cone as is obtained from a Jahn – Teller problem with only linear vibronic coupling. The top right is a sloped conical intersection representing a general vibronic coupling situation where all three linear vibronic coupling constants are different. The cone is tilted because the force (gradient) vectors on both the upper and lower surfaces point in the same direction. The first-order topology (sloped *vs.* peaked) controls the nature of the photochemical reaction dynamics, and whether reactants are regenerated or photoproducts are formed. The bottom left to right show type-I, type-II and type-III Renner – Teller surfaces. These are obtained when only second-order vibronic coupling is included. Type-I involves destabilization on both the upper and lower surfaces with respect to the vibration, whereas type-II involves the stabilization on the lower surface and destabilization on the upper one. Type-III involves stabilization on both surfaces.[88]

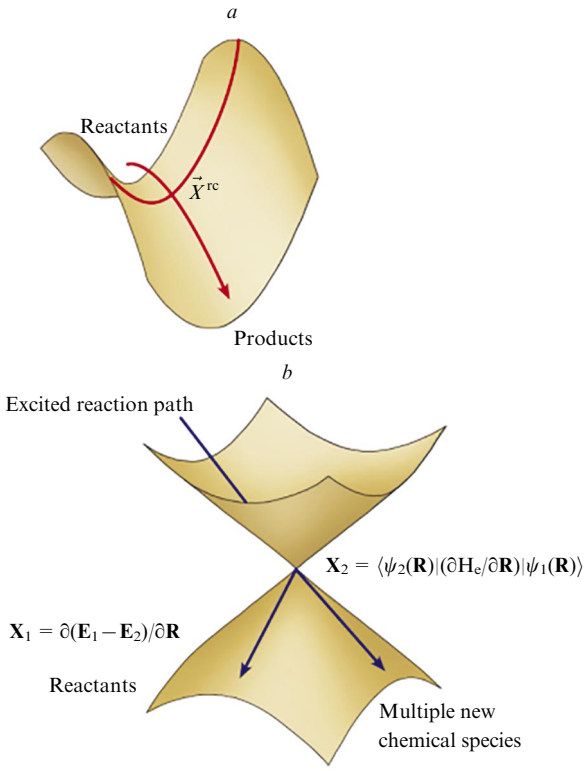


Figure 4. Reaction paths through a transition state (*a*) and a conical intersection (*b*).[93]

solutions of the electronic Schrödinger equation in a configuration interaction problem, *i.e.*, any standard representation of electronic states expanded in a basis of electron configurations.

An alternative way of thinking of these two vectors is that if one is at a degeneracy then (infinitesimal) movement in the plane spanned by these vectors (the so-called branching space) will lift the degeneracy.[92] When the electronic energy is plotted against these two vectors, one obtains the famous double-cone PESs (Fig. 4 *b*). Such regions represent 'photochemical funnels' that drive the system from the upper to the lower surfaces on the timescale of a single vibrational period. The cone may be circular in shape or possibly elliptic when the $\mathbf{X}_1$ and $\mathbf{X}_2$ vectors have different lengths (both representing the so-called peaked intersections, Fig. 4).

Conical intersections have been the subject of an increasing number of studies in the past two decades. They occur at degeneracies between molecular PESs and provide radiationless decay channels that influence the formation of different photoproducts. Two states are degenerate when they have the same electronic energy. In high-symmetry molecular systems, degeneracy leads to the Jahn – Teller effect[94 – 97] in which CIs are imposed by symmetry (the degenerate states are simply any pair of linearly independent combinations of the components of the degenerate electronic state). Studies of the mechanisms of such photoreactions and the molecular structures causing the radiationless decay are now routine. It is worth noting the differences of photochemical reactions occurring *via* a CI relative to thermal reactions confined to a single PES. A transition state connects the reactants with a single product in a single reaction path (*via* a motion along the transition vector $\mathbf{X}^{rc}$ (Fig. 4)). Conical intersections can connect reactants to two or more photoproducts by including many reaction paths (branching of the reaction path in the plane $\mathbf{X}_1$ and $\mathbf{X}_2$). The $\mathbf{X}_1$ and $\mathbf{X}_2$ vectors presented in Fig. 4 are known as the gradient difference and derivative coupling vectors, which are special internal coordinates that lift the degeneracy to first order in nuclear motion. The remaining $3N-8$ internal coordinates do not lift the degeneracy at the first order, and they span the intersection space, which is a hyperline consisting of an infinite number of CI points (known as the seam).

The position and local topology of a CI is crucial in determining the photochemical reactivity of a molecule. A peaked CI occurs when both PESs have orthogonal gradients near the intersection (such as that in Fig. 4). Such a topology leads to very efficient transitions from the excited state to the ground state. Examples of such CIs will be presented below for several systems. A sloped CI occurs when both APES have almost parallel gradients near the intersection. When two APESs of different spin states cross, such as in an intersystem crossing (ISC), the $\mathbf{X}_2$ vector is zero by symmetry and the surfaces cross in a seam of

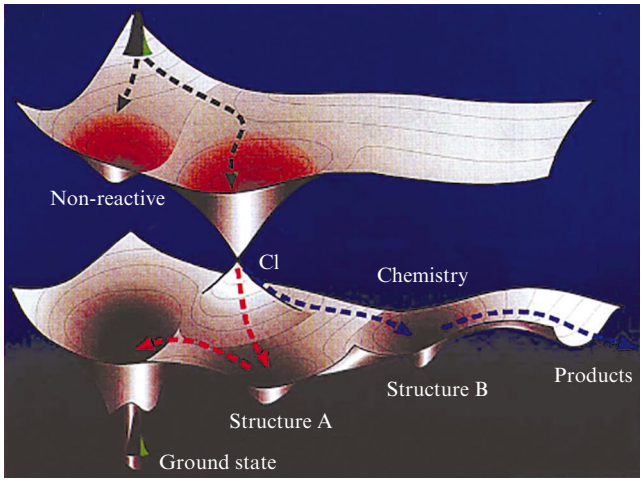


Figure 5. Illustration of reactive and non-reactive pathways (bifurcation) of wave packets near conical intersections.[72] Both non-reactive photophysical and reactive photochemical processes are shown.

dimension $3N-7$. Conical intersections are often called 'photochemical funnels' in organic photochemistry because they work as very efficient mechanisms for passing a system from an upper (excited) to a lower potential surface. The system can cross to the lower surface within a few (possibly only one) vibrational period(s). This is especially important in, for example, photostabilization mechanisms. In order to evaluate the efficiency of going through a CI, dynamics calculations are required as the system can cross at any point on the seam of the intersection. Different methods are available for this task, each with their own advantages and disadvantages (primarily computational cost and scaling) from classical trajectory to quantum wave packet simulations.

A generalized scheme showing reactive and non-reactive pathways (bifurcation) of the wave packets is shown in Fig. 5. Both photophysical and photochemical processes are shown with the CIs playing a crucial role. Examples are given in Refs 98 – 100.

Qualitative information can be obtained for larger systems with classical trajectory simulations, and for relatively small systems with quantum wave packet calculations with a suitable model Hamiltonian (*e.g.*, linear vibronic coupling[94 – 97]). As the Born – Oppenheimer approximation breaks down at the point of intersection, care must be taken when performing dynamics calculations. For further information on this point the reader is referred to several excellent articles.[83, 101] As recent publications show, the existence and relevance of CIs is no longer in doubt (see, *e.g.*, Refs 83, 91, 94 – 97, 101 – 105).

IV. Theory elements of time-resolved electron diffraction

The most direct way to study chemical reaction dynamics is to resolve, in real time, the molecular structures. There are numerous experimental probes that provide information related to structural changes. As a small subset, these include time-resolved absorption spectroscopy, IR spectroscopy, X-ray absorption/emission (resonant and near edge variants), XAFS, high harmonic attosecond methods, *etc.* These methods all require varying levels of theory to connect the observable to the structural changes without enough constraints to provide what could be construed at direct observation.

At present, only diffraction methods are able to provide sufficient constraints on the structures to constitute a direct observation. Even here, there are limits to the information content, and models are often needed to invert diffraction data to real-space structures. The power of diffraction methods is that the imaging source, either hard X-rays or high-energy electrons, can be fully characterized independently of the interaction of the system. The problem then reduces to an image reconstruction problem. In this respect, the spatial and temporal coherences of the sources can be determined to high accuracy such that the experiment is sensitive to even minute changes in molecular bond lengths (0.01 Å, *vide infra*). Nevertheless, even with orders of magnitude more constraints compared to spectroscopic observables, the problem still remains undetermined. The diffraction observable is an intensity measurement. Thus, the scattered electron or X-ray signal intensity depends on the modulus squared of the amplitude and the phase shift in the scattering process. There is not enough information to rigorously invert diffraction or reciprocal space images to real space. This issue is referred to as the phase problem and is a common problem associated with any scattering observable. To retrieve molecular structures, additional information is needed. The use of multiple wavelengths, anomalous scattering, known heavy atom scattering source terms, and reference fields for heterodyne detection, have been used to provide this information for static structure determination. However, in most cases, a model (*e.g.*, molecular replacement models for proteins) or theoretical refinement are employed for even static structure determination. More recently, it has been realized that for time-resolved structural studies one is not dealing with unknown initial structures and there are known constraints on conserved structural elements (bond lengths, bond angles) during the chemical transition. This additional information is sufficient to uniquely invert from reciprocal space to structural changes in real space with what can be considered well-defined causal relations.[17] This section provides the background to appreciate the challenges and recent advances in electron diffraction to yield atomically resolved, time-dependent views of structural transitions and chemical reactions.

It is important to emphasize that similar advances are occurring with X-ray diffraction, particularly with the recent introduction of X-ray free electron lasers (XFELs) as major international user facilities.[30] These so-called 4th generation light sources are many orders of magnitude brighter than previous generations. The issue of required source brightness for atomically resolved structural dynamics was first realized with electron sources. The spatial resolution and effective brightness of electron sources have undergone a major revolution comparable to X-rays. These table-top instruments have achieved the highest space-time image contrast for atomically resolved chemical reaction dynamics,[106] which is the major focus of the present review.

IV.1. Basic assumptions and approximations

A plane wave electron that is elastically scattered by an atom emerges as a spherical wave with the amplitude given by[107]

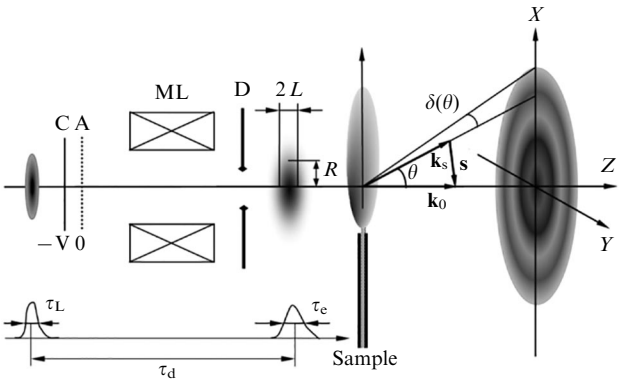


Figure 6. Illustration of the TRED for randomly oriented molecules and determination of the coordinates of the scattered electron: θ is the scattering angle; $\delta(\theta)$ is a correction to the scattering angle caused by Coulomb repulsion in the electron bunch; $\mathbf{k}_0$ and $\mathbf{k}_s$ are the wave vectors of the incident and scattered electrons, respectively; **s** is the momentum transfer vector in the laboratory frame XYZ; and λ is the wavelength of electrons. 'C' denotes photocathode, 'A' denotes anode, 'ML' denotes magnetic lenses, 'D' is diaphragm; τ_L is the duration of the laser pulse; τ_e is the electron pulse duration; L is the axis of the electron bunch in the direction of its motion; R is the axis of the electron bunch in the transverse direction; and τ_d is the time delay between the excitation laser pulse and the diagnosing electron pulse.

$$\Psi(R,\theta) = \frac{\exp(\boldsymbol{i}kR)}{R} f(\theta) \tag{1}$$

where R is the distance between the scattering centre and the detector plane and the absolute value of the wave vector **k** is given by $k = |\mathbf{k}| = 2\pi/\lambda$ with λ being the wavelength of the electron, and $\boldsymbol{i}$ is the imaginary unit. For an isolated atom, the atomic electron scattering amplitude $f(\theta)$ determines the amplitude of the electron beam scattered into the angle θ (Fig. 6).

As the electron traverses the atom, it experiences a phase shift, making the scattering factor complex. While for scattering from a single atom this phase shift is inconsequential, scattering from multiple atoms may entail different phase shifts from each individual atom.

The amplitude of the wave scattered by an atom i within a molecule is written as:[107]

$$\Psi_i(R,\theta) = [\exp(\boldsymbol{i}\mathbf{k}|\boldsymbol{R}-\mathbf{r}_i|)/|\boldsymbol{R}-\mathbf{r}_i|]\exp(\boldsymbol{i}\,\mathbf{k}_0 z_i)\cdot f_i(\theta) \tag{2}$$

where z_i is the projection of the atomic position vector $\mathbf{r}_i$ onto the Z axis (Fig. 6) and R is the scattering distance. Since R is a macroscopic parameter (*i.e.*, $\mathbf{r}_i \ll R$), Eqn (2) can be expressed as:

$$\Psi_i(R,\theta) = [\exp(\boldsymbol{i}kR)/R]\exp[\boldsymbol{i}(\mathbf{k}_0-\mathbf{k}_s)\mathbf{r}_i]\cdot f_i(\theta), \tag{3}$$

where $\mathbf{k}_0$ and $\mathbf{k}_s$ are the wave vectors of the incident and scattered electrons, respectively, and $|\mathbf{k}_0| = |\mathbf{k}_s|$ for elastic scattering.

Introducing the momentum transfer vector **s** with a magnitude of $|\mathbf{s}| = |\mathbf{k}_0-\mathbf{k}_s| = (4\pi/\lambda)\sin(\theta/2)$, and invoking the superposition principle, one obtains the amplitude of the electron wave scattered by the molecular system of N atoms as

$$\Psi = \sum_{i=1,N} \Psi_i = [\exp(\boldsymbol{i}kR)/R] \sum_{i=1,N} f_i(s)\exp(\boldsymbol{i}\mathbf{s}\mathbf{r}_i) \tag{4}$$

The intensity of the scattered electrons can be expressed in terms of the electron current density **j**:

$$\mathbf{j(s)} = (h\mathrm{e}/4\pi m_\mathrm{e}\boldsymbol{i})(\Psi^*\nabla\Psi - \Psi\nabla\Psi^*) \tag{5}$$

where h is the Planck constant; e and m_e are the electron charge and mass, respectively; ∇ is the gradient operator and Ψ^* is the complex conjugate wave function.

Using Eqns (4) and (5), one gets for the intensity:

$$\mathrm{I(s)} = \mathrm{I}_0(\mathbf{j}_{sc}/\mathbf{j}_0) = \mathrm{I}_0\mathrm{Re}\left\{(1/2\boldsymbol{i}\,\mathbf{k}_0)\sum_{i=1,N}(\Psi_i^*\nabla\Psi_i - \Psi_i\nabla\Psi_i^*)\right\} = \tag{6}$$

$$= (\mathrm{I}_0/R^2)\mathrm{Re}\left\{\sum_{i=1,N} f_i(s)\exp(\boldsymbol{i}\mathbf{s}\mathbf{r}_i)\sum_{j=1,N} f_j^*(s)\exp(-\boldsymbol{i}\mathbf{s}\mathbf{r}_j)\right\} =$$

$$= (\mathrm{I}_0/R^2)\left\{\sum_{i=1,N}|f_i(s)|^2 + \mathrm{Re}\sum_{i\neq j=1,N} f_i(s)f_j^*\exp[\boldsymbol{i}\mathbf{s}(\mathbf{r}_i-\mathbf{r}_j)]\right\}$$

In Eqn (6), I_0 is the intensity of the incident electron beam; $\mathbf{j}_0 = (hk_0\mathrm{e}/2\pi m_\mathrm{e})$ and $\mathbf{j}_{sc}$ are the current densities for the incident and the scattered electrons, respectively; and Re denotes the real part of the function. Higher-order terms corresponding to multiple scattering are neglected for the current purpose.

Equation (6) is often written as $\mathrm{I(s)} = \mathrm{I_a(s)} + \mathrm{I_{mol}(s)}$, where the first term is ascribed to the 'atomic scattering' because it does not depend on the internuclear distances. The second term, which depends on the internuclear distances, is ascribed to the 'molecular scattering'. For each pair of atoms (i,j) separated by the instantaneous internuclear distance $\mathbf{r}_{ij} = \mathbf{r}_i - \mathbf{r}_j$, Eqn (6) yields the molecular intensity function

$$\mathrm{I_{mol}(s)} = \tag{7}$$

$$= (\mathrm{I}_0/R^2)\mathrm{Re}\left\{\sum\sum_{i\neq j=1,N}|f_i(s)||f_j(s)|\exp[\boldsymbol{i}\Delta\eta_{ij}(s)]\cdot\exp(\boldsymbol{i}\mathbf{s}\mathbf{r}_{ij})\right\}$$

where $\Delta\eta_{ij}(s)$ is the difference in the phase shifts incurred by the electrons while scattering from the atoms i and j, respectively.[107, 108]

Inherent in Eqn (7) is an approximation known as the independent atom model (IAM), which assumes that the electronic wave function of each atom in a molecule is just that of the isolated atom.[36] This implies that the effects of chemical bonding on the electron density distribution of the atoms are ignored. Within the IAM approximation, the molecular environment of an atom does not affect its scattering, so that tabulated atomic scattering factors can be used for each atom in a molecule.

Assuming single scattering processes for fast electrons (> 10 keV) with short (attosecond) coherence time, the electrons encounter molecules that are essentially 'frozen' in their rotational and vibrational states. Thus, the latter can be accounted for by using the probability density functions (PDF) that characterize the ensemble under investigation. If the molecular systems investigated are not at equilibrium, as is the case in studies of laser-excited molecules, a time-dependent PDF must be used to describe the structural evolution of the system. In addition, rotational and vibrational motions can be separated adiabati-

cally, since the latter involves much faster processes. The time-dependent molecular intensities can then be represented by averaging Eqn (7) with the PDF that represents the spatial and vibrational distributions of the scattering ensemble:[109]

$$\mathrm{I_{mol}(s,t)} = \langle\langle \mathrm{I_{mol}(s)}\rangle_{\mathrm{vib}}\rangle_{\mathrm{sp}} = \tag{8}$$

$$= (\mathrm{I_0}/R^2)\sum \sum_{i\neq j=1,N} |f_i(s)||f_j(s)| \times$$

$$\times \mathrm{Re}\{\exp[i\Delta\eta_{ij}(s)]\langle\langle \exp(i\mathbf{s}\mathbf{r}_{ij})\rangle_{\mathrm{vib}}\rangle_{\mathrm{sp}}\} =$$

$$= (\mathbf{I_0}/R^2)\sum \sum_{i\neq j=1,N} |f_i(s)||f_j(s)|\cos(\Delta\eta_{ij}(s)) \times$$

$$\times \mathrm{Re}\int_{0,\infty} P_{\mathrm{vib}}(\mathrm{r}_{ij},t)\left[\int_{0,\pi}\int_{0,2\pi} P_{\mathrm{sp}}(\alpha_{ij},\beta_{ij},t)\exp(i\mathbf{s}\mathbf{r}_{ij})\cdot\sin\alpha_{ij}\,\mathrm{d}\beta_{ij}\,\mathrm{d}\alpha_{ij}\right]\mathrm{d}\mathrm{r}_{ij}$$

In Eqn (8), $\langle ... \rangle$ denotes the vibrational and spatial (orientation) averaging over the scattering ensemble; $P_{\mathrm{vib}}(r_{ij},t)$ and $P_{\mathrm{sp}}(\alpha_{ij},\beta_{ij},t)$ are the vibrational and spatial PDF, respectively; and α_{ij} and β_{ij} are the angles of the spherical polar coordinate system (Fig. 7) that define the orientation of the internuclear distance vector $\mathbf{r}_{ij}$ in the scattering coordinate frame.

For spatially isotropic, randomly oriented molecules, $P_{\mathrm{sp}}(\alpha_{ij},\beta_{ij}) = 1/4\pi$, and Eqn (8) simplifies to the following expression for the time-dependent molecular intensity function:

$$\mathrm{I_{mol}}(s,t) = (\mathrm{I_0}/R^2)\sum_{i\neq j=1,N} |f_i(s)||f_j(s)|\cos(\Delta\eta_{ij}(s)) \times \tag{8a}$$
$$\times \int P_{\mathrm{vib}}(\mathrm{r}_{ij},t)[\sin(\mathrm{sr}_{ij})/\mathrm{sr}_{ij}]\mathrm{d}\mathrm{r}_{ij}$$

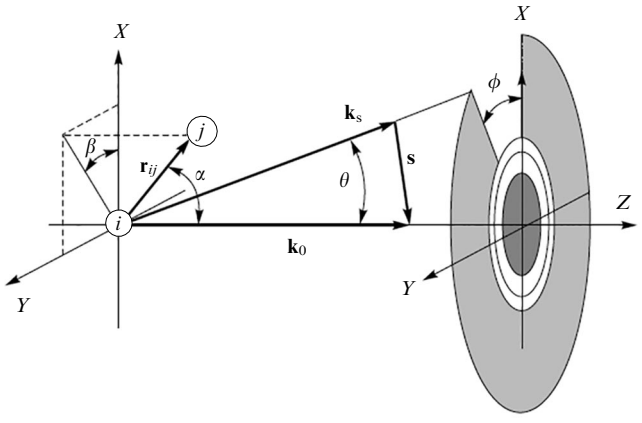


Figure 7. Definition of scattering coordinates used for the development of intensity equations in electron diffraction. Expanded view from Fig. 6. Here, θ is the scattering angle and ϕ the azimuthal angle in the detector plane; $\mathbf{k}_0$ and $\mathbf{k}_s$ are the wave vectors of the incident and scattered electrons, respectively; $\mathbf{s}$ is the momentum transfer vector; $\mathbf{r}_{ij}$ is the internuclear distance vector between the nuclei of atoms i and j, which are positioned at $\mathbf{r}_i$ and $\mathbf{r}_j$, respectively; and α and β give the orientation of the molecular framework with respect to the XYZ laboratory frame.

The time-dependent PDF $P_{\mathrm{sp}}(\alpha_{ij},\beta_{ij},t)$ and $P_{\mathrm{vib}}(\mathrm{r}_{ij},t)$ in Eqn (8) determine the molecular intensity function, $\mathrm{I_{mol}}(s,t)$, at time t. The former describes the evolution of the spatial distribution in the system under investigation. The vibrational PDF describes the evolution of the structure in the ensemble of laser-excited species. In what follows, we concentrate on the internuclear dynamics that evolves on a time-scale much shorter than the orientation effects, such as the rotational recurrence.[5] Therefore, only the time-independent spatial PDF, $P_{\mathrm{sp}}(\alpha_{\mathrm{ij}},\beta_{\mathrm{ij}})$, will be considered in the current analysis. For the particular case of a molecular ensemble at thermal equilibrium, Eqn (8) can be written in the form first derived by Debye:[110]

$$\mathrm{I_{mol}}(s) \propto \mathrm{Re}\sum \sum_{i\neq j=1,N} f_i^* f_j \langle \sin(\mathrm{sr}_{ij})/\mathrm{sr}_{ij}\rangle_{\text{vib-rot}} = \tag{9}$$

$$= \sum \sum_{i\neq j=1,N} |f_i||f_j|\cos[\eta_i(s)-\eta_j(s)]\int[\sin(\mathrm{sr}_{ij})/\mathrm{sr}_{ij}]\mathrm{d}F_T(\mathrm{r}_{ij})$$

where $F_T(\mathrm{r}_{ij})$ is the probability distribution function at the vibrational temperature T and $\mathrm{d}F_T(\mathrm{r}_{ij}) = P_T(\mathrm{r}_{ij})\mathrm{d}\mathrm{r}_{ij}$.

As in the time-independent case, the method of averaging in Eqn (8) may be defined freely, so long as certain conditions of convergence and normalization are fulfilled. The modified molecular intensity function $sM(s,t)$ can be calculated as:

$$sM(s,t) = sI_{\mathrm{mol}}(s,t)/I_{\mathrm{at}}(s) \tag{10}$$

where $I_{\mathrm{at}}(s)$ is the atomic background [108] considered here to be time-independent.

We now consider more generally the intensities of electrons scattered by a molecular ensemble after excitation by a short laser pulse. Let us assume that the laser field produces a wave packet of highly vibrationally excited states that propagates on the PES of the excited electronic state of the molecule. The time-dependent function $\Psi(r,t)$ of the wave packet can be expanded in terms of the orthonormal basis functions $\varphi_n(r)$ in the following way (see, for example, Ref. 111):

$$\Psi(r,t) = \sum_{n=0,\infty} C_n\varphi_n(r)\exp(-2\pi i E_n t/h) \tag{11}$$

where n is the quantum number identifying the state with the energy E_n, C_n is the amplitude and $\varphi_n(r)$ are a complete set of arbitrary analytic functions.

The modified molecular intensity for randomly oriented species can then be represented by:[112]

$$sM(s,t) = g(s)\int \Psi^*(r,t)\Psi(r,t)[\sin(\mathrm{sr})/\mathrm{r}]\mathrm{d}\mathrm{r} = \tag{12}$$

$$= g(s)\mathrm{Re}\left\{\sum \sum_{n,m=0,\infty} C_m^* C_n \exp(-2\pi i\Delta E_{mn}t/h)\times\right.$$

$$\left.\times \int \varphi_m^*(r)\varphi_n(r)\,[\sin(\mathrm{sr})/\mathrm{r}]\mathrm{d}\mathrm{r}\right\}$$

where $\Delta E_{mn} = E_m - E_n$, and $g(s)$ is the reduced atomic scattering factor.[108]

Therefore, the radial distribution function obtained from a TRED experiment, *i.e.*, the Fourier transform,

$f(r,t)$, of the modified molecular intensity $sM(s,t)$, also depends explicitly on both the internuclear distances *and* the time. Thus, it contains direct information on the time evolution of the molecular structure through:

$$f(r,t) = (2/\pi)^{1/2}\,\mathrm{Re}\int sM(s,t)\exp(\boldsymbol{i}\mathbf{sr})\mathrm{d}s \qquad (13)$$

Applying the general form of the molecular intensity, Eqn (8), to the 1D case, it is possible to write:

$$sM(s,t) = g(s)\int P(r,t)[\sin(\mathrm{sr})/\mathrm{r}]\mathrm{d}r \qquad (14)$$

where $P(r,t) = \Psi^*(r,t)\Psi(r,t)$ and, consequently:

$$F(r,t) \propto P(r,t)/\mathrm{r} \qquad (15)$$

Thus, Eqns (12) – (15) show that in TRED, the modified molecular intensities of scattered electrons depend explicitly on both the time evolution of internuclear distances and the energy distribution. Averaging the molecular intensity function $sM(s,t)$ over an electron pulse profile function $I_0(t,t_\mathrm{d})$ yields the TRED diffraction intensities $sM(s,t_\mathrm{d})$, parametrically dependent on the time delay t_d between the pump laser pulse and the electron probe pulse of duration τ:

$$\langle sM(s,t_\mathrm{d})\rangle_\tau = \int\limits_{t,t+\tau} I_0(t',t_\mathrm{d})sM(s,t')\mathrm{d}t' \qquad (16)$$

In this way data refinement involves minimization of the functional:

$$\sum_{i=1,m}[\langle s_iM(s_i,t_\mathrm{d})\rangle_{\tau,\mathrm{exp}} - \boldsymbol{R}\langle s_iM(s_i,t_\mathrm{d})\rangle_{\tau,\mathrm{theor}}]^2 \qquad (17)$$

where m is the number of data points and $\boldsymbol{R}$ the index of resolution.

As mentioned above, the solution of the inverse diffraction problem is a characteristically ill-posed problem [113, 114] and is described for TRED data refinement in Chapters 2 and 4 of the monograph.[6]

IV.2. Aligned molecules

The application of femtosecond laser pulses made it possible to observe for the first time the real-time dynamics of fast elementary molecular processes and to obtain snapshots of molecules at different stages of chemical reactions. The new discipline, *Femtochemistry* [72, 80, 115, 116] or *Coherent chemistry*,[40] emerged. The time resolution provided by femtosecond laser pulses proved sufficient for investigations into the nuclear dynamics in the molecule.

Because of the random orientation of molecules in the gas phase, unlike X-ray diffraction of a crystal, the electron diffraction technique in the absence of additional information (*e.g.*, about the equilibrium configuration symmetry of the system studied, equivalence of certain chemical bonds, character of vibrational energy distribution) permits determining only a 1D molecular structure or a set of internuclear distances. It restricts applications of the electron diffraction method for studying the structure and dynamics of complex polyatomic molecules. The solution of a structure-related problem even in the case of relatively small molecules implies the involvement of results obtained by other experimental methods, such as vibrational spectroscopy and/or quantum chemical computation.

X-ray and electron crystallography are believed to be the most adequate tools for the structure elucidation of complex polyatomic molecules. However, these methods can be applied only for the study of crystalline objects. Moreover, the local environment of a molecule in the crystals can alter its conformational distribution and imposes barriers to certain motions through intermolecular contacts that makes it difficult to connect the nuclear dynamics from the condensed phase to isolated systems.

An approach to increase the information content takes advantage of the TRED method as applied to anisotropic ensembles ('oriented' molecules whose dipole transitions are oriented in the direction of polarization of the laser radiation) in the gas phase. The anisotropic environment of laser-excited molecules can be formed, for example, under the action of femtosecond pulses of polarized laser radiation. It was theoretically predicted [5, 109, 117 – 121] that the electron diffraction pattern from 'oriented' molecules in the gas phase furnishes an opportunity of determining not only internuclear distances but also bond angles.

The theory was for the first time confirmed experimentally [122, 123] for adiabatically oriented CS_2 molecules using the TRED method with a resolution of 10 ns. To elucidate the structure of organic molecules, such as low-molecular-mass proteins scarcely amenable to crystallization, the authors of Ref. 124 used a jet of liquid gel droplets and a continuous electron beam producing a diffraction pattern. Organic molecules, *e.g.*, small proteins, in a droplet or inside a glassy ice shell can be spatially oriented under the action of polarized radiation of a powerful continuous wave laser. Iterative methods for solving the phase problem have been proposed.

The action of ultrashort pulses of polarized laser radiation on an isotropic medium of randomly oriented molecules leads to photoexcitation of those molecules with transition dipole moments oriented in the direction of the laser radiation polarization. Thus, a spatial anisotropy of coherently excited molecules is created, generating different types of spatial order in the ensemble. The electron scattering theory for spatially oriented ensembles of molecules requires substantial modification of the electron diffraction theory for randomly oriented molecules in the gas phase (see Chapter IV in Ref. 6 or Ref. 8). Assume as above single scattering processes for fast electrons (> 10 keV) within the 'frozen' snapshot scattering process of molecules that are now in nonequilibrium rotational and vibrational excited states. One must use a time-dependent PDF to describe the structural evolution of the system. In addition, rotational and vibrational motions can be separated adiabatically as above, since the latter involves much faster processes.

The orientational PDF for an ensemble of laser-excited molecules was described in several publications.[125 – 127] A systematic study was carried out by Zare.[126] In that study, equations were obtained using classical and QM approximations. For spatial anisotropies produced by linearly polarized laser beams, these approximations yield similar results.

While Eqn (8) is general enough for the description of polyatomic molecules, we first consider the case of linear polyatomic molecules. For electron scattering from oriented linear molecules we need to consider two main cases, *viz.*, scattering from molecules oriented parallel to the primary electron beam, which will be called parallel scattering, and

scattering from molecules oriented perpendicular to the incident electron beam, which we call perpendicular scattering. In the first case, $P_{sp}(\alpha,\beta;t)$ depends only on angle α (Fig. 7), since the polarization of the laser beam is collinear to the Z axis. Laser radiation at $t = 0$ separates the excited and unexcited molecules ensembles. In this case, the orientational PDF can be written as:[125, 126]

$$||P_{sp}^{ex}(\alpha) = (3/4\pi)\cos^2\alpha \quad (18)$$

$$||P_{sp}^{unex}(\alpha) = (3/8\pi)\sin^2\alpha \quad (19)$$

where $||P_{sp}^{ex}$ and $||P_{sp}^{unex}$ refer to the excited and unexcited ensembles, respectively.

For perpendicular scattering, the polarization vector of the laser beam is perpendicular to the Z axis and the orientational PDF depends on the angles α and β:

$$\perp P_{sp}^{ex}(\alpha,\beta) = (3/4\pi)\sin^2\alpha\cdot\cos^2\beta \quad (20)$$

$$\perp P_{sp}^{unex}(\alpha,\beta) = (3/8\pi)(1-\sin^2\alpha\cdot\cos^2\beta) \quad (21)$$

The scalar product $(\mathbf{sr}_{ij})$ in Eqn (8) can be written in terms of trigonometric functions of the angles α and β, which determine the orientation of the vector $\mathbf{r}_{ij}$ in the coordinates of the scattering angles θ and ϕ, which describe electron scattering:

$$(\mathbf{sr}_{ij}) = [-\cos\phi\cdot\cos(\theta/2)\cdot\sin\alpha\cdot\cos\beta - \quad (22)$$
$$-\sin\phi\cdot\cos(\theta/2)\cdot\sin\alpha\cdot\sin\beta + \sin(\theta/2)\cdot\cos\alpha]sr_{ij}$$

Using the Eqn (8) and the orientational PDF given by Eqns (18) – (21), after integration over α and β (Refs 128, 129) we obtain the intensities for parallel molecular scattering of electrons:

$$||I_{mol}^{ex}(s,t) = (I_0/R^2)\sum_{i\neq j=1,N}|f_i(s)||f_j(s)|\cos(\Delta\eta_{ij}(s))\times \quad (23)$$
$$\times\int P_{vib}(r_{ij},t)\{[\sin(sr_{ij})/sr_{ij}][(1/s^2r_{ij}^2)(1-3s^2/4k_0^2)+$$
$$+ s^2/4k_0^2]-[\cos(sr_{ij})/s^2r_{ij}^2](1-3s^2/4k_0^2)\}dr_{ij}$$

$$||I_{mol}^{unex}(s,t) = (I_0/R^2)\sum_{i\neq j=1,N}|f_i(s)||f_j(s)|\cos(\Delta\eta_{ij}(s))\times \quad (24)$$
$$\times\int P_{vib}(r_{ij},t)\{[\sin(sr_{ij})/(sr_{ij})][(1-s^2/4k_0^2]-[\cos(sr_{ij})-$$
$$-\sin(sr_{ij})/(sr_{ij})](1/s^2r_{ij}^2)(1-3s^2/4k_0^2)\}dr_{ij}$$

As can be seen from Eqns (23) and (24), the dependence on the electron wavelength ($k_0 = 2\pi/\lambda$) is weak for electrons with energies greater than 10 keV in the whole range of typical values of s. Moreover, just as in the case of isotropically oriented molecules, the scattering intensity is axially symmetric and depends only on the scattering angle θ.

In contrast to this result, the intensity of perpendicular molecular scattering is not axially symmetric and explicitly depends on the azimuthal angle ϕ:

$$\perp \mathbf{I}_{mol}^{ex}(s,\phi,t) = (I_0/R^2)\sum_{i\neq j=1,N}|f_i(s)||f_j(s)|\cos(\Delta\eta_{ij}(s))\times \quad (25)$$
$$\times\int P_{vib}(r_{ij},t)\{[\sin(sr_{ij})/(sr_{ij})-\cos(sr_{ij})](1/sr_{ij})^2-(1-s^2/4k_0^2)\times$$
$$[(3/s^3r_{ij}^3-1/sr_{ij})\sin(sr_{ij})-(3/s^2r_{ij}^2)\cos(sr_{ij})]\cos^2\phi\}dr_{ij}$$

$$\perp \mathbf{I}_{mol}^{unex}(s,\phi,t) = (I_0/R^2)\sum_{i\neq j=1,N}|f_i(s)||f_j(s)|\cos(\Delta\eta_{ij}(s))\times \quad (26)$$
$$\times\int P_{vib}(r_{ij},t)\{[\sin(sr_{ij})/(sr_{ij})][1-(1-s^2/4k_0^2)\cos^2\phi]+$$
$$+[\cos(sr_{ij})-\sin(sr_{ij})/(sr_{ij})](1/sr_{ij})^2[1-(1-s^2/4k_0^2)3\cos^2\phi]\}dr_{ij}$$

For derivation of those equations, each orientational PDF specified by Eqns (18) – (21) was normalized. Therefore, $\mathbf{I}_{mol}(s,t)$ represented by Eqns (23) – (26) are also normalized. In the ensemble of excited and unexcited particles, the corresponding relative weights of these states must be introduced.[109] Equations (8) – (11) require explicit equations for $P_{vib}(\mathbf{r}_{ij},t)$, which can be calculated using, *e.g.*, a stochastic approach.[109]

In order to account for quantum effects in the diffraction intensity, it is required to define time-dependent PDFs, $P(r,t) = |\psi(r,t)|^2$ by solving the corresponding time-dependent Schrödinger equation. Various approaches for solving this problem were suggested.[130 – 132] It was also proposed [109] to use the Fourier grid Hamiltonian (FGH) method.[132 – 135]

The key point in the above treatment is to illustrate that the very act of photoexcitation with polarized light introduces anisotropy into the electron scattering problem that, with proper care, can be explicitly used to extract more information on the structural dynamics in the same manner as the use of external perturbations to align the molecules. The photoexcitation process is intrinsic to time-resolved measurements and inherently provides effective alignment of the photoexcited ensemble, which can be readily separated from the unexcited ensemble with differential detection.

IV.3. Solution of the inversion problem

The averaging of the molecular intensity function $sM(s,t)$ *via* the temporal profile of the electron bunch $\mathbf{I}_0(t,t_d)$ gives the diffraction intensities in TRED, $sM(s,t_d)$, with parametric dependence on the time delay t_d between the pump laser pulse and the electron probe pulse τ:

$$\langle sM(s,t_d)\rangle_\tau = \int_{t,t+\tau} I_0(t',t_d)sM(s,t')dt' \quad (27)$$

In this case, to solve the inversion problem of the revision of the parameters in the model used, it is necessary to minimize the functional

$$\sum_{i=1,m}[\langle s_iM(s_i,t_d)\rangle_{\tau,exp} - \Re\langle s_iM(s_i,t_d)\rangle_{\tau,theor}]^2 \quad (28)$$

where m is the number of points (number of experimental values of the scattering intensity $s_iM(s_i,t_d)$) for the time delay t_d and $\Re$ is the index of resolution. The solution of the inversion problem in diffraction is an ill-posed problem. To solve multi-parameter problems, one can use a rather effective regularization method.[113, 114, 136] In this case, it is

possible to extract the so-called quasi-solution by minimizing the functional

$$M^{\alpha} = \sum_{i=1,m} [\langle s_i M(s_i,t_d)\rangle_{\tau,exp} - \Re\langle s_i M(s_i,t_d)\rangle_{\tau,theor}]^2 + \quad (29)$$

$$+ \alpha\Omega[\langle P(r,t_d)\rangle_{\tau}] \to \min$$

where the stabilizing term $\Omega(P(r,t_d))_{\tau}$ is expressed by a polynomial:

$$\Omega[\langle P(r,t_d)\rangle_{\tau}] = \sum \sum_{i\neq j=1,N} \int \sum_{n=0,p} q_n(r_{ij}) \times \quad (30)$$

$$\times [d^n\langle P(r,t_d)\rangle_{\tau} / dr_{ij}^n]^2 \, dr_{ij}$$

where $q_n(r_{ij})$ are non-negative functions, and $\langle P(r,t_d)\rangle_{\tau}$ is the probability density of the distribution of interatomic distances for the time delay t_d averaged over time.

Two approaches to the choice of the regularization parameter α have been tested. In the first technique, the parameter α has been calculated following Miller [137] and Miller and Viano:[138]

$$\alpha = \alpha(\sigma,E) = \sigma^2/E^2 \quad (31)$$

$$\sigma^2 \geqslant ||\langle s_i M(s_i,t_d)\rangle_{\tau,exp} - \Re\langle s_i M(s_i,t_d)\rangle_{\tau,theor}|| \quad (32)$$

$$E^2 \geqslant \sum \sum_{i\neq j=1,N} \int \sum_{n=0,p} q_n(r_{ij}) [d^n\langle P(r,t_d)\rangle_{\tau}/dr_{ij}^n]^2 dr_{ij} \quad (33)$$

The regularization method [137, 138] was chosen because it allows one to estimate the accuracy of parameters. In an alternative approach,[139] the regularization parameter α can be optimized by minimizing the functional

$$R_f^2(\alpha,\xi^{\alpha}) = \sum_{i=1,m} [\langle s_i M(s_i,t_d)\rangle_{\tau,exp} - \quad (34)$$

$$- \Re\langle s_i M(s_i,t_d,\xi^{\alpha})\rangle_{\tau,\tau theor}]^2 / \sum_{i=1,m} [\langle s_i M(s_i,t_d)\rangle_{\tau,exp}]^2$$

where ξ^{α} is the set of refined parameters that depend on the regularization parameter α as described in Refs 140 and 141. The use of the regularization method in TRED experiments was reported.[23] It was shown that the stabilizing functional $\Omega(P(r,t_d))$ makes it possible to significantly stabilize the minimization process.[5]

IV.4. The difference method for time-dependent diffraction data analysis

The recorded diffraction patterns are dependent on the time delay between the pump (laser) pulse and the probe (electron) pulse. Having denoted the difference curves related to the structural changes in the transition state as $\Delta I(s,t_{ref},t)$,

$$\Delta I(s,t_{ref},t) = I(s,t_{ref}) - I(s,t) \quad (35)$$

we get

$$\Delta sM(s,t_{ref},t) = sM(s,t_{ref}) - sM(s,t) \quad (36)$$

The difference radial distribution curves $\Delta f(r,t_{ref},t)$ in the space of interatomic distances r are then obtained by the Fourier transform of the difference curves $\Delta sM(s,t_{ref},t)$ given by Eqn (36).

The theoretical equivalent of the time-dependent scattering intensity with the non-equilibrium distribution in this system can be calculated using a cumulant representation of the scattering intensity and, for example, a stochastic approach to the analysis of diffraction data, as was shown to be effective in the TRED analysis of photodissociation of CS_2.[23]

IV.5. Time-dependent diffraction from single crystals and the solution of the inversion problem

The highest spatial resolution of structures is obtained from single crystals. This fact is owed to the amplification factor of N^2 in diffraction and the further amplification into specific diffraction orders reflecting the underlying lattice periodicity and alignment of all the molecules into the particular symmetry group of the crystal lattice. Electrons scatter off the electrostatic potential, whereas X-rays scatter from the polarization induced to the electron density. The difference in the scattering mechanisms and a more-than-ten-times shorter wavelength typical of electrons over X-rays makes electron diffraction more sensitive to nuclear positions and able to achieve a higher spatial resolution. For certain chemical reactions, a spatial resolution of the order of 0.01 – 0.1 Å (*vide supra*) is needed as even such small motions significantly contribute to the reaction energetics. Electron diffraction is well capable of this level of spatial resolution for single crystal studies. As above with gas-phase diffraction, the inversion from reciprocal space to real space is challenging.

The electrostatic potential giving rise to the observable is defined by:[142]

$$\phi(\mathbf{k}) = (1/\Omega) \sum_{j=1,N} [f_j^B(\mathbf{k})/A] \exp(\boldsymbol{i}\,\mathbf{k}\mathbf{r}_j) \quad (37)$$

where $A = 2\pi/h^2 m_e e$ and f_j^B are the atomic form factors or scattering amplitudes for atom j, which depends on the atomic properties (scales as Z), the thermal vibrations of the atoms in the molecule, and the scattering angle. In Eqn (37), Ω is the unit cell volume, m_e is the electron mass and e is the electron charge. The term $\phi(\mathbf{k})$ is related to the diffracted intensity through the structure factor $F(\mathbf{k})$,

$$F(\mathbf{k}) = (2\pi m_e e\Omega/h^2)\phi(\mathbf{k}) = \sum_{j=1,N} f_j^B(\mathbf{k}) \exp(\boldsymbol{i}\mathbf{k}\mathbf{r}_j) \quad (38)$$

and has to be made more general to include the specific (*hkl*) Miller indices defining the particular crystal symmetry and unit cell parameters. From inspection, this relation gives the modulus of the lattice potential, whereas one measures diffraction intensities that are then proportional to the square of the structure factors $|F|^2$. The phase factor of the exponential term $(\boldsymbol{i}\mathbf{k}\mathbf{r}_j)$ in this equation leads to the inversion problem. The structure factors are the most important quantities in structure determination. As written, Eqn (38) only considers diffraction from a lattice structure. Therefore, the phase could be anything and this would weight the observed amplitude similar to a change in spatial relationship between atoms.

For time-resolved measurements, the observable is again the differential detection of the change in the structure factors in which both the excited and unexcited fraction of unit cells need to be included. The excitation process involves random absorption events such that the observed diffraction pattern is just the sum of the excited and unexcited unit cells, *i.e*,

$$|F_{on}(\mathbf{k},t)|^2 = |\eta_{exc}F_{exc}(\mathbf{k},t)|^2 + |(1-\eta_{exc})F_{off}(\mathbf{k})|^2 \quad (39)$$

where $F_{on}(\mathbf{k},t)$ is the weighted sum of the excited and total unit cell structure factor, η_{exc} is the fraction excited, which can be measured independently, and the structure factors F_{exc} and F_{off} refer to the excited and unexcited unit cells, respectively. The challenge is to determine the structure factors $|F_{exc}(\mathbf{k},t)|$ in the face of the unknown phase term weighting the diffracted intensity. In conventional crystallography, one normally samples a large number of different crystal orientations to fully sample the reciprocal space and then uses a model for refinement. The larger the sampling of the reciprocal space the more accurate this procedure, although it remains model dependent. For femtosecond electron diffraction studies, there are limitations on the number of samples and problems with maintaining alignment of excitation and probe for crystal rotation. There are limited means of preparing different crystal orientations, such that femtosecond electron diffraction (FED) generally undersamples the reciprocal space relative to conventional crystallography. It must be born in mind that the objective is to determine structural changes on going from a known initial structure (reactant state) to a known final structure (product state) rather than an unknown structure. It has recently been shown that the known initial structure and known conserved terms in the molecular structure provide sufficient information for a unique inversion – as a solution of the inversion problem.

In this respect, the are a number of tests for convergence. The most commonly used version is the R_f-factor:[143]

$$R_f = \left(\sum_{hkl}||F_{obs}(hkl)| - |F_{cal}(hkl)||\right) \Big/ \left(\sum_{hkl}|F_{obs}(hkl)|\right) \quad (40)$$

where F_{obs} and F_{cal} are the observed and experimental unit cell structure factors, respectively.

Another measure is the Pearson correlation function, which has the advantage that it is not sensitive to exchange between where F_{obs} and F_{cal}, if one overestimates one or the other value. The Pearson correlation coefficient, $\gamma(F_1, F_2)$, is defined as [144]

$$\gamma(F_1, F_2) = \frac{\sum_{\mathbf{k}} c_1(\mathbf{k})c_2(\mathbf{k})}{\sqrt{\sum_{\mathbf{k}} c_1(\mathbf{k})^2}\sqrt{\sum_{\mathbf{k}} c_2(\mathbf{k})^2}} \quad (41)$$

$$c_i(\mathbf{k}) = \frac{|F_i(\mathbf{k})|}{\bar{F}_i} - 1$$

$$\bar{F}_i = \frac{1}{N}\sum_{\mathbf{k}}|F_i(\mathbf{k})|$$

The terms F_1 and F_2 represent F_{obs} and F_{cal} in this formalism and N is the number of atoms per unit cell. In this case, a perfect correlation is 1, while -1 is a perfect anticorrelation and 0 represents no correlation. This correlation function will be discussed below in terms of optimizing structures.

The above prescription is used for structure refinement of static structures. For time-resolved measurements, one knows the initial, and to some extent the final structure, causally connected through the structural transition. As recently demonstrated, this additional information is sufficient to uniquely invert diffraction data to structures even with limited sampling of the reciprocal space.[17] The accuracy improves with better signal-to-noise ratios (SNR) and more orientations, but the degree of accuracy can be assessed by varying the initial and final constraints. The procedure is to simulate diffraction for the initial structure and the (partially) known fully relaxed structure. The signal in the detector plane needs to be transformed. The intensity (I) at each pixel position (a,b) is calculated according to

$$I(a,b) = \quad (42)$$

$$= \sum_{hkl}\exp\left(-\frac{\Delta q^2_{radial}}{2\sigma^2_{radial}} - \frac{\Delta q^2_{parallel}}{2(|\mathbf{q}|\sigma_{parallel})^2} - \frac{\Delta q^2_{rotational}}{2(|\mathbf{q}|\sigma_{rotational})^2}\right)|F_{hkl}|^2$$

Here, F_{hkl} is the structure factor for the reflection (hkl) calculated from the X-ray structure and using the parametrized electron scattering factors found in Ref. 145. The scattering geometry is shown in Fig. 5.2 in Ref. 17 and defined as:

$$\Delta q_{radial} = \Delta\mathbf{q}\cdot\hat{\mathbf{q}}_{a,b} \quad (43)$$

$$\Delta q_{parallel} = \Delta\mathbf{q}\cdot\hat{\mathbf{k}}_0 \quad (44)$$

$$\Delta q_{rotational} = \Delta\mathbf{q}\cdot(\hat{\mathbf{k}}_0 \times \hat{\mathbf{q}}_{a,b}) \quad (45)$$

$$\Delta\mathbf{q} = (\mathbf{q}_{a,b} - \mathbf{q}_{hkl}) \quad (46)$$

The values of the three σ components in Eqn (42) are estimated from the orientation fitting and tested by trial-and-error to give good qualitative agreement with the experiment. The effect of the finite beam size needs to be included as a Gaussian convolution. The resulting simulated diffraction pattern is optimized for the static initial structure to provide an excellent approximation to the experimental diffraction and experimental parameters. The time series of diffraction patterns is subjected to a minimization function that encodes all of the information about the experiment in terms of the experimental data and uncertainties, and prior knowledge about the structure and structural transition by adding penalty functions, which bias the refinement of the atomic positions towards chemically reasonable structures and towards a continuous path between the initial and final structures determined by either X-ray diffraction or other means. Equation (42) gives the general construction of the function and Eqns (47) and (48) provide more detail:

$$f(x,t) = \sum\text{Intensity ratio differences (Experiment} - \text{Theory}) + \\ + \sum\text{deviations of bonded distances and angles form mean ground state values} + \\ + \lambda\sum\text{deviations from linear path between thermally equilibrated structures} \quad (47)$$

Where specifically each diffraction spot's intensity ratio (IR) is determined to give the constraints:

$$f(\mathbf{x},t) = \sum_{spots}\frac{|(IR)^{exp}_{spots}(t) - (IR)^{theory}_{spots}(\mathbf{x})|^2}{\sigma(IR)^2_{spots}} + \quad (48)$$

$$+ \sum_{b-bonds}\frac{\left(r^{ES}_b(\mathbf{x}) - r^{GS}_b\right)^2}{\left(r^{LT} - r^{RT}\right)^2_b} + \sum_{\alpha-angles}\frac{\left(\theta^{ES}_\alpha(\mathbf{x}) - \theta^{GS}_\alpha\right)^2}{\left(\theta^{LT} - \theta^{RT}\right)^2_\alpha} + \\ + \lambda\sum_{a-atoms}\left|\mathbf{x}_a - \mathbf{x}^{GS}_a\right|^2$$

In Eqn (48), r is the bond length, **x** stands for Cartesian coordinates, θ is the bond angle, LT stands for low temperature, RT stands for room temperature, GS stands for ground state (linear combination of LT and RT) and ES stands for excited state. The first term in Eqn (48) describes the agreement of the theoretical and experimental intensity ratios, which is weighted differently for each spot according to the experimental uncertainty, σIR_{spot}. The theoretical intensities are then calculated, taking into account the photoinduced change in an isotropic Debye – Waller factor, and the ratio of excited species. $F_{hkl}(\mathbf{x})$ is the structure factor of the excited portion of the structure with the Miller indices (hkl) and, similarly, $F_{hkl}(\mathbf{x}^{GS})$ is the structure factor for the unexcited initial structure. Calculations of these structure factors are similar to the established method in time-resolved crystallography,[146] but using parameterized electron scattering factors.[145] The remaining terms in Eqn (48) are the penalty functions to act as constraints to guide the refinement to physically reasonable geometries. The second and third terms in Eqn (48) give restraints on the bond lengths and bond angles, respectively, where the denominators represent the uncertainties in these parameters, estimated as the differences between the corresponding values for the initial and fully relaxed structures. This is the key feature of this approach. The features of the molecular structural transition that are known or invariant provide additional constraints needed to find unique solutions. These terms effectively act as phasing centres or reference points to find the other phases by using the weighting factors through the least squares fit to find the best values. In this way, all atomic coordinates in an asymmetric unit cell can be efficiently handled and optimized for each time point to give full atom-resolved dynamics. This procedure provides a robust method that can be automated for generating molecular movies of photoinduced structural changes and chemical reactions. This approach is similar to the solution of the gas-phase problem described above (Eqn (34)), where the first term describing the agreement between theory and experiment in the gas phase is simply replaced by the sum of the relative intensity changes over all observable diffraction spots, and the stabilizing term, Ω, is constructed based on the known structures for the thermal phase transition as given by the remaining terms in Eqns (47) and (48). The regularization parameter of Eqn 34 is partially included in Eqns (47) and (48) by way of the uncertainties (sigma values) in the terms 1, 2 and 3, with the free term (λ) that must be chosen carefully as described in the supplementary material of Ref. 17. The constraints do not rely on any level of theory per se but on the inherent knowledge of the initial and conserved components in the final structure. This information content within the limitations of the SNR and sampled reciprocal space is sufficient to find fully converged, unique solutions to the photoinduced structural changes and reactions. One is exploiting the fact that the structures along a given time series after the excitation are causally connected to this perturbation. This additional information provides sufficient data for inverting to real space with a high level of accuracy without the need of theoretically predicted structures in the refinement process. The importance of this relatively recent advance needs to be fully appreciated as it is now possible to generate full atom-resolved reaction dynamics in a model-independent way. The inclusion of additional information on the conserved structure relationships completely avoids the uncertainty in choice of model and sampling sufficient configurations in generating a model response function to the excitation.

The development of new analytical tools that completely exploit known information on the system response will also enable the use of fewer electrons in the image reconstruction and open up the study of larger and more complex systems. We are far from being quantum-limited in extracting the maximum amount of information from diffraction data (see, *e.g.*, Ref. 147 for a treatment of the minimum information content needed for alignment of images). This topic is cited as a key area for further development that will be essential for pushing imaging of chemical reactions to the ultimate space-time limits in resolution.

V. The dynamics of wave packets

We now turn our attention to the time evolution of the structural dynamics following photoexcitation. Experimental exploration of isolated molecular systems with high time resolution involves the creation and detection of wave packets. A wave packet can be described as a coherent superposition of certain eigenstates. By definition, the exact (not in the Born – Oppenheimer approximation) eigenstates are stationary solutions of the time-independent Schrödinger equation. The time dependence of non-stationary systems arises only from superposition of N different eigenstates, each with a quantum mechanical (QM) time-dependent phase $\exp(-2\pi i E_N t/h)$. Conceptually, a 'pump-probe' experiment has three stages, *viz.*, (1) preparation of the molecule in the excited state (the pump); (2) dynamical

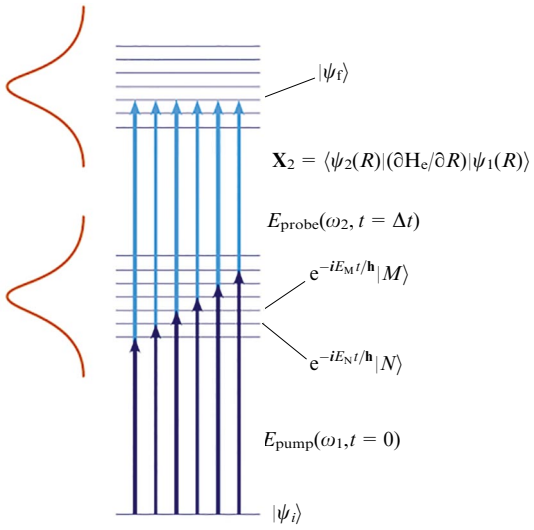


Figure 8. The generation, time evolution and detection of a wave packet. At time $t = 0$, a pump laser pulse E_{pump} (black) generates a coherent superposition of molecular eigenstates (wave packet) from the ground state $|\Psi_i\rangle$. Each of the eigenstates $|N\rangle$ in the wave packet has a different phase factor, the superposition of which results in non-stationary behaviour. As a result, the time evolution of the wave packet leads to an observable time dependence of the system. At time $t = \Delta t$, the wave package is projected by the probe pulse E_{probe} (gray) to a set of the final states $|\Psi_f\rangle$, which act as a 'template' for the dynamics. The time-dependent probability of the final state $|\Psi_f\rangle$ is modulated by the interference between the amplitudes of all degenerate coherent two-photon transitions that lead to the final state. (From Ref. 151 with minor revision).

evolution of the wave packet; and (3) probe of the transient superposition of states.[42, 148 – 150] A typical femtosecond 'pump-probe' experiment is illustrated in Fig. 8.[151] As a result of sequential photon transitions created by the pump and probe pulses, the final state $|\Psi_f\rangle$ arises at the end of the sequence of two laser pulses. Since this process involving two sequential photon transitions is coherent (within the coherence time of the induced molecular polarization), we should sum up the transition amplitudes and then square the sum to get the final probability. As will be discussed later, the signal contains the interference between all components of these degenerate photon transitions.

If the time delay between the two laser pulses is changed, the phase relations between the amplitudes of the two-photon transitions also change, which in turn leads to a change in the interference in the final state of the wave packet.

During the interaction of the system with the pump laser pulse, the amplitudes and the initial phases of the set of eigenstates of the excited state are determined by the amplitude and phase of this laser pulse and by the amplitudes of the transition dipole moments between the ground and excited states. After the pump pulse, the wave packet $\Psi(t)$ evolves freely in accordance with the equation:

$$|\Psi(t)\rangle = \sum_N A_N \exp(-2\pi i E_N t/h)\,|N\rangle \qquad (49)$$

The complex coefficients A_N in Eqn (49) contain both the amplitudes and the initial phases of the eigenstates of the molecule, $|N\rangle$, each with the energy E_N, which are prepared by the action of the pump laser pulse. The probe laser pulse interacts with the wave packet after a set time delay, projecting the wave packet onto the chosen final state $|\Psi_f\rangle$ at some time delay $t = \Delta t$. This final state is the 'template' onto which the wave packet dynamics is projected. The temporal dependence of the differential signal for the projection onto a single final state can be written as

$$S_f(t) = |\langle\Psi_f|\mathbf{E}_{\text{probe}}(\omega)\mathbf{d}|\Psi(t)\rangle|^2 = \left|\sum_N B_N \exp(-2\pi i E_N t/h)\right|^2 \qquad (50)$$

where the complex coefficients B_N contain both the amplitudes of the wave packet A_N and the (complex) matrix elements of the transition dipole moment (**d**) under the action of the pump pulse and link each state with the final state in the superposition $|\mathrm{N}\rangle$:

$$B_N = A_N \langle\Psi_f|\mathbf{E}_{\text{probe}}(\omega)\mathbf{d}|N\rangle \qquad (51)$$

Thus, Eqn (50) can be rewritten as

$$S_f(t) = 2\sum_N \sum_{M<N} |\boldsymbol{B}_N||\boldsymbol{B}_M|\cos[2\pi(E_N - E_M)t/h + \Phi_{NM}] \qquad (52)$$

where the phase factor Φ_{NM} contains the initial phase differences of the eigenstates of the molecule and the phase differences of the matrix elements of the transition dipole moment to the excited state by the action of the pump pulse, connecting the states $|N\rangle$ and $|M\rangle$ to the final state. This differential signal of the final state, $S_f(t)$, contains the most detailed information because it arises from the coherent sum over all amplitudes of two-photon transitions within the bandwidth of the laser pump and probe pulses and contains the interference components between all degenerate two-photon transitions as mentioned above.[151] It is clearly seen that the signal, as a function of time delay $t = \Delta t$, contains modulations at the frequencies $2\pi(E_N - E_M)/h$ corresponding to the energy differences between the states in the superposition. This equation gives the relationship between the wave packet dynamics and the observed pump-probe signal. It is the interference between the individual two-photon transitions through different excited eigenstates terminating in the same final state. Therefore, the Fourier transform of the signal in this temporal interval contains the frequencies that yield the energy level differences of the excited state. There is a similar expression for the intensity of electron scattering in the diffraction experiments. We note here that for condensed-phase systems there may be collisional processes that lead to dephasing.[42, 148 – 150] The above treatment can be readily modified to include an incoherent summation of population states in this case.

V.1. Real-time dynamics of transition states in photodissociation and photopredissociation

The first real-time studies of the dynamics of transition states in photodissociation and predissociation were carried out by FTS.[45, 80, 84, 115, 152 – 156] The method uses ultrashort pulsed laser excitation followed by application of a femtosecond probe laser pulse with controlled time delay. In these experiments, the probe pulse prepares the system in a higher electronic state, which is observed by laser-induced fluorescence (LIF), a rather important source of information about the dynamics of transition states in photodissociation,[69, 73, 157 – 159] predissociation,[45, 70, 160 – 163] and van der Waals complexes [164, 165] and other problems associated with femtochemistry.[80, 115, 158, 166] It was shown [109, 112, 167, 168] that the TRED method can be used to directly monitor the nuclear dynamics of photodissociation that previously was only accessible to optical methods. Since fast electron scattering is mainly elastic, TRED is a non-destructive method. Moreover, because the molecular diffraction intensity depends strongly on the parameters of the PES that governs the photodissociation, TRED is a new method for studying the coherent nuclear dynamics of transition states.

V.1.a. The dynamics of photodissociation

To illustrate the effects arising from time-dependent molecular structures in the scattering intensities and their corresponding Fourier transforms (radial distribution functions of the interatomic distances), we will focus on diatomic (A – B) and linear triatomic (A – B – C) molecules in which the action of a laser pulse breaks the bond A – B. In many cases, the potential function for such systems can be expressed as [169]

$$V(R, r) = V_0 \exp[-(R - \gamma r)/\rho] \qquad (53)$$

where R is the distance between the nuclei A and B in the molecule A – B or the distance between the nucleus A and the centre of mass of the fragment B – C in the molecule A – B – C. Further, $\gamma = m_C/(m_B + m_C)$ is the reduced mass and $r = r_0(\mathrm{BC}) - r_e(\mathrm{BC})$ with $r_0(\mathrm{BC})$ and $r_e(\mathrm{BC})$ being the internuclear distance in the ground vibrational state and the equilibrium internuclear distance in the fragment B – C, respectively; and ρ is a so-called range parameter.[169, 170] The reactions and PESs of this kind are well known for a number of molecular systems.[169 – 171] In the first stage of analysis, manifestation of the nuclear dynamics in the scattering of ultrashort electron pulses has been explored for adiabatic potential functions. Subsequently, the process

of predissociation controlled by the adiabatic potential was considered taking the NaI molecule as an example. For IBr, photoexcitation and subsequent dissociation can be divided into the following stages (please, see Refs 172, 173 and the references therein):

$$IBr(X^1\Sigma_0^+) \rightarrow IBr(B^3\Pi_0^+),\ 400 < \lambda < 620\ nm \quad (54)$$

$$IBr(B^3\Pi_0^+) \rightarrow I + Br(^2P_{1/2}),\ \lambda < 256\ nm \quad (55)$$

$$IBr(B^3\Pi_0^+) \rightarrow IBr(BO^+) \rightarrow I + Br(^2P_{3/2}) \quad (56)$$

The photoexcitation in Eqn (54) is accompanied either by the dissociation of the diabatic type (Eqn (55)), yielding Br atoms in the excited state, or by the dissociation of adiabatic type (Eqn 56)), in which the molecule dissociates into atoms in their ground states. Note that only the last channel is realized for wavelengths in the range of $526 < \lambda < 620$ nm.[172, 173] In this connection, it should be mentioned that dissociative potentials of a number of electronic states of different interhalogens are described in the literature.[174] One approach that can be used to describe the dynamics of excited molecules is the wave packet approximation.[175, 176] The wave packet carries information on the relative positions and nuclear momenta, as well as their components on different APES corresponding to different electronic states.[176] The wave functions can be approximated by Gaussian functions with minimum uncertainty.[177–179] Considering the classical trajectory in the phase space where the Hamiltonian in the vicinity of the moving point can be expressed in terms of the degrees of $(p - \langle p(t)\rangle)$ and $(R - \langle R(t)\rangle)$ up to the second order, the wave function is defined as follows [177]:

$$\psi(R,t) = \quad (57)$$
$$= \exp\{(2\pi i/h)[\alpha(t)(R - \langle R(t)\rangle)^2 + \langle p(t)\rangle(R - \langle R(t)\rangle) + \gamma(t)]\}$$

where $\alpha(t)$ gives the spreading of the wave packet, $\gamma(t)$ is its complex phase and $\langle ...\rangle$ is the expectation value. Using the time-dependent Schrödinger equation, we can obtain the differential equations for the position and the momentum [175]:

$$\partial\langle R(t)\rangle/\partial t = \langle p(t)\rangle/m \quad (58)$$
$$\partial\langle p(t)\rangle/\partial t = -\langle \partial V(R)/\partial R\rangle$$

where $V(R)$ is the potential in the Born – Oppenheimer approximation. Equations (58) describe the trajectory of the wave packet. For large time delays after the excitation of molecules and for the use of long probe pulses, the increase in the width (spreading) of the wave packet should be considered. In this case, the probability density of the interatomic distances in the ensemble of dissociated molecules can be represented as follows:

$$P(R,t) = [2\pi\sigma^2(t)]^{-1/2}\exp\{-[R - R(t)]^2/2\sigma^2(t)\} \quad (59)$$

where $\sigma(t = 0)$ is the dispersion of the wave packet at the initial time of the laser excitation and $R(t)$ is the classical trajectory of the centre of gravity of the wave packet. Consequently, the dispersion of the propagating wave packet can be expressed as a linear function of time during its free motion:

$$\sigma(t) = \sigma(0)[1 + h^2t^2/16\pi^2m^2\sigma^4(0)]^{1/2} \quad (60)$$

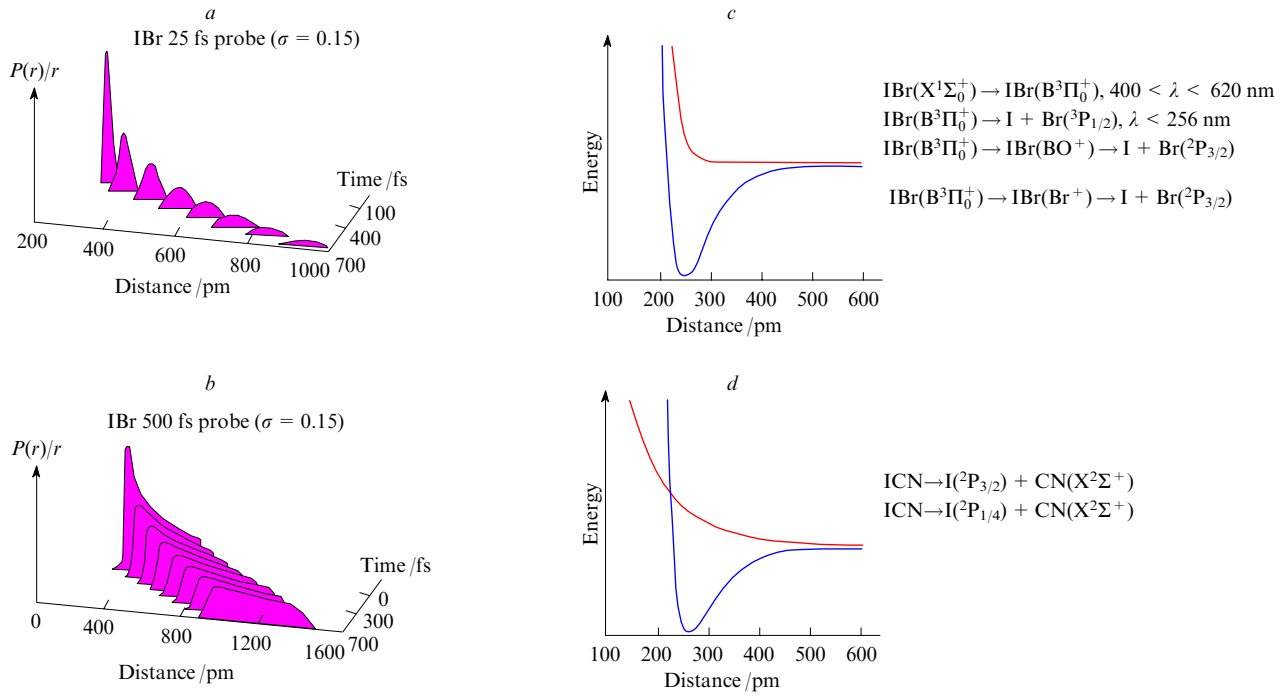


Figure 9. Radial distribution curves for IBr. The wave packets are approximated by Gaussian functions, averaged over 25 fs and displayed every 100 fs (*a*). The parameter σ accounts for the spreading of the wave packet. The wave packets are approximated by Gaussian functions, and averaged over 500 fs (*b*). While the longer electron pulses don't resolve the actual profile of the wave packet, some important details are still visible. Model potentials for the ground and excited states of IBr (*c*) and ICN (*d*). (From Ref. 180 with minor revision).

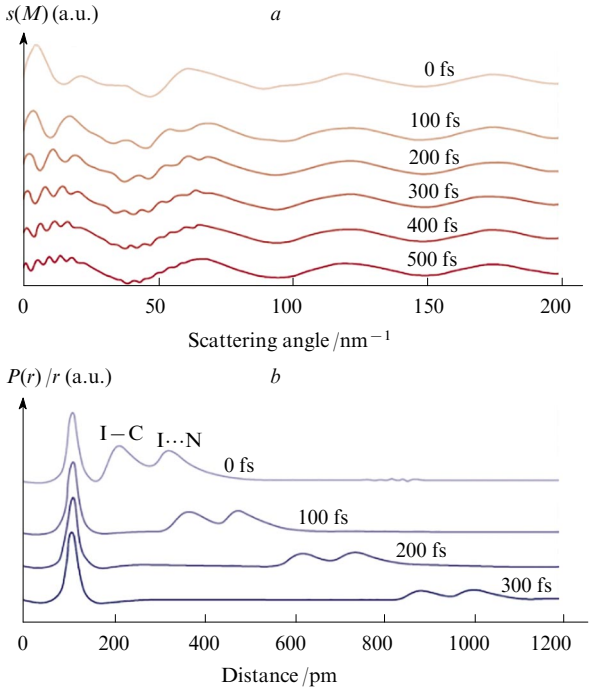


Figure 10. Manifestation of the structural dynamics of the dissociation of ICN for the time-dependent molecular scattering intensities (*a*) and for the radial distributions (*b*). (From Ref. 180 with minor revision).

If the pump laser pulse has the shape of a δ-function at $t = 0$, the temporal dependence of the molecular intensity is given by

$$sM(s,t) = g(s)\int(\sin(sR)/R)P(R,t)\mathrm{d}R \quad (61)$$

When the shape of the electron probe pulse is approximated by a Gaussian function with the central point at $t = t_0$ and a duration of τ, the averaged molecular intensities can be written as:

$$\langle sM(s,t)\rangle_\tau = (2\pi\tau^2)^{-1/2}\int \exp[-(t-t_0)^2/2\tau^2]\cdot sM(s,t)\mathrm{d}t \quad (62)$$

Using the above theory, the time-dependent intensities of the molecular scattering and the corresponding radial distribution curves of the internuclear distances during the photodissociation of IBr and ICN (Figs 9 and 10) were calculated.[180] The results shown in Figs 9 and 10 were obtained using the wave packets (Eqn (57)) approximated by Gaussian functions. From Fig. 9 *b* it is clear that the radial distribution curves obtained with a relatively long probe pulses are significantly different from those presented in Fig. 9 *a*. However, some details of the dynamics of the wave packets are still revealed at a time interval that is much shorter than the duration of the probe pulse. Figure 9 also shows that the distribution of the time-dependent wave packet can be observed using the TRED technique if the electron probe pulse will be short enough. Similar calculations were performed for the triatomic molecule ICN.[180]

These studies show that the time-dependent electron diffraction intensity observed for dissociative states is strongly dependent on the PES shape. The results obtained also demonstrate that the diffraction intensities in TRED can be calculated with ease for dissociative processes provided that the PES is known. Thus, in principle, it is possible to solve the inversion problem or alternatively determine the PES parameters using time-resolved diffraction techniques.

V.1.b. The dynamics of photopredissociation

To account for the oscillations of the wave packet in the bound state, the action – angle variables (J,ω) (Refs 181 – 183) are convenient coordinates, allowing simplification of tasks associated with periodic motion. They can be easily generalized to multidimensional systems. Following Marcus,[183] we can derive the probability density in the variables of the angle of the molecular wave packet:

$$P(\omega,t) = |\Psi(\omega,t)|^2 = 1/(2\pi|\sigma_\omega|^2)\cdot\exp[-(\omega - v_0 t)^2\mathrm{Re}(1/\sigma_\omega^2)] \quad (63)$$

where

$$\mathrm{Re}(1/\sigma_\omega^2) = [(hv_0/2\pi\sigma_E)^2 + (\sigma_E v_0' t/hv_0)^2]^{-1} \quad (64)$$

with $v_0' = \mathrm{d}v(n)/\mathrm{d}n|_0$ and v_0 is the most probable vibrational frequency of the wave packet and σ_E is its variance according to the wave packet energy distribution.

For the integration of Eqn (63) at the intra-molecular coordinate, it is necessary to transform from the action-angle variables (J,ω) to the momentum p and the internuclear distance r. For the Morse oscillator, corresponding relations can be expressed in analytical form (see, *e.g*, Ref. 184):

$$r(\omega) = r_e^\dagger + \alpha^{-1}\ln[(1 + b\cos\{\omega\})/\lambda^2] \quad (65)$$

$$p(\omega) = m\omega_e\lambda\, b\sin\{\omega\}/\alpha(1 + b\cos\{\omega\}) \quad (66)$$

where $\lambda = (1 - E/D_e^\dagger)^{1/2}$, $b = (E/D_e^\dagger)^{1/2}$, $D_e^\dagger$ is the dissociation energy, α is the Morse parameter, E is the available energy (depending on the excitation frequency) and $\omega_e = \alpha(2D_e^\dagger/m)^{1/2}$.

To describe a dissociative state of a molecule, when the corresponding potential energy decreases rapidly, but the wave packet has already spread into the region where the potential energy is close to zero, it is possible to propose the PDF $P(r,t)$ specified by expressions (59) and (60). Equation (61) gives the time-dependent molecular intensities $sM(s,t)$ and the radial distributions (after the Fourier transformations), starting from $t = t_0$, when the population of the excited molecular state is maximal.

The above theory has been used to interpret spectroscopic studies of the predissociation process of laser-excited NaI.[45, 160 – 162, 185 – 187] When NaI is excited by laser radiation at a wavelength of 320 – 333 nm, the molecules are almost completely transferred to the excited electronic states $\Omega = 0^+$ and $\Omega = 1$.[45] The rapidly-dissociating electronic state $\Omega = 1$ is usually neglected, as attention is focused on the excited state $\mathrm{NaI}(0^+)$ and the ground state $\mathrm{NaI}(^1\Sigma_{0+})$. Accordingly, in the work of (Ref. 112) the modeling took into account the predissociation reaction:

$$\mathrm{NaI}(0^+) \rightarrow [\mathrm{Na}\cdots\mathrm{I}]^\dagger \rightarrow \mathrm{Na}(^2\mathrm{S}_{1/2}) + \mathrm{I}(^2\mathrm{P}_{3/2}) \quad (67)$$

assuming that the process of electronic excitation

$$\mathrm{NaI}(^1\Sigma_{0+}) \rightarrow \mathrm{NaI}(0^+) \quad (68)$$

was very fast compared to the time required for the evolution of the transition state $[\mathrm{Na}\cdots\mathrm{I}]^\dagger$. This assumption

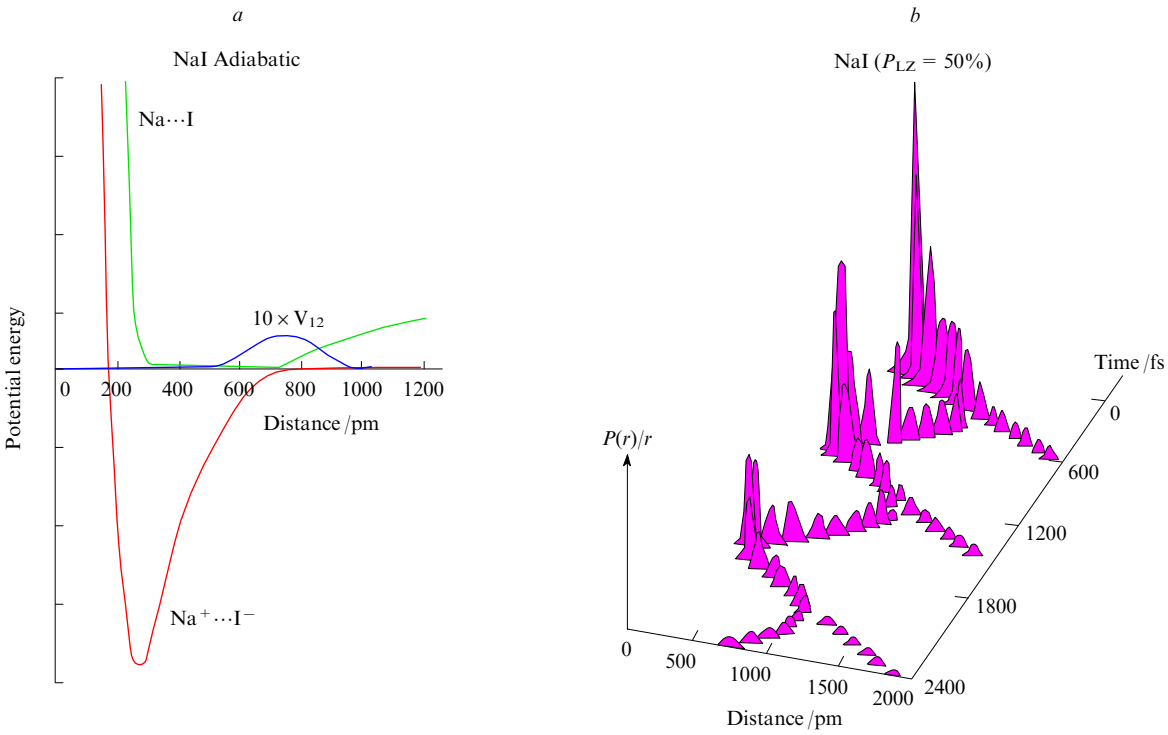


Figure 11. The adiabatic approximation to the diabatic potential for sodium iodide, NaI; the maximal probability of the Landau – Zener transition (P_{LZ}) for the covalent-ionic case corresponds to a internuclear distance of ~720 pm for the transition state of NaI (*a*). The radial distribution curves for the predissociation of NaI calculated using a semiclassical approximation (*b*).[112] A similar behaviour can be obtained using Gaussian wave packets. (From Ref. 112 with minor revision).

was confirmed in a number of FTS studies (see Refs. 45 and 70 – 72).

Fig. 8 shows the functions of the adiabatic potential energy $U_{1(2)}(r)$.[187 – 193] In the limit of weak interactions, the probability amplitude P_{LZ} for diabatic passage through the intersection of the corresponding potentials is determined by the Landau – Zener formula [194, 195]

$$P_{LZ} = \exp(-2\pi\varepsilon) \quad (69)$$

$$\varepsilon = V_{12}^2/\hbar v(E,J)|(\mathrm{d}U_1(r)/\mathrm{d}r) - (\mathrm{d}U_2(r)/\mathrm{d}r)|_{r=r_x} \quad (70)$$

where the derivatives correspond to the intersection point at $r = r_x$, $U_1(r) = U_2(r)$; $v(E,J)$ is the group velocity of the wave packet, and V_{12} is the parameter characterizing the interaction in the crossing of the potentials (Fig. 11 *a*). In the adiabatic case, the motion is controlled by a single PES, while the Eqns (61) and (62) can be used to describe the electron diffraction intensities for an ensemble of scattering molecules. In the diabatic case, each bifurcation of the ensemble at every passage through the intersection should be taken into account. The details of the calculations are given elsewhere.[112] Some of the results are presented in Fig. 11.

Calculations [112] illustrate that TRED can be used to obtain direct information on the intramolecular nuclear dynamics of the transition states in the process of photopredissociation. It is seen that even with relatively large time delays the diffraction signal continues to reveal significant details about the structural dynamics of both the bound states and the dissociative states. In a number of publications devoted to the study of NaI photodissociation [45, 71, 161, 187] it was reported that the semiclassical and QM calculations give similar results about the reaction dynamics only for the first few periods of oscillations of the transient state. In later time delay after the excitation, the quantum mechanically calculated dynamics of wave packets demonstrate a more complex behaviour of molecules [188, 191, 192] compared to calculations in the semiclassical approximation.

V.2. Quantum dynamics simulations of photodissociation

Gaussian wave packets are often used to simulate the structural dynamics of photodissociations such as in IBr.[180] By comparing with the results of quantum dynamics calculations one can test the validity of the Gaussian approximation. All the results shown below were derived from the quantum dynamics calculations using the FGH method.[134, 135, 196 – 200]

Calculations were performed using the potential functions for the ground state and the BO^+ state of IBr.[174] In accordance with the Franck – Condon principle, the value of the transition dipole moment was considered constant. As shown in Fig. 12, the results of quantum dynamics calculations are similar to those of the model calculations [180] based on the Gaussian wave packet approximation (Fig. 9 *a*).

Importantly, these calculations show good agreement between the results obtained using semiclassical and quantum dynamics methods. The semiclassical approach allows one to write in explicit form the equation for the time-dependent component of the molecular scattering intensity and, therefore, provides a convenient way to solve the inversion problem for the determination of the structural dynamical parameters of a molecular system during disso-

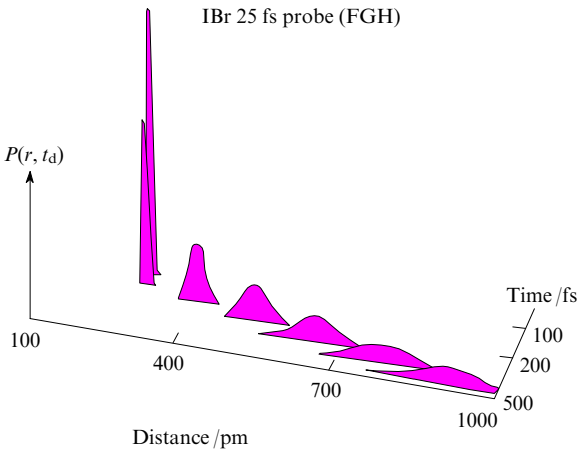


Figure 12. The $P(r,t_d)$ PDF for the excited state of IBr obtained from quantum dynamics calculations using the FGH method. Here, r is the internuclear distance and t_d is the delay between the excitation pulse and the probe pulse. The instantaneous PDF values for the distribution of the interatomic distances were averaged for an electron pulse duration of $\tau_e = 25$ fs; the original curve corresponds to the ground-state PDF. These results are in good agreement with those obtained using the Gaussian wave packet approximation. (From Ref. 5 with minor revision).

ciation or predissociation with theoretical input on the shape of the potential. This offers a direct and convenient method for data analysis in time-resolved diffraction measurements.

VI. The diffraction signatures of excited molecules

The separation of conventional gas-phase electron diffraction (GED) signatures into an incoherent 'atomic' scattering term and a coherent 'molecular' scattering term, $I_{total}(s) = I_{atomic}(s) + I_{mol}(s)$, is a mathematical construct that aids the extraction of the oscillations due to the molecular structure from the overall electron diffraction signal that decays rapidly with increasing momentum transfer. But it would, of course, not be correct to understand the scattering from a molecule as comprised of distinct and additive atomic and molecular intensity terms. Rather, the diffraction signal represents the Fourier transform of the molecular structure, as defined by the complete, rovibronic molecular probability density function. The small modulation depth of the observed electron diffraction signal of gas-phase samples stems from the orientational averaging over isotropic molecular ensembles and from the Gaussian-like distributions of internuclear separations in most thermal samples. It is then interesting and instructive to consider the diffraction patterns that would result from molecules excited to specific, well-defined quantum states.[109, 118 – 120, 201, 202]

Laser-based femtosecond pump-probe experiments have been a powerful method for studying molecular dynamics in the gas phase. For example, a femtosecond probe laser pulse can ionize a molecule and the resulting fragments (electrons and ions) can be studied using kinetic-energy-resolved velocity map imaging (VMI).[203, 204] However, due to the long wavelength of optical photons, laser-based probes do not spatially resolve molecular structures.

X-Ray diffraction using an X-ray free electron laser (XFEL) can also be utilized to observe structural changes with Ångstrom spatial resolution provided that sub-Ångstrom wavelength X-ray pulses with high fluence are available.[16, 87, 205, 206] Vibrational excitation of a molecule imparts additional modulations to the diffraction pattern.[18, 120] This was first illustrated for carbon monosulfide (CS)[5, 18] and linear CS_2 molecules aligned in polarized laser fields.[120]

VI.1. Molecular tomography of the quantum state

In accordance with the basic principles of quantum mechanics, the state of a single molecule cannot be determined experimentally.[182] However, it is possible to determine the density matrix of an ensemble of identical systems. Knowing the status of the system means that we have the most information about all physically measurable quantities.[207] The density matrix and the PDF in the phase space — the Wigner function[208, 209] — have a one-to-one correspondence,[210] which describes the maximum of the available statistical information. Therefore, when the term 'molecular quantum state' is used, the quantum state of a molecular ensemble is assumed.

In 1933, it was demonstrated[211] that a pure quantum state $|\Psi>$ can be recovered from the time-dependent PDF $P(r,t) = |\Psi(r,t)|^2$ and its derivative $\partial P(r,t)/\partial t$. The pure quantum state can also be recovered by measuring $P(r,t)$ at time t and the time evolution of $P(r,t)$ through a fairly short intervals Δt, that is, as shown in $P(r,t + N\Delta t) = |\Psi(r,t + N\Delta t)|^2$, $(N = 0, 1, 2 \ldots)$.[212]

The scattering intensities in TRED have a direct correlation with the time-dependent PDF of internuclear distances $P(r,t)$. In TRED, a pulsed electron source is utilized for probing the ensemble of particles in a certain time sequence. Synchronized electron and laser pulses provide a stroboscopic picture of the evolving process. Thus, an additional variable, *viz.*, time, is introduced into the measurements. It becomes possible to study the coherent dynamics of atomic nuclei in laser-excited systems, the TS of chemical reactions and the dynamics of molecular wave packets.[5, 180, 202, 213 – 215] The TRED method can be utilized for probing the dynamics of wave packets, *i.e.*, a coherent superposition of quantum states created by short optical pulses with controlled phase.[216 – 224] Consequently, it becomes possible to directly observe the coherent nuclear dynamics of excited molecules[5, 112, 180, 202] as a single act of elastic electron scattering occurs on the attosecond time scale.[5, 18]

The time-dependent intensities of molecular scattering of electrons $M(s,t)$ obtained using TRED with coherent excitation of a molecular system provide the possibility of determining the fundamental elements of the density matrix and the tomographic reconstruction of the molecular quantum state of the system.

In classical mechanics, there are no equations describing the evolution of the PDF $P(r,t)$ and $P(p,t)$; only the joint PDF, $W_{cl}(p,r,t)$, can be expressed using the Liouville equation.[208] Therefore, there are no corresponding quantum equations for $P(r,t)$ and $P(p,t)$. However, the known Wigner – Liouville equation[209] can be used to describe the evolution of the Wigner function $W(r,p,t)$. To derive the equation describing the time-dependent function of the molecular component of the scattering intensity $M(s,t)$ *via* the Wigner function, consider some boundary properties of $W(r,p,t)$:

$$\int W(p,r,t)\mathrm{d}p = P(r,t) \tag{71}$$

$$\int W(p,r,t)\mathrm{d}r = P(p,t) \tag{72}$$

The TRED molecular intensity function, $M(s,t)$ can be written as [23]

$$M(s,t) = (I_0/R^2)g(s)\mathrm{Re}\int \mathrm{d}p \int W(r,p,t)\exp(\boldsymbol{i}\mathbf{sr})\mathrm{d}r \tag{73}$$

Equation (73) is the most general representation of the molecular scattering intensity in TRED, expressed in terms of the Wigner function. In this representation, $M(s,t)$ can be interpreted as a filtered projection of the Wigner function, where the scattering operator $\exp(\boldsymbol{i}\mathbf{sr})$ is a filter, modified by the scattering function $g(s)$. For many problems, the Wigner function $W(r,p,t)$ can be derived in analytical form (see, *e.g.*, a review article [209]) or by solving the Wigner – Liouville equation numerically with the corresponding potential function of the molecule.

In Eqn (71), $P(r,t) = |\Psi(r,t)|^2$, and, generally, it is assumed that $\Psi(r,t)$ can describe a mixed quantum state. The wave function $\Psi(r,t)$ can be represented as an expansion in orthonormal basis functions $\psi_n(r)$ as follows:

$$\Psi(r,t) = \sum_n C_n \psi_n(r)\exp(-\boldsymbol{i}\omega_n t) \tag{74}$$

where n is the quantum number of the state with the energy E_n, ω_n the frequency of oscillations, and C_n is the probability amplitude. Then, Eqn (73) can be written as:

$$M(s,t) = (I_0/R^2)\, g(s)\mathrm{Re}\sum_{m,n}\boldsymbol{\rho}_{mn}\exp[\boldsymbol{i}(\omega_m - \omega_n)t]\times$$

$$\times\langle\psi_m(r)|\exp(\boldsymbol{i}\mathbf{sr})|\psi_n(r)\rangle \tag{75}$$

where $\boldsymbol{\rho}_{nm}$ are the elements of the density matrix.

Equation (75) shows that the molecular scattering intensity explicitly depends on the quantum state of the molecular system. Correspondingly, the $P(r,t)$ PDF which can be obtained using the TRED data as the Fourier transform

$$P(r,t) = (2/\pi)^{1/2}(R^2/I_0)\mathrm{Re}\int M(s,t)[g(s)]^{-1}\exp(-\boldsymbol{i}\mathbf{sr})\,\mathrm{d}s = \tag{76}$$

$$= (2/\pi)^{1/2}\mathrm{Re}\sum_{m,n}\boldsymbol{\rho}_{mn}\exp(\boldsymbol{i}(\boldsymbol{\omega}_m - \boldsymbol{\omega}_n)t)\times$$

$$\times\int\langle\psi_m(r)|\exp(\boldsymbol{i}\mathbf{sr})|\psi_n(r)\rangle\exp(-\boldsymbol{i}\mathbf{sr})\,\mathrm{d}s$$

depends on the internuclear distance r and time t and explicitly contains all the information about the quantum state of the system, being a projection (or 'shadow' [225, 226]) of the Wigner function.

The interference term in the molecular electron-scattering intensity (Eqn (63) and its Fourier image, Eqn (76)) gives, in principle, the possibility to determine the density matrix $\boldsymbol{\rho}$ and to perform tomographic reconstruction of the molecular quantum state of the system.[5, 227] Therefore, the time sequence of measurements of the scattering intensity $M(s,t)$ the Fourier transform (Eqn (76)), which transforms from the space of the scattering variable s into the space of the interatomic distances r, provides the required information for tomographic reconstruction of the Wigner function $W(r,p)$. For this purpose, the Radon transform may be utilized:[226, 228, 229]

$$W(r,p) = \tag{77}$$

$$= -P/(2\pi^2\hbar)\int\int P(x,\Theta)(r\cos\Theta + p\sin\Theta - x)^{-2}\mathrm{d}x\,\mathrm{d}\Theta$$

where P is the Cauchy principal value and $\Theta = \omega t$ is the angle of rotation in the phase space,[228] corresponding to the time of motion t on the PES of the molecule.

In Eqn (77), integration should be performed in the range of $0 \leqslant \Theta \leqslant 2\pi$. This means that to determine the full quantum state of the system, TRED measurements should be performed to generate a 'complete tomographic' set,[230] in which a full period of reconstruction of the wave packet, T_{rev},[5] takes place (that is, in the interval $0 \leqslant t \leqslant T_{\mathrm{rev}} = 2p/\omega$ corresponding to a complete cycle of rotation of the Wigner function). When using the full data set for tomographic reconstruction of a coherent state of the wave packet at $t = 0$, the Wigner function $W(r,p,0)$ can be recovered using the inverse Radon transform using Eqn (65). Similarly, by measuring the scattering intensity in the time interval of $0 + N\tau_{\mathrm{d}} \leqslant t \leqslant T_{\mathrm{rev}} + Nt_{\mathrm{d}}$, where N is an integer and τ_{d} is the delay of the electron pulse with respect to the laser pulse, the Wigner function can be restored for the time $N\tau_{\mathrm{d}}$. Therefore, TRED provides the possibility of recovering the quantum state of molecules in the ensemble.

Yet another method to recover the molecular quantum state is the determinaton of the density matrix elements, $\boldsymbol{\rho}_{mn}$, which have a one-to-one correspondence [210, 231] with the Wigner function:

$$W(r,p) = (1/\pi\hbar)\int\exp(2\boldsymbol{i}px/\hbar)\langle r - x|\boldsymbol{\rho}|r + x\rangle\mathrm{d}x \tag{78}$$

where $\boldsymbol{\rho}$ is the density matrix:[207]

$$\boldsymbol{\rho} = \sum_{n,m}\boldsymbol{\rho}_{nm}|\psi_n(r)\rangle\langle\psi_m(r)| \tag{79}$$

If measurements are performed for an incomplete cycle, as determined by the time interval $0 + \mathrm{N}\tau_{\mathrm{d}} \leqslant t \leqslant T_{\mathrm{rev}} + Nt_{\mathrm{d}}$, only the diagonal elements of the density matrix, $\boldsymbol{\rho}_n = \boldsymbol{\rho}_{nn}$, can be obtained. Determination can be performed using a PDF $\langle P(r,t)\rangle_\tau$ averaged over the time interval $\tau \gg \sup(|\boldsymbol{\omega}_m - \boldsymbol{\omega}_n|^{-1})$, $m \neq n$, as was demonstrated earlier:[226, 229, 230, 232 – 234]

$$\boldsymbol{\rho}_{nn} = \int\langle P(r,t)\rangle_\tau\{\partial[\psi_n(r)\varphi_n(r)]/\partial\mathrm{r}\}\mathrm{d}r, \tag{80}$$

where $\psi_n(r)$ is a regular normalizable solution of the time-independent Schrödinger equation and $\varphi_n(r)$ is the second linearly independent non-normalizable solution.[235 – 239]

The results of tomographic reconstruction [5, 240] of the molecular quantum state of N_2 and CS are presented in Fig. 13.

VI.2. Non-adiabatic two-channel photodissociation of the CS_2 molecule

The first TRED experiments were performed with multiphoton IR dissociation of CF_3I,[11] 193 nm dissociation of CS_2 molecules,[241] photofragmentation of $Fe(CO)_5$,[242] and 193 nm photolysis of 1,2-dichloroethenes.[243] A study on 193-nm photofragmentation of CS_2 molecules [241] initiated investigations of the photodissociation of CS_2 followed by energy transfer to the vibrational energy of the formed CS fragments.[168] When excited with 193 nm photons, CS_2

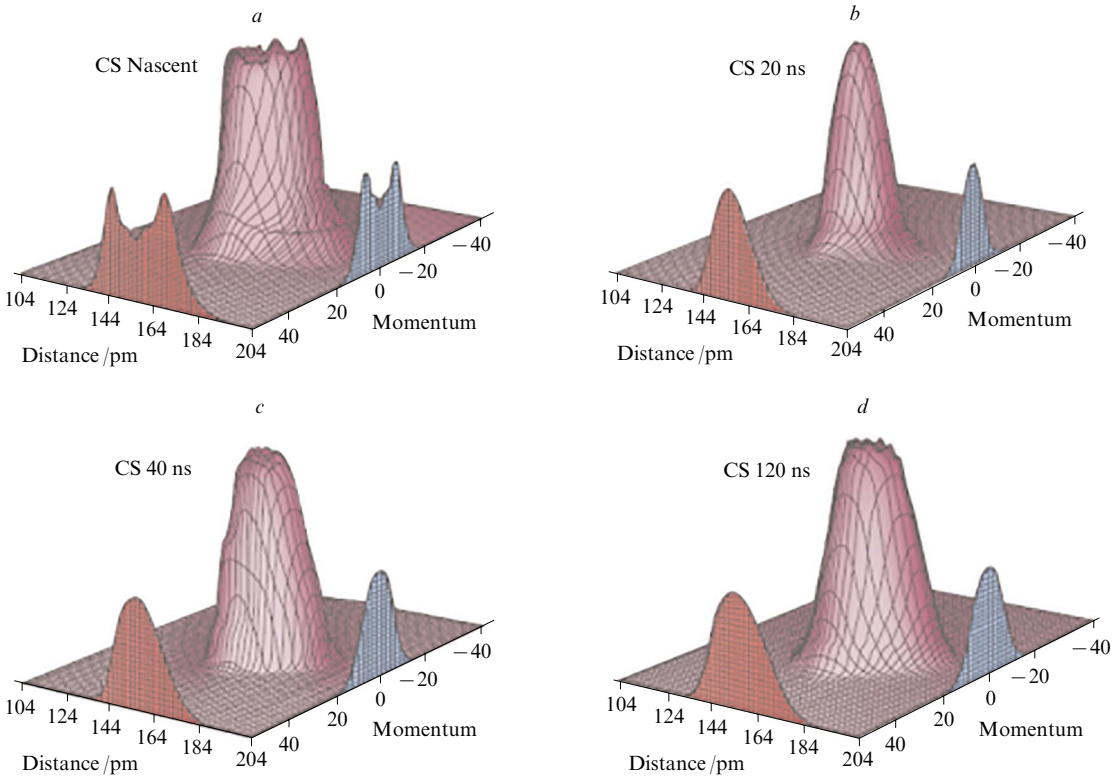


Figure 13. The Wigner function for the CS molecule. For the initial distribution ($\sim$1ps), the Wigner function is determined using the full density matrix (*a*). The Wigner function for a delay (τ_d) of 20 (*b*), 40 (*c*) and 120 ns (*d*) was obtained by tomographic reconstruction using the procedure described in Refs 23 and 240. (From Ref. 240 with minor revision).

undergoes photodissociation *via* a non-adiabatic two-channel mechanism:

$$CS_2(X^1\Sigma_g^+) \rightarrow CS_2(^1B_2^1\Sigma_u^-) \rightarrow CS(X^1\Sigma_g^+) + S(^3P_J) + S(^1D_J) \quad (81)$$

The CS_2 molecule in the excited state is quasi-linear, but the equilibrium internuclear distances differ from those in the ground electronic state.[244] Predissociation of CS_2 occurs in about 1 ps.

When CS_2 in a supersonic molecular beam is irradiated at a wavelength of 193 nm, the initial vibrational energy distribution in the CS fragment is inverted for both the $^1D_2$ and $^3P_2$ dissociation channels.[245, 246] The vibrational energy distribution with low level of population at $n = 0$ and $n \geqslant 10$ was described as bimodal[245] or wide.[246]

The experimental results show that in the first 20 ns, the system rapidly evolves towards an equilibrium which corresponds to the collisionless intermolecular transfer of vibrational energy (probably due to dipole – dipole interactions). During this time, a bimodal distribution in the momentum space and in the space of interatomic distances, approaches a monomodal, more narrow distribution (Fig. 13). In the interval from τ_d from 20 to 40 ns, collisional energy transfer begins to dominate the collisionless process. Thus, changes between 20 and 40 ns demonstrate the conversion of electronic energy into vibrational energy *via* collisions with $S(^1D_J)$ atoms and molecules $CS(X^1\Sigma_g^+)$. Between 40 and 120 ns, saturation of this process takes place. The evolving diffraction pattern in the time interval between 20 and 120 ns following the excitation of CS_2 was the first direct observation of electronic-to-vibrational (-rotational) energy transfer from one product of a non-adiabatic two-channel reaction (81) to the other reaction product.[23, 168, 202]

The populations of the first three vibrational levels of CS significantly decrease between 20 and 120 ns.[23, 240] The most likely explanation of this effect is the transfer of vibrational energy to the rotational and translational degrees of freedom of the CS molecule. This hypothesis is supported by an increase in the rotational temperature of CS in the process from $T_{rot} = 4200 \pm 300$ K at 20 ns to 5000 ± 600 K at 120 ns.[23] The bimodality of the PDFs $P(p,t)$ in the momentum space and $P(r,t)$ in the space of interatomic distances (Fig. 13) reflects the fact that photodissociation of CS_2 at a pump photon wavelength of 193 nm is a non-adiabatic process following two channels with the formation of $S(^3P_J)$ and $S(^1D_J)$ atoms.

VI.3. Diffraction signatures of aligned molecules

The understanding of the relationship between the molecular structure and function is a central problem in chemistry. Experiments that allow for the creation of structurally pure samples and investigation of their molecular dynamics and chemical function have been intensively pursued over the past decades. A recent review[247] presented a detailed description of the use of inhomogeneous electric fields for the manipulation of neutral molecules in the gas phase, *i.e.*, for the separation of complex molecules according to the size, structural isomers, and quantum states. For these complex molecules, all quantum states are strong-field seeking and require dynamic fields for their confinement. Current applications of these spatially-controlled complex

molecules are summarized and interesting future applications discussed by Chang *et al.*[247]

Consider an ensemble of molecules in the ground electronic and vibrational state. Such an ensemble can be prepared by cooling molecules in a gas jet, where the gas leaks into the vacuum chamber through a small orifice. A pulsed nozzle allows one to reduce the gas load and thereby the pumping speed of the vacuum pumps. In the jet expansion, the molecules are in different rotational levels. As is well known, the energy difference between adjacent levels increases linearly with increasing angular momentum of the molecule and its quantum number J (when $J \gg 1$). But when the molecules are irradiated by a strong linearly polarized laser field, the picture changes dramatically. First, the molecular spectrum in a strong laser field becomes equidistant.[248] Second, the 3D spatial distribution of molecules tends to become 1D, *viz.*, the molecules are aligned in the laser field[249] and begin to execute pendular motions around the polarization axes. This can be easily understood using the following rather simple considerations. The electron polarizability of the molecule, α_{pol}, relating the induced dipole moment of the system to the amplitude of the external field is an anisotropic function. For example, the polarizability of the simplest diatomic structures along the molecular axis is about 1.5 – 2 times higher than in the perpendicular direction. Therefore, when such a molecule is aligned in the external field, its potential energy reaches a minimum. In most cases, when laser radiation is not in resonance with electronic or vibrational transitions, it is convenient to carry out calculations taking into account only the static electron susceptibility instead of α_{pol}. It should be noted that the aligned molecular states persist only for a limited period of time. After switching off the pulsed laser field, the alignment is quickly destroyed, and the ensemble ceases to be quasi-1D. However, under certain conditions, the alignment can be restored subsequently even without the laser pulse through rotational recurrences. A review of experimental and theoretical research in this area is available.[250]

Additional interesting effects can be explored using rotating laser polarization axes. This can be realized experimentally by adding two specially-chirped laser beams.[251, 252] Under certain conditions (original molecules are cold enough, and the laser field is quite intense), a significant portion of the molecular ensemble begins to rotate with acceleration, followed by the laser field. Such molecular 'propellers', or superrotors, can even dissociate and be broken into atomic fragments when acquired sufficiently high rotational energy.[252] The state of the art in this area of molecular physics has been described in the work.[253]

The alignment of molecules by intense laser radiation can greatly aid the determination of molecular structures from electron diffraction data. As will be discussed below, this canbe done by observing GED signals with subpicosecond time resolution.[254] Importantly, no additional

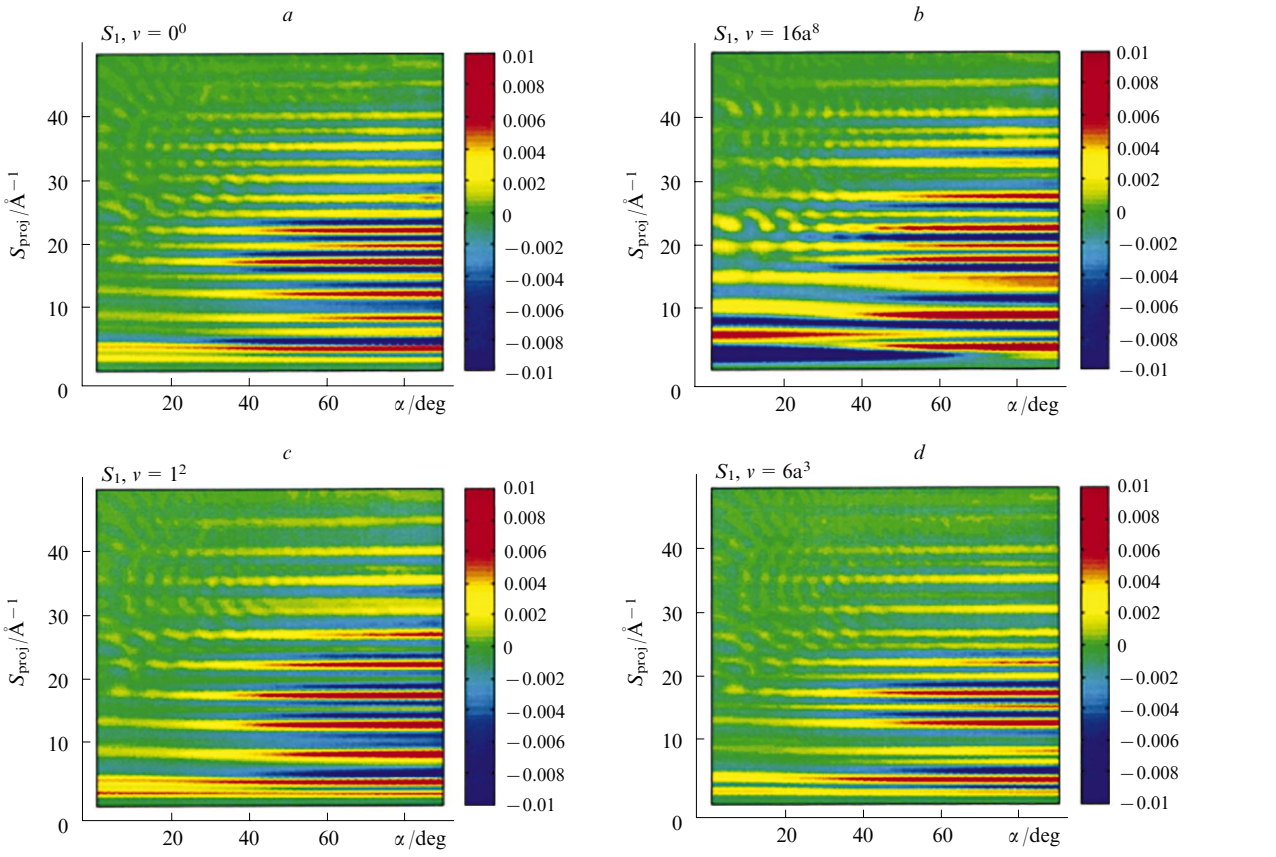


Figure 14. Calculated difference diffraction patterns (difference between the excited-state patterns and the ground-state patterns) of s-tetrazine, where a polarized laser beam excites the molecules of an isotropic sample to specific vibronic states as indicated above each panel.[119] The abscissa gives the rotation about the electron beam axis, with the laser polarization at $\alpha = 0°$, and the ordinate (in Å^{-1}) is the projection of the scattering vector onto the detector.

parameters are necessary to recover the structures of the laser-aligned molecular systems.

The alignment of molecules is of considerable interest for many applications, namely, possible control of chemical reactions, simplification of analysis procedures (1D case instead of a 3D distribution) and investigation of molecules in strong laser fields (high harmonic generation, photoionization studies, changes in the molecular orientation with respect to the laser polarization direction, *etc.*).

Even a single-photon excitation by a polarized laser beam can induce (partial) alignment of the molecular sample. The diffraction signatures of aligned excited states of vibrating polyatomic molecules were discussed by Ryu *et al.*[118, 119] and by Weber *et al.*[255] They calculated the patterns expected when the cyclic six-atomic aromatic ring molecule of s-tetrazine ($C_2H_2N_4$) is excited to specific vibrations in its electronically excited state S_1 (Fig. 14). In the polyatomic s-tetrazine molecule, vibrational excitation leads to additional structure in the diffraction patterns because the vibrational probability density function modulates the molecular structure.

Importantly, this modulation still manifests itself when isotropically distributed molecules in the gas phase are investigated. Excitation with a linearly polarized laser beam induces sufficient anisotropy to make the observation of the vibrational modes possible. Figure 14 illustrates this on two vibrational motions in the S_1 excited electronic state of s-tetrazine. Noteworthy is that the out-of-plane bending vibrations (mode 16a) have qualitatively different diffraction signatures than the in-plane stretching vibrations (modes 1 and 6a).

The concepts summarized above for the s-tetrazine molecule in a far-from-equilibrium state are directly relevant to complex molecular structures where energy redistribution may or may not be complete, and where certain bonds determine the reaction coordinate.[256] As an example, consider the ultrafast dynamics of the ring-opening reaction of 1,3-cyclohexadiene (CHD) and 1,3,5-hexatriene (HT) studied in the Zewail laboratory[257] and independently and at the same time in Weber's laboratory.[258] The product-only HT diffraction curves were significantly damped at all time points, indicating the vibrationally hot nature of the product structure. A systematic comparison of the *ab initio* PDF curves extrapolated to 2100 K for the three hot conformers of HT (cZc, cZt, and tZt) with the experimentally obtained radial distribution revealed greater similarity to the theoretical cZc curve rather than that of the lowest-energy tZt conformer.[256] A detailed study of the TRED imaging of the electrocyclic ring-opening reaction of CHD with ultrafast time resolution is described in Section VII.

VI.4. Photodissociation dynamics of aligned CS_2 and ICN molecules

The alignment, electronic excitation, and dissociation dynamics of the CS_2 molecule have drawn much interest.[244, 259 – 268] Although being one of the simplest polyatomic molecules, CS_2 shares many general and important properties with other polyatomic molecules, including the presence of CIs and the ability to be photoexcited into dissociative states.

Recently, Yang *et al.*[269] used TRED with femtosecond time resolution from aligned molecules (UEDAM)[270] to investigate the dynamics of CS_2 upon excitation with an intense ($10^{12} – 10^{13}$ W cm^{-2}) femtosecond infrared (IR) pulse. UEDAM allows the retrieval of both the transient molecular structure with atomic spatial resolution and the angular distribution of the molecular ensemble directly from the data without relying on theoretical modeling.[270]

Laser pulses with intensities in the range of $10^{12} – 10^{14}$ W cm^{-2} are often used to align molecules or to probe excited molecules by multiphoton ionization,[264, 266, 267] but their influence on the molecular structure has not yet been fully explored. High-intensity light pulses excite a broad range of dynamical phenomena including excitation of rotational, vibrational and electronic states leading to alignment, deformation, dissociation and ionization. With UEDAM it is possible to investigate all these dynamical processes simultaneously.

TRED has been used to measure the conformational changes in molecules in the gas phase with a time resolution of a few picoseconds,[271 – 273] while UEDAM was used to measure 3D static molecular structures.[254] It is possible to probe molecules with electrons in a field-free environment by using impulsive alignment. To this end, molecules are probed after they interact with the alignment pulse. The electric field of the electron pulse is very weak and does not disturb the molecules. In contrast to previous TRED experiments investigating conformational changes,[271] impulsive alignment makes it possible to obtain 2D images of the molecular ensemble rather than only 1D interatomic distances.[254]

A schematic of an experimental setup is shown in Fig. 15 *a*. An intense 800-nm IR laser pulse excites molecules and a femtosecond electron pulse is used to record the diffraction patterns at different time delays with respect to the laser pulse. The electron beam, laser beam and gas jet are mutually perpendicular. The anisotropy of the diffraction pattern is used to monitor the degree of alignment (Fig. 15 *b*). The time delay is fixed at the alignment maximum closest to zero delay and about 10^9 scattering events are accumulated to obtain a diffraction pattern with a high SNR.

The inverse Fourier transform of the diffraction pattern intensity $I(s)$ is the autocorrelation function of the molecular structure convolved with its angular distribution.[269, 274] The image of the structure of a perfectly aligned linear molecule can be determined directly from the autocorrelation function. Figures 15 *c* and 15 *d* show a simulation of the diffraction pattern $I(s)$ and its inverse Fourier transform $f(r)$ for perfectly aligned CS_2 molecules. The two bright spots in Fig. 15 *d* represent the C – S and S···S distances in the CS_2 molecule, as shown by the two white arrows. The spot at the centre of the image, which contains no structural information, was removed for clarity. Figure 15 *e* displays a model of the CS_2 molecule with the C – S and S···S distances marked for comparison. If the alignment is not perfect, the inverse Fourier transform gives a 2D projection of the 3D image of the molecular ensemble, or an Abel transform[275] of all the molecules along the direction of electron propagation.

The measured bond lengths are consistent with those of the electronic ground state. The C – S and S – S interatomic distances determined from the data[274] are 153(3) and 311(3) pm, respectively. For the excited $_1B^2(_1\Sigma_u^+)$ state of CS_2 molecule, the C – S and S – S interatomic distances obtained from the data[274] are 165(3) and 324(3) pm, respectively, which corresponds to a bent (quasi-linear) molecule with a C=S=C angle of 166°. The uncertainties are due to the finite spatial and angular resolution of the measurements and are calculated using simulated data.[269] In both cases,

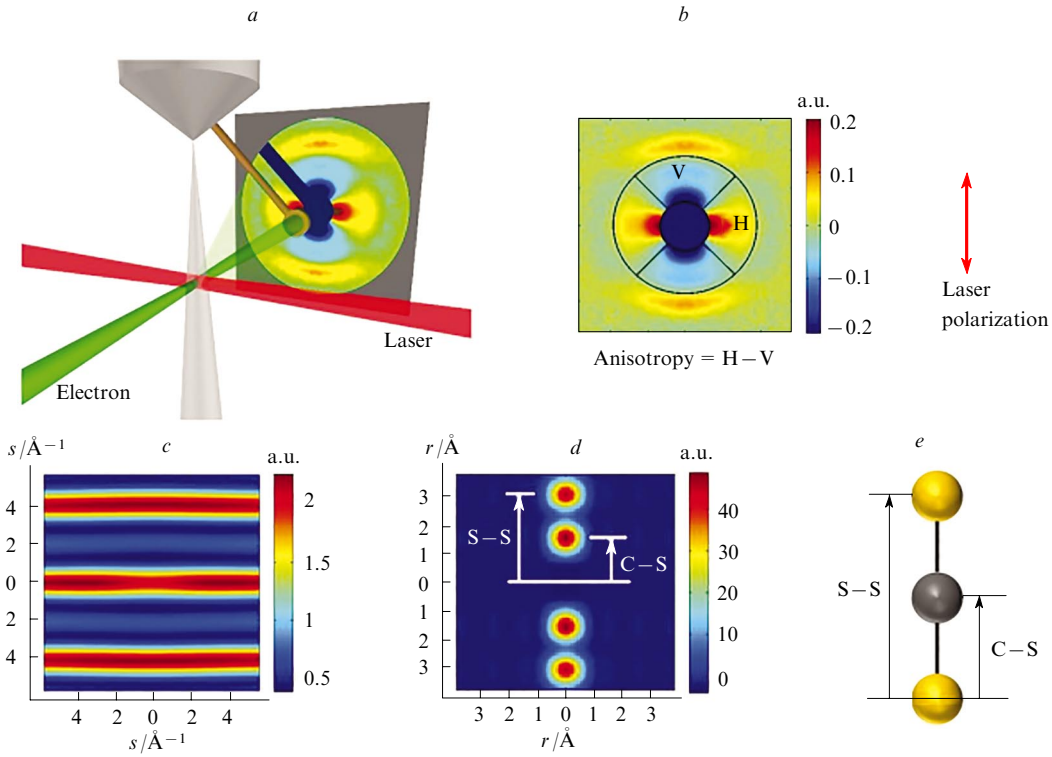


Figure 15. Alignment of molecules in pulsed electron diffraction. Experimental arrangement, where the green beam represents the electron beam, the red beam is the alignment laser beam, and the grey beam is the gas jet (*a*). With the primary electron beam blocked by a beam stop, the scattering pattern is projected onto a phosphor screen, which in turn is imaged on a CCD camera. The anisotropy is calculated by taking the difference of the total counts in the horizontal (marked by 'H') and the vertical (marked by 'V') directions between two circles (for more detail, see Ref. 274), for linear laser polarization (*b*). Simulated diffraction pattern for perfect alignment (*c*). Autocorrelation function of the molecule resulting from an inverse Fourier transform of the computed diffraction pattern (*d*).[274] Each off-centre spot represents an interatomic distance of CS_2, as indicated by the two arrows. A ball-and-stick model of CS_2 molecule with C – S and S – S distances indicated (*e*).

the results obtained are consistent with the bond lengths in the electronic ground state, while additionally revealing evidence for a bending vibration with a frequency of 396.8 cm^{-1}.[276,277] The corresponding vibrational mode can be excited by an impulsive Raman process. The period of this vibration is shorter than the time resolution of the experiment, but it would manifest itself as a broadening of the spot corresponding to the C – S distance in the autocorrelation function.[274]

The maximum degree of alignment that can be reached by impulsive excitation in the limit of very short pulses depends on the laser fluence rather than intensity.[278] For example, two very short pulses with different pulse durations and the same energy will produce the same alignment. Other processes, such as multiphoton excitation and ionization, depend strongly on the laser intensity. In order to differentiate between these processes, Yang *et al.*[274] carried out experiments with two different pulse durations (60 fs and 200 fs) for each value of the laser pulse energy. The 200 fs pulse was generated by chirping the 60 fs pulse; both pulses thus had the same spectrum. Six different laser fluences were used, namely, 0.16, 0.48, 0.79, 1.10, 1.42 and 1.73 J cm^{-2}. The laser power density ranged from 8×10^{11} W cm^{-2} to 2.4×10^{13} W cm^{-2}. At the point with the highest fluence (1.73 J cm^{-2} at 60 fs), the alignment pulse also ionized the gas, and the diffraction pattern was distorted by the plasma. Therefore, this point was excluded from the analysis.[274]

The study by Yang *et al.*[274] demonstrated a new way to probe the excitation and dissociation dynamics of molecules. The method can be extended to study photoexcited molecular reactions by using two laser pulses, one pulse to align the molecules and the other one to trigger the dynamics of interest. Compared to laser-based spectroscopic probes, the method has several strengths and weaknesses.[269,274] The advantages are as follows: (1) the molecular structure is imaged with atomic resolution by a direct inverse Fourier transform of the data, with no input from theory (with caveats about unknown corrections for the excited state and ionization contributions) and (2) the probe does not perturb the target molecule. The limitations of the method are that it does not provide information on the electronic structure and that currently the instrument response time is limited to about ps. For future experiments, the time resolution could be improved to around 100 fs by using keV electron pulses compressed by a radio-frequency cavity[279] in combination with tilted laser pulses,[280] or by using MeV electron beams.[21,281–284] The spatial resolution can be improved by increasing the beam current, which will allow increasing the area of the momentum space captured in the diffraction patterns.

Using the above theory, the time-dependent intensities of the molecular scattering and the corresponding radial

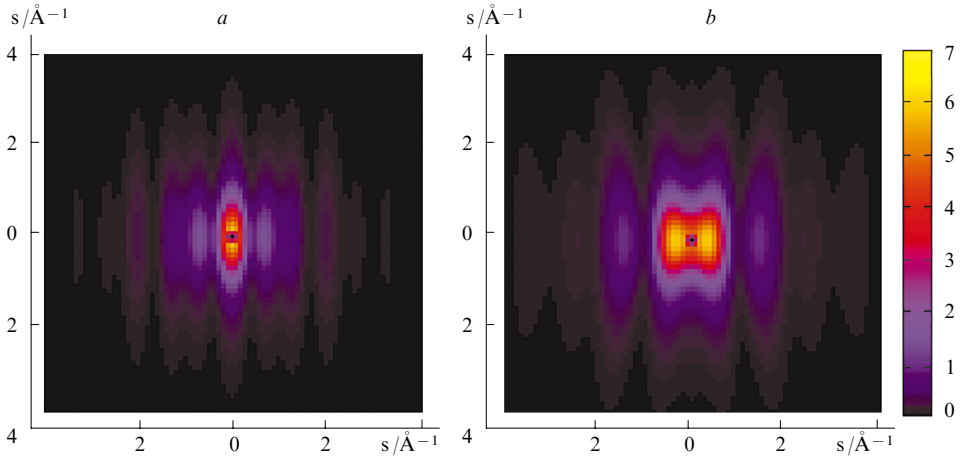


Figure 16. Molecular scattering intensities sM(s,ϕ) of anisotropic vibrationally excited nonequilibrium molecular ensembles of ICN molecules for angles $\phi = 0^\circ$ (*a*), and 45° (*b*). Linear polarization of laser radiation is along the axis X (perpendicular scattering). The color scale is the intensity in relative units.[285]

distributions of the internuclear distances were calculated for the processes of photodissociation of ICN, Fig. 16 (see Ref. 180 for comparison of the results).

A comparison of the diffraction intensities for parallel and perpendicular scattering (Eqns (23) and (25)) shows differences (Fig. 16) in the angular dependence of the molecular intensities. The intensity pattern of the latter is no longer axially symmetric, the essential features can still be recorded with a linear detector system, such as CCD camera. This is because all angular effects at the detector can be measured by rotating the plane of polarization of the laser light. The vibrational PDF is rather flexible for use in studies of different types of vibrational distributions in laser-excited molecules.[5, 109] It can be used in analyses of the TRED data by refining the parameters that define $P_{vib}(r,t)$, directly from the experimental data. However, it cannot be applied to dissociative processes, because the cumulant expansion does not converge in such cases.

Correlations between wave packet dynamics and the modes of laser excitation are important for spectroscopic investigations, but not for electron scattering. Thus, they were not taken into account in the model calculations.[285] Some representative results for ICN obtained in this way are given in Fig. 17.

The speed of propagation of the ICN wave packet is found to be faster in the calculations[285] than in those reported previously.[109] This is so because the speed of propagation of the centre of gravity of the wave packet in the calculations[109] depends on the asymptotic group velocity $v = (2E/m)^{1/2}$, which in turn depends on the available energy E. The calculations[285] refer to slightly higher available energy values.

The good agreement between the two sets of results — those based on quantum dynamics calculations and those based on the Gaussian wave packet approximation[109] is an important finding because the latter represent a more straightforward and convenient method for analyzing TRED data in terms of a limited number of adjustable parameters, which can be refined more readily from the experimental data.

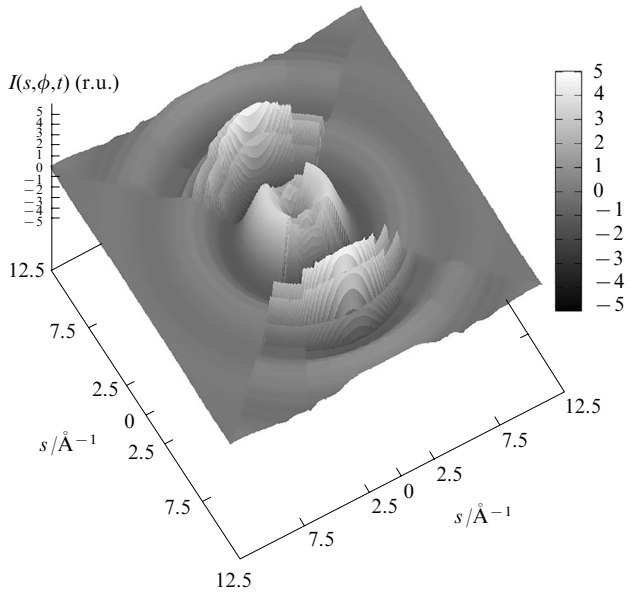
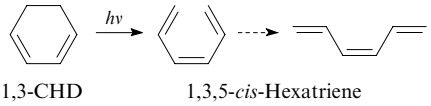


Figure 17. Diffraction intensity $I(s,\phi,t)$ of anisotropic vibrationally excited nonequilibrium molecular ensembles of ICN molecules for angles $\phi = 0^\circ$ simulated according to Eqn (11) of Ref. 285. The probe time, $t = 200$ fs and the probe pulse duration, $\tau = 25$ fs. The color scale is the intensity in relative units.[285]

VII. Imaging the electrocyclic ring-opening reaction of 1,3-cyclohexadiene

The light-activated ring-opening reaction of the 1,3-cyclohexadiene (CHD) chromophore (Scheme 1) finds application in optical control, optical switching, optical memory, light-activated molecular machines, photobiology, photochromic materials, and conformation-specific photocatalysts (see Refs 286, 287 and references therein). 1,3-Cyclohexadiene is an important prototypical system because its photochemically induced ring-opening reaction carries great relevance to synthetic organic chemistry and natural product synthesis.[286, 288, 289] For example, the synthesis of vitamin D involves a ring-closing reaction that is the reverse of the CHD ring opening.

Scheme 1



The development of time-resolved diffraction, ultrafast spectroscopy and powerful computational methods have greatly advanced our understanding of this important chromophore in a wide range of systems.

VII.1. The structure of the ground-state CHD molecule

Structural parameters of the ground-state CHD molecule were determined from GED data[290–292] as well as from TRED data with nearly 4 ps time resolution.[257,214] The most accurate structural parameters of CHD in its ground state are probably those obtained from the GED data by Oberhammer and Bauer,[292] *viz.*, r_a(C(5)–C(6)) = 153.4(2) pm, r_a(C(1)=C(2)) = 135.0(4) pm, and by Traetteberg,[291] namely, r_a(C(5)–C(6)) = 153.8(3) pm, r_a(C(1)=C(2)) = 134.8(1) pm, both of which were carefully determined using large scattering angles. They are in excellent agreement with the results of *ab initio* calculations by Autrey *et al.*[293] and by Merchán *et al.*[294] that were specifically optimized for the ground-state structure, and with the values recently reported by Mori and Kato[295] and Li *et al.*[296] Those values average to r_e(C(5)–C(6)) = 153.4(3) pm.

According to the high-temperature vapor-phase Raman study,[293] the double minimum in the ring-twisting vibration has an inversion barrier of 1132 cm^{-1}. Autrey *et al.*[293] also determined that the bond between the carbon atoms C(5) and C(6), *i.e.* the bond that breaks during the ring-opening reaction, is tilted by 30.1° out of the plane of the molecule. In contrast, the C(2)–C(3) bond on the opposite side of the ring is tilted only by 9.1°. The ground-state CHD molecule has a C_2 symmetry with two equivalent geometries that arise from a reflection about the molecular plane defined by the C_2 axis and the carbon atoms C(1) and C(4) (see the detailed review article of Deb and Weber[286]).

VII.2. Time-resolved electron diffraction and time-resolved X-ray diffraction of CHD

The first TRED studies of the electrocyclic ring-opening reaction of CHD with picosecond time resolution were published in 2001, carried out independently in the laboratories of A.H.Zewail[257,297,298] and P.M.Weber.[258] Changes in electron diffraction patterns were observed on ultrashort time scales upon irradiation of CHD with femtosecond laser pulses. 1,3-Cyclohexadiene is known to experience a ring opening reaction to hexatriene upon excitation to its $1B^2$ electronic state.[299] Internal conversion brings the molecule to a saddle point, from where one pathway leads back to cyclohexadiene, while the other path generates 1,3,5-hexatriene in one of its isomeric forms. Structural observations are made at picosecond time delays using an ultrashort electron pulse that is diffracted off the nascent product molecules. The diffraction images demonstrate that structural observations of prototypical organic reactions can be made in real time, opening a new methodology for studying chemical reaction dynamics.[258]

Ruan *et al.*[257] suggested that the ring-opening reaction of CHD results in hot molecular structures. Least-squares refinement of the structural parameters[257] yielded an HT molecular structure at each time slice. To locate the global minimum, Monte Carlo techniques were first applied for searching the configuration space, and finally the structure at each time represents the average over the local minima closest to the global minimum (Fig. 18). These HT structures showed no tZt character, but consistently manifested a configuration intermediate between *cZc* and *cZt*, far removed from a thermally equilibrated conformer distribution of 41% (*tZt*) : 45% (*cZt*) : 14% (*cZc*) at 2100 K (estimated from the conformer energies obtained from *ab initio* calculations).[256]

The departure from the lowest energy conformation suggests a far-from-equilibrium nature of the resulting hot structure of HT. The existence of a *cZc* like conformation indicates an inverted population on the PES (projected along the coordinate of torsional motion), with significant density at the classical turning points; this nuclear motion is shown schematically in Fig. 18. This far-from-equilibrium structure was reported to persist for more than 400 ps, suggesting a bottleneck in energy transfer from the inferred hybrid motion to other (higher frequency) modes, after the initial energy deposition. This energy localization could result from a mismatch in the frequencies of the coherent

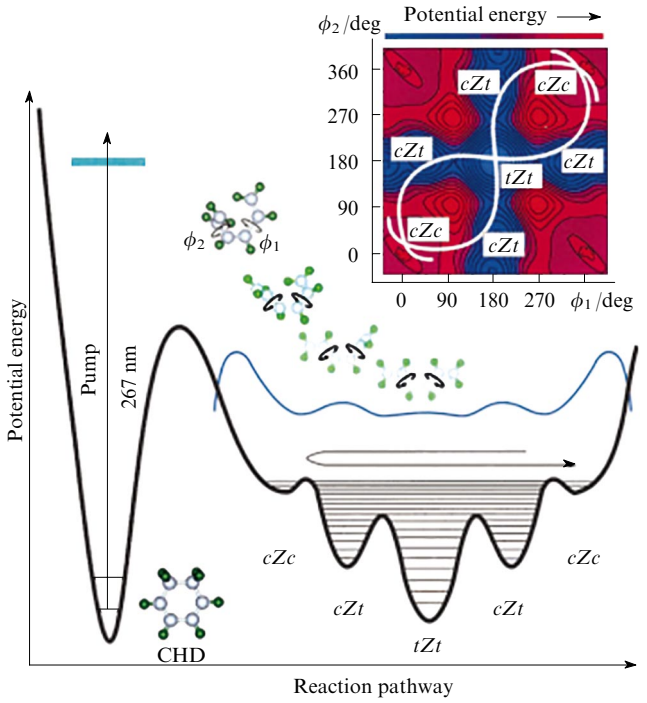


Figure 18. Potential energy landscape upon photochemical ring opening of CHD to form HT (see text).[256] The illustration shows the probability density distribution and the potential energy curve of ground-state HT, which demonstrate the nonequilibrium nature of the reaction product. The increased probability densities in the vicinity of the classical turning points suggest the dominance of a near-*cZc* conformation. The refined cZc-type molecular structure at one of the turning points is the statistical average, nonequilibrium structure obtained at long time delays. The equilibrium structures of the *cZc*, *cZt* and *tZt* conformers of HT are shown in pale colours. An isocontour plot of the *ab initio* PES $V = V(\phi_1, \phi_2)$ restricting the two internal rotational motions ϕ_1 and ϕ_2 in HT is shown at the upper-right. Possible trajectories leading to a time-averaged structure with a considerable *cZc* character are drawn with a white solid line.

modes compared with all other modes (at these high internal energies). It was noted [256] that this type of torsional modes was isolated in dynamical calculations of polypeptides.[289]

Ruan *et al.*[257] also observed an elongated C(5)–C(6) bond distance of over 170 pm, which is about 20 pm away from the expected equilibrium value, r_e(C(5)–C(6)) = 153.4(3) pm. This structure was also suggested to persist even up to 400 ps and was ascribed to a coherent oscillation where the stretched C–C distance is shifted continuously from one single C–C bond to another, and at the turning points, the torsional energy is partially stored in the C–C bond stretch.[256, 257] The authors concluded that energy redistribution within HT is slow with respect to both the rate of product formation and the time scale of the UED experiment. Given the large density of rotational and vibration modes for this molecule, it is, however, unclear that intramolecular vibrational energy redistribution (IVR) could take so long. An alternative explanation might involve unknown barriers between conformers along the interconversion between *cZc*, *cZt*, *tZt* forms. Higher time resolution to observe the putative long-lived coherent modes would resolve this issue.

Deb and Weber [286] and Arruda and Sension [287] have recently reviewed our fairly extensive knowledge of the photochemistry of CHD. The picture shown in Fig. 19 is based on some 30 years of time-resolved experiments and computational studies: the optical pulse excites the molecule to the Franck–Condon region of the 1B state from where the wave packet rapidly slides past a CI and down the well of the 2A state. At that point (labeled 2A/1A CI in Fig. 19), the conrotatory stereochemistry of the reaction is already decided.

A symmetry-breaking displacement through the second CI brings the molecule back to the 1A ground state. In CHD, the geometry of the latter intersection causes the molecule to continue its downhill slide such that it ends up in the open structure, *i.e.*, as HT. Cyclohexadiene is an attractive experimental system for time-resolved diffraction experiments because it moves down this path in a ballistic fashion,[301] so that the 'structure' remains a well-defined and observable concept throughout the reaction.

The time scales of this reaction are such that the molecule crosses into the 2A surface within 55 fs and to the 1A surface after 84 fs.[302] Detailed calculations of the photochemical dynamics are challenging in a molecule the size of CHD, but from multiple computational studies, the nature of the surfaces is well established, and the motions of the wave packet have, at least in the coordinate systems of reduced dimensionality, been carefully calculated.[286, 287]

While spectroscopic experiments have yielded much insight, many unanswered questions and mysteries remain that purely spectroscopic studies could not answer. A complementary view, such as that afforded by diffraction, is eminently desirable. In 2014, Minitti *et al.*[16] published a pioneering article in which the authors aim to settle this question and to determine the molecular structures as the reaction proceeds on a sub-picosecond time scale. To

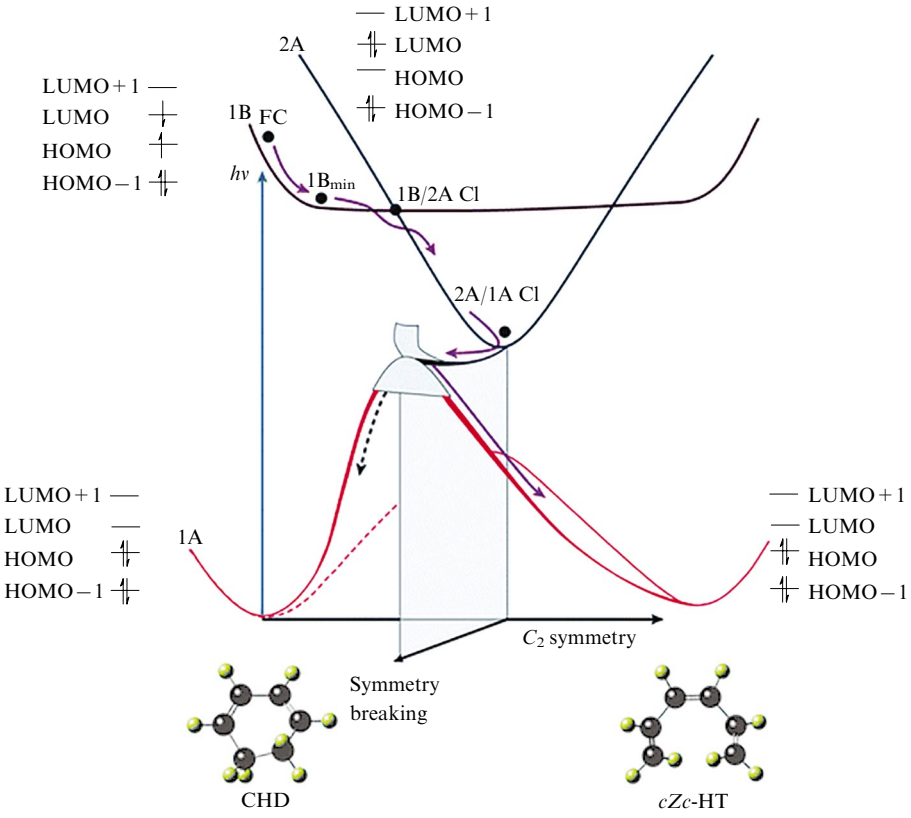


Figure 19. Illustration of the photochemical pathway leading to the ring-opening of CHD upon excitation with a near-UV pump photon (blue).[286] The molecule slides down the 1B surface, and crosses to the 2A surface by avoiding a CI. The ground state is reached upon crossing in a symmetry-breaking coordinate, which leads to the fully opened structure of hexatriene. The potential surfaces are drawn after Nenov *et al.*[300]

achieve this, the authors used gas-phase time-resolved X-ray diffraction (TRXD) with CHD at a very low pressure.

The experimental concept of the TRXD studies by Minitti and co-workers [16, 87, 206] is illustrated in Fig. 20. The CHD molecules are isotropically distributed in the low-pressure gas. A linearly polarized ultraviolet laser pulse ($\lambda = 266 - 275$ nm, 65 fs, 4 – 18 μJ, 100 μm FWHM focal spot) excites the CHD target molecule to the 1B state and thereby initiates the reaction. At a variable time delay with respect to the optical pump, the X-ray pulse originating from a free-electron laser (FEL), in this case from the Linac Coherent Light Source (LCLS; at Stanford University, California, USA; 8.3 or 20.1 keV, 30 – 50 fs, 30 μm FWHM focal spot) intersects the gas sample in a collinear geometry. Both the ultraviolet pump and FEL probe pulses are aligned through a 250 μm upstream alignment/differential-pumping aperture. X-Rays scattered from CHD are projected onto a CSPAD [303] detector. Given the diffusion of the photogenerated HT through the CHD one is reasonably assured that fresh CHD molecules are observed by each pump and probe pulse pair.

The observed TRXD diffraction pattern of a reacting molecule is not very different from that of a molecule in the ground state. In the example of the ring opening of CHD to form HT, most carbon – carbon distances retain a value typical of a conjugated double bond, while the carbon – hydrogen distances change little and contribute less to the overall difference diffraction signal. The atom – atom distances across the ring change substantially, but their overall contribution to the signal is comparatively small because their separation is large.

To interpret the TRXD data, Minitti and co-workers [16, 87, 206] presented a theory of time-dependent elastic X-ray scattering of photoinduced nonequilibrium ensembles of reacting transient species. The theory is an essential development of the earlier approaches [304 – 308] to this problem. Minitti *et al.* simulated the photoinduced dynamics of CHD using *ab initio* Ehrenfest trajectories.[309] Each trajectory corresponds to a nonadiabatic coherent wave packet that propagates on an APES [16]:

$$|\chi(\mathbf{R},t)\rangle = \left(\frac{\gamma}{\pi}\right)^{M/4} \exp\left\{-\frac{\gamma}{2}\left[\mathbf{R}-\bar{\mathbf{Q}}(t)\right]^2 + \right. \tag{82}$$

$$\left. + \frac{i}{\hbar}\bar{\mathbf{P}}(t)[\mathbf{R}-\bar{\mathbf{Q}}(t)] + \frac{i}{2\hbar}\bar{\mathbf{P}}(t)\bar{\mathbf{Q}}(t)\right\}$$

where $M = 3N_{at}$ in Cartesian coordinates and N_{at} is the number of atoms. The Ehrenfest trajectory, given by the phase-space coordinates $(\bar{\mathbf{P}}(t), \bar{\mathbf{Q}}(t))$, is generated by Hamilton's equations *via* a semiclassical propagation of the quantum averaged molecular Hamiltonian. The electronic structure calculations are performed using the *ab initio* package MOLPRO,[310] which supplies the adiabatic electronic states and the nonadiabatic couplings using the 3SA-CAS(6,4)-SCF/cc-pVDZ level of theory. An important point is that these calculations are made *on-the-fly* for each trajectory, eschewing the cumbersome task of calculating global APESs. The calculated Ehrenfest trajectories are used to fit the experiment with the target function:[16]

$$F(\mathbf{w}) = \left|\sum_{i=1}^{N_{traj}} w_i I_{theor}^{(i)} - I_{exp}\right|^2 \tag{83}$$

where w_i are the weights to be optimized. In practice, it is often better to fit percentage changes in the signal rather than absolute intensities. The weights were calculated [16] using a multi-start nonlinear least-square optimization

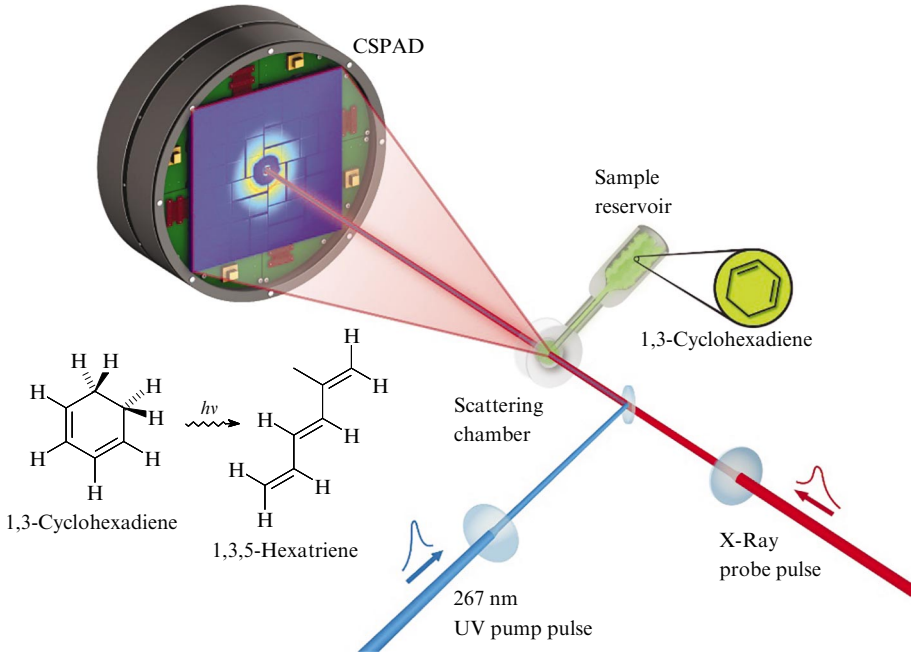


Figure 20. Schematic of the ultrafast time-resolved X-ray diffraction experiment using an X-ray free-electron laser. The target molecules are photochemically excited by a linearly polarized UV laser pulse (blue) and, after a fixed time delay (Δt_P), probed by the polarized X-ray pulse (red).[87] The X-ray scattering signal images the evolving reaction. The graphic superposition of the diffraction pattern on the detector shows the scattering from a dilute target of xenon gas recorded in the experiment.

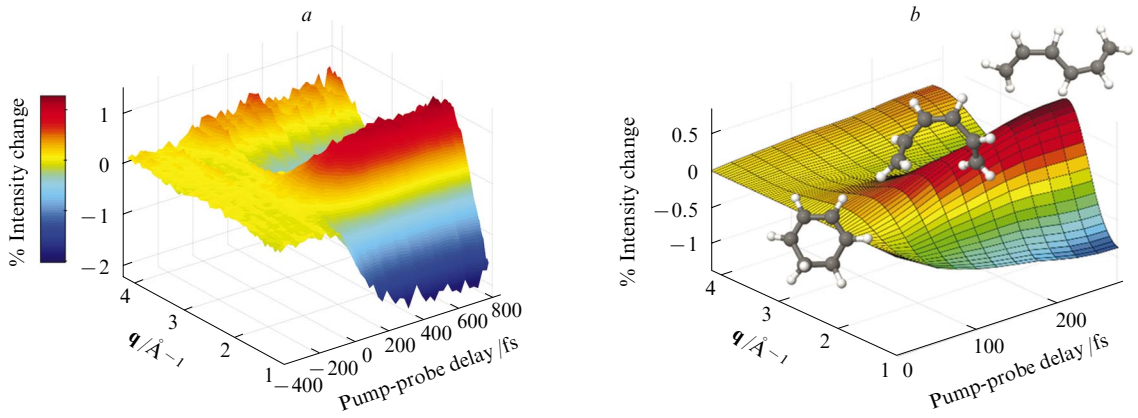


Figure 21. The difference signal, $I_{UV} - I_{noUV}$ ('laser on' – 'laser off') as a function of time (fs) and scattering vector **q** ($Å^{-1}$). Experimental (*a*) and computed (*b*) signal.[87]

routine using a trust-region-reflection algorithm with a finite-difference gradient. A best-fit theoretical signal,

$$I_{opt}(q,t) = \sum_i w_i I^{(i)}_{theor} \qquad (84)$$

to the experimental data shown in Fig. 21 *a* gives the time-evolving molecular structures (Fig. 21 *b*). It was shown that four of the Ehrenfest phase-space trajectories combine to give 76% of the weights.[87]

As shown in Fig. 22, the time resolution of the ultrafast X-ray diffraction experiment is well below 100 fs, being sufficient to follow the dynamic evolution of the molecular ring-opening reaction.[87]

A recent study by Northey *et al.*[311] discussed the *ab initio* calculations of molecular diffraction with application to the interpretation of time-resolved and static X-ray diffraction data. In this approach, elastic X-ray scattering was calculated directly from the *ab initio* multiconfigurational wave functions *via* a Fourier transform of the electron density using the first Born approximation for elastic scattering. Significant gains in efficiency can be obtained by performing the required Fourier transforms analytically, making it possible to combine the calculation of *ab initio* X-ray diffraction with expensive quantum dynamics simulations. It was shown that time-resolved X-ray diffraction can detect not only changes in the molecular geometry, but also changes in the electronic state of a molecule.

An important question for the gas-phase X-ray data interpretation is if it is possible to identify the electronic state of a molecule, or at least detect changes in the electronic state. The difficulty lies in the comparatively small number of valence electrons that change configuration during a transition between two electronic states, compared to the number of chemically inert electrons, which dominate the diffraction signal. Especially during chemical reactions that are accompanied by structural changes, such as for instance a photochemical ring-opening or an isomerization reaction, it is nontrivial to distinguish the changes in the diffraction signal that are indicative of changes in the electronic configuration from those that are due to changes in geometry. Furthermore, experiments only excite a fraction of the molecules and there will always be a background of ground state molecules, which must be subtracted.[311]

The TRXD investigations [16, 87, 206] have proven the feasibility of the experiment when high-intensity ultrafast pulsed X-ray sources are used. The experiment places high demands on the stability of the experiment and the data acquisition to recover the small changes in the diffraction

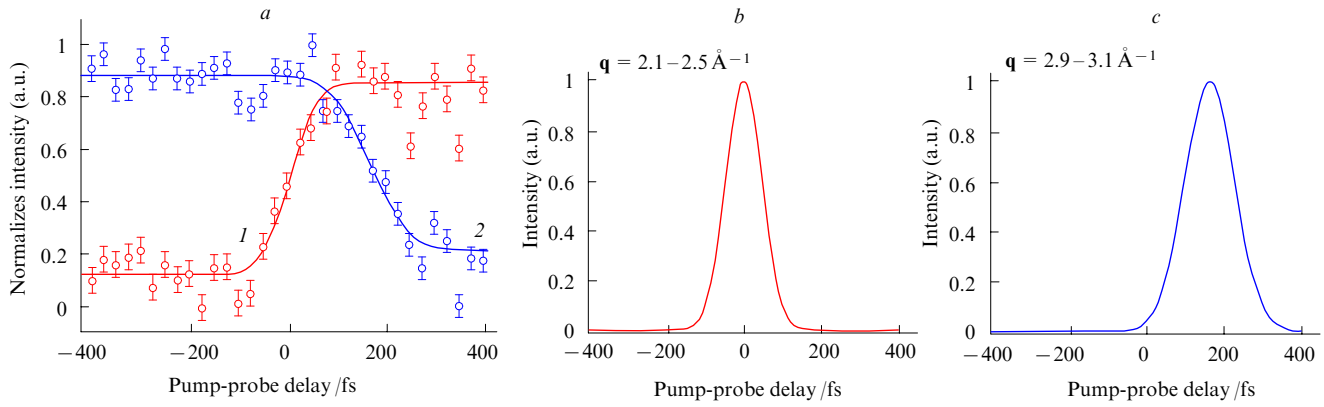


Figure 22. Time-dependent scattered signal intensities at scattering vectors of 2.1 – 2.5 $Å^{-1}$ (red circles, *1*) and 2.9 – 3.1 $Å^{-1}$ (blue circles, *2*) (*a*). The fits to the data are shown as solid red and blue lines. The derivatives of the fits show transients of 82 ± 24 fs (*b*) and 75 ± 35 fs (*c*).[87]

patterns. Yet with a sufficiently careful setup, those demands can be met. Moreover, it is possible to compute the time-dependent diffraction pattern of a wave packet as it evolves on an excited electronic surface. Consideration of the electron density of the electronically excited molecule and the time-evolving vibrational wave packet provide benchmarks against which to compare the experiment.[87]

VII.3. Convergence of time-resolved electron and X-ray diffraction, femtosecond spectroscopy and quantum chemistry

The ring-opening reaction of CHD is a textbook example of the Woodward – Hoffman rules that describe the conservation of orbital symmetry.[288, 312] The Woodward – Hoffman rules use symmetry arguments to rationalize whether an electrocyclic ring-opening reaction is thermally or photochemically allowed, and whether it proceeds in a conrotatory or disrotatory fashion (Fig. 23).

Theoretical studies [286, 287] have led to a convergence on a basic picture of this excited-state reaction, although important questions remain regarding the quantum dynamics and regions of space containing CIs. An illustration depicting the PESs involved in the ring opening and ground-state photoproduct relaxation is shown in Fig. 24. The reaction proceeds *via* excitation to the 1B state followed by ultrafast relaxation through a 2A state back to the ground state.

The transient ionization experiments of Fuss, Schmid, and Trushin in the 2000s, culminating with their experiment in 2009 that utilized a hollow core argon-filled fiber to generate laser pulses of 13 fs duration, have yielded much insight into the decay dynamics of CHD.[301, 313 – 317] These measurements have further refined and isolated each step in the ultrafast relaxation pathway.

Absorption of a photon at 266 nm excites the molecule from the 1A state and creates a wave packet on the optically bright 1B state. This wave packet experiences a steep potential slope and quickly decays with two distinct time constants of 21 and 35 fs. The former corresponds to the rapid movement out of the Franck – Condon region along a symmetric C=C stretch and C–C stretch, while the latter corresponds to the internal conversion from 1B to 2A accompanied by a ring puckering motion.[317] This pathway is illustrated in Fig. 24. Correlation of the observed wave numbers of the low-frequency vibrations with the calculated distances d of the two (CH_2) groups is possible, even without detailed knowledge of the nature of the ν_3 mode [301] (Fig. 25).

The low-frequency modes are understood to be delocalized over the ring [317] and are likely of twisting or bending character. The measured frequencies suggest that the ring is already weakened upon optical excitation, consistent with the calculated lengthening of the fracturing bond near the first CI. A further decrease in the vibrational force constant occurs once the 2A minimum is reached. This is consistent with the very long bond distance and the weak interaction between the two ends of the ring. The vibrational spectrum

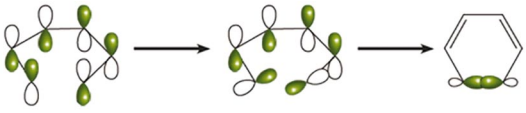


Figure 23. A conrotatory excited-state ring closure reaction.

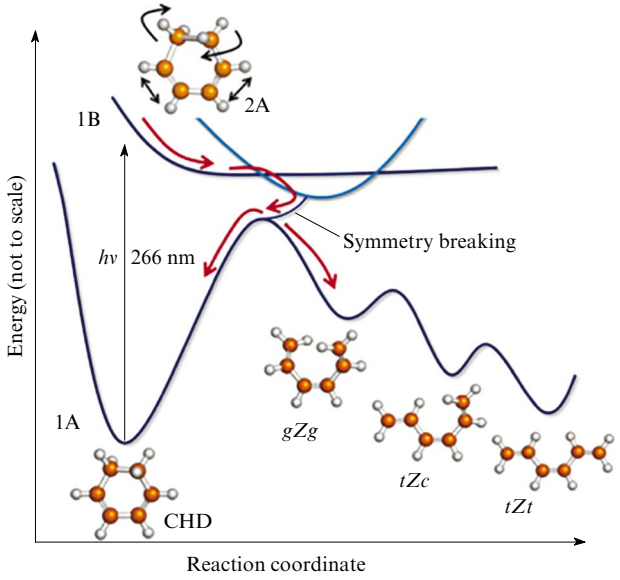


Figure 24. Illustration of the PES for the CHD ring-opening reaction and the hexatriene isomerization. The excited state undergoes an ultrafast relaxation through two conical intersections. Recovery to the ground state occurs on a sub-150 fs timescale.[287]

hence demonstrates (in agreement with theory) that the ring opening begins near the 1B/2A CI but continues to advance on the 2A surface. Even so, the reaction is not completed in the excited state as evidenced by the existence of the ring vibration.

According to the TRED studies by Ruan and co-workers [214, 257] and by Dudek and Weber,[258] gas-phase generation of HT following the excitation of CHD appears to occur with a quantum yield of unity.[286] The primary evidence for this is the absence of signatures of vibrationally hot CHD. A subsequent study by Rudakov and Weber [299] using a structure-sensitive photoionization-photoelectron technique also reports a quantum yield of nearly unity for

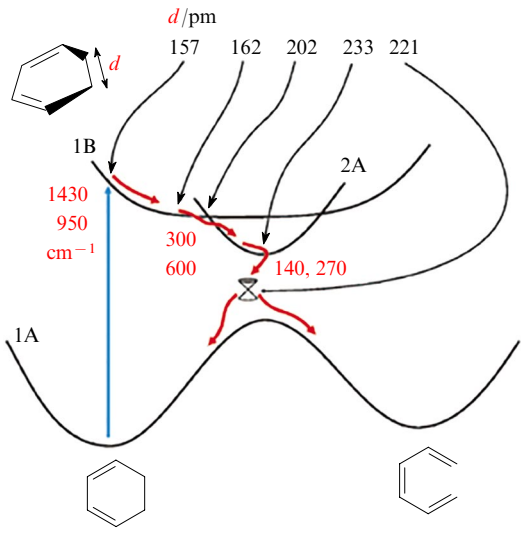


Figure 25. Correlation of wavenumbers of the ring vibrations with those calculated [301] with the CH_2-CH_2 distance d.[317]

the ring-opening reaction of CHD. The technique used in this more recent study is blind to vibrational excitation, but the magnitude of the CHD depletion is in agreement with the expected excitation of CHD (21%) based on the laser power, beam size, sample density, and extinction coefficient.[287] More recently, however, transient photoelectron spectra reported by Adachi *et al.*[318] revealed a HT : CHD branching ratio of 3 : 7 upon photoexcitation at 270 nm. Using TDDFT calculations, Tapavicza *et al.*[319] found the quantum yields of the ring-opening products ranging from 60% – 70%. This is larger than the 20% – 40% quantum yields measured in solution. It is possible that the difference arises from the solvent effects that prevent the two ends of the hexatriene fragment from drifting apart. TDDFT simulations[319] explored the process of rotational isomerization in detail. A fast rotation around ϕ_1 immediately after the ring opening was found, followed by a slower rotation around ϕ_2. According to gas-phase calculations,[319] this rotation takes 6 ps to reach the distribution of the two dihedral angles present at thermal equilibrium. Experiments in solution predict this process to happen in approximately 100 ps. Thus the molecule in solution is expected to stay longer in the *cZc* conformation.

The ultrafast ring opening of CHD yields HT products with high internal energy, equivalent to a vibrational temperature of *ca.* 2200 K.[256] As indicated in Fig. 25, three distinct conformations result from local minima on the HT ground-state potential. They are identified according to the conformation about the two single bonds (*cis*, *gauche*, or *trans* denoted below as c, g, or t, respectively) and with respect to the central double bond (*Z* or *E*). The initial photoproduct is *gZg*-HT, or *gauche* in either of the single bonds and *cis* with respect to the central double bond.[320] Arruda and Sension[287] pointed out that the initial conformation is *gauche* rather than *cis* because steric hindrances prevent a totally planar conformation. The *gZg*-HT product has an angle of *ca.* 40° as a result of these steric interactions.[321, 322] The excess vibrational energy present in HT following return to the ground state results in a highly fluxional species with rapid interchange between various accessible conformations. This results in a broad structureless peak in the time-resolved Rydberg electron binding energy spectra[299] and diffuse structures in TRED data.[257, 258, 323] A careful analysis of the electron diffraction signals suggests that the *tZt*-HT conformation appears on a 20 ps time scale providing an estimate of the time scale for diffusion from the initial *gZg*-HT conformation to a thermally distributed mixture of conformations.[256 – 258, 287, 297, 323]

A refined picture of the ring-opening mechanism has been developed for CHD.[300, 317] Absorption of UV light promotes the system into the first excited singlet state (S_1), which corresponds to the 1B state if C_2 symmetry is assumed.[324] Excitation induces a stretch of the double bonds followed by twisting around the central single bond C(2) – C(3), which activates the ring opening, *i.e.*, the stretching of the C(5) – C(6) bond. According to the Woodward – Hoffmann rules,[288, 312] this occurs in a conrotatory fashion. During these rearrangements, the character of the excited state changes adiabatically from B to A. The van der Lugt/Oosterhof model[325] predicts an avoided crossing (AC) between the S_1 state and the ground state (S_0) if the bond breaking occurs along the C_2-symmetric pathway. Symmetry breaking is thought to be necessary to reach the S_1/S_0 minimum energy conical intersection (CX).[300] The entire excited state process terminates within 200 fs.[301] Three processes with distinct decay constants (t_1 = 21 fs, t_2 = 35 fs, t_3 = 80 fs) have been identified in the excited state decay.[317]

To scan the APES along the excited state reaction, MD simulations of CHD were performed at 10 K.[319] Starting from the ground-state equilibrium structure of CHD, nuclear coordinates were propagated in time using excited-state TDDFT forces. The resulting potential energy curve of CHD shows that the largest part of the energy relaxation takes place within the first 10 fs after excitation (Fig. 26).

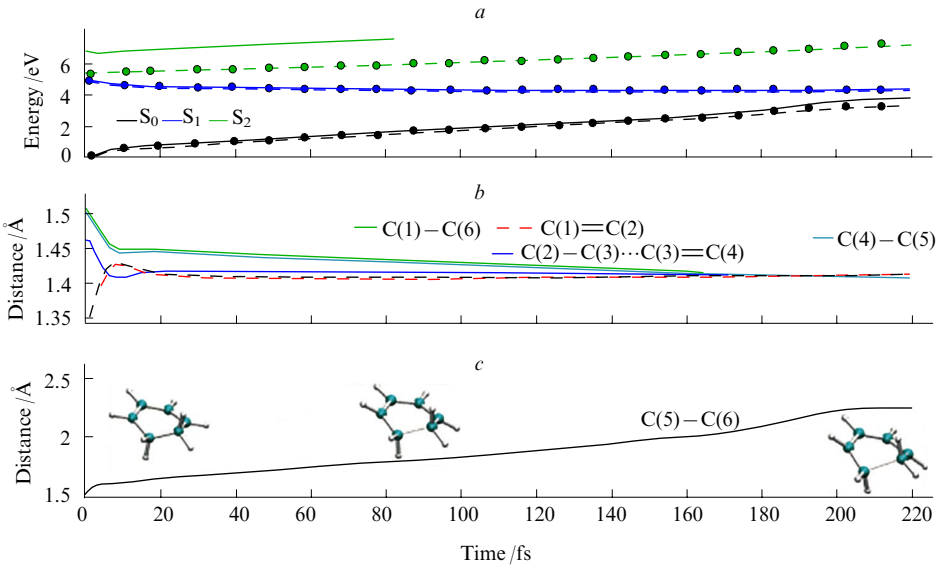


Figure 26. Time-dependent electronic energies and bond distances during the ring opening reaction of CHD.[319] Upper panel: potential energy curves along the low-temperature excited-state pathway (*a*). Solid lines: obtained from TDPBE0/TDA calculations, dashed lines: obtained from CC2/aug-cc-pVTZ calculations. Middle (*b*) and lower (*c*) panels: bond distances as indicated.

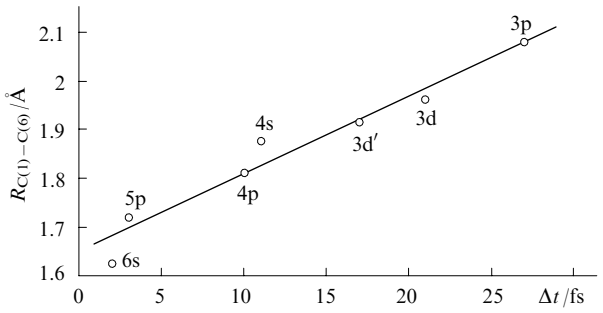


Figure 27. Distance between the terminal carbon atoms C(1) and C(6) in the ring-opening reaction of CHD as a function of time, as determined by the time sequence of Rydberg ionization peaks (as labeled) in connection with SA3-CASSCF calculations.[85]

This relaxation time is in the same range as the first experimental rate constant (t_1)[317] and can be attributed to the initial stretching of the double bonds (C(1)–C(2), C(3)–C(4)) and shortening of the single bonds C(2)–C(3), C(4)–C(5), and C(6)–C(1) (Fig. 26). After this rearrangement the atoms C(5) and C(6) drift apart, eventually forming hexatriene. After approximately 210 fs, an AC with an energy gap of 0.65 eV is reached.[319] At this point, the molecule exhibits a nearly C_2 symmetric structure, which is consistent with the excited state decay proposed on the basis of CASSCF minimum energy pathway calculations.[300]

A closer view of the early time dynamics was obtained in a time-resolved photoionization-photoelectron study by Pemberton *et al.*[85] The path down the steeply descending potential at early reaction times is mapped by ionizing the molecule onto Rydberg states, which are visible as fast transients in the photoelectron spectrum: for a fixed ionization frequency, only at certain points on the reaction coordinate is the resonance condition between the repulsive surface and the Rydberg state fulfilled, so that the time sequence of Rydberg signals reveals the progress of the reaction (Fig. 27). To connect the time-dependent Rydberg signals to the separation of the terminal carbon atoms C(6)–C(1), complete active space self-consistent field (SA3-CASSCF) calculations using the cc-pVDZ (correlation-consistent polarized valence double ζ) basis set were performed. Importantly, these were the same calculations that were used to find the optimal reaction path from the time-resolved X-ray diffraction study.[87] As seen in Fig. 27, after an initial transition from the 1B state to the 2A surface, the terminal carbon atoms separate at a rate of 16 Å ps^{-1}. The fact that both X-ray diffraction and time-resolved photoelectron data are matched by the same computation gives confidence that different views of the important photochemical dissociation of CHD are now starting to converge.

VIII. The dynamics of spectrally invisible structures

Radiationless transitions are ubiquitous in molecular systems and result in phenomena as the conversion of radiation into heat, photo-ageing, and photocarcinogenesis of DNA.[326–328] The absorption of light can induce two types of nonradiative events: (1) photochemical processes including breaking bonds or isomerization, (2) photophysical processes, which retain the molecular identity but induce transitions between electronic states such as internal conversion or ISC. For more than eight decades,[329] the exploration of nonradiative processes was focused on measuring the reaction rates. Theoretical studies have introduced the concept of CI in the energy landscape.[330–333]

Experimental evidence for nonradiative electronic transitions arises from the fluorescence quantum yield of molecules even at low pressures.[334] More recently, pulsed laser systems made it possible to study nonradiative processes directly. Yet some of the states involved in nonradiative electronic transitions may remain unobservable, depending on the spectroscopic technique employed, giving rise to 'dark' states, which make interpretation of the dynamics observed in 'bright' states challenging. Diffraction experiments measure the structures of molecules, implying that they are not affected by optically 'dark' states (please, see Ref. 333).

Srinivasan *et al.*[333] studied the molecular structures involved in radiationless transitions that are accelerated by vibrational excitation of the molecules in the so-called 'channel 3 region' (Ref. 335) and/or the proximity of electronic states.[326] They investigated four prototypical heteroaromatic compounds, *viz.*, pyridine, 2-methylpyridine, 2,6-dimethylpyridine and benzaldehyde. The cleavage and formation of new bonds in the transition states of the pyridine and 2-methylpyridine molecules, as well as the formation of highly vibrationally excited structures of 2,6 — dimethylpyridine and of the triplet state of quinoid form of benzaldehyde allowed them to clarify the effect of the original structure on the dynamic evolution of these molecules.

Pyridine, 2-methylpyridine and 2,6-dimethylpyridine. Photoexcitation of these molecules can lead to valence isomerization, fragmentation, or ring opening, as shown at the top of Figure 28 for zpyridine molecule. Using TRED, the dominant isomerization pathway and the structures of the intermediates were determined.[333]

To observe the structural changes as the chemical reaction unfolds, diffraction patterns were acquired for several time delays from −90 ps to 185 ps for pyridine and from −90 ps to 215 ps for 2.6-dimethylpyridine. The 2D difference diffraction patterns (Fig. 28) clearly demonstrate that the diffraction pattern changes with increasing time. The rings in the difference diffraction patterns directly reflect the changes in the molecular structure. The corresponding difference radial distribution curves $\Delta f(t;t_{ref};\boldsymbol{r})$ shown in Fig. 29 contain peaks with positive and negative amplitudes; negative amplitudes (highlighted in blue) are positioned near 1.3 Å and 2.5 Å and attributed to breaking bonds. Peaks with positive amplitudes (in red) correspond to the formation of new bonds.

In order to distinguish between the possible reaction channels, ultrafast electron diffraction (UED) data were analyzed for a number of structural models. Figure 30 shows some of the structures proposed in the literature for these aromatic molecules in the gas phase (Dewar and Hückel isomers and C_4H_4 + HCN fragmentation), liquid phase (Dewar isomer and azaprefulvene isomer), matrix (Dewar isomer and C_4H_4 + HCN fragmentation), and results of quantum chemical calculations (see Ref. 333 and references therein).

Figure 31 shows the experimental radial distribution curves $f(r)$ for the isolated transient structures corresponding to four time slices (from 60 to 185 ps for pyridine and to

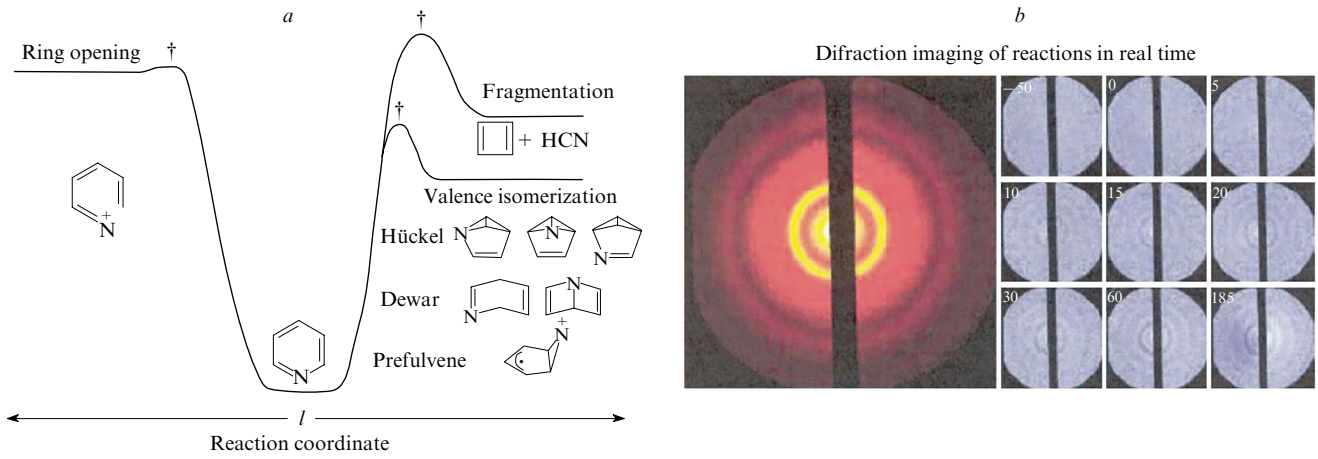


Figure 28. Potential pathways for photochemical transformations of pyridine (*a*).[333] TRED diffraction patterns of pyridine (*b*). The left side shows the diffraction pattern of the molecules in the ground electronic state, without laser excitation. The right panel shows the difference patterns obtained for different time delays between the pump laser pulse and the electron probe pulse (in ps).

215 ps for 2,6-dimethylpyridine) and theoretical curves for different models (which account of an excess internal energy). Curves were calculated for vibrationally excited molecules. The Kekulé, Dewar and Hückel structures and the $C_4H_4 + HCN$ fragmentation structure are all in poor agreement with experiment. It was therefore concluded that, on the time scale of the UED experiment, those reaction channels are not dominant. A mixture of the Dewar and Hückel isomers and a vibrationally 'cold' (403 K) open-ring structure shows good agreement with the experimental data. Therefore, the ring opening reaction is concluded to be the major reaction channel. Isomerization of the intermediate into the Dewar structure is a minor channel, while the contribution of the Hückel isomer is negligible.

The best agreement was achieved for the ring-opening reaction of pyridine and 2-methylpyridine. The mean vibrational amplitudes of the transient structures were 70 – 100% higher than those of the 'cold' molecules (403 K). This is probably due to a non-thermal (non-Boltzmann) distribution of vibrational energy in the molecule. The contribu-

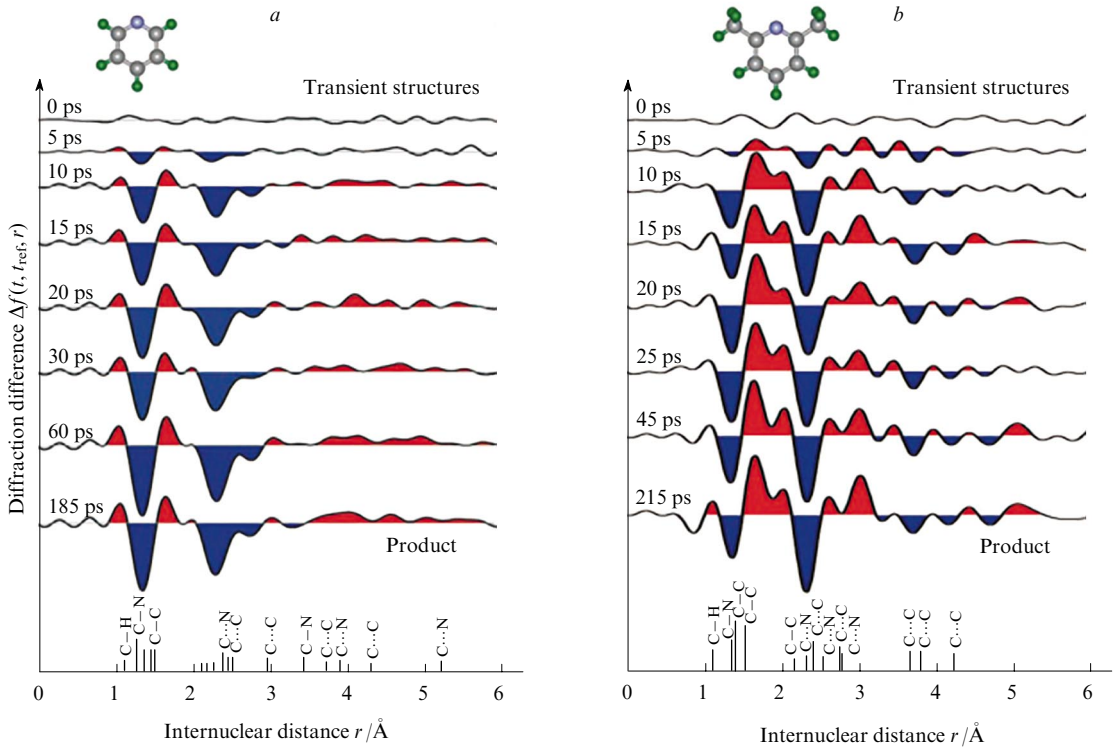


Figure 29. Structural dynamics of pyridine (*a*) and 2,6-dimethylpyridine (*b*) as observed with time-resolved electron diffraction.[271] Shown are the differences in the radial distribution functions. Vertical lines on the scale of interatomic distances *r* indicate the relative contribution of the different pairs of nuclei (*ij*).

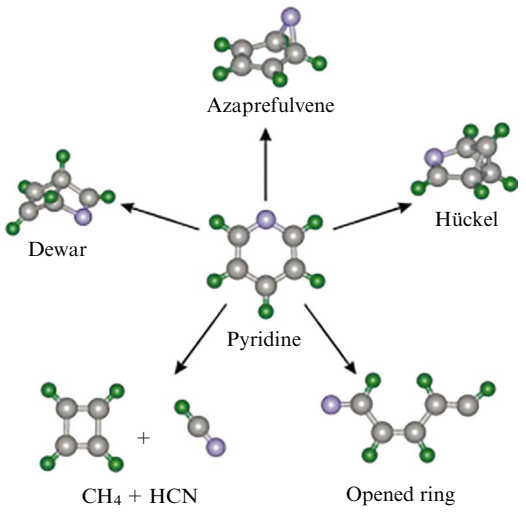


Figure 30. Possible pyridine phototransformation pathways (see Fig. 28).[333]

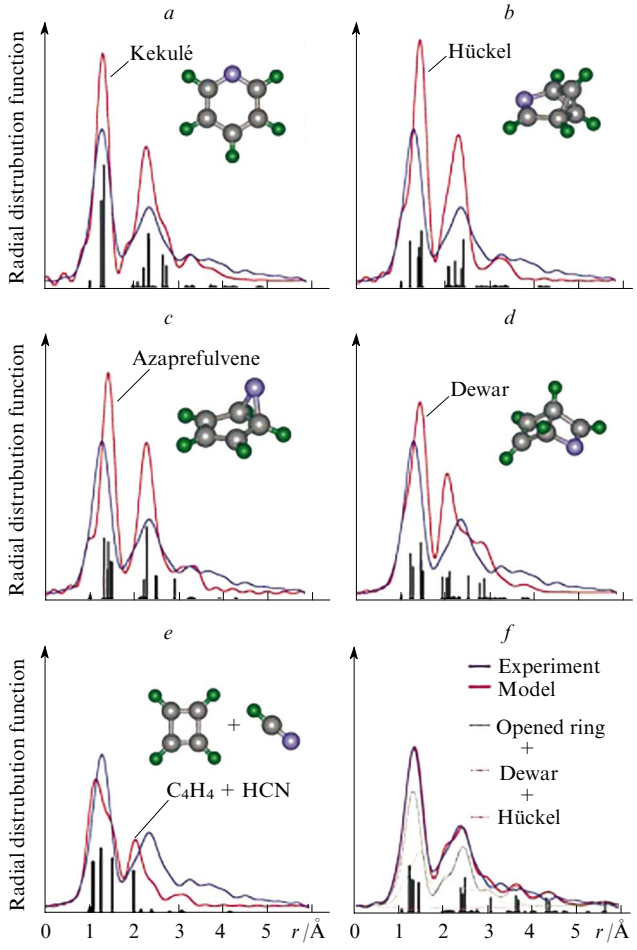


Figure 31. Comparison of the computed (red) and observed (blue) radial distribution functions for different conceivable reaction pathways. There is a significant mismatch for all proposed reaction channels except for the ring opening reaction with a minor contribution of isomeric structures of pyridine.[333]

tions of the Kekule and Dewar structures are very small. Thus, the ring opening reaction leading to formation of vibrationally excited acyclic transient structures[333] was concluded to be the primary reaction pathway.

Figure 32 illustrates the results of a least-squares refinement of internuclear distances and mean vibrational amplitudes for the molecular component of the scattering intensity sM(s) and the radial distribution function $f(r)$ for the acyclic structure of the transition state of the laser-induced pyridine ring-opening reaction. The calculated structural parameters match the observed structural dynamics of the reaction. For example, r_a (C(1) – N) = 5.23 Å and r_a(C(1) – C(5)) = 4.33 Å correspond to the appearance of long internuclear distances.

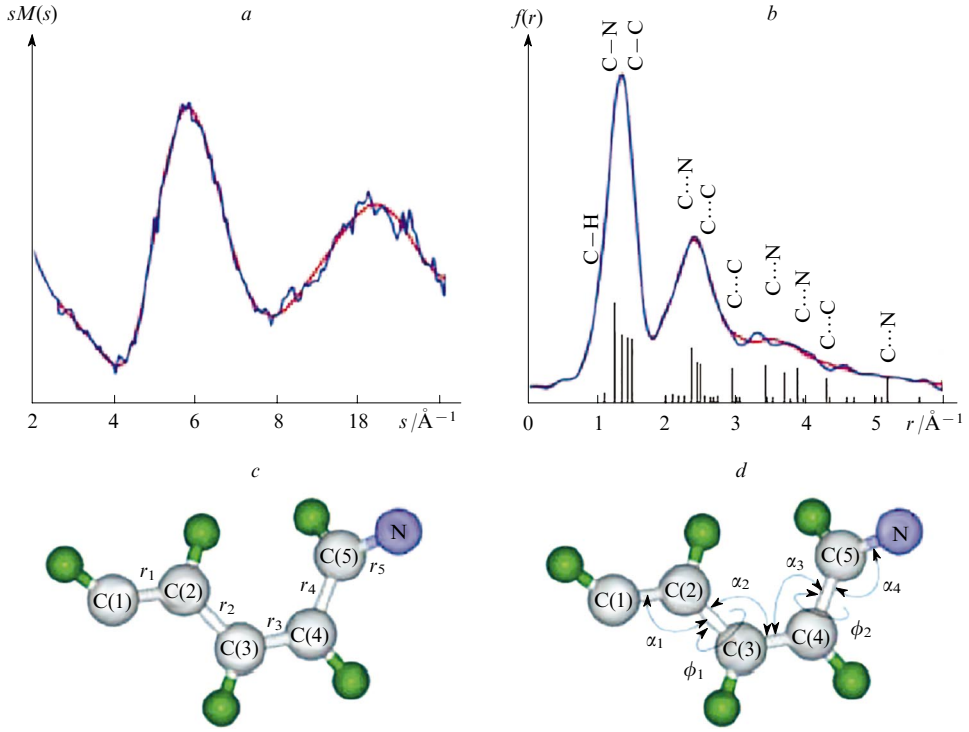
Satisfactory agreement between all structural parameters and results of quantum chemical calculations was reported except for the internuclear separation r_a(C(1) – C(2)) = 1.366(11) Å (*cf.* 1.318 Å obtained from DFT quantum chemical calculations) and one of the skeletal torsion angles. Experimental data correspond to an N – C(5) – C(4) – C(3) torsion angle (ϕ) of 123° instead of 180°, as was calculated quantum chemically. This discrepancy may be due to the fact that quantum chemical calculations give the equilibrium geometric parameters of the molecule, while the TRED data demonstrate vibrational effects, the nonequilibrium distribution of vibrational energy over various TS vibrational modes, which is essentially manifested in the diffraction data. Neglect of this factor can lead to the significant distortions of the parameters of the transient structure studied.

Similar results, showing a ring opening and the formation of acyclic transition state were obtained for 2-methylpyridine. For 2,6-dimethylpyridine, it was shown with a time resolution of ~1 ps that ring opening did not occur in the temporal interval of up to 215 ps. The TS corresponds to the highly vibrationally excited cyclic structure.[333]

The structural evolution of the isolated TS as revealed by the time-dependent radial distribution curves is shown in Fig. 33. Except for their relative intensities, the forms of the radial distributions $f(r)$ are almost unchanged over time. This was interpreted to imply that the structure of the transition state remains essentially constant on the timescale of the experiment. Only the value of the population of this state changes. The time-dependent population gives a time constant of 17(1) ps (Fig. 33). These results, combined with the analysis of the difference intensity curves, show that the ring-opening leads to the disruption of its aromaticity and the subsequent increase in the population of the acyclic transition state occurs with the time constant of 17(1) ps. In this condition, the internuclear distance C – C of the aromatic ring of pyridine should transform into the distance of C = C, characteristic for aliphatic compounds.

The corresponding time constants determined for 2-methylpyridine and 2,6-dimethylpyridine are 28(7) and 16(2) ps, respectively.[271] Thus, for the pyridine and 2-methylpyridine molecules there is a so-called 'channel 3' (Ref. 326) due to the ring opening and the formation of the acyclic biradical structure, while for 2,6-dimethylpyridine a highly excited cyclic TS is observed. This explains the significant differences observed in the study of this group of molecules by transient absorption spectroscopy with femtosecond time resolution.[75]

Refinement of ring-opened pyridine structure



Distance	experiment /Å	DFT /Å
r_1(C(1)–C(2))	1.366 ± 0.011	1.318
r_2(C(2)–C(3))	1.433 ± 0.012	1.456
r_3(C(3)–C(4))	1.346 ± 0.033	1.348
r_4(C(5)–C(6))	1.487 ± 0.018	1.466
r_5(C(5)–N)	1.244 ± 0.014	1.256

Angle	experiment /deg	DFT /deg
α_1(C(1)–C(2)–C(3))	127.7 ± 4.3	124.4
α_2(C(2)–C(3)–C(4))	124.3 ± 3.3	127.0
α_3(C(3)–C(4)–C(5))	123.4 ± 3.6	125.7
α_4(C(4)–C(5)–N)	121.1 ± 2.7	124.4
ϕ_1(C(1)C(2)–C(3)C(4))	185 ± 36	180
ϕ_2(NC(5)–C(4)C(3))	−123 ± 4	−180

Figure 32. Structures of the acyclic TS, which is formed by photoexcitation of pyridine molecules at 266 nm in the gas phase in a collisionless environment.[333]
Shown are the experimental (blue) and theoretical (red) molecular scattering intensity curves $sM(s)$ (*a*) and the radial distribution functions $f(r)$ (*b*) for the isolated TS. The interatomic distances (*c*) and angles (*d*) are obtained using UED and DFT quantum chemical calculations.

IX. Photodissociation and ultrafast relaxation of iron pentacarbonyl

Transition-metal complexes have long attracted interest because of their interesting chemical reactivity and the possible use for solar energy conversion.[336, 337] Electronic excitation, ligand loss from the metal centre, or a combination of both, creates changes in the charge and spin density at the metal site[338 – 345] that need to be controlled to optimize complexes for photocatalytic hydrogen production and selective carbon – hydrogen bond activation.[343 – 346] Understanding at the molecular level of how transition-metal complexes catalyze reactions, and, in particular, of the role of the short-lived and reactive intermediate states involved will be critical for such optimization.[346]

It has long been known that metal carbonyl compounds eliminate a CO group upon UV photolysis.[347, 348] It was not known however, whether this reaction proceeds as a simple bond breaking on a directly repulsive PES, such as is the case of, *e.g.*, some organic iodides. Some of the unsaturated reaction products are formed as triplets, raising the question if ISC plays a role.[349] The dissociation was believed to occur *via* a directly repulsive potential energy curve[347, 348] to produce the ground state of an unsaturated carbonyl (so sometimes a triplet). It has also been claimed that several CO groups can be more or less synchronously eliminated.[350] Modern femtosecond spectroscopy[349] and TRED can investigate the dynamics during the photodissociation and provide information about the PESs.[84]

Among the transition-metal carbonyls, $Fe(CO)_5$ is one of the most extensively studied molecular systems.[351 – 353] Having five carbonyl ligands, $Fe(CO)_5$ can dissociate into five different products $Fe(CO)_x$ (x = 4, 3, 2, 1, 0) depending on the excitation wavelength.[256, 349, 354] In these reactions, $Fe(CO)_4$ is the primary intermediate and serves as a doorway molecule for various subsequent reactions, such as decomposition, recombination with the carbonyl ligand, and coordination with solvent molecules.[355]

The first GED study of $Fe(CO)_5$ was performed by Ewens and Lister in 1939,[356] and numerous further studies

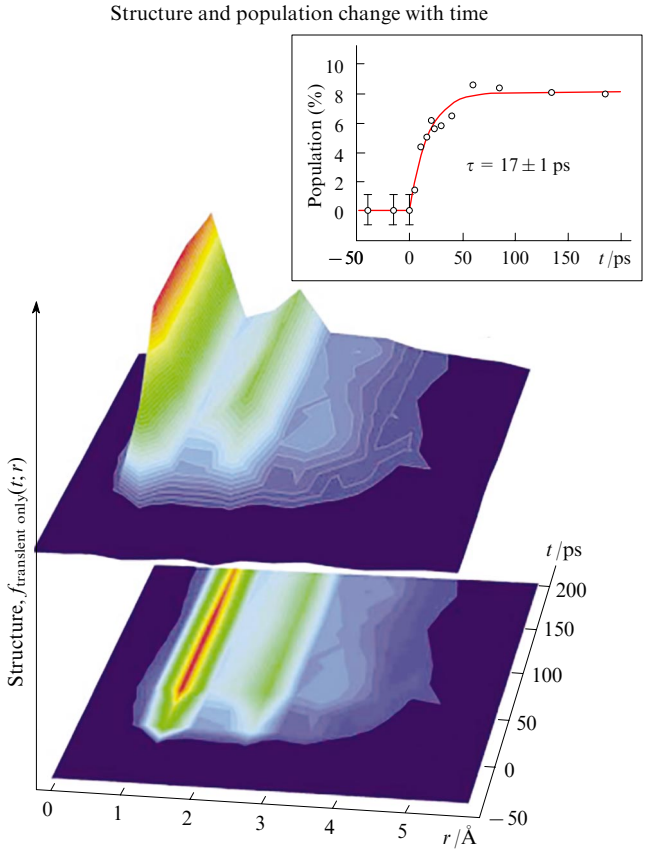


Figure 33. The population of the acyclic transient as function of time.[333] The radial distribution curve $f_{\text{transient-only}}(t,r)$ shows the formation of acyclic transient. The inset shows the time dependence of the population with a fit to an exponential rise time of 17 (1) ps. The contour plots indicate the range of interatomic distances (0 – 6 Å) and their changes over time.

followed.[357 – 361] In the GED study by Beagley and Schmidling[360] the average distances in the trigonal bipyramidal (D_{3h}) structure of $Fe(CO)_5$ were determined to be r_g(Fe – C) = 182.1(3) pm and r_g(C – O) = 115.3(3) pm at 303 K. It was also shown that the equatorial distances r_g(Fe – C)$_{eq}$ are longer than the axial ones, r_g(Fe – C)$_{ax}$, with the difference being $\Delta(FeC_{eq} - FeC_{ax})$ = 2.0(6) pm.

In 2001, $Fe(CO)_5$ was re-investigated in K.Hedberg's laboratory with a focus on the question: 'Are the Axial or the Equatorial Iron – Carbon Bonds Longer in the Gaseous Molecule?' (Ref. 361) The structure of iron pentacarbonyl was studied at 295 – 298 K using an experimental rotational constant available from the literature as a constraint on the structural parameters. The study utilized a B3LYP/6-311 + G(d) *ab initio* quadratic force field, scaled to fit the observed infrared wavenumbers, from which corrections were calculated for the effects of vibrational averaging on distances and certain other quantities useful for the structural analysis. The Hedberg results confirmed that the equatorial Fe – C bonds are longer than the axial ones, an important difference to the structure in the crystalline phases where the equatorial Fe – C bonds are shorter. Some distance (r_g/pm) and vibrational amplitude (l_α/pm) parameter values (with estimated 2σ uncertainties) based on the assumption of D_{3h} symmetry are: [r(Fe – C)] average = 182.9(2), [r(Fe – C)$_{eq}$ – r(Fe – C)$_{ax}$] = 3.2(2.0), [r(C – O)] average 114.6(2), r(C – O)$_{eq}$ – r(C – O)$_{ax}$ = 6(27), r(Fe – C)$_{ax}$ = 181.0(1.6), r(Fe – C)$_{eq}$ = 184.2(1.1), r(C – O)$_{ax}$ = 114.2(2.3), r(C – O)$_{eq}$ = 114.9(1.6), l(Fe – C)$_{ax}$ = l(Fe – C)$_{eq}$ = 4.7(5), and l(C – O)$_{ax}$ = l(C – O)$_{eq}$ = 3.6(3).

Pseudorotation in $Fe(CO)_5$ was not studied by GED. In 1998, Jang *et al.*[362] calculated the barrier to pseudorotation suggesting a Berry mechanism (*i.e.*, a C_{4v} transition state). The energy difference between the D_{3h} and C_{4v} configurations of $Fe(CO)_5$ was found to be equal to 2.25 (DZ B3LYP), 2.28 (DZP BP86) and 2.33(DZP B3LYP) kcal mol^{-1}.

The electronic structure of $Fe(CO)_5$ was studied with quantum chemical calculations at different levels by a number of groups (see Ref. 363 and references therein). It was found that $Fe(CO)_5$ is a trigonal prismatic molecule (D_{3h} symmetry) with a closed-shell $^1A'$ ground state corresponding to a formal Fe $^3d_8$ occupation.

In 1998, Hoffmann and co-workers[364] calculated the decomposition energies, fragment orbital overlaps, and fragment orbital populations for $Fe(CO)_4AB$ (AB = N_2, CO, BF, SiO) within the framework of the density functional theory using the NL-SCF/TZ(2P) basis set. Arguably, the main reason for the special character of CO (especially important to the experimentalist) is the excellent balance within this diatomic molecule between its internal stability and its excellent binding. The carbonyl group has an intermediate HOMO – LUMO gap, which makes it stable (one can handle the stable gas easily in a laboratory) yet moderately reactive.[364] The HOMO of CO, 5σ, is an orbital relatively high in energy that is most suitable for M – CO bonding. But, as shown for $Fe(CO)_5$, back-bonding into 2π (CO) orbitals is in many cases even more important than σ-donation. It is this balance between the donating and accepting capabilities that makes CO a special ligand for transition-metal chemistry. CO is in many cases strongly bound and inert, a good spectator ligand, but not so inert as to never react. The 2π acceptor orbital is low enough in energy to enable reactions at the CO ligand, depending on the metal and the ligand environment involved.[364]

Two types of covalent interactions between Fe3d orbital and CO are important for the bonding in this organometallic complex: a σ-donation from the CO into the formally empty $Fe3d_{z2}$ orbital of a' symmetry, and a concomitant π back-donation from the four doubly occupied Fe3d orbitals of symmetry e′ and e″ into the CO π^* orbitals.[363] A qualitative MO scheme representing both bonding types is shown in Fig. 34.

Excitations from the bonding orbitals e′ and e″ into the antibonding a_1' orbital give rise to four ligand-field (LF) excited states $^3E'$, $^3E''$, $^1E'$ and $^1E''$, with the CASPT2 excitation energies ranging between 28 000 and 42 000 cm^{-1}. The qualitative MO energy level scheme for $Fe(CO)_5$ shows the ten orbitals involved in covalent σ-donation from CO σ-orbital to Fe3d orbital and π back-donation from the Fe3d orbital to CO π^* orbital.[363]

IX.1. Ultrafast electron diffraction

In an UED study[297,298] of the photodecomposition of $Fe(CO)_5$ published in 2001, the determination of the molecular structure of transient $Fe(CO)_4$ was reported and the primary photodecomposition reaction pathway was identified. The major issue resolved in that study was indeed the dissociation pathway problem. Based on the evidence of UED experimental data, Ihee *et al.*[297,298] concluded that the gas-phase structure of the transient $Fe(CO)_4$ was in good

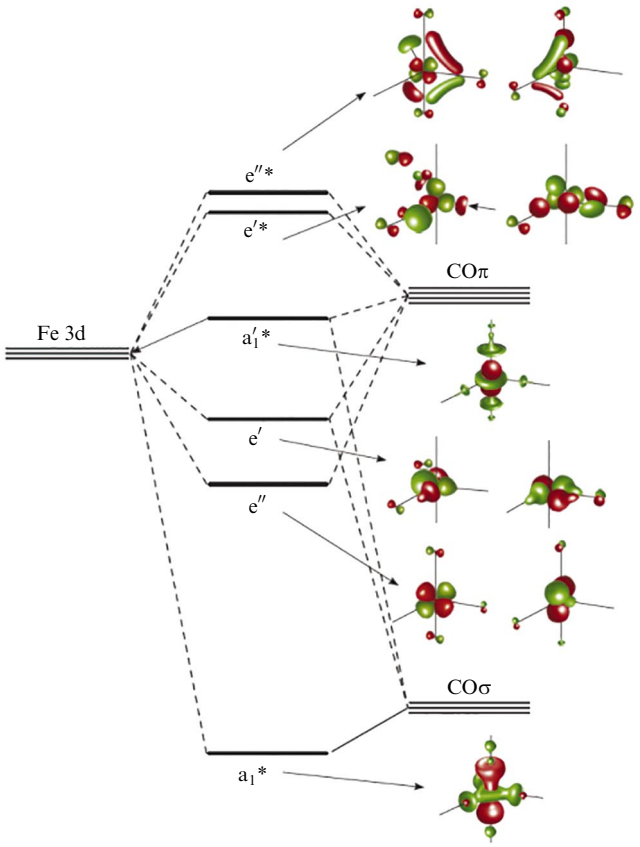


Figure 34. Qualitative MO energy level scheme for $Fe(CO)_5$, showing the ten orbitals involved in covalent σ-donation from CO to Fe 3d orbital and π back-donation from Fe 3d orbital to CO π^* orbital. (From Ref. 363 with minor revision).

agreement with that predicted for $Fe(CO)_4$ ($^1A_1$, C_{2v}). Moreover, they stated that 'the $[Fe(CO)_4]$ structure in the $^1A_1$ state is very similar to that of $Fe(CO)_5$ with one equatorial carbonyl group removed, while the structure of $Fe(CO)_4$ in the $^3B_2$ state is significantly distorted'.[297, 298] This also supports the equatorial CO elimination. The diffraction-difference curves $\Delta sM(+200$ ps; -180 ps) and $\Delta f(+200$ ps; -180 ps; r) and the GED patterns of isolated $Fe(CO)_5$ ($^1A_1'$, D_{3h}), $Fe(CO)_4$ ($^1A_1$, C_{2v}), and $Fe(CO)_4$ ($^3B_2$, C_{2v}) shown in Fig. 35 were simulated at $T = 341$ K using different codes to fit the diffraction data.[297, 298] The fraction of $Fe(CO)_5$ ($^1A_1'$, D_{3h}) was set equal to 1.0 and 0.86 at -180 and $+200$ ps, respectively,[297, 298] which scales the amplitude of the difference signal. In agreement with what was stated in Refs 297 and 298, the diffraction-difference curves characterizing $Fe(CO)_4$ ($^1A_1$, C_{2v}) and $Fe(CO)_4$ ($^3B_2$, C_{2v}) turned out to be very different (Figs. 35*e* and 35*f*). Though the singlet – triplet diffraction difference obtained using the UED approach decreased significantly upon the inclusion of more realistic vibrational amplitudes (Figs 35*c* and 35*d*), there was hardly any change in the inner r- and s-regions of the diffraction-difference curves where it could be detected experimentally with a sufficient degree of reliability. In the UED study, the exact temperature of reactants and products can only be roughly estimated. Though the temperature change of ~ 200 K appears to have a certain impact on the molecular intensity and radial distribution curves, the overall shape of the diffraction pattern does not seem to be significantly affected within the framework of the model (Fig. 35).

On the basis of an extensive testing and analyses of both UED models and software, it was concluded [297, 298] that the challenging task of distinguishing between the singlet and triplet states of transient $Fe(CO)_4$ in an electron diffraction experiment has been successfully resolved. It should be born in mind that this conclusion depends on the level of theory used and should be considered model dependent.

Photochemical reactions may involve many electronic states, each of different character, and they may be coupled strongly at certain geometrical arrangements of the nuclei. In these regions, the vibronic coupling allows vibrational motion of nuclei to change the nature of the electronic wave functions. Such regions therefore involve a breakdown of the Born – Oppenheimer approximation, a cornerstone of modern computational chemistry.[365, 366] Experimental advances using femtosecond laser pulses have seen detailed studies of fundamental molecular processes occurring on an ultrafast (sub-picosecond) timescale.[72, 297, 298, 349, 354, 367 – 370] Concomitant with experimental spectroscopic advances have been the development of computational methods to explore the nature of the electronic states involved,[371, 372] and the subsequent dynamical motion of atomic nuclei across multiple PESs.[83]

IX.2. Time-resolved femtosecond spectroscopy and mass spectrometry

The development of experimental techniques such as time-resolved femtosecond spectroscopy allows us to follow photochemical reactions in 'real time', resulting in greater insight into the mechanisms of light-induced chemistry. However, the chemistry investigated can be very complex and the analysis of data sets can be very challenging. After photodissociation of a single carbonyl ligand, the resulting unsaturated complex may be capable of achieving a geometry of non-Abelian symmetry (and degenerate irreducible representations of the point group).[366] Such degenerate states are Jahn – Teller active, the geometry being on a CI seam as discussed above. Two aspects need to be considered: (1) are there Jahn – Teller geometries that connect the excited and ground electronic states and (2) if there are, are they accessible on the excited reaction path following the photodissociation?

Multiconfigurational methods are required to describe different geometries with partial orbital occupancies and possible degenerate states. The CASSCF is the method of choice to model reactive PESs as degeneracies and quasi-degeneracies are automatically accounted for, and by virtue of the orbital optimization, the mixing of metal and ligand orbitals as the geometry changes is also included.[366] In considering what orbitals are needed in the CASSCF active space, the metal 3d orbitals are perhaps the most obvious choice, as the different arrangements of electrons in these orbitals gives rise to the textbook examples of Jahn – Teller instabilities.[373] This gives an active space (8.5) for the coordinatively unsaturated $Fe(CO)_4$ complex. However, this active space does not converge well, and the wave functions obtained are prone to spurious symmetry breaking, which can cause inaccurate energetics and geometries. It is important to realize that metal carbonyls are paradigm systems for dative bonding involving electron pair donation from the ligand. Thus, if an active space only includes a single set of orbitals, the electrons are unable to dynamically correlate their respective motions and are on the average

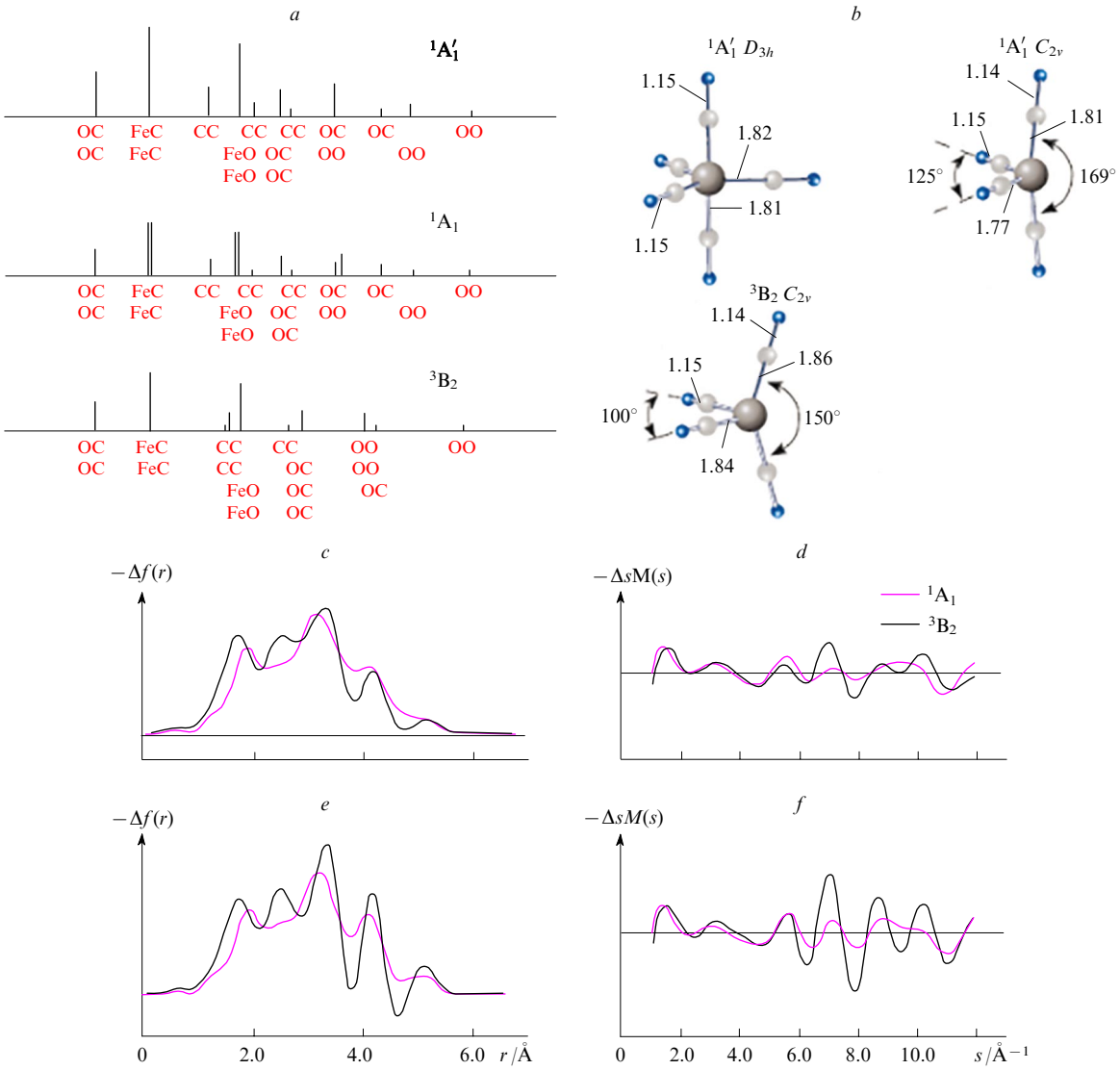


Figure 35. Schematically represented scattering terms of the gas-phase structures (*a*) of $Fe(CO)_5$ ($^1A_1'$, D_{3h}), $Fe(CO)_4$ ($^1A_1$, C_{2v}), and $Fe(CO)_4$ ($^3B_2$, C_{2v}) (*b*); bond distances in Angstroms, bond angles in degrees. Diffraction-difference curves $\Delta sM(+200$ ps; -180 ps; *s*) (*c*–*f*), (right) and $\Delta f(+200$ ps; -180 ps; *r*) (left) for $^1A_1$ and $^3B_2$ states of $Fe(CO)_4$ using calculated vibrational amplitudes, l_{ij} obtained from ASYM99 (*c*, *d*), and estimated empirically (*e*,*f*) (see text).[256]

too close together. A successful technique to handle this is to augment the active space with a set of empty orbitals with an extra node in the internuclear metal – ligand (M – L) region. These orbitals are notionally the 4d counterparts of the occupied 3d orbitals. For example, for $Cr(CO)_5$, the active space would increase from (6.5) to (6.10). Such active spaces now give accurate barrier heights relative to correlated single-configuration methods,[374] but crucially are also capable of treating excited states and degeneracies as well in a balanced manner. A related active-space augmentation has been successfully used in CASPT2 calculations of metal carbonyl bonding in the ground state[375] and for the electronic spectroscopy of metal carbonyls.[376] From the optimized CASSCF wave functions it was found that the occupancies of the 4d orbitals (as obtained from the diagonal elements of the one electron-density matrix) are non-negligible, being about 0.1 in the ground electronic state relative to their occupied counterparts ($\sim$1.9). For $Cr(CO)_5$, a smaller active space is actually possible by dropping both the 3*d* orbital and its 4*d* counterpart. This is because there is one unoccupied 3d orbital at all geometries for $Cr(CO)_5$ in the ground and lowest electronic excited states.[377,378] For further discussion, see Ref. 374. Fuß *et al.*[349] showed that $Cr(CO)_5$, $Mn(CO)_5$, and $Fe(CO)_4$ return to the lowest electronic states of the initially excited multiplicity within several hundred femtoseconds of the photodissociation of the parent carbonyl. This timescale precludes a spin-orbit induced change from the low-spin manifold and anticipates the accessibility of a CI seam to facilitate radiationless population transfer to the ground state.[366]

Trushin *et al.*[354] studied the femtosecond dynamics of $Fe(CO)_5$ photodissociation at 267 nm by transient ionization. The photodissociation of the trigonal bipyramidal $Fe(CO)_5$, whose photochemistry is one of the most investigated among the binary transition metal carbonyls,[379] results in $Fe(CO)_4$. This photoproduct has been found to

be generated on an ultrafast timescale (Fig. 36) with a Jahn – Teller CI inferred to be at a tetrahedral geometry.[354]

The finding reveal five purported separable time constants, *i.e.*, 15, 21, 30, 47 and 3300 fs after excitation in the gas phase.[354] The initial dynamics should be viewed as a continuous relaxation pathway from the initially prepared Franck – Condon region to the lowest singlet state (S_0) of $Fe(CO)_4$ *via* Jahn – Teller distortions leading to the dynamic formation of CIs between the ground and excited states. The initial motion is expected to involve all ligand bonds with one ultimately leading to dissociation of a CO. The resultant $Fe(CO)_4$ is generated in an excited state S_1 state and ultimately relaxes to tetrahedral geometry. The slowest relaxtion component is assigned to the dissociation of a second CO *via* thermal sampled coordinates of the vibrationally hot excited state. These elimination steps are though to occur by a pseudorotation process that would involve the coupling of more than one mode. Subsequent relaxation of the $Fe(CO)_4$ and $Fe(CO)_3$ to the triplet ground states occurs within 500 ps (Fig. 37).

The dissociation of the first CO of $Fe(CO)_5$ with its individual steps is remarkably fast. The sum of the first three time constants (21 + 15 + 30) fs) is below 100 fs. These time constants are not separable and should be considered more as a continuous nonexponential relaxation process. As argued in Ref. 354, this implies that the acceleration already begins in the Franck – Condon region, a statement that is not self-evident. If the excited state were nondegenerate, the potential energy curve along the Fe – CO dissociation coordinate would begin with zero slope, since there are symmetry-equivalent ligands. The Jahn – Teller splitting of a degenerate state, however, gives rise to a nonvanishing slope. It thus explains the initial fast acceleration and predicts that it involves more than one CO ligand. Superposition with a totally symmetric stretch coordinate, which involves several ligands, is not excluded. Such a degenerate ($2E'$) state is available in the right wavelength region; due to its metal-to ligand charge transfer character the corresponding absorption is intense and, due to its short lifetime (steep slope), also broad so that it can overlap with the pump wavelength.[354] On the other hand, a nondegenerate $1A_2''$ MLCT state has also been predicted in this region.[380] To explain the lack of anisotropy, Trushin *et al.*[354] also assumed an intermediate population of the $1A_2''$ state (*via* the $2E'/1A_2''$ CI), which then rapidly returns to the main relaxation path.

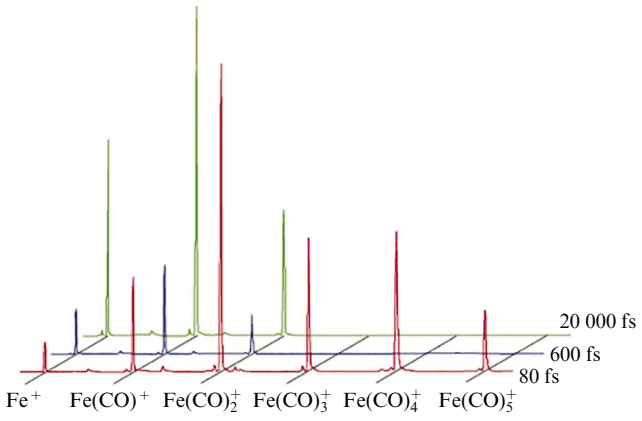


Figure 36. Transient time-of-flight spectra obtained after irradiation of $Fe(CO)_5$ with 267-nm pump pulses and 800-nm probe pulses delayed by 80, 600, and 20000 fs. The background, which is due to ionization by the probe pulses alone, is subtracted.[354]

In previous experiments with high-intensity nanosecond UV laser pulses, it has been suggested that resonant two-photon excitation could populate states with energies above the ionization limit and that the neutral molecule subsequently loses all its ligands explosively.[381] However, the ultrafast dissociation found in Ref. 354 hardly leaves time for absorption of a second photon with the pulses employed. Possibly, further excitation took place after the dissociation. The observed fast rates imply not only real crossings, but also that they are accessible without barriers. In view of the closely spaced upper states, the absence of barriers is natural. In the dissociation product, it was concluded[354] from the easy accessibility, that the singlet T_2 state of tetrahedral $Fe(CO)_4$ lies energetically between the S_0 and S_1 states of the molecule in the equilibrium C_{2v} geometry. The fast rate through this CI is also remarkable for another reason. As in all cases with a triply degenerate state, the intersection space is only $(f-5)$-dimensional,[382] where $f = 23$ is the number of internal coordinates. The branching space is then five-dimensional and is spanned by two e and three t_2 coordinates. The common case is a twofold degeneracy with an $(f-2)$-dimensional intersection space. Although it has been shown that a CI presents no bottleneck for the molecular trajectories,[383] it is often asked whether the molecule can find such a small 'point' ($(f-2)$-dimensional space) as the tip of the cone. The results show that even the $(f-5)$-dimensional space presents no problem. The reason is, of course, that the wave packet has a nonzero extension in f dimensions and can already cross over in the near surroundings of the 'point'.[354]

A very useful tool to predict suitable stable geometries around the point of a Jahn – Teller CI is the epikernel principle of Ceulemans and Vanquickenborne.[384] This states that the highest-ranking epikernels are the point groups of minima, and that lower-ranking epikernels, and kernels will be point groups for saddle points for any Jahn – Teller distortion. Kernels are the groups of symmetry elements that are preserved when distorting along a vector spanning an irreducible representation of a given point group. Epikernels are groups of higher symmetry that are selectively preserved in part of the distortion space.[374, 384, 385]

The $Fe(CO)_5$ molecule presents further challenges, *viz.*, either an axial or an equatorial ligand may be initially ejected. Although the axial path is likely to be favored, both need to be considered and modeled. The tetrahedral geometry has triply degenerate irreducible representations leading to possible three-state Jahn – Teller CIs and associated five-dimensional branching spaces.[89] Roos[372] has studied the $Fe(CO)_4$ Jahn – Teller surface using CASSCF with an (8,10) active space. Iron tetracarbonyl at tetrahedral geometries is $d^8(e^4t_2^4)$, which leads to the following electronic states: $t_2 \otimes t_2 = {}^1A_1 \oplus {}^1E \oplus {}^1T_2 \oplus {}^3T_1$. The ${}^3T_1$ state can be discarded due to the timescales involved in the radiationless relaxation.[354] The only way to determine the energetic ordering of the singlet states is *via* a high-level computation. In their spectroscopic analysis, Fuß *et al.*[349] and Trushin *et al.*[354] proposed a pathway through a Jahn – Teller CI imposed by the ${}^1T_2$ state. Furthermore, this intersection explains the nature of the photoproduct, which was previously determined using ultrafast electron diffraction by Zewail and co-workers.[214, 215] as C_{2v} $Fe(CO)_4$

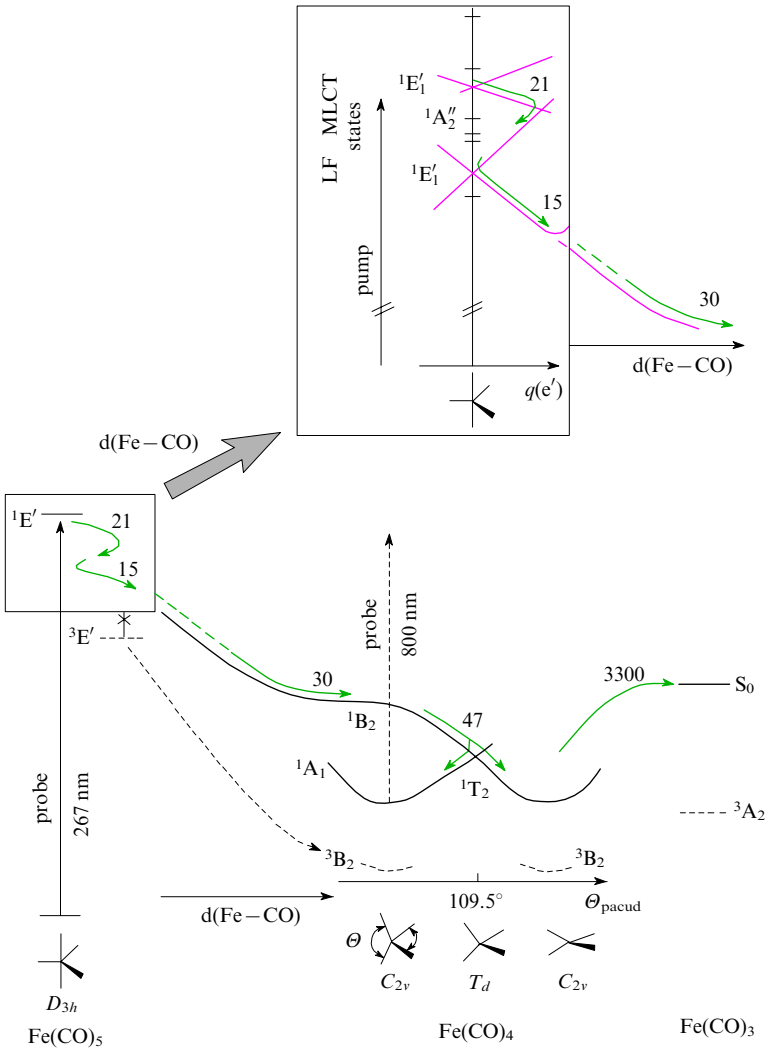


Figure 37. Schematic representation of the UV photodissociation pathways for $Fe(CO)_5$.[354] The excited state involvement of the $Fe(CO)_5$ parent is depicted as short lines to indicate low probability. The inset expands upon the initial relaxation pathway, the symmetry species $^1E'$ designates the states before the Jahn – Teller splitting, *i.e.*, on the q axis (e′ is the direction in the plane of the Figure). The $A_2'' \rightarrow E'$ pathway is shown as a broken line, indicating displacement along an e″ direction outside the drawing plane. The drawing is not to scale. To put this to scale, the experimental dissociation energies and the calculated excited-state positions (both in eV) are: $(Fe(CO)_4)$ $^3B_2$, 1.8; $^1A_1$, 2.56; $^1B_2$, 3.08; $(Fe(CO)_3)$ $^3A_2$, 2.3; S_0, 3.5. 'MLCT' stands for metal-to-ligand charge transfer; 'LF' stands for ligand field.

in a singlet electronic state. Geometrically, they found that one of the pair of the C – Fe – C angles is $169 \pm 2°$, and the other is $125 \pm 3°$ (see Figs 35 and 38). CASSCF calculations have found the Jahn – Teller geometries present in the photodissociation pathways for these systems, with tetrahedral symmetry for singlet $Fe(CO)_4$, and a D_{3h} trigonal bipyramid for singlet $Cr(CO)_5$ and doublet $Mn(CO)_5$. The topology on the lower surface around the point of intersection has a number of symmetry-equivalent minima separated by equivalent transition states (see Fig. 38). In the case of $Cr(CO)_5$ and $Mn(CO)_5$ the surfaces are very similar, involving three C_{4v} square pyramidal minima separated by three C_{2v} TSs. For $Fe(CO)_4$, this has six equivalent C_{2v} symmetry minima separated by 12 equivalent C_s TSs shown schematically in Fig. 38.

The C_{4v} square pyramidal minima are separated by three C_{2v} transition states. The barrier height for $Fe(CO)_4$ is less than 2 kcal mol^{-1}, indicating effectively free pseudorotation in the vibrational hot photoproducts. For $Cr(CO)_5$, there is a more substantial barrier of about 12 kcal mol^{-1}, and dynamics simulations indicate that the pseudorotation may become trapped around a single minimum. This is consistent with experimental observation of coherent oscillations with a frequency of a magnitude that matches an OC – M – CO bending vibration (which is a linear combination of the branching modes). Further information on each surface and how they were calculated can be found elsewhere.[366, 374] An important point to note is that this type of behaviour appears common to binary carbonyls and it is suggested that such a photodissociation scheme should be applicable to most binary carbonyls (with an unfilled d-shell, thus excluding $Ni(CO)_4$).

The simplest Jahn – Teller intersection is of $T \otimes t_2$ type (*i.e.*, a triply degenerate electronic state whose components are coupled *via* a triply-degenerate vibration). Optimization of a triply degenerate CI is not routinely possible at present. The vibrational modes of T_d $Fe(CO)_4$ span $\mathbf{Q}_{3N-6} \in 2A_1 \oplus 2E \oplus T_1 \oplus 4T_2$, so there are clearly sev-

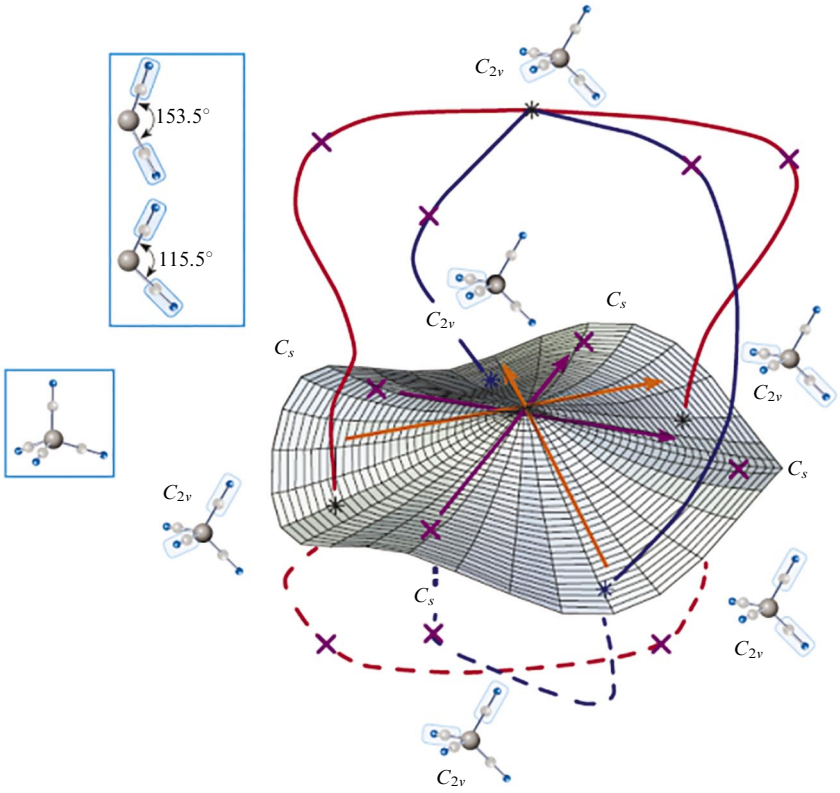


Figure 38. The surface topology for the resultant triply degenerate Jahn – Teller CIs for $Fe(CO)_4$.[374] The pathways connecting the potential minima and barrier crossings are shown in colour. The triple degenerate surface about its tetrahedral (T_d) geometry is indicated as a two-dimensional cross-section through the 3D Jahn – Teller generated surface. The four equivalent C_{2v} minima connected *via* four equivalent C_s saddle points are shown, while other C_{2v} minima and C_s saddle points exist along the remaining orthogonal coordinate. The CASSCF optimized geometric parameters for the singlet state are shown at the top left.

eral candidate vibrations. This $T\otimes t$ type of intersection has received much attention in the triplet manifold ($T\otimes t_1$ in this case),[351, 352, 386, 387] as this corresponds to the global minimum of $Fe(CO)_4$.

Bending of the CO ligands in a pairwise fashion leads from T_d to C_{2v}, and both the triplet and singlet Jahn – Teller surfaces are similar. The epikernel principle[384] predicts that the number of equivalent C_{2v} minima will be given by the quotient of the size of the T_d group and the C_{2v} group ($n_{Td}/n_{C2v} = 24/4 = 6$). Figure 38 shows a 2D cross-section of the full 3D surface using a pair of orthogonal bending coordinates, each obtained as a linear combination of the three triply degenerate (CFeC) bending modes. Note that the full triply degenerate Jahn – Teller problem is $T\otimes(t_2 \oplus e)$, where the branching space is five-dimensional in keeping with the von Neumann—Wigner theorem.[388] Only the $T\otimes t_2$ interaction has been considered in any detail for $Fe(CO)_4$ in either the singlet or triplet manifolds. In the 2D cross-section shown in Fig. 38 there are four C_{2v} minima (two per bending coordinate) connected *via* four C_s saddle points. The total number of the C_{2v} minima is given by the quotient of the size of the T_d group and the C_s group ($n_{Td}/n_{Cs} = 24/2 = 12$). An attractive visual representation of this is given by the octahedral model of Poliakoff and Weitz.[387] in which each minimum is placed at the vertex of an octahedron. As shown in Fig. 38, the barrier to pseudo-rotation between C_{2v} minima is quite low (about 4 kcal mol^{-1}).

Although the CASSCF Jahn – Teller surface in the singlet manifold helps to explain the experimental data relating to the ultrafast relaxation of $Fe(CO)_4$, there is a remaining issue that reminds us of the complexity of this system. Both CASSCF and multireference configuration interaction (MRCI) calculations predict that the $^1T_2$ state is, in fact, not the lowest singlet electronic state at T_d geometries. For example, CASSCF predicts that the ^1E state is 5 kcal mol^{-1} below the $^1T_2$ state. However, an $E\otimes e$ Jahn – Teller intersection does not correctly give the observed photoproduct. A complete Jahn – Teller model will involve both Jahn – Teller and pseudo-Jahn – Teller coupling: $(T \oplus E)\otimes(t_2 \oplus e)$, *i.e.*, a five-state, five-mode model.[351, 352, 386, 387] This is due to the proximity of the ^1E and $^1T_2$ states; the components of these states can strongly pseudo-Jahn – Teller couple *via* the same vibrations that are separately Jahn – Teller active within each degenerate manifold.

Having established that CIs are accessible to connect excited state with ground-state PESs, the next stage in modeling the reactive photochemistry is to simulate the dynamical motion of the nuclei on those coupled PESs. Guillaumont *et al.*[389] performed a large number of dynamics simulations in inorganic photochemistry using quantum wave packet approaches.[389 – 391] The majority of these studies used 1D or 2D simulations that are appropriate for studying phenomena such as direct photodissociation.[374]

Fuß *et al.*[349] investigated $M(CO)_6$ (M = Cr, Mo, W), $Fe(CO)_5$, $Ni(CO)_4$ and $M_2(CO)_{10}$ (M = Mn, Re) by femto-

second spectroscopy. The molecules were pumped by one photon at 267 nm and then probed by multiphoton ionization at 800 nm and mass-selective detection of the resulting parent and fragment ions. Whereas it was previously believed that such metal carbonyls are excited to a repulsive potential, leading to elimination of one or several CO, it was concluded [349] that only one CO is photochemically split off at times below 100 fs and that this is already a multistep process involving relaxation between excited-state surfaces. The elimination of the second CO takes place in the ground state of the unsaturated carbonyl and requires a much longer time (> 1 ps with a pump wavelength of 267 nm). The unsaturated carbonyl is initially generated in its first excited singlet state S_1. If this molecule is tetracoordinate, it can relax from this S_1 state to S_0 within about 50 fs, the pathway leading through a symmetry-induced CI involving pseudorotation of the ligands. Coherent oscillations along such coordinates were observed in several molecules. In the case of tricoordinate $Ni(CO)_3$, however, there is no such relaxation pathway. Therefore, this photofragment shows a beautiful luminescence with a lifetime longer than 10 ps. All the described processes only involve the singlet manifold.

Fuß *et al.*[349] also observed oscillations with periods of 400 to 700 fs, which is in the range of bending vibrations. The authors assigned them to pseudorotation, since along this coordinate the $S_0 \rightarrow S_1$ transition is tuned from CI *via* a resonance with the probe laser (800 nm, 1.55 eV) to a larger energy distance (*e.g.*, 2 eV in $Cr(CO)_5$). Using a 400 nm (3.1 eV) probe, the oscillations remain invisible. And in $Fe(CO)_4$, where the $S_0 \rightarrow S_1$ transition energy is about 0.5 eV, no oscillations were detected either.[349] Excitation of the vibrations is plausible since it proceeds along the coordinate that leads with steepest descent from S_1 to S_0.

It has repeatedly been assumed that dissociation takes place *via* a triplet state formed *via* ISC. In particular, this was suggested for $Fe(CO)_5$, where the ground state of the $Fe(CO)_4$ product is a triplet, and for the splitting of the $Mn-Mn$ bond in $Mn_2(CO)_{10}$, where only the triplet excited state $^3B_2$ correlates with the ground state of the products $Mn(CO)_5$. In the $Fe(CO)_5$ system, singlet $Fe(CO)_4$ and $Fe(CO)_3$ were observed by IR absorption even after nanoseconds.[392, 393] This suggests that ISC cannot take place in a time much shorter than 1 ns. Additionally, the times until dissociation (typically, below 100 fs for each step) are too short for ISC to occur.[394] Furthermore, dissociation was found to be slower for the carbonyls of heavier metals in a group than of lighter ones. The opposite would be expected if ISC played a role. After the dissociation, in the Group VI pentacarbonyls, pseudorotation would have no counterpart in the triplet manifold. With ISC thus excluded, the only remaining process for the elimination of a second CO in the sequential dissociation of metal carbonyls involves the thermal reaction of the hot molecules on the ground-state surface S_0. If this were the process, the rate should depend on the excess energy and thus on the pump-laser wavelength. Experiments to explore this option remain to be done.

The range of photochemical dynamics phenomena in simple metal carbonyls is surprisingly rich. Although some of the possible steps are not yet definitely identified, it is anticipated that future studies may contribute to a better understanding of the photochemistry of the metal carbonyls and their derivatives, including the stereochemistry (*cis*- and *trans*-effect of substituents) or photocatalysis.

One interesting effect observed at resonance of sufficiently intense IR radiation with the vibrations of polyatomic molecules is their multiphoton excitation until, above the dissociation threshold, the molecule falls apart. Research in IR multiphoton excitation showed that with durations of the IR pulses in the range of 10 – 100 ns, the randomization of vibrational energy leads to excitement of all vibrations. The subsequent monomolecular reactions (dissociation, isomerization) are statistical in nature.[74, 75, 395, 396] The fast energy redistribution from the pumped mode to other vibrations of the molecule (intramolecular vibrational redistribution, IVR; see review articles [397 – 400]) also limits the possibility of selective vibrational multiphoton excitation of the selected modes of polyatomic molecules above the randomization threshold. Research on intramolecular relaxation, *i.e.*, the measurement of the characteristic time scales, is the subject of a large number of studies. This interest is motivated, in part, by the idea of implementing non-statistical reactions by the use of laser pulses with a duration shorter than the characteristic times of the intramolecular relaxation. A recent review discusses the research methods used and the results obtained in those studies.[400]

Photoprocesses induced by resonant vibrational excitation were studied in free $Fe(CO)_5$ and its molecular clusters.[401, 402] Intense femtosecond pulsed radiation in the region of 5 μm was used to excite intense CO stretching bands (ν_6 and ν_{10} modes) of $Fe(CO)_5$. An analysis of the results obtained led to the conclusion that the IR pulse selectively excites the CO vibrational modes. This excitation decreases the multiphoton ionization cross-section for the probe pulse, which leads to a reduction of the signal from the $Fe(CO)_5^+$ molecular ion. Relaxation of the signal was found that could be described by two characteristic times, a fast component ($\tau_1 = 10 \pm 2$ ps) and a slow one ($\tau_2 = 670 \pm 40$ ps). The slow relaxation with τ_2 is ascribed to intramolecular energy relaxation that transfers the excitation of the CO vibrational energy to other vibrations of the molecule. The time τ_1 it is probably associated with a Berry-type intramolecular pseudorotation.

In experiments on $[Fe(CO)_5]_n$ clusters, relaxation of vibrational energy stored by individual cluster molecules leads to an increase in the temperature of the clusters and subsequent evaporation of molecules. Free $Fe(CO)_5$ molecules formed as a result of the cluster dissociation were ionized by femtosecond laser radiation at $\lambda = 400$ nm and detected with a time-of-flight mass-spectrometer. The yield of free molecules from clusters is determined by the magnitude of the energy absorbed by the cluster and its temporal dependence is described by the sequential evaporation of molecules (Fig. 39).

IX.3. Femtosecond-resolution Resonant Inelastic X-ray Scattering

The prospect for femtosecond characterization of electronic excited state dynamics was realized by Wernet *et al.*[346] who used X-ray laser-based femtosecond-resolution spectroscopy in combination with theory to probe the reaction dynamics of $Fe(CO)_5$ in solution. The unsaturated carbonyl $Fe(CO)_4$ was generated in ethanol (EtOH) solution by the photodissociation of $Fe(CO)_5$ with optical (266 nm) femtosecond laser pulses in less than 100 fs. The subsequent photodissociation of CO generated a 16-electron $Fe(CO)_4$ species, which contained an electron deficiency at the Fe metal centre that would act as a homogeneous cata-

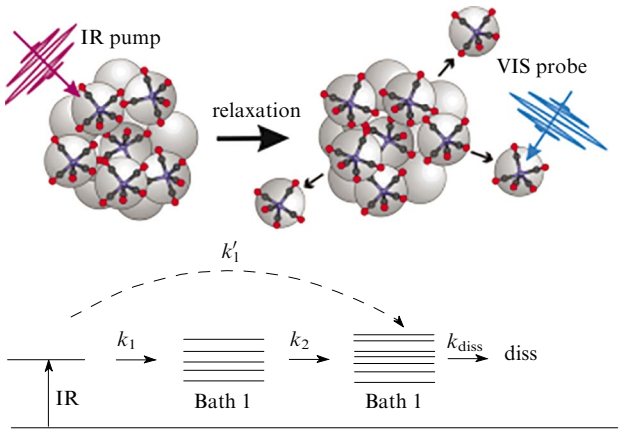


Figure 39. Schematic diagram of the energy flow during the cluster dissociation.[401] Two relaxation schemes are shown: single-bath mode scheme (k_1') and sequential two-bath-mode scheme (k_1 and k_2).

lyst.[403–406] Wernet *et al.*[346] reported a previously unobserved excited singlet state that either combines with CO or a solvent molecule to regenerate the parent pentavalent configuration or undergo ISC to the triplet ground state. In their experiment (see Fig. 40 *a*) the valence electronic structure of $Fe(CO)_5$ was probed with resonant inelastic X-ray scattering (RIXS) at the Fe L_3-edge (Fe L_3-RIXS, illustrated in Fig. 40 *b*). Using this approach, Wernet *et al.*[346] were able to probe the frontier orbitals of iron pentacarbonyl and the resultant Fe-centred d_π and d_σ^* orbitals following photodissociation. The probe with an energy of 710 eV selectively monitors the $2\pi \rightarrow$ LUMO(d_σ^*) transition and its inelastic scattering to the valence-excited LF states with $d_\pi^7 d_s^{*1}$ configuration. This process effectively probes the $d_\pi \rightarrow d_\sigma^*$ transitions, in which single electron orbital pictures are applied at the level of treatment used in Ref. 346. The different scattering processes are indicated as 'in' and 'out' in Fig. 40 *b*, which an be related with appropriate levels of theory to the changes in chemical bonding and ligand coordination. The transitions and pathways are shown in Fig. 40 *c* (top) in which the dominant intensity changes involve the $2\pi \rightarrow 2\pi^*$ excitations at 711.5 eV to the ligand-centred $2\pi^*$ orbitals and inelastic scattering to $d_\pi^7 2\pi^{*1}$ charge-transfer states (Fig. 40 *c*) that are not further analyzed in Ref. 346.

The experiment of Wernet *et al.*[346] consisted of recording Fe L_3-RIXS intensities *vs.* energy transfer while scanning incident photon energy and pump – probe time delay with a time resolution of 300 fs. The observed bimodal spectral distribution shows different intensities for different delays (Fig. 40 *c*, middle and bottom), reflecting changes in $2p \rightarrow$ LUMO resonance energies within the range 706.5 – 710 eV and changes in $d_\pi \rightarrow d_\sigma^*$ transition energies within the range −1 to 6 eV. These changes quantify the changes in the frontier orbital interactions caused by changes in ligand coordination when going from $Fe(CO)_5$ to $Fe(CO)_4$ and during the subsequent excited-state dynamics. Ligand dissociation is expected to create a 'localized hole on the metal' (Ref. 406) with a concomitant decrease in the $d_\pi - d_\sigma^*$ splitting (see the molecular orbital diagram in

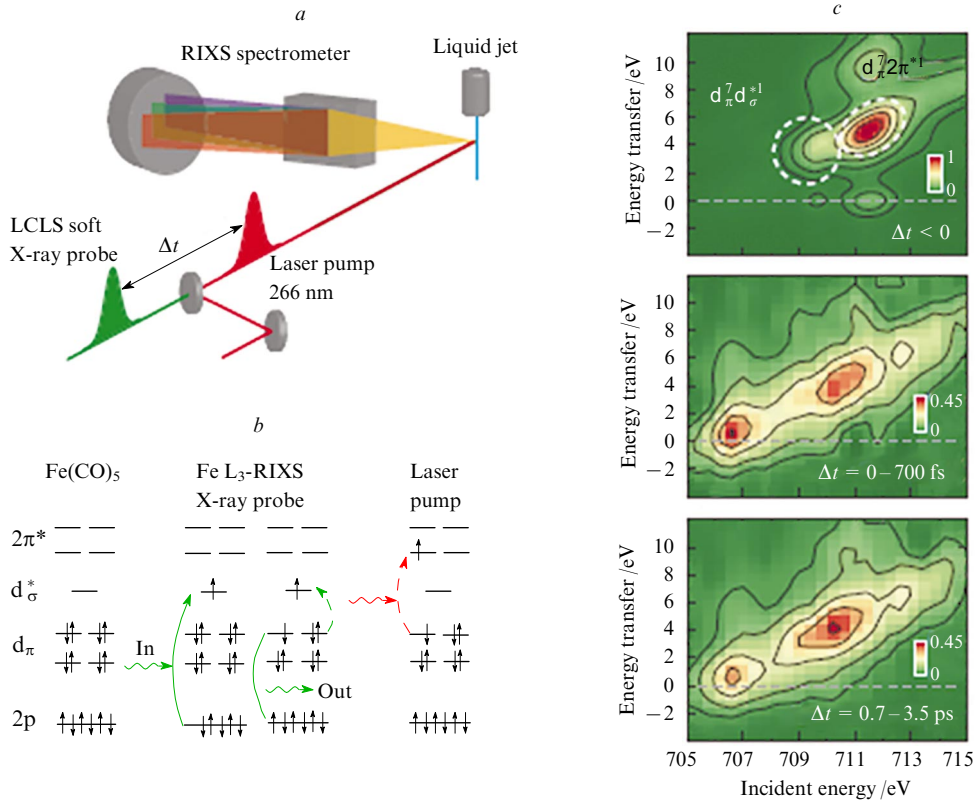


Figure 40. Experimental concept (*a*), probed transitions (*b*) and results (*c*) obtained by Wernet *et al.*[346] The observed changes in the Fe L_3-RIXS intensities (encoded in colour) are depicted as contour plots *vs.* probe photon energy. The relaxation to the lower-energy d orbital using differential detection is clearly observable in the windows from of 0 – 0.7 ps and 0.7 – 3.5 ps.[346]

Fig. 34). This manifests itself in the Fe L_3-RIXS spectra at time delays of 0 – 700 fs (Fig. 40 *c*, middle) as a new 2p → LUMO resonance at 706.5 eV and as the maximum of the $d_\pi \rightarrow d_\sigma^*$ transitions shifted to lower energies by 24 eV relative to $Fe(CO)_5$.

Coordinative saturation through ligation with CO or EtOH restores the $d_\pi - d_s^*$ splitting, mostly as a result of σ-bonding between $Fe(CO)_4$ and CO or EtOH. This could explain the occurrence of 2p → LUMO and $d_\pi \rightarrow d_\sigma^*$ transition energies comparable to $Fe(CO)_5$ at late delays of 0.7 – 3.5 ps (at 709.5 and 3 eV; Fig. 40 *c*, bottom). To substantiate this and to quantitatively analyze the time-resolved data, Wernet *et al.*[346] performed *ab initio* Fe L_3-RIXS calculations for selected structures. The calculated spectra of the three lowest electronic states of $Fe(CO)_4$, of the lowest states of $Fe(CO)_4$ – EtOH complexes and of $Fe(CO)_5$ in optimized and distorted geometries account for all experimental features.

The excited singlet-state $Fe(CO)_4$ ($^1B_2$) was found to decay into the triplet $Fe(CO)_4$ ($^3B_2$), with a time constant of 300(100) fs. There is a noted parallel build up of 'hot' $Fe(CO)_5$ arising from geminate recombination with CO and of $Fe(CO)_4$ – EtOH with a time constant of 200(100) fs. The model employing three distinct photoproducts was found to fit the data quite well; whereas other sequential kinetic models did not provide satisfactory fits, the triplet state formation was an essential element to the fitting.[346] It should be noted that it was not possible to spectroscopically distinguish geminately recombined 'hot' $Fe(CO)_5$ from solvent complexed $Fe(CO)_4$ – EtOH so that the ratio in the kinetic model was fixed at 1 : 1,[346] being consistent with the measured quantum yield of 0.8 for solvent-separated $Fe(CO)_4$ and CO.[407]

Figure 41 sketches the reaction pathways established by Wernet *et al.*,[346] with detection of the excited singlet-state $Fe(CO)_4$ ($^1B_2$) confirming the suggestion[352] that the primary reaction steps in solution also involve the singlet pathway as seen in the gas phase.[354] The proposed relaxation of excited singlet $Fe(CO)_4$ ($^1B_2$) to singlet $Fe(CO)_4$ ($^1A_1$) through internal conversion[354] is consistent with the RIXS data,[346] but the authors of Ref. 346 also observed triplet $Fe(CO)_4$ ($^3B_2$) that was previously seen in solution[338, 408] and in rare-gas matrix[352] experiments. This triplet from a singlet state with a time constant of 300 fs, consolidating the notion[340] that sub-picosecond ISC seems to be common in the excited-state dynamics of transition-metal complexes.[341, 409 – 411] The persistence of the triplet $Fe(CO)_4$ ($^3B_2$) up to maximum time delay of 3 ps is consistent with its undergoing a slow, spin-forbidden reaction with ISC to a solvent-complexed singlet state on a 50 – 100 ps timescale.[338, 339, 355] However, the observed branching on a sub-picosecond timescale into the competing and simultaneous reaction channels of spin crossover and ligation to form coordinatively saturated species introduces an efficient pathway circumventing this spin barrier. It also supports the idea that the high density of electronic excited states and the relatively large amount of excess energy available in the system determine the course of the excited-state dynamics, rather than spin selection rules alone.[339, 340] Fast ligation could be facilitated along the singlet pathway, confirming the general notion that solvent-stabilized metal centres form fast;[338, 345, 412] this is also consistent with the observation of the unsaturated carbonyl $Cr(CO)_5$ forming a solvent complex in alcohol solution within 1.6 ps.[413] An alternative proposal[414] for $Fe(CO)_5$ involves a concerted exchange of CO and EtOH on the timescale of ligand dissociation of 100 – 150 fs.

This would also proceed along a singlet pathway and would be in agreement with the results,[346] because the time resolution of the measurements[346] is not sufficient to distinguish between this concerted process and the alternative sequential process. Revealing in detail the influence of solvent – solute interactions remains the subject of future studies, which could also explore whether the structure of

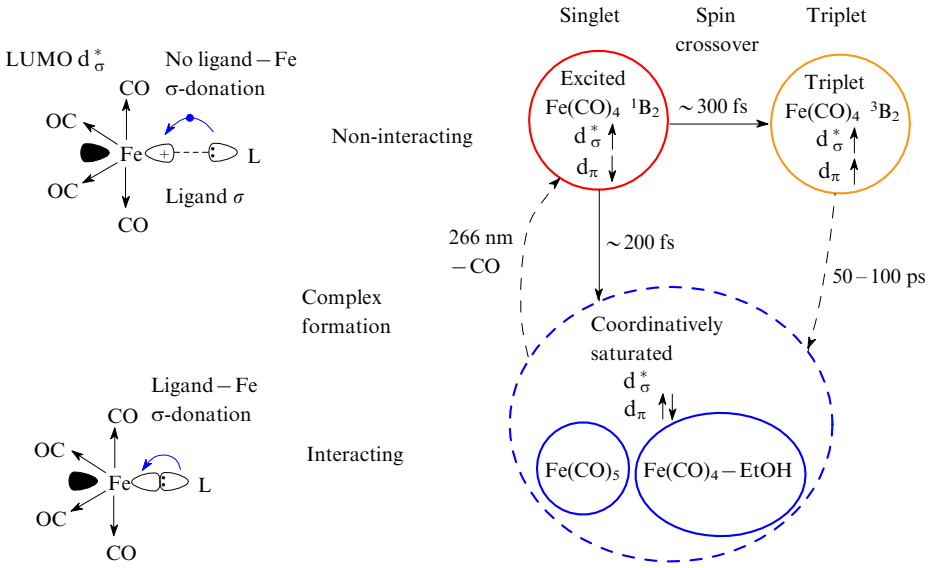


Figure 41. Schematic reaction pathways of $Fe(CO)_4$ in EtOH.[346] There is a parallel pathway depicted involving triplet-state $Fe(CO)_4$ formation through spin crossover (rise of triplet with a time constant of 300(100) fs) and to coordinatively saturated 'hot' singlet $Fe(CO)_5$ with a time constant 200(100) fs. A triplet pathway to $Fe(CO)_4$ – EtOH complex formation within 50 – 100 ps leads to recovery of the ground state as indicated.

the solute before dissociation [414] influences the excited-state branching ratio between the different pathways.[346]

The work of Werner *et al.*[346] suggests that the ligation capability of the tetravalent Fe is determined mostly by its d_σ^* LUMO through σ-donation from the occupied CO or EtOH ligand orbitals. In the excited state, the antibonding d_σ^* orbital (singlet ($^1B^2$) and triplet ($^3B_2$) $Fe(CO)_4$) reduces the σ-donation from ligands (see Fig. 41), which accounts for the lack of subsequent further and the inertness of these species against ligation. This situation is absent in the ligation channel that produces coordinatively saturated species.[346] The connection between the Fe-centred orbitals and the effect of spin multiplicity on reactivity [415] was enabled by the atom specificity by which the X-ray spectroscopy probes frontier-orbital interactions. The element specificity, however, also needs some caution in the interpretation and in this case dominance of electron density considerations at metal centres as the the reaction mechanism involves modes, not single atoms. These modes modulate the electron distribution and energetics and thereby direct the chemistry. X-ray spectroscopy only provides information on the electronic state much like transient absorption spectroscopy. There is no atom-specific chemistry. The most important feature of X-ray spectroscopy is that it gives specific information on the transition-metal contributions to the transient electronic states. This information helps rationalize the role of metal centres in the observed photochemistry and contribution towards transient species.[40, 41, 416 – 418] This work complements the reaction mechanisms of metals studied using methods that probe structural dynamics in ultrafast chemical processes in solution.[419 – 421]

X. The structure and nuclear dynamics in free radicals: the Jahn – Teller effect and pseudorotation in cyclopentadienyl radicals

There are a number of radicals that are stable enough to isolate and study by steady-state spectroscopic methods. The structural relationships leading to long-lived stable radicals have not been well treated or appreciated in a comprehensive manner.[422] Methods such as spin labeling, spin trapping and EPR imaging can provide a wealth of information using stable radicals as probes. Morever, there are important applications of stable radicals with respect to developing new materials for spintronics, magnetism for memory, and affects on conductivity. Molecular properties leading to stable radicals would provide excellent building blocks for such new materials by virtue of having unpaired electrons.[422]

Pioneering studies of persistent, long-lived radicals [423] by GED were performed in 1968 by L.Schäfer [424] (see also Ref. 425). In these studies, a high-temperature nozzle tip was used to decompose diindenylcobalt $Co(C_9H_7)_2$ to produce indenyl radicals C_9H_7. An analysis of experimental data showed the presence of indenyl free radical in the gaseous phase in a purity of at least 80%. This made possible a structural investigation of indenyl which produced the following results: $r(C(1)-H(1))_{av}$ = 107.2(2.0) pm and $r(C(1)-C(2))_{av}$ = 141.5(1.0) pm. The C – C bond-length average was found to be in good agreement with quantum chemical calculations. Experimental evidence was found that the molecule possesses different C – C bonds, some of which seem to deviate more from the average than is predicted by calculations. Schäfer's experiment represents the first example of investigation of an unstable compound by GED. It proves that the method may be expected to be a powerful tool in the study of similar cases. Other achievements in the study of persistent [423] radical structures by GED are described in a review.[18]

The first study of short-lived CF_3 radicals by TRED was reported by Ischenko *et al.* in 1983.[11, 12] The gaseous target (CF_3I molecules) was excited by a TEA CO_2 laser. Multiphoton infrared excitation caused dissociation of CF_3I

$$CF_3I + nhv \longrightarrow CF_3 + I$$

and diffraction patterns of CF_3 free radicals were recorded. For the experimental integrity of the studies [11, 12] it was important that almost all of the CF_3I molecules dissociated under the action of a single 10^{-7} s IR laser pulse.[426] This means that the scattering pattern was recorded from the bulk (inside the IR laser beam) containing no molecular components except CF_3, so that the resulting diffraction pattern was unambiguously associated with CF_3 radicals. To record the diffraction pattern with the use of a secondary electron multiplier, the pulse-resonance method was employed.[427, 428]

The cyclopentadienyl radical (Cp) is another reactive intermediate that plays an important role in different areas of chemistry. For this reasons, it has been intensively studied by theoretical [429 – 437] and experimental methods.[438 – 442]

In 2002, TRED was applied to study the photodissociation of cyclopentadienylcobalt dicarbonyl $CpCo(CO)_2$, which proceeds to give product structures [443] that were probed by picosecond electron pulses. Three conceivable reaction channels for the dissociation of $CpCo(CO)_2$ are illustrated in Fig. 42.[443] Femtosecond and nanosecond multiphoton excitation was found to result in a total detachment of all ligands from the cobalt centre thereby leaving a bare Cp ring.

The experimental TRED results were compared with theory to explore the dynamics of the structural changes [443] (Figs 43 and 44). The dynamic nature of the radical was best represented by a pentagonal molecular structure having D_{5h} symmetry with increased mean amplitudes of vibration. A comparison between theory and experiment [443] suggested that the structure of the TS between the compressed (dienylic) and the elongated (allylic) conformations reflects the dynamics of the pseudorotary surface.[443]

To analyze the data, a DFT electronic structure of D_{5h} Cp was used as the starting point of the refinement. The best fit of the data [443] was obtained using r_a = 146(3) pm for the C – C bond of the D_{5h} ring. Density functional calculations gave r_e = 142 pm, which is consistent with the results obtained by rotationally resolved laser-induced fluorescence spectroscopy.[440] The DFT calculations refer to the bond distance of 142 pm of the D_{5h}-TS (Fig. 45), so that the observed 4-pm extension of the equilibrium bond length was attributed to the pseudorotary dynamics about the Cp ring.[443]

A planar Cp radical has a degenerate $^2E_1$ electronic ground state of D_{5h} symmetry. The degeneracy is lifted by the Jahn – Teller distortion and the bonds become unequal in length. Due to the near energetic degeneracy of the two Jahn – Teller isomers and the low barrier to pseudorotation on the surface connecting them, the two structures among the many in Fig. 45 are not static. Estimates of the pseudorotary barrier around the circular landscape (not across

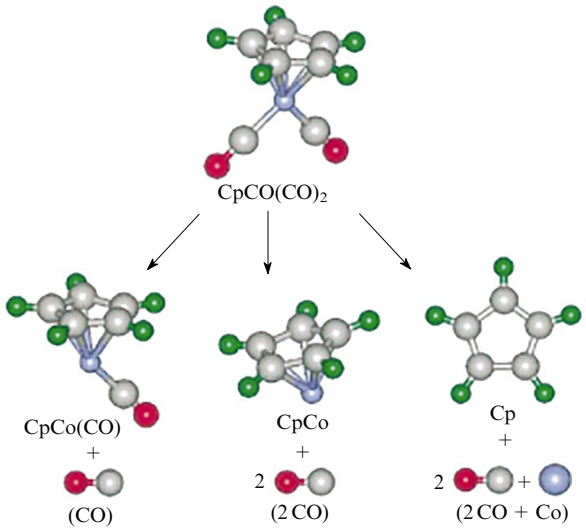


Figure 42. Three possible fragmentation pathways of $CpCo(CO)_2$.[443]

the centre) in Cp range between zero and ~2 kcal mol^{-1}.[439] If no energy is channeled into the translational energies of the fragments, a maximum of ~104 kcal mol^{-1} in internal energy for the products is available. If this energy is then completely thermalized between and among all modes of Cp, the vibrational ensemble temperature would be ~2900 K. In reality, however, a significant fraction of the available energy would go into translational kinetic energy of the fragments and the equilibrium temperature of Cp would be lower than this value.[443] A refinement of the molecular temperature, based on the mean-amplitudes of vibration (l_a) of the bonds, was also performed and the best-fit temperature of the product of D_{5h} symmetry was 2600(150) K (Fig. 45).[443] This apparent high temperature

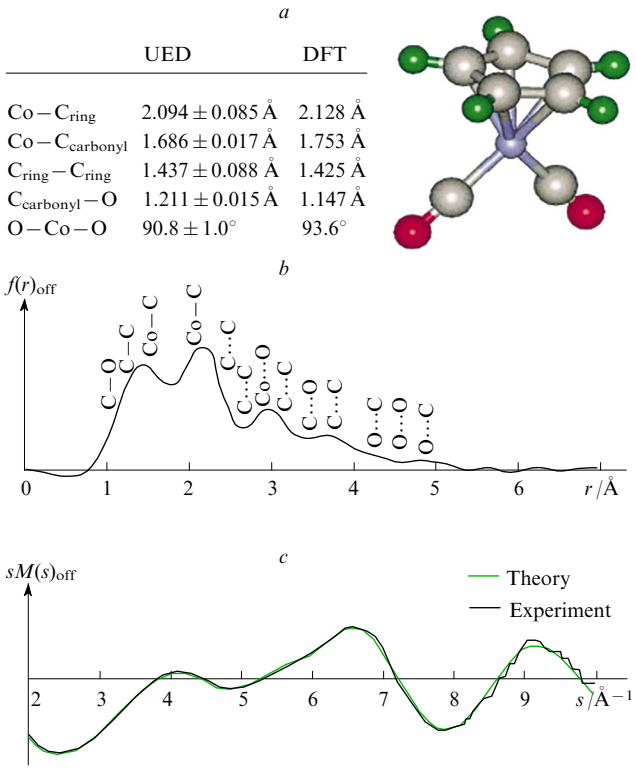


Figure 43. Structure of $CpCo(CO)_2$ (*a*) and DFT predicted bond lengths in comparison to the UED determined distances with structure refinement (*a*).[443]
The associated diffraction data showing the radial distribution function (*b*) and the modified molecular scattering intensity (*c*) are shown for pump-off conditions. Black lines are experimental curves and green lines are the least-squares fits.

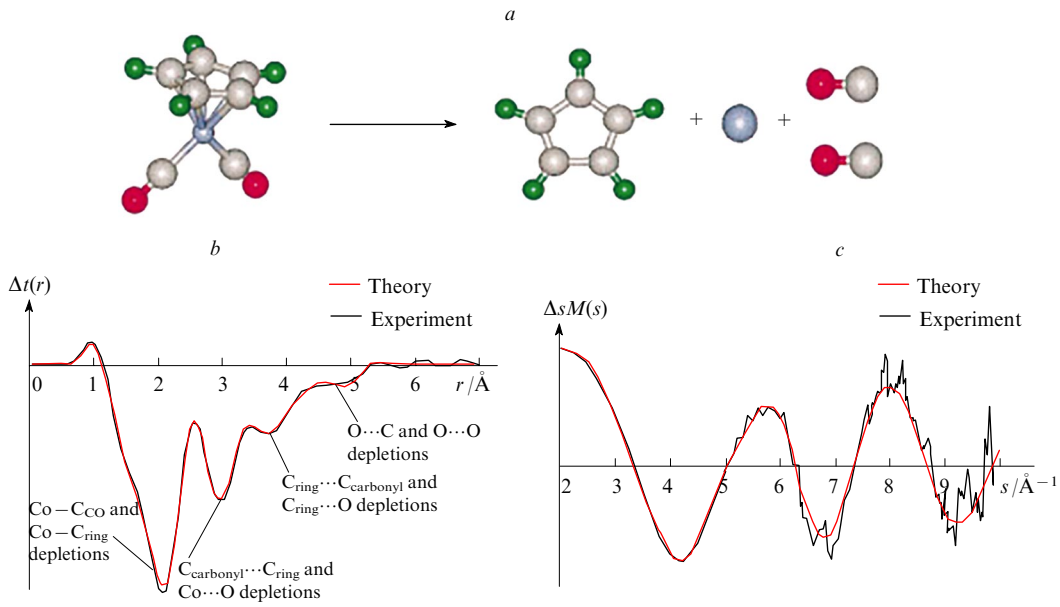


Figure 44. UED study of the photochemistry of cylcopentadienylcobalt dicarbonyl with the reaction process (*a*). The diffraction – difference radial distribution curve (*b*) and the diffraction – difference of the modified molecular scattering curve (*c*) compared to the least-squares fits (red curves).[443]

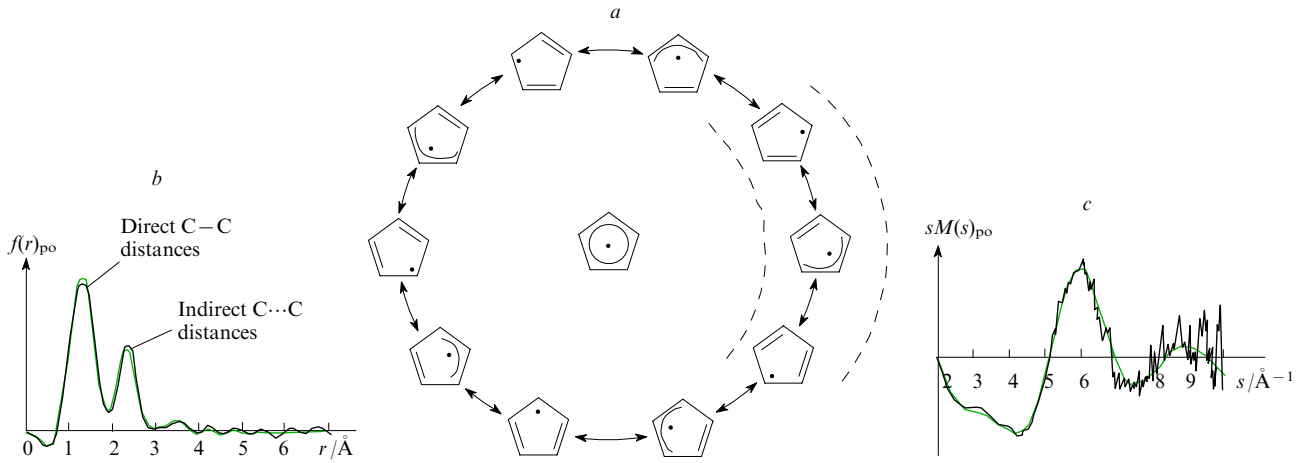


Figure 45. Pseudorotation in the Cp radical (*a*). The transition state of D_{5h} symmetry shown in the centre is 3.5 kcal mol^{-1} (data from Ref. 431) above the circular pseudorotary surface connecting the elongated and compressed Jahn – Teller isomers of Cp. There are estimates of zero to ~2 kcal mol^{-1} increases in the TS location along this pseudorotation pathway.[439] The dotted circles indicate two of the many other possible paths. The refined best fits obtained for the radial distribution curve ($f(r)_{po}$) of the D_{5h} molecular structure of Cp at 2600 K (*b*) and for the product-only modified molecular scattering curve $sM(s)_{po}$ (*c*); the best fit was given by the stretched structure of D_{5h} symmetry with increased mean amplitudes of vibration.[443]

is a consequence of the highly entropic phase space, which results from the many vibrations involved in the transformations of the structures shown (not all shown) in Fig. 45; note that the arrowed circle represents just one path in the basin of the energy landscape and a few of the many others are represented by dotted circles. The long bonds of the structure and the high vibrational temperature are in agreement with the dynamic nature of pseudorotation. An active pseudorotary state involves many bonds, changing lengths as the molecule constantly converts between elongated and compressed isomers. The rapid movement of Cp through these pathways at high internal energy is represented by a hot and enlarged D_{5h} structure as obtained by UED, from the bond lengths and mean amplitudes of vibration.[443]

It is tempting to ascribe some of the stability of Cp radicals to delocalization of the spin around the five positions of the ring (as represented canonically by the structure in Fig. 46, left). However, the fully delocalized, symmetric (D_{5h}) structure of the parent cyclopentadienyl radical is known to be unstable with respect to a first order Jahn – Teller distortion. Two possible distorted states both have C_{2v} symmetry (Fig. 46); one of these ($^2B_1$) is essentially a localized radical while the other ($^2A_2$) state can be described as an allyl-type radical.

The cyclopentadienyl radical consists of essentially (within experimental crystallographic error) symmetric (D_{5h}) Cp rings. However, this structure may represent a dynamic average because the barrier to interconversion between distorted structures is low and the magnitude of the distortion may just be within the crystallographic error limits. Interestingly, the X-ray structure shows a distinctly localized Cp ring: the two 'double bonds' depicted in Fig. 46, are 138.5 pm on the average, the two 'single bonds' flanking the radical site are nearly identical at 145 pm and the remaining single bond is 148 pm. Computational studies accurately reproduce the X-ray structure and suggest that the radical is in a distorted $^2B_1$ state with the allyl moiety centred at the *tret*-butyl substituent position,

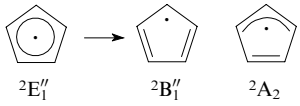


Figure 46. Electronic states of the cyclopentadienyl radical before (left) and after (right) Jahn – Teller distortion.

creating an essentially localized cyclopentadienyl radical.[422,436]

The D_{5h} Jahn – Teller crossing and associated C_{2v} minima and saddle points in cyclopentadienyl have been optimized at the CASSCF: cc-pVDZ level of theory. The C_{2v} structures were characterized by computing analytic force constants. Zero point energies calculated for all C_5H_4D and C_5HD_4 isomers of the C_{2v} minima suggest an alternative interpretation of the experimentally observed degeneracy resolution.[440]

The cyclopentadienyl radical provides an example of a CI enforced by symmetry: a Jahn – Teller crossing.[171,444,445] The $^2E_1$ degenerate ground state at D_{5h} geometry was predicted to distort along the e_2' coordinate, leading to the alternating C_{2v} minima M ($^2B_2$ electronically) and saddle points TS ($^2A_2$) illustrated in Fig. 47.[446]

However, the early ESR spectra at 120 K suggested that the spin distribution around the ring was uniform,[447] implying that the height of the barrier to pseudorotation[448] between the five equivalent minima was of the order of a cm^{-1}, leading to a time-averaged D_{5h} structure.

Carrington *et al.*[449] predicted that static distorted geometries might be observed as a result of deuterium substitution (*e.g.*, C_5H_4D or C_5HD_4, see Fig. 48): if previously equivalent minima now differed in zero-point energy, the time-averaged structure would be biased towards those that are most stable. Degenerate vibronic levels would then be split, and might be resolved at sufficiently low temperatures. Such an effect has been observed for cyclopentadienyl radicals in matrices[450,451] and for the isolated radical in a

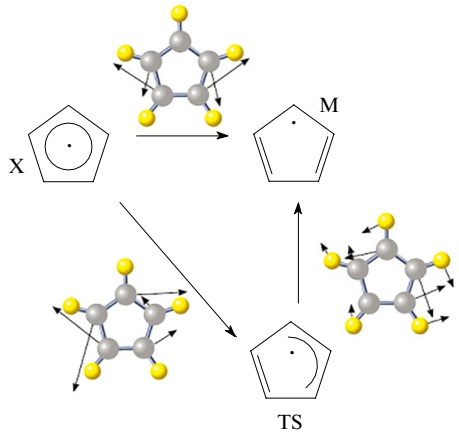


Figure 47. Cyclopentadienyl $D_0 : D_1$ surface topology. At the D_{5h} Jahn – Teller crossing **X**, there are two vectors, *viz.*, the derivative coupling (top) and the gradient difference (left), which lift the degeneracy. One each of the surrounding five minima **M** and transition structures **TS** are shown, linked by the transition vector (right). (From Ref. 433 with minor revision).

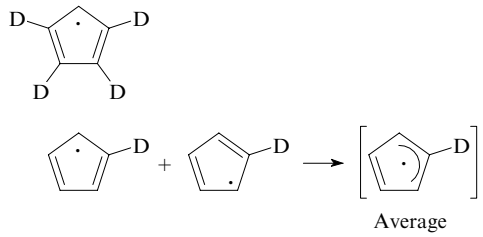


Figure 48. For C_5H_4D, the two equivalent isotopically-substituted minima with the lowest zero point energy lead to a time-averaged C_{2v} structure that resembles the transition structure TS in the moat around the Jahn – Teller intersection.[433] The unique lowest energy structure C_{2v} for C_5HD_4 is also shown.

supersonic jet.[439, 440, 452, 453] The observed splitting is *ca.* 8 – 9 cm^{-1}, being smaller than the barrier to pseudorotation predicted by previous *ab initio* studies.[429, 454]

From rotational constants derived from the spectra recorded at 3 and 10 K [440] it was deduced that the most stable C_5HD_4 isomer has a dienylic geometry like that of **M** in Fig. 49. By contrast, the most stable C_5H_4D isomer was found to have the allylic ring structure of **TS** (Fig. 49). In terms of APESs — which are unchanged by the H : D substitution — this interpretation did not appear to be consistent with the suggestion of Carrington *et al.*[449] Furthermore, the size of the $D_{5h} - C_{2v}$ distortion calculated from the rotational constants was less than that suggested by the *ab initio* calculations.[429, 454]

The optimized CASSCF:cc-pVDZ structures are shown in Fig. 49. The energy difference between the minima M and the transition structure TS is found to be 3.6 cm^{-1}, much smaller than the 2100 cm^{-1} stabilization energy due to the static Jahn – Teller distortion from the D_{5h} geometry X, and an order of magnitude smaller than the lowest previous *ab initio* value of 44 cm^{-1}.[429] Bearpark *et al.*[433] found a dienylic geometry with electronic symmetry B_2 to be the D_0 minimum **M** in agreement with the results of Refs 454 and 429. As a test of the method for calculating energy differences,[433] they also optimized the D_{5h} minimum structure labelled M(D_2) on D_2 ($^2A_2'$). The value for the 0 – 0 electronic transition was calculated as 86.6 kcal mol^{-1}, being in good agreement with the experimental value of 84.6 kcal mol^{-1} (29573 cm^{-1}).[455, 456]

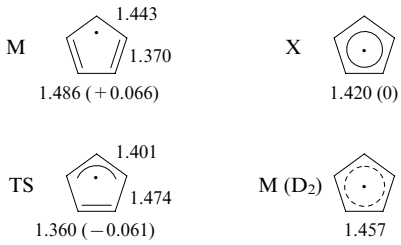


Figure 49. Cyclopentadienyl structures optimized at the CASSCF:cc-pVDZ level of theory: the diene-like C_{2v} minimum **M** (D_0); allylic C_{2v} transition structure **TS** (D_0); D_{5h} Jahn-Teller crossing **X** ($D_0 : D_1$); and D_{5h} minimum on D_2 **M**(D_2). Corresponding energies are given in Table 1 of Ref. 433. All bond lengths are given in Å. The relative lengths of the basal bond (Å) are also indicated. (From Ref. 433 with minor revision).

The interrelations between M, TS and X are emphasized in Fig. 50 (referring to Figs 48 and 49). The transition vector determined by the frequency calculation at the TS is shown at the right, and in this direction clearly points towards one of the five equivalent M.[171] One of the five possible pairs of directions that lift the degeneracy at X are also shown, one leading towards M, the other to TS. For the D_{5h} Jahn – Teller crossing X, the two C – C bond length values are almost identical, namely, 1.420 Å (Ref. 433) *vs.* 1.421 Å (Ref. 440). The corresponding value of 1.457 Å for the D_{5h} minimum on D_2 is within 910 mÅ of the experimental value of 1.449 Å.[440] These results (together with the 92 kcal mol^{-1} difference between the calculated and experimental O – O transition energies) suggest that the CASSCF:cc-pVDZ method used is a reliable one for the $^2E_1'$ and $^2A_2'$ states of cyclopentadienyl at these geometries. However, the changes in the C – C bond length at the base

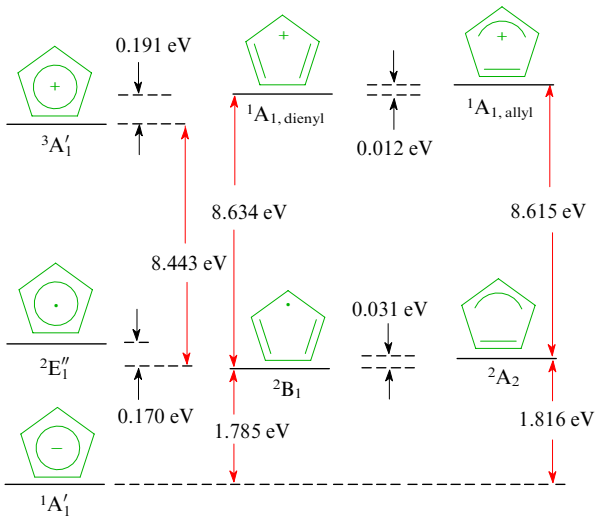


Figure 50. Schematic illustration of the relative energy levels of C_5H_5 ($^2B_1$ and $^2A_2$), $C_5H_5^+$ ($^1A_1$ and $^3A_1'$), and $C_5H_5^-$ ($^1A_1'$) at the CCSDT/CBS level of theory. (From Ref. 437 with minor revision).

of the pentagon (~66, ~61 mÅ, Fig. 49) are significantly larger than the 937 mÅ determined experimentally.[440]

The D_{5h} Jahn – Teller intersection is 'peaked': the lowest point on the PES of the upper state, but one at which the energy gradient does not go to zero overall. At this point there are two directions (Fig. 47) that lift the degeneracy (nonzero gradient), and $3N-8$ that preserve it (zero gradient). Since the gradient at the D_{5h} geometry is not zero in the full $3N-6$ coordinates, a conventional frequency calculation is meaningless. However, for those $3N-8$ coordinates that preserve the degeneracy (and along which the gradient is zero) frequencies and normal modes could be calculated in principle by a projection similar to that used for modes orthogonal to a reaction path.[433]

Recently, the ionization energy (IE), electron affinity (EA), and heats of formation for cyclopentadienyl radical, cation, and anion, $C_5H_5/C_5H_5^+/C_5H_5^-$, have been calculated by wave function-based *ab initio* CCSDT/CBS approach, which involves an approximation to a complete basis set (CBS) limit at the coupled-cluster level with up to full triple excitations (CCSDT).[437] The zero-point vibrational energy correction, core-valence electronic correction, scalar relativistic effect, and higher-order corrections beyond the CCSD(T) wave function are included in these calculations. The allylic [$C_5H_5(^2A_2)$] and dienylic [$C_5H_5(^2B_1)$] forms of cyclopentadienyl radical were considered: the ground state structure exists in the dienyl form and it is about 30 meV more stable than the allylic structure. Both structures are lying closely and are interconvertible along the normal mode of b_2 in-plane vibration.

The $C_5H_5(^2E_1'')$, D_{5h}) normally undergoes Jahn – Teller distortion along the degenerate e_2'-type vibration and its electronic configuration $[...(a_2'')^2(e_1'')^2(e_1'')^1]$ is split into two nearly degenerate electronic states: $^2B_1$ $[...(b_1)^2(a_2)^2(b_1)^1]$ (dienylic form) and $^2A_2$ $[...(b_1)^2(b_1)^2(a_2)^1]$ (allylic form), where the doubly degenerate e_1'' orbitals (in D_{5h} symmetry) correspond to a_2 and b_1 orbitals (C_{2v} symmetry). The highest (doubly) occupied molecular orbital (HOMO) in the dienylic form [$C_5H_5(^2B_1)$] possesses a_2 symmetry and the singly occupied molecular orbital (SOMO) is in b_1 symmetry. The order of HOMO and SOMO are swapped in the allylic form [$C_5H_5(^2A_2)$]. The SOMOs in $C_5H_5(^2A_2)$ and $C_5H_5(^2B_1)$ have identical orbital energies of -0.199 a.u., which lie above the HOMOs by ~0.035 a.u. (see Ref. 437), Fig. 50.

The ground state of cyclopentadienyl radical is found by Lo and Lau [437] to be the C_5H_5 ($^2B_1$) form, and it is about 30 meV more stable than the C_5H_5 ($^2A_2$) structure. Both structures lie very closely on the APES, being interconvertible *via* the normal mode of b_2 in plane vibration.

XI. Unimolecular photodissociation of 1,2-diiodotetrafluoroethane

The photochemistry of haloalkanes provide a nice test system for understanding dissociation processes that are stereochemically controlled by groups positioned about an emerging C – C double bond.[457] For example, systems such as $CH_2ICH_2^{\bullet}$ and $CF_2ICF_2^{\bullet}$ radicals are intermediates in elimination reactions of halogens. There are various models for the conserved stereochemistry. One model assumes a symmetric bridge in which the halogen spans the two carbon atoms. The alternative, more classical picture views the process as a mixture of anti-and gauche conformers with the putative halogen located predominantly near one carbon atom to direct the bond formation from these conformations.[458] The question is how much steric effect does the halogen provide. If it is substantial then there is no need for a brigded intermediate. Despite numerous experimental and theoretical studies of these reactions, the specific role of the halogen in direction the stereochemistry has been unresolved.

XI.1. Structural dynamics of the elimination reaction of iodine atoms from the free $C_2F_4I_2$ molecules under collisionless conditions

Ihee *et al.*[459, 460] has investigated the reaction of elimination of two iodine atoms from $C_2F_4I_2$ using UED (Fig. 51). Structures of all the intermediates are unknown and the problem is to determine the structural dynamics of the reaction as a whole.

The molecular structure of the intermediate C_2F_4I was determined from the difference curves $\Delta sM(s,t)$. The theoretical curves $\Delta sM(s,t)$ and $\Delta f(r,t)$ for classical structures are in agreement with the experimental data, while the line, provide a theoretical bridge structure (the iodine atom is symmetrically connected to two carbon atoms) is not in agreement with experimental data (Fig. 52). The structure of the C_2F_4I intermediate was concluded to be classical. One of the open issues is whether there was sufficient time resolution to catch a bridged intermediate. However, it is clear from this data that if a bridged intermediate exits it is not a stable intermediate.

The structural parameters of the C_2F_4I intermediate are shown in Fig. 51. In the intermediate the interatomic distance C – I is longer and C – C distance is shorter than those in the reagent, while the internuclear distance C – F′ in the radical ($-CF_2'$) is shorter than that in CF_2I. These results explain the increased bond multiplicity of C – C and reduced bond strength of C – I as a result of formation of a transient intermediate structure CF_2I. Moreover, the angles ∠CCF′ and ∠F′CF′ are larger than the corresponding angles in the reagent (by ~9° and ~12° respectively). This suggests that the radical centre ($-CF_2'$) of C_2F_4I intermediate relaxes with subsequent loss of the first atom I. The structure and dynamics studied by UED are required for understanding the conservation of the stereochemistry of this class of reactions,[459 – 462] and this is the first example of the determination of these structures.

XI.2. Structural dynamics of iodine cleavage reaction in $C_2H_4I_2$ and $C_2F_4I_2$ molecules in solution

As discussed above, cleavage of iodine atoms from the free molecules 1,2-diiodo-tetrafluoroethane in collisionless environment takes place *via* two steps and results in tetrafluoroethylene (Fig. 51). Cleavage of the first iodine atom occurs in ~200 fs with formation of an intermediate product — the monoiodotetrafluoroethane radical which has a classical structure. The second stage — the splitting of the second iodine atom, goes up to 25(7) ps and completes at 26(7) ps with the formation of tetrafluoroethylene.[459, 460]

It would be interesting to study the ellimination reaction in solution and to compare the results to those obtained for free molecules. This will provide information on the effect of the solvent. Some information may be provided by the X-ray absorption near-edge structure (XANES) and extended X-ray absorption fine structure (EXAFS) methods. However, compared with the data provided by time-resolved X-ray diffraction, these methods yield much less precise information about the structure of molecules.

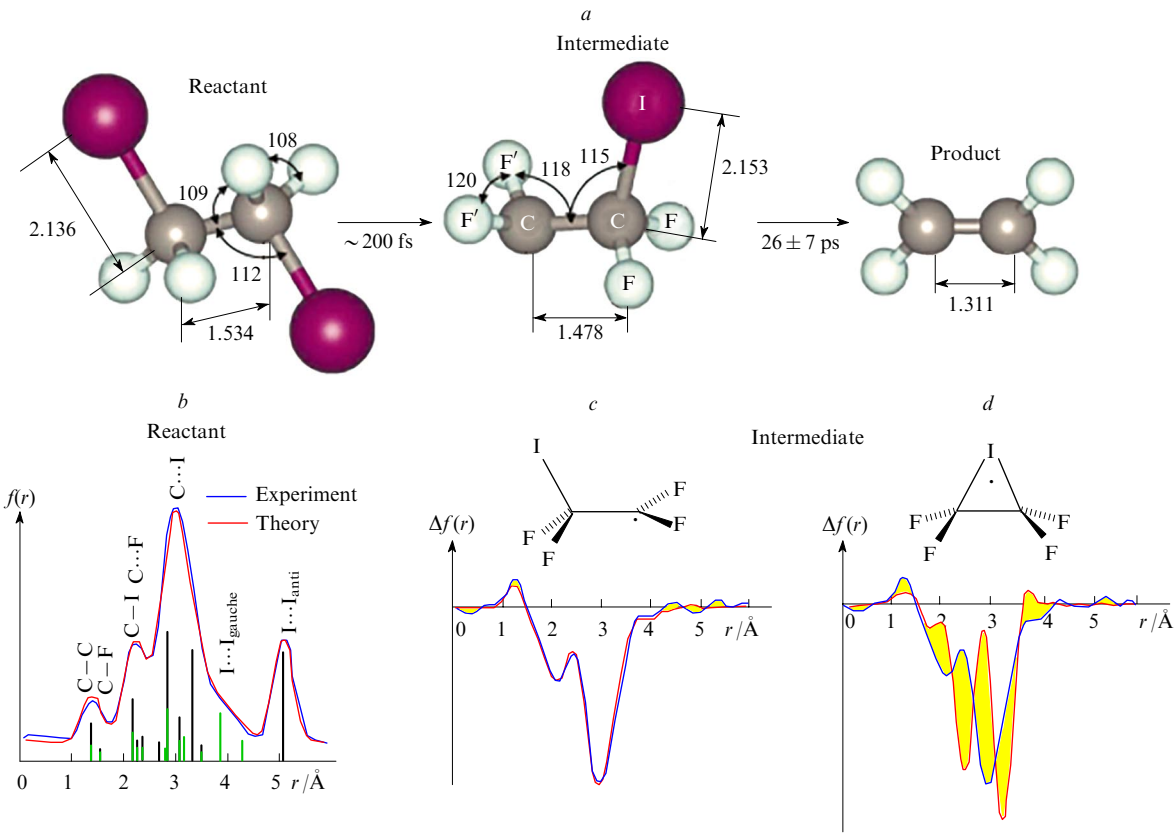


Figure 51. UED study [461] of the structural dynamics of the $C_2F_4I_2$ dissociation reaction is shown in *a*. The average interatomic distances, *r* (Å), and bond angles (degrees) are given. The data within the given time resolution suggests the bridging intermediate is not involved in the final product formation. UED patterns of the *anti*–*gauche* conformation mixture (ground state) are shown in *b*–*d*. Internuclear distances for the *anti* (black) and *gauche* (green) isomers are denoted by vertical bars (*b*). Intermediates with the classical (*c*) and bridging (*d*) structures are given.

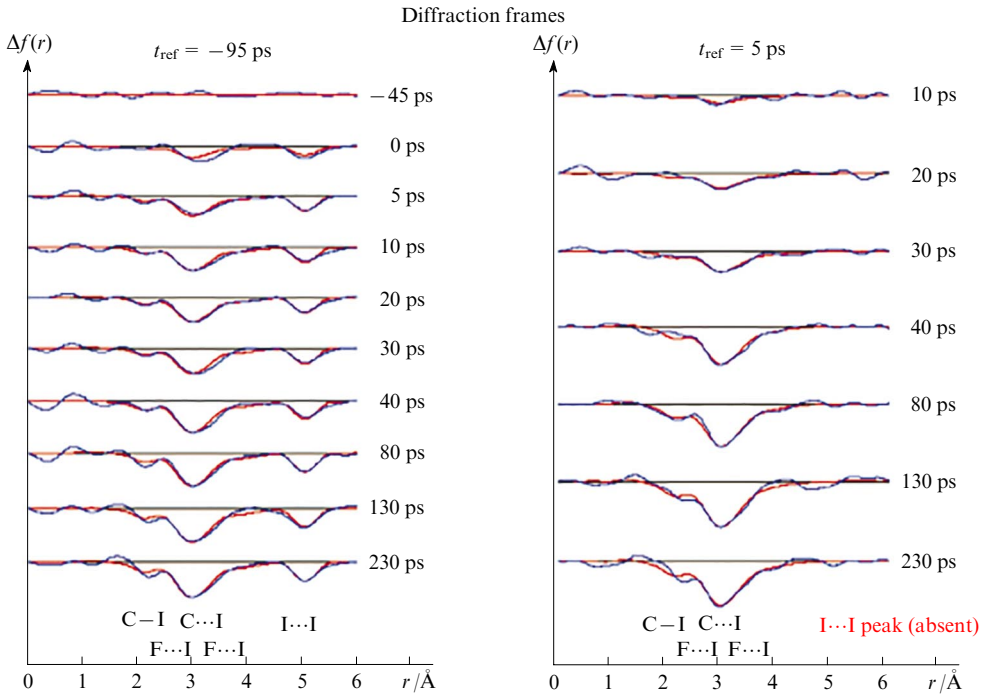


Figure 52. Time dependence of the difference radial distribution curves, $\Delta f(r,t)$ for two different starting points: before the arrival of the exciting laser radiation ($t_{ref} = -95$ ps, left) and after the arrival of the laser pulse ($t_{ref} = +5$ ps, right).[461] Peak corresponding to unbound iodine atoms, I···I, does not exist, as is seen from the right side of the figure. See also Ref. 460.

Elimination reactions of halogen molecules from haloalkanes were studied using time-resolved X-ray liquidography (TRXL) — X-ray diffraction with a time resolution of ~100 ps in solution (see review articles [463, 464]). It was found that as in the gas phase in a collision-free conditions, the elimination reaction of iodine atoms in the solution passes through the intermediate $I-CF_2CF_2$ which has a classical structure. However, the next stage — the splitting of the second atom of iodine is about six times slower than that observed for free molecules in collisionless conditions. The authors attribute this result to the influence of a polar solvent — methanol. The presence of solvent molecules environment may lead to increased rate of redistribution of energy, change in the barrier height of the reaction, and/or isolation of the fragments in the solvation shell. Kim and co-workes [463, 464] proposed a mechanism for the elimination iodine atoms in $C_2H_4I_2$, similar to that for isolated $C_2F_4I_2$ molecules: the cleavage of the first atom of iodine leads to the bridge structure of the radical CH_2ICH_2 (Fig. 53). Then the iodine atom joins to CH_2ICH_2 resulting in C_2H_4I-I, an isomer of $C_2H_4I_2$. The next step is the dissociation of C_2H_4I-I molecules and formation of C_2H_4 and iodine molecules (Fig. 53).

The kinetics of the reactions and the changes in the populations of intermediate particles and the reaction products of the photoelimination of $C_2H_4I_2$ (Fig. 53 *c*) and $C_2F_4I_2$ (Fig. 53 *d*) molecules depend on the time delay between the excitation pulses and the probe. Figure 53 *c* with the black curve corresponds to the bridged structure C_2H_4I, red — to the isomeric form and blue — to the final reaction product, C_2H_4. The figure (Fig. 53 *d*) with green curve corresponds to the atom I, black — to the classic structure C_2F_4I, red — to C_2F_4 and blue — to the molecule I_2. Figure 53 *e* shows a model of the reaction of $C_2H_4I_2$. After photoexcitation, one iodine atom splits off from the iodine molecule and the radical C_2H_4I has a bridging configuration. Then, C_2H_4I recombines with the atom I, separated from the molecule and forms the isomeric of the ground state: $I\cdots I-C_2H_4$. Furthermore, the isomer decays into the molecule C_2H_4 and I_2. Figure 53 *f* represents a model of the reaction of $C_2F_4I_2$. After photoexcitation one iodine atom is cleaved from the molecule and the intermediate radical C_2F_4I has a classical structure. A part of the

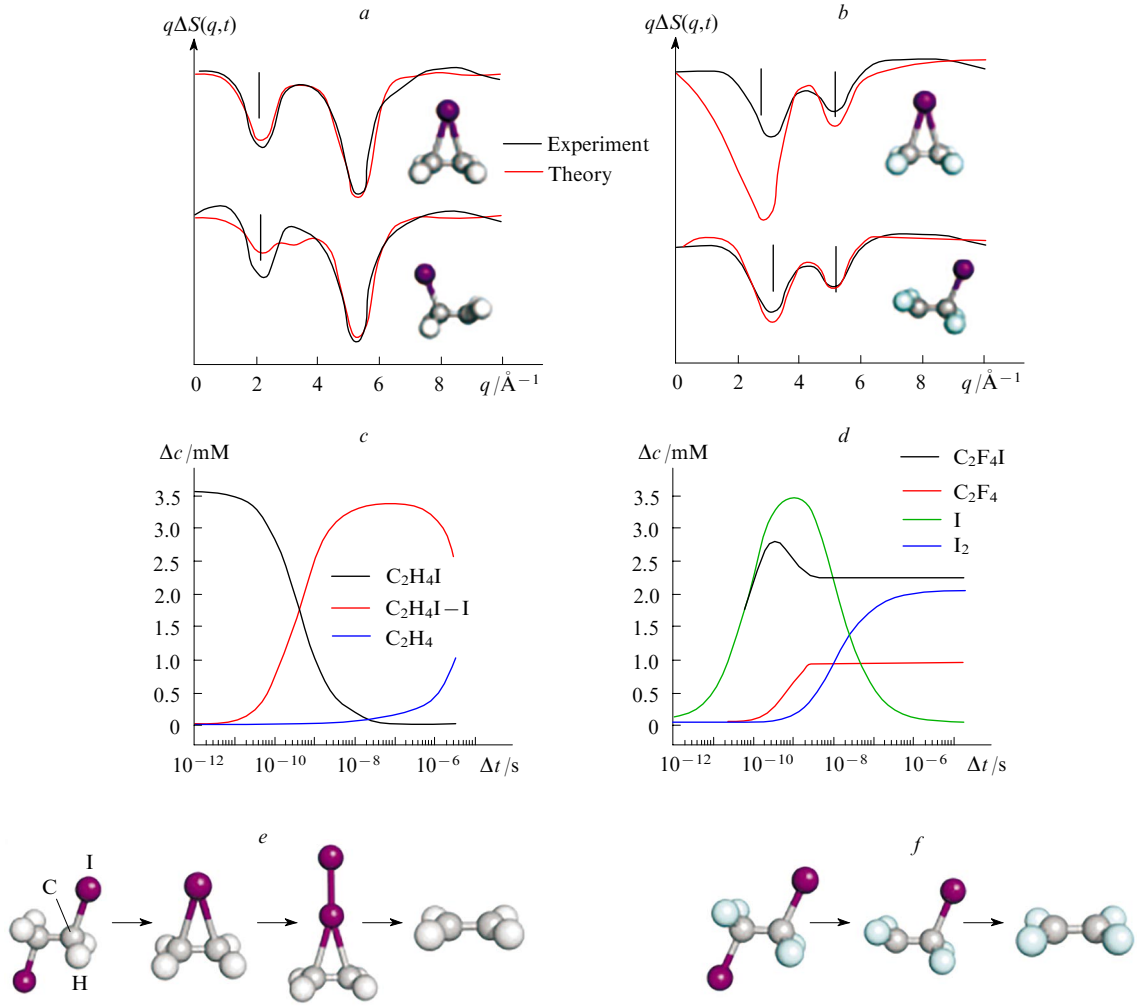


Figure 53. TRXL studies of the structural dynamics of iodine elimination reaction from $C_2H_4I_2$ and $C_2F_4I_2$ in methanol.[463] The time-dependent difference diffraction signals, $q\Delta S(q,t)$ (*a*, *b*), were obtained by subtracting the diffraction patterns of $C_2H_4I_2$ and $C_2F_4I_2$ in the excited state, background subtraction of the diffraction patterns of solvent, and modeling of the effects caused by heating of solvent by laser radiation. Reaction kinetics and population changes of intermediates and products are shown in *c*, *d*. The overall interpretation from these results is shown by the molecular model at the bottom (*e*, *f*). Within the time resolution, the contributions from the bridging and classical structures differ for the two cases.

C_2F_4I radicals decay into C_2F_4 molecules and iodine atoms. Finally, iodine atoms nongeminately recombine to form I_2 molecules.

To interpret the experimental data, Ihee *et al.*[463, 464] reviewed all the previously proposed structures. It was found that the elimination of iodine molecules from $C_2H_4I_2$ and $C_2F_4I_2$ proceeds by different mechanisms (Fig. 53). Elimination of iodine from $C_2H_4I_2$ results in C_2H_4I and I and $C_2H_4I\cdots I$ (as measured at a time delay of 100 ps) and no formation of the final products, that is, C_2H_4 and I_2, was observed. Besides, C_2H_4I does not dissociate into C_2H_4 and iodine atom but reacts with iodine atoms to form $C_2H_4I\cdots I$. The rate constants for a bimolecular reaction resulting in this isomer was estimated as $k = 7.9\ (3.5) \times 10^{11}\ m^{-1}\ s^{-1}$, which appeared to be two orders of magnitude higher than the rate of recombination of molecular iodine in a solution of CCl_4. This implied that the $C_2H_4I\cdots I$ isomer is mainly formed in the 'cage' formed by the solvent shell. This isomer dissociates into $C_2H_4 + I_2$ on a microsecond time scale at a rate constant of $k = 2.0\ (1.4) \times 10^5\ m^{-1}\ s^{-1}$. On the contrary, C_2F_4I and I are the primary particles that are detected after the first 100 ps and apparently formed on a few picosecond time scale, 20(1)% of C_2F_4I radicals dissociate into C_2F_4 and I with a time constant of 306 (48) ps. These values can be compared with the data [459, 460] for the gas phase: 55(5)% of C_2F_4 and I with a time constant of 26 (7) ps. This clearly illustrates the effect of the solvent molecules, which significantly reduce the rate and yield of the second stage of the elimination reaction. This is not surprising since the residual internal energy in the radical C_2F_4I after the first stage of molecular decay of $C_2F_4I_2$ in solution is much lower than that in the gas phase as a result of the transfer of the excess energy to the solvent. Molecular iodine, I_2, is formed *via* recombination of two iodine atoms in $\sim$100 ns at a rate constant of $4.4\ (1.2) \times 10^{10}\ m^{-1}\ s^{-1}$, which is comparable with the rate constant for recombination of molecular iodine in solution. Of particular interest in the study of the structural dynamics is the structure of the transient species. As already noted, can TRXL answer the question whether the structure of the radical is bridged or classical? It is possible to calculate the diffraction intensities for the proposed intermediates and to compare the results obtained with experimental data, making correction for the scattering of the solvent. The results of calculations are presented in Figs 53 *a*, *b*. The intensities of scattering of the intermediate species are determined after subtracting the contribution from the solvent, 'cage' of the shell, and other structures and comparing the calculated data of alleged molecules. The removal of the solvent background was based on calculations of the heating effect and the difference was very small. The degree to which a bridged intermedicate is formed and distribution of other possible intermediates is difficult to judge. This background subtraction method and use of theory for distinguishing possible structures is similar to the approach used in TRED. Comparison of the data for 100 ps, and the alleged intermediates demonstrate that the C_2H_4I radical has bridged structure, while C_2F_4I is represented by a mixture of classical and anti-gauche conformers. This conclusion is supported by the results of quantum chemical calculations, which show a significant effect of the fluorine atoms.

A number of photodissociation reactions of free molecules were studied by UED.[2, 5, 25, 117, 333] However, it should be noted that the solution of the inverse scattering problem in the determination of intermediate products of both photoexcitation and photodissociation in most studies carried out to date was conducted using the theoretical counterpart of the electron scattering intensity assuming an equilibrium distribution of the vibrational and rotational degrees of freedom of the molecules. As was shown in the case study of the CS_2 photodissociation even with nanosecond time resolution this assumption may be inaccurate.[5, 18, 23, 25, 240]

XII. Laser-induced electron diffraction

In traditional electron diffraction studies of molecular structures, electrons travel as plane waves that come from a distant source. They are scattered by atomic nuclei and their electron shells, creating a diffraction pattern that is projected onto the detector.[108, 465, 466] In a new paradigm,[467] a high-intensity laser field ejects an electron from a molecule and then returns it to the ionized molecule from which it scatters. That is, the re-colliding electron wave diffracts off the parent ion. This approach to molecular imaging has been named 'laser-induced electron diffraction' (LIED).[467, 468] The method is similar to conventional electron diffraction and uses the spatial coherence of the re-colliding electron. Measuring the 3D momentum of the scattered electron, one gets the information necessary for the reconstruction of the atomic positions inside the molecule.[469, 470] Unlike the electrons generated from a distant source, the re-colliding electron is coherent: it is prepared from a well-defined electron orbital and controlled by the coherent light. These unique properties open new opportunities for electron holography.[470] For example, one part of the laser pulse can produce the reference electron wave packet (using light with circular polarization), while the second, coherently related part of the laser pulse creates the electron wave packet that re-collides with the parent ion. The interference pattern between these two wave packets is a 3D hologram of the scattering potential. Thus, it seems possible to realize the original vision of Gabor [471] concerning electron holography, *i.e.*, to generate frames for a holographic movie. The problem is that there are many scattering source terms and one is necessarily limited to the study of ionization processes in this high-field regime. The reconstruction is not theory independent as in the case proposed by Gabor with a well-defined reference. The problem will be to connect what is learned to other classes of chemical processes, other than high-field ionization. A very elegant picture of the electron scattering process has emerged from this work. When the electron ejected from a molecule is turned around by the electric field of the ionizing laser pulse and re-accelerated towards the molecular ion, the entire process must take place in a fraction of the period of the laser radiation.[472] The distribution of the momentum of the extracted electron was shown to be a 'fingerprint' of the highest occupied molecular orbital, while the diffraction pattern of the elastically scattered electrons from the nuclear subsystem of the molecules allows the determination of their coordinates. Thus, in one method, the photoelectrons provide detailed information about both the electronic orbitals and the positions of the nuclei (Fig. 54). The ejection of the electron proceeds by tunneling of the electron through the barrier created by the Coulomb potential with the ion core and the external electric field of the intense laser.

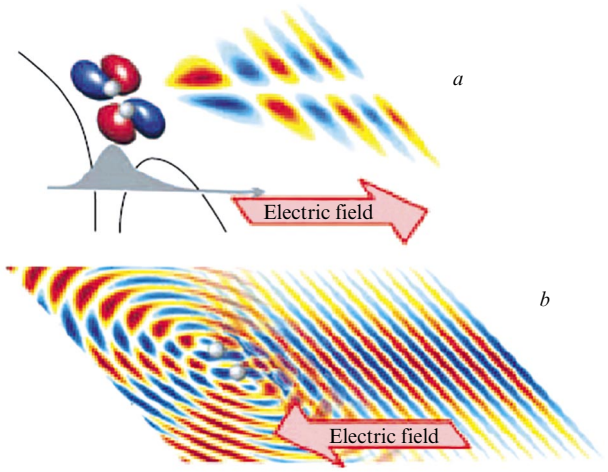


Figure 54. Tunneling creates a filtered projection of the molecular orbitals (*a*). Approximately half of the electron wave packet travels directly to the detector. The rest part goes back to the parent ion (*b*). Shown here is the central part of the re-colliding wave packet that is diffracted from the molecule. The outer part of the wave packet, not shown, interacts weakly with the potential of the ion. The relative amplitude of each component depends on the filtered projection of the molecular orbitals and, therefore, on the spatial alignment of molecules.[472]

The wave packet of the electron ejected into the vacuum during the tunneling process retains information about the orbitals of the studied molecule. The electric field of the laser pulse oscillates and causes the tunneled electron wave packet to return to the parent ion, where it can diffract (lower part of Fig. 54). In LIED the molecule under study also serves as the photocathode and the strong laser field accelerates the electrons. The approach enables extremely high current densities within the attosecond pulse durations. Meckel *et al.*[472] reported the results obtained both by molecular tunneling spectroscopy (MTS) and by LIED. The former method was used to measure the 3D distribution of the momenta of the electrons formed by spatially oriented O_2 and N_2 molecules. Comparing the theory with the experiment, it was shown that in two orthogonal directions perpendicular to the direction of the field, the momentum distribution of the generated electrons was determined by the HOMO, which it was observed by lowering by the laser field[473,474] and thereby the molecular binding potential (Fig. 55) through which the electron

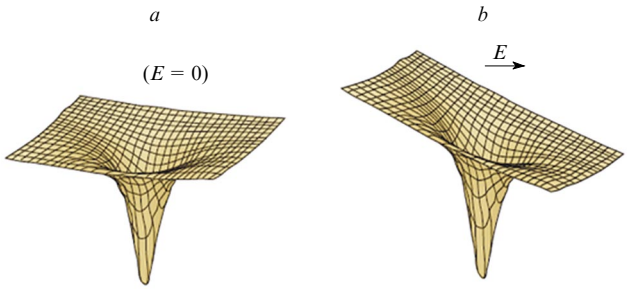


Figure 55. The action of laser field on the electron potential surface in the atom: the illustration to the Keldysh theory[473] the unperturbed Coulomb potential (*a*) and the action of laser field on the Coulomb potential (*b*). (From Ref. 475 with minor revision).

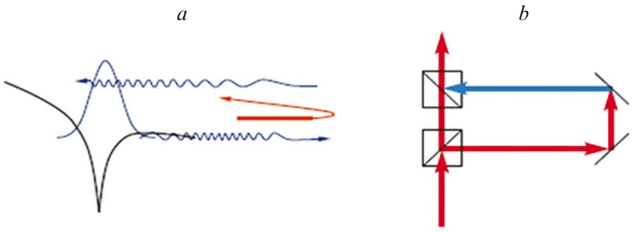


Figure 56. One-dimensional cross-section of the potential surface (*a*) (Fig. 55). The electron wave function is included in this simple picture. The wave function consists of two parts: the part, captured by the ion, and the wave packet, which travels out of the core. The principles of the optical interferometer can be displayed in laser-induced electron re-collisions (*b*). (From Ref. 475 with minor revision).

tunneled. When the wavelength of the electron that re-collides with the parent ion is changed, the diffraction pattern also changes. Thus, a set of such measurements simultaneously determines both the orbital wave functions of the molecule and the positions of the nuclei of the atoms.

Laser-induced tunneling and diffraction use different parts of the electron wave packet produced by the ionization of the investigated molecule. The part of the electron wave packet that is created while the field strength increases in the optical half-cycle emits directly from the parent ion and does not return. The wave packet that is born at decreasing field returns to the parent ion, where it can be elastically scattered (diffracted), inelastically scattered, or recombine (interact) with the orbital from which it was ejected. These three scattering processes open different perspectives for molecular studies (Fig. 56). The underlying tunneling process opens opportunities to probe the electronic structure in neutral molecules. Recombination radiation, known as high harmonic radiation, yields the information about the structure of the orbitals of a neutral molecule. But, because high harmonic generation starts by tunneling and ends with interference, these processes should be separated before the method can be generalized to investigate complex orbitals.

Both elastic and inelastic scattering occurs at the ion of the molecule that serves as the electron source. The action of an ultrashort laser pulse on a molecule can lead to multiple ionization, and then even to Coulomb explosion as predicted by the Keldysh theory (for a review, see Ref. 474). The data on the molecular structure can be extracted from the momentum vectors of the correlated fragment ions. The elastic scattering is also sensitive to the structure of the potential of the molecular ion. Here the molecular structure is encoded in the diffracting electron wave packet, which makes this imaging technique applicable to complex molecules.

Electron diffraction is observed when the de Broglie wavelength of the electron is of the order of the molecular size. Small diatomic molecules have internuclear distances of $\sim 1-2$ Å ($\sim 2-4$ atomic units). In order to achieve this wavelength, the electrons should have a kinetic energy of ~ 150 eV.

The electrons accelerated by the laser field easily reach such kinetic energies. In cold target recoil ion momentum spectroscopy (COLTRIMS) experiments (Fig. 57) a coincidence technique is used to measure the 3D momentum vectors of single electrons and ions associated with tunnel-

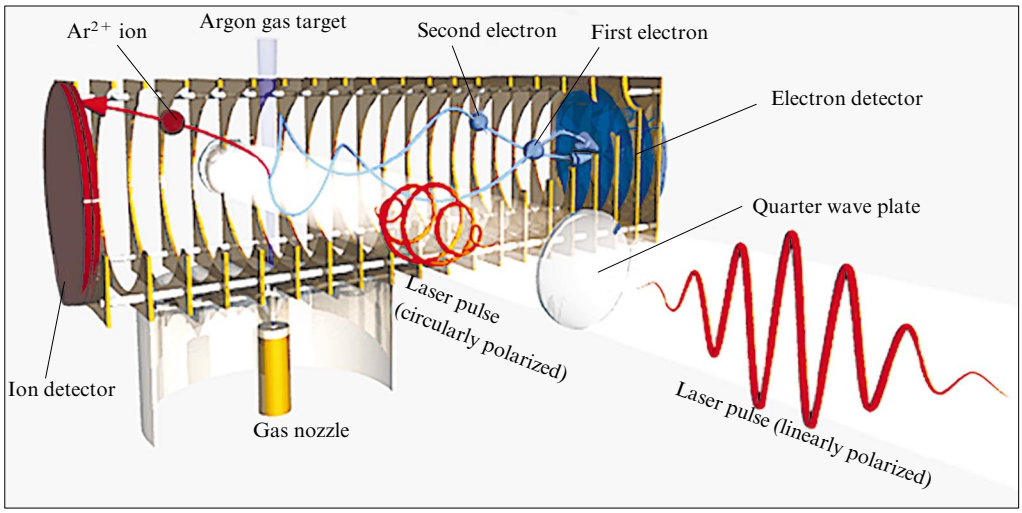


Figure 57. A schematic of a cold target recoil ion momentum spectroscopy (COLTRIMS) apparatus.
The key features are the two time- and position-sensitive detectors for detecting negatively and positively charged particles driven from the interaction region to the detectors by homogeneous electric and magnetic fields axis (from http://www.nccrmust.ch/technology_transfer/tools/advanced_must_infrastructure/coltrims_attoclock.html).

ing ionization from spatially oriented O_2 and N_2 molecules. The experiment was used to measure O_2 and N_2 at the same time under the same conditions, using a mixture of the gases. It also allows one to eliminate any contributions to the electron spectra from inelastic scattering processes that result from the fragmentation or multiple ionization of the molecules. Coincidence techniques permit also the study of rather weak fragmentation channels that provide information about the quality of the spatial molecular orientation.

XII.1. Ultrafast electron diffraction imaging of bond breaking in di-ionized acetylene

Wolter *et al.*[476] used LIED to image the ionization/fragmentation of acetylene at 9 fs and tracked the proton motion in the exit channel (Fig. 58). Using mid-infrared LIED, the authors obtained snapshots as a proton departs the $[C_2H_2]^{2+}$ ion. The exit channel could be controlled using an additional laser field. The results were found to be in excellent agreement with a quantum chemical description including the high-field interaction.

The strong field conditions required for the LIED method necessarily lead to many different fragmentation channels and ionization states that occur simultaneoously. The different channels can be separated using single-molecule coincidence detection. This approach was specifically used to isolate the C_2H_2 dication:[476]

$$C_2H_2^{2+} \longrightarrow H^+ + C_2H^+$$

because it results in a proton H^+ and an ethynyl C_2H^+ moiety. This dissociation pathway involves two different pathways with the fastest proton motions due to the extremely large forces resulting from the highly excited ion state and applied field condition.

The relevant cuts through the APES of C_2H_2 along one C – H direction are shown in Fig. 58 *a*, including states that are relevant for the desired dissociation channel of $C_2H_2^{2+}$ (see Refs 477 and 478) at the present experimental conditions by using a 65-fs (6.3 cycle), 3100-nm pulse (see Refs 479 and 480) with a peak intensity of (65 ± 16) TW cm^{-2}. The pulse parameters were chosen in order to position the experiment in the sequential double ionization (SDI) regime in which the LIED imaging electron is ejected independently from the first electron in a second tunnel ionization step before scattering off the C_2H_2 dication. It is known[477, 478, 481] that the resulting pair of proton H^+ and ethynyl C_2H^+ moiety originates *via* different possible pathways from the $C_2H_2^{2+}$ dication: (i) the first dissociative excited singlet and triplet states, the $^1\Pi_u$ and the $^3\Pi_u$ states, can be reached through ionization from the σ_g-type HOMO-1 orbital of the neutral ground state ($1\sigma_g^2$, $1\sigma_u^2$, $2\sigma_g^2$, $2\sigma_u^2$, $3\sigma_g^2$, $1\pi_g^2$, $1\pi_u^2$) followed by tunnel ionization from the π_u-type HOMO of the excited cationic $^2\Sigma_g^+$ state;[481, 482] (ii) the dication possesses a long-lived metastable triplet state [$^3\Sigma_g^-$ lifetime 108 ns[483]] and two metastable singlet states ($^1\Sigma_g^+$ and $^1\Delta_g$) that can be reached *via* sequential tunnel ionization of two π_u-electrons. In this case, first one electron tunnels from the HOMO of the neutral ground state ($^1\Sigma_g^+$), populating the singly ionic doublet $^2\Pi_u$ state; then, a second electron tunnels from the HOMO of the singly ionic ground state to populate one of the aforementioned dicationic states. A direct dissociation channel that leads to fast proton loss was studied. A simple estimation of the initial speed of the C – H bond elongation, which is based on the curvature of the $^3\Pi_u$ APES, yields an initial elongation velocity of 9 pm/fs from the initi

$$C_2H_2^{2+} \longrightarrow H^+ + C_2^+ + H$$

Both of these processes, as well as the slow proton loss channel, occur with a probability two orders of magnitude lower than that for the fast proton loss channel. Nevertheless, it is possible explicitly excluded those channels by isolating the 3D momentum distribution of the electrons that correspond to the reaction moieties originating from the fast proton loss channel.[476] This permits extraction of structural information only from electrons that rescattered off the H^+ and C_2H^+ fragment pairs from direct dissociation. The magnitudes of the scattering process are heavily weighted to the C_2H^+ fragment. It is normally extremely

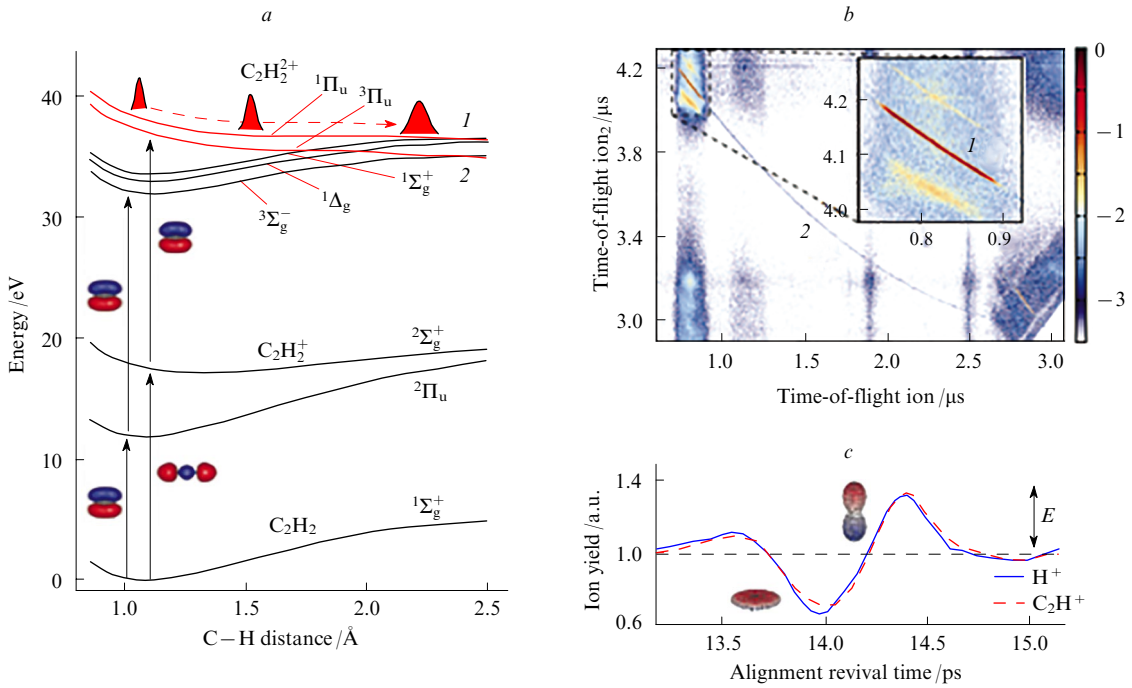


Figure 58. Identification of the relevant states leading to proton ejection.[476] The calculated relevant energy levels and possible pathways leading to dissociation of C_2H_2 and departure of one proton (*a*). Two main pathways are identified, one leading to dissociative PES and fast dissociation (*1*), the other *via* metastable states to slow dissociation (*2*). These pathways are identified in the photo-ion/photo-ion coincidence (PIPICO) analysis (*b*) and exhibit alignment — dependent fragment yields (*c*). Fugure *b* is shown here for perpendicularly oriented C_2H_2.

difficult to observe H atoms with electron diffraction and it should be the same here. It is not clear what other fields may be contributing to the scattering process. The observed dynamics are clear. Additional support to identify population of the fast proton ejection channel (i) stems from measurements of the fragment pair ion yield ($H^+ + C_2H^+$) as a function of delay between alignment and LIED pulse. The results are shown in Fig. 58 *c* and are in excellent agreement with a previous work [484] in which this temporal dependence was used to identify the two different dication fragmentation channels. Having identified the direct proton ejection channel (*via* $^1\Pi_u$ and $^3\Pi_u$), Wolter *et al.*[476] turned to extracting structural information from its scattered electrons. The LIED methodology [485] permits the use of momentum coincidence arguments to associate the scattering electron to only the moieties of the fast proton loss channel. Applying such constraints to the data analysis reduces the event rate by a factor of 83, but the elimination of the general electron scattering background ensures that the resulting momentum map of the electrons bears only structural information of the dissociating C_2H_2 dication.

Because the LIED field does not noticeably distort the PESs in the perpendicular orientation, the C_2H_2 dication behaves like a quasi-field-free electronic system and can be imaged as such. Moreover, the dependence of proton loss dynamics on alignment permits control over the speed and visualization of molecular dissociation. Having corroborated the dependence of proton loss on alignment, Wolter *et al.*[476] next linked the measured structures to the times when the snapshots were taken. The authors experimentally analyzed electrons with 50-eV return energy because they yielded the highest number of counts for the largest angular coverage and hence the best scattering momentum transfer. On the basis of the semiclassical model [486, 487] which pertains well for the Keldysh parameter (see Ref. 474) of $\gamma = 0.31$, it was determined the time of return and the backscattering energy for the scattering electron. Wolter *et al.*[476] only had to consider the long trajectory pathway because of its much higher ionization probability as compared with the short trajectory. Figure 59 *a* shows that these electrons have reencountered the target after 9.15 fs (10.3 fs correspond to one optical cycle at 3100 nm) and backscatter with a maximum energy of 188 eV.

Wolter *et al.*[476] additionally analyzed measurements for two closely neighboring energies of 48 and 52 eV, which correspond to backscattering energies of 181 and 195 eV and for which it was achieved high count rates with excellent signal-to-noise ratio. The overall temporal spread is negligible because these three measurements interrogated the molecular structure during a short span between 9.1 and 9.2 fs, as indicated by the vertical grey bars in Fig. 59. The experimental results for the three scattering energies (Fig. 59, circles with error bars) are overlaid with calculated values for all bond distances and for all orientations.

The theoretical calculate trajectories of the ionization process are based on combined quantum/classical MD formalism to treat the field interaction with the modification of the dication states of C_2H_2 by the LIED field fully taken into account. Figure 59 *b* – *g* shows the calculated responses for the C – H and C – C bond elongations for different alignments with respect to the applied field. There is a rapid elongation of one C – H bond (Fig. 59 *b*) and dissociation defined to occur at twice its equilibrium distance, This event occurs within the window depicted in the figure, between 8 and 10 fs. As can be seen in Fig. 59, the dynamics are significantly different for the perpendicular

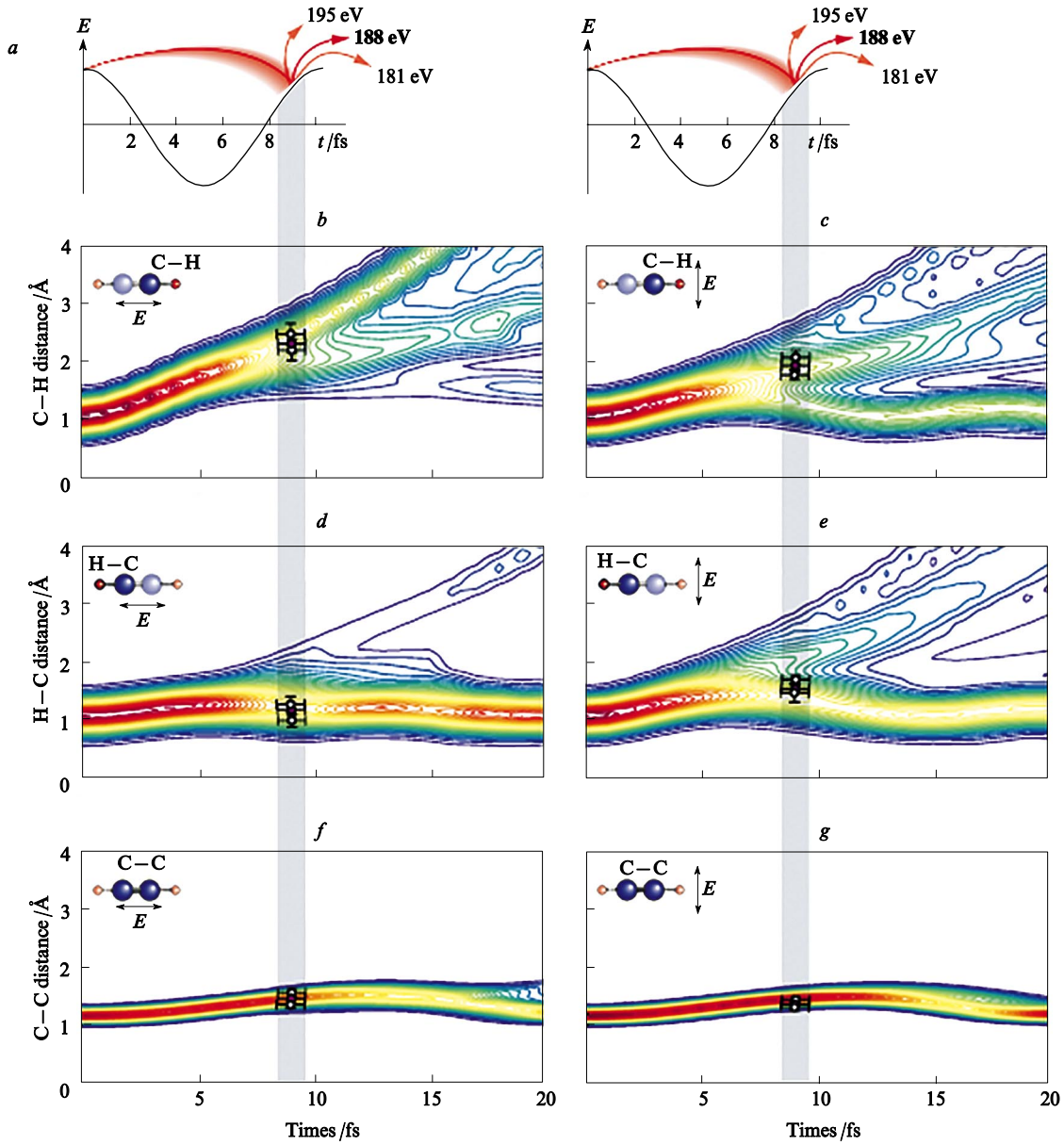


Figure 59. LIED study of the temporal dynamics of C_2H_2 for different bonds and function of alignment.[476] Temporal range imaged for electron energies ranging up to 195 eV (*a*). Theoretical calculations are shown for [(*b*), (*d*), and (*f*)] parallel and [(*c*), (*e*), and (*g*)] perpendicularly aligned C_2H_2. The estimated bond distances found between 9.1 and 9.2 fs (grey shading) are shown as data points superimposed onto the calculations to show the degree of agreement. The expected differences for bond elongation between the CH and CC for different alignments are born out.

orientation (Fig. 59 *c*, *e*, *g*), which closely approximates a quasi-field-free imaging scenario. The difference is most dramatic for the CH bond, with only small difference for the C – C bond, attributed to the greater stiffness of the CC bond that requires a larger driving force to attain the same displacements as the CH bond. The two C – H bonds are driven in phase by the high applied LIED field with equal probability for dissociation. The structure determination requires theory for treating the different interference terms and then the compared to theory as shown in Fig. 59 *b*, *d*, *f* (circles). The degree of agreement gives confidence in the structural dynamics inferred for the formation of the C_2H_2 dication 9 fs after ionization. The space-time resolution by which motions could be detected was estimated to be of the order of 0.6 fs time resolution. As one example, for the parallel case, the C – H bond dissociation for the high-field condition drove the proton 1.24 Å away from its equilibrium position. In contrast, for the perpendicular case the structural dynamics were more representative of a quasi-field-free scenario for the dissociative dication.[476]

XII.2. Molecular dynamics and electron density tomography

Itatani *et al.*[488] had recourse to computed tomography (CT) for image reconstruction and obtained a 3D image of a single molecular orbital. The notion of one-electron wave functions (orbitals) was introduced to describe the electron structure of molecules. It characterizes the state of an individual electron resided in an averaged field of all other electrons and nuclei.

This notion has remained a 'mathematical abstraction' for many decades because of the impossibility of directly observing them untill the advent of methods allowing detailed investigations of intramolecular electron density distribution. Such investigations are carried out using, for instance, scanning tunneling microscopy of molecules on a solid surface (with the inevitable distortion of electron density distribution). Moreover, there are methods for work with molecules in the gaseous phase, such as a variant of photoelectron spectroscopy, permitting the 'illumination' of molecules by electrons from the inside and thereby recording the diffraction pattern reflecting the electron wave propagation in the 3D potential of the molecule. However, none of the available methods permitted us to obtain an undistorted 3D image of the electron wave function and information about its phase.

Computed tomography was applied [488] for the study of complex objects including reconstruction of the image of an object with a complicated internal structure based on the analysis of spatial distribution of radiation intensity that passed through the object (3D image reconstruction from a large number of 1D or 2D projections). The highest filled orbitals responsible for the formation of chemical bonds are the most interesting objects studied. The authors of Ref. 488 reconstructed nitrogen molecule orbitals, generating higher harmonics by intense femtosecond laser pulses. As already noted, this method is currently employed to obtain electromagmetic (EM) radiation pulses of extremely short duration, *i.e.*, attosecond pulses.

The desired set of projections can be obtained by rotating a molecule. Because the researchers had to work with a macroscopic number of molecules rather than an isolated nitrogen molecule, an indispensable preliminary stage of the experiment was the same alignment of molecular axes. For this purpose, a stream of nitrogen molecules with a diameter of 1 mm was tentatively subjected to a 60-fs laser pulse, which caused them to rotate. The rate of rotation depended on their initial orientation with respect to the axis of laser radiation polarization. At some instant of time after the passage of the preliminary pulse, all the molecules became uniformly oriented. Thereafter, the oriented molecules were subjected to a second (more intense) femtosecond laser pulse (wavelength 800 nm, duration 30 fs). Radiation power density (2×10^{14} W cm^{-2}) was high enough to ensure tunnel ionization of the highest filled molecular orbital by virtue of suppressing the Coulomb potential barrier with the electric field of the laser pulse (Fig. 55). Part of the electron wave function was liberated in the course of tunnel ionization: this electron wave packet began to move under the action of a varying electric field of the laser pulse (Fig. 60).

The packet first moved away from the molecule, but then returned and interacted with it. While the electron wave packet travelled back to the donor molecule, it expanded in the direction perpendicular to the direction of motion up to roughly 9 Å, *i.e.*, in excess of the molecule size. The returning wave packet can be regarded as a set of plane waves 'probing' a properly oriented molecule. As the

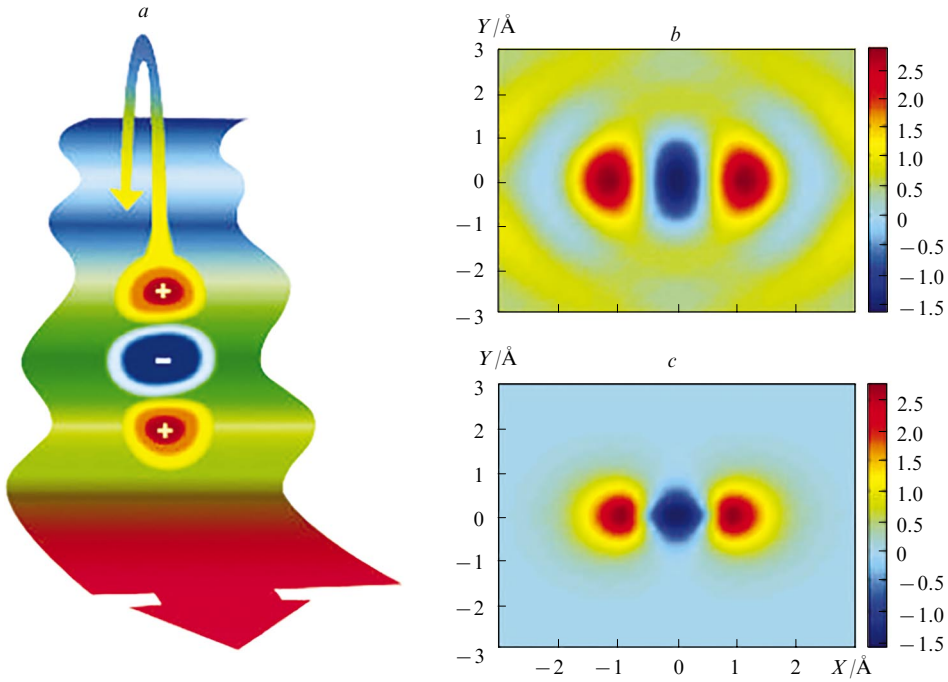


Figure 60. Orbital tomography.[475] The basic physics of orbital tomography are shown in this figure in which the recollision electron experiences many different Fourier components in the combination of the atomic potentials and the applied field to generate high harmonics (*a*). The specific relationship of the harmonics are generated through interference effects involving the sampled potential gradients related to the atomic positions and associated electron density. The interference effects are very different earlier (when the wavelength of the recollision electron is longer, less energy acquired from the applied field) or later (when the electron's de Broglie wavelength is shorter. This specific information is contained within the correlations of the high harmonic generation which can be used to tomographically reconstruct the wave function (*b*, *c*) or more precisely the electron probability distribution with the assumption of perturbative sampling by the applied field. The measured orbital of N_2 (*b*) is compared to the calculated image in *c* (from Ref. 488).

returning wave packet and the molecule collide, the packet overlaps the remaining part of the molecular orbital.

Because both packets originate from a single source, the coherent combining of two wave functions takes place (it is this fact that permits 'working' with a separate molecular orbital). The arising asymmetric electron density distribution varying in time (as the wave packet travels back) can be regarded as an oscillating dipole which emits EM waves. The spectrum of EM radiation thus generated depends on both the molecular orbital shape and the molecule orientation; it is limited from above by the kinetic energy of the oncoming wave packet.

Having registrated the set of spectra ('projections') for different orientations of the molecular axis with respect to the axis of laser radiation polarization makes it possible to reconstruct the 3D structure of an individual molecular orbital (Fig. 60).

The natural extension of work [488] would be to use the approach to observe the evolution of electron distribution in chemical reactions. However, it must be born mind that this approach is limited to high-field interactions in which the chemistry is strictly speaking high-field ionization processes. The study of one-photon photochemical processes with well-defined, chemicaly relevant potential surfaces, will require means to use weak pump/extremely strong probe protocols. It is not clear that the applied field, no matter how short the applied field, will not perturb the electron distribution. For example, the electron distribution at CI's will be prone to high field distortions. This aspect of the problem needs to be included and will certainly lead to new physics in the control of matter.

Theoretical studies of X-ray radiation, as well as simulation of the coherent dynamics processes in a molecular electron subsystem, were undertaken for the first time in Refs. 306 and 489. As shown in the preceding sections, ultrafast electron diffraction makes possible the observation of transient structures in chemical reactions and nonstationary events in condensed media. However, the time resolution, from femto- to picoseconds, proves insufficient to study electron motion in atoms and molecules. Recently proposed methods for generating attosecond pulses [475, 490 – 494] open up new principal possibilities for investigations into the 4D coherent dynamics of electrons in a molecule. These electron sources must necessarily work in the single-electron regime. Normal image reconstruction, without considering differences in noise terms with signal acquisition, require of the order of 10^6 detected electrons depending on the complexity of the object. This simple consideration means it will take of the order of 10^8 longer to collect images and associated sample needs. The SNR limitations and relationship to the space-time resolution has been given, which provide an important baseline for guiding potential experiments.[495]

The prospect of using this electron source for the study of structural dynamics has been analyzed in terms of the potentially observable dynamics. This analysis did not take into account the aforementioned limitation of SNR in the image reconstruction. In this analysis, a laser pulse a few femtoseconds in duration creates the superposition of electronic states that are further diagnosed using an attosecond one-electron pulse with an energy of 10 keV at different time delays. The dynamics of coherent electronic state superposition in atomic hydrogen (H) and the tritium molecular ion T_2^+ were studied theoretically.[496] The diffraction patterns reflect the time dependence of the effective radius of the electron charge density. Changes in the diffraction patterns, in turn, reflect the localization or delocalization of the electron charge density oscillating in time, in fact its 'breath'. Figure 61 illustrates the electron dynamics of a T_2^+ molecular ion.

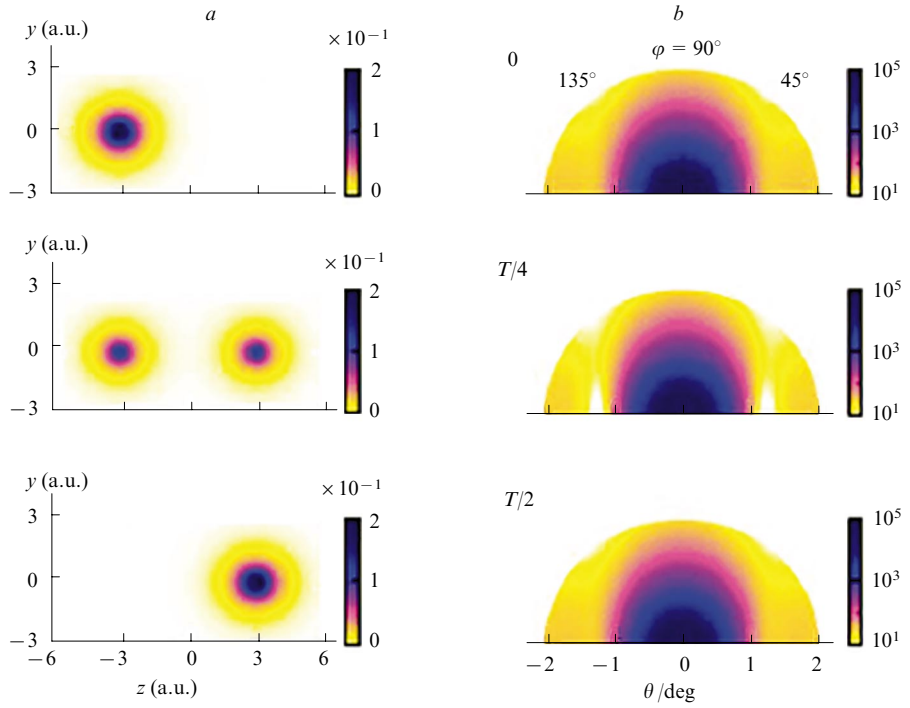


Figure 61. Orbital tomography.[496] Tritium T_2^+ ion charge density oscillation (*a*). Differential scattering cross-sections of an electron bunch with an energy of 10 keV and length of 0.1 fs (*b*). Figures from top to bottom correspond to time delays 0, T/4, and T/2, respectively.

It may be hoped that the exploration of 4D dynamics of electron density can be followed for fully reversible excited state processes where sample limitations are not an issue. The high time resolution may well reveal new features in excited state potentials.

XIII. Atom-resolved reaction dynamics: realization of the chemists' Gedankenexperiment

This Section is updated excerpt from Ref. 106. The important distinction of this Section is that it focuses on the importance of source brightness to achieve the highest possible space-time resolution. The work discussed above used low-brightness electron sources. The first work to achieve atomic resolution on subpicosecond timescales was the work of Siwick *et al.*,[22] which was based on the use of a new concept in ultrabright electron sources to provide the structural probe. The use of high bunch charge femtosecond electron pulses, or ultrabright electrons in this context, was the key enabling technology that made real time viewing of atomic motions possible.

Prior to this work, it was largely believed that the inherent electron-electron repulsion between electrons, or space charge effects, would kill any chance of achieving femtosceond time resolution with sufficient electrons for single-shot conditions needed for following irreversible processes such as chemistry. The advance in electron source brightness for time-resolved studies was based on an effectively exact solution to the coupled equations of motions of some 10^4 electrons within an approximately 100-fs temporal profile.[497] This number of electrons is sufficient for single-shot structure determination for simple unit cells (assuming 100% efficient detectors). The exact numerical simulation of the electron propagation showed that there are indeed strong Coulombic repulsion or space charge effects at the required bunch charge densities. However, one does not lose space-time correlation in the longitudinal or temporal profile related to the electron pulse duration. This finding was completely missed in previous treatments of electron pulse propagation dynamics. Most important, the transverse coherence of the electrons was found to be sufficiently conserved to enable atomic imaging of even complex systems. Two solutions to producing ultrabright electron sources were immediately apparent from this work. One solution is to use a dispersive electron optic to provide the opposite linear chirp to temporally refocus the electron pulse back to the original 100-fs pulse duration at the sample position.[497, 498] The work of the Luiten group in the development of radiofrequency cavities for this purpose is particularly notable.[498, 499] The most robust solution is to use a compact electron gun design and not allow the pulse to broaden after the high-field extraction zone.[22, 38, 500, 501]

To give some idea of the source brightness, it is now possible with the newest generations of compact electron guns to get to electron numbers of $10^5 - 10^6$ electrons per pulse (100 μm beam diameter) with pulses as short as 80 fs and coherences of several nanometres, sufficient for systems as large as proteins.[17, 502] These systems reduce the complexity of the experiment down the same level as conventional all optical pump-probe time-resolved studies. More complex radiofrequency pulse compression systems can achieve a 30-fs time resolution with time stamping to remove radiofrequency timing jitter[503] and approximately 10x more electrons per pulse. Both source concepts are capable of single shot atomic resolution. For comparison, XFELs are major international facilities with fully coherent beams and fluxes of 10^{12} X-ray photons/pulse. Given the 10^6 higher scattering cross-section of electrons relative to hard X-rays for this purpose, the diffracted signal intensity (detected electrons or photons) for typical samples are comparable. These are very bright sources for atomic imaging.

The term atomic movie needs to be defined in relation to imaging chemistry, the central theme of this review. The definition must embrace the ability to observe a correlation of events in time to understand causal connections of force and action. Here, we define an atomic movie to mean a measurement of atomic structure with sufficient space-time resolution to observe atomic motions faster than collisional processes blur out the details, *i.e.*, resolve how atoms move relative to one another during changes in atomic structure. The first atomic movie meeting this criterion focused on the simplest possible structural transition, melting, albeit under strongly driven conditions to capture the primary motions.[22] This advance was only made possible with the development of high-brightness electron sources as each laser shot destroyed the sample, which was in limited supply. This work is distinctive from similar work that followed the picosecond acoustic modes of Al, a fully reversible process with forces on the 10 nm scale (not atomic scale),[504] and from earlier reports of Al melting that could not have resolved this process and were near or more likely below the melting threshold (neglected heat of fusion).[505]

The first atomic movie resolved a long-standing issue on the speed limit for driving phase transitions.[22, 506] It was discovered that at sufficient degrees of laser-induced superheating, the system could melt faster than conventional heterogeneous nucleation by over an order of magnitude through the long predicted mechanism of homogeneous nucleation. The time resolution achieved was 600 fs, which was required to clearly distinguish a controversial point on thermal *vs.* electronic or nonthermal driving forces for the phase transition.[506] The first femtosecond electron diffraction studies showed that the strongly driven phase transition of Al was a purely thermal process and occurred through homogeneous nucleation (now confirmed by all optical studies [507]).

The remarkable finding was that the once the melting threshold was reached, the Al lattice underwent spinoidal decomposition within 1 ps. All the bonds in the lattice broke within 1 ps, with complete collapse of the transverse barrier to allow atomic motions to acquire the radial distribution of the disordered liquid state. The time scale for the collective bond breaking is faster than collisions could wash out the details. Inspection of the time-dependent reduced density (atom pair correlation function) shows the major motions involve shear type motions to the interstitial spaces in the lattice. We teach in physical chemistry that it is thermal motions exceeding the shear barrier to transverse motions that leads to the liquid state. We can now see this at the atomic level. These results also demonstrated that the nucleation sites had to occur homogeneously throughout the sample and could only be of the order of 10 atoms. The insight gained from the first atom-resolved structural transition helped solve the problem in laser driven ablation and shock wave formation that leads to collateral damage in laser surgery.[508] The long-held promise of the laser to achieve the fundamental (single cell) limit to minimally invasive surgery has now been achieved and for the first

time without scar tissue formation.[509, 510] This application is noted here as it is the perfect example of how basic research can lead in unexpected ways to important real life applications. This outcome was derived from an atomic level perspective of the simplest structural transition, *i.e.*, melting. One can well imagine what the outcome might be for a complete atomic level understanding of catalysis, or the chemistry of structure-function relationships in biological systems, as just two other examples.

In the years that followed, most the work using high brightness electron sources focused on photoinduced phase transitions from collective many-body effects in the formation of charge density waves and bond hardening or changes in nuclear screening with the onset of warm dense matter at electronic temperatures of several hundred thousand K.[24, 511 – 514] There has been a continual increase in source brightness, but equally important developments in source characterization, and detector development. The evolution of source brightness and improvements in space-time resolution of structural transitions is shown in Fig. 62 to give an impression of the rapid progress made towards imaging chemistry once source brightness was realized as the major impediment.

The first molecular movie of a chemical reaction was that of electrocyclization with conserved stereochemistry.[517] The specific system was the ring-closing reaction of diarylethene, which is a photochromic material pioneered by Irie *et al.*[518] They deliberately designed the electrocyclization process by including electron-withdrawing groups on the aryl rings to specifically weaken the ethene double bond in the bridge position to allow torsional motions to close the ring. The ideas behind the synthesis of this molecular and its photoactive functionalization are not too dissimilar to the discussion above in thinking about reaction routes to strategic molecular targets. The photoactive process is centred on the bond formation process in electrocyclization and as such represents the formation of collisional complexes in otherwise two-body or second-order reaction mechanisms.

The spatial relationship of the interacting carbon atoms for bond formation had to be fixed by the molecular moiety to reduce the nuclear configuration space so that the dynamics are determined primarily by the very motions involved in bond formation. It was critical to maintain the stereochemistry to ensure a single photoproduct state and some degree of reversibility. The system is set up as if to watch the formation of a collision complex upon photoexcitation. In this respect, it is an ideal system to test the ideas used for maintaining stereochemistry in synthetic routes in general. What are the key motions involved in electrocyclization? Given the enormous phase space for random rotation about multiple points, how is stereochemistry conserved? This latter question is related to the prospect of any long-lived intermediate states and the relative dynamics by which the reaction forces (potential energy gradients) in the barrier-crossing region drive the system from the open to the closed ring form. Ultrafast time scales for barrier crossing are implied just from consideration of the competing timescales for random rotational/torsional motions sampling other configurations than the desired pathway.

The ultrafast aspect of the reaction dynamics was fully characterized *in situ* with femtosecond absorption spectroscopy on 100-nm thin single crystals.[519] There is an initial fast 200 – 300 fs inertial like component to the excited state dynamics followed by a 4 – 5 ps component leading to the formation of the ring-closed form. The full characterization of the excited-state dynamics is essential background work to this class of studies to correlate the electronic and nuclear degrees of freedom in undergoing photochemical processes. At the excitation level needed for the structural studies, the photochromic nature of the open and closed ring forms was exploited to optically cycle the closed ring photoproduct back to the open-ring form.[517] Even with the increased sampling per crystal location, the repetition rate was limited to the 0.1 Hz range due to the slow photorecovery and low thermal conductivity of organic crystals. Again, the ultrabright nature of the electron source used, in this case a radiofrequency pulse compression scheme, was essential to obtaining sufficient SNR and signal contrast to capture the atomic motions.

The main findings are shown in Fig. 63. The initial fast motion is due to a flexing of the backbone and slight ring torsional motion to bring the two labile carbon atoms into wave function overlap. This specific mode involved is a spatially delocalized mode at approximately 55 cm^{-1} assigned from DFT calculations of the full molecule ground state vibrational mode, which matches well the initial projections based on an *ab initio* calculation at the CASSCF level for a truncated model system of the diarylethene core. There was however no well-defined minimum but rather continuous motion involving primarily the backbone flexing and three localized torsions at opposing sides of the closed ring which close the ring in a conrotary fashion. We now see directly at the atomic level how stereochemistry is conserved. The steric groups instinctively put in place by synthetic chemists do create forces that are sufficiently large to steer the system into bond formation. The ensuing vibrational relaxation to the product minimum occurs faster than sampling other coordinate space. The process is dynamically controlled.

The TS in which the labile carbon atoms are within wave function overlap of each other could have involved a flat potential with multiple barriers to other orientations that would otherwise cascade into other possible photoproducts with torsional motions leading to loss of stereochemistry. However, this is not the case. The system is strongly driven directly to the closed ring form with conserved stereochemistry. The other main point is that this system has hundreds of degrees of freedom including the surrounding lattice. We see directly now for the first time this distillation of chemistry down to a few key modes. This point will be further reinforced below. To get an appreciation of the specific time ordering of the motions involved in conserved stereochemistry see the movie (**Supplement**:‡ Molecular movie 1).

The next system to come under atomic scrutiny was the intermolecular electron transfer process exhibited in the charge ordered organic crystal ethylenedioxytetrathiafulvalene (EDO-TTF).[516] This system undergoes a thermally driven phase transition from an insulator to a metal at 280 K. This phase transition involves a net transfer of an electron from one EDO-TTF molecule to another within the unit cell to create a delocalized electron distribution. In the low-temperature insulating phase, the alternating EDO-TTF cations have a deformed ring as part of the

‡ iopscience.iop.ogr/journal/0036-021X

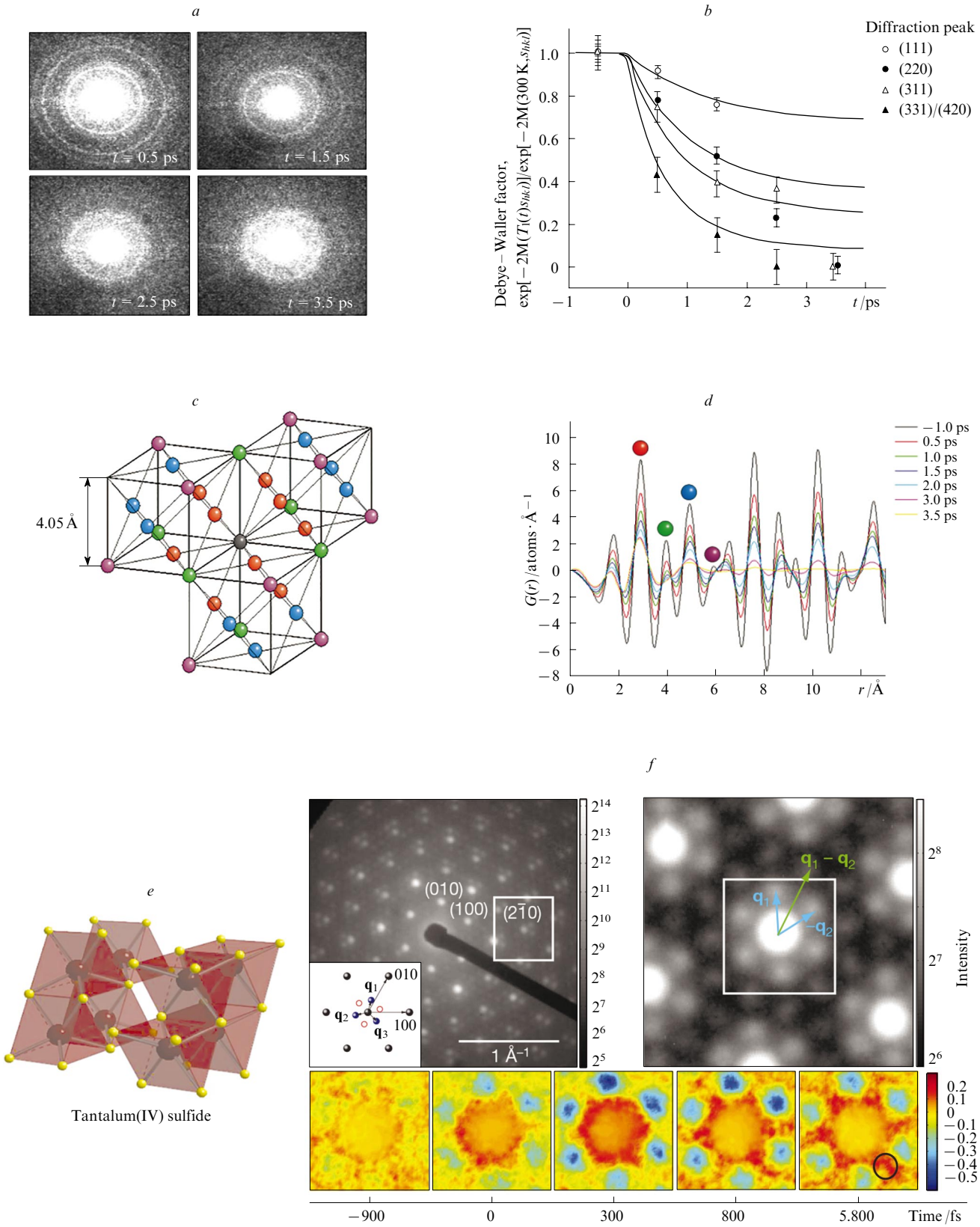


Figure 62. (to be continued at the next page) Evolution of atom-resolved structural dynamics.
Very grainy images from the first atomic movie (*a*), which appear much like the first images in the early days of photography, are shown in *a*.[22] The onset of melting occurs within 1 ps between t = 2.5 and 3.5 ps (*b*).[515] The corresponding real space transform is shown in *c*, *d*. $G(r)$ is the radial density function. The dramatically improved diffraction quality in the study of the collective phenomena associated with charge density waves is shown in *e*, *f*.[513]

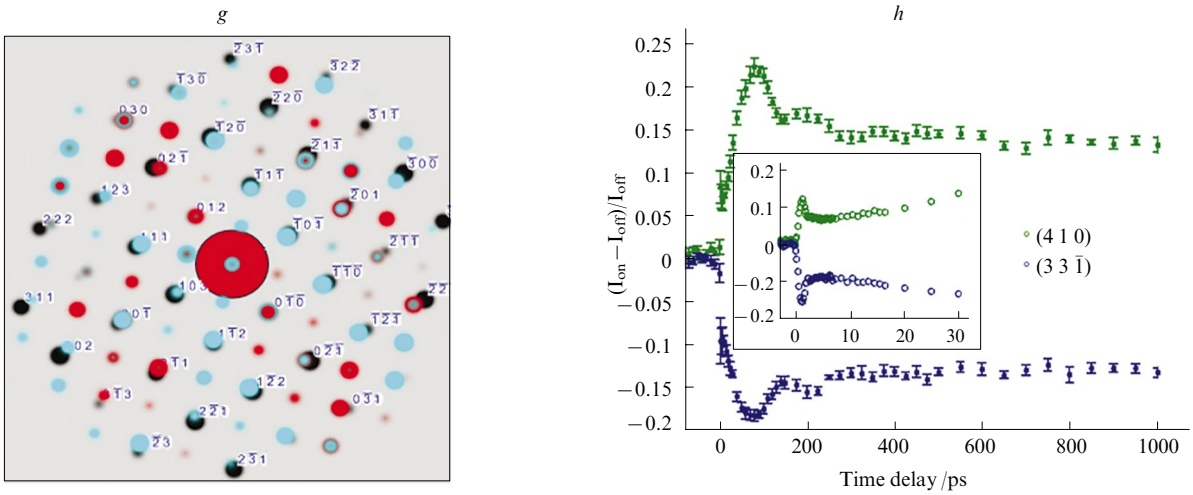


Figure 62. (continued) Evolution of atom-resolved structural dynamics.
The extremely high spatial imaging quality for even poorly diffracting organic systems — ethylenedioxytetrathiafulvalene (EDO-TTF) with diffraction well beyond 0.1 Å (reciprocal space) is shown in *g*, *h*.[516] The SNR of just 2 diffraction orders are shown (*g*), which is comparable to high-quality all optical pump probe signal (*h*), to give an impression of the outstanding SNR now possible in the image contrast. There are hundreds of such diffraction orders of this quality to help constrain the inversion to real space atom-resolved movies of chemistry. (From Ref. 106 with minor revision).

intramolecular reorganization to minimize the energy of the cation state. There is a structural change between the insulating to conducting phases in which the rings all flatten and shift slightly for better ππ wave function overlap as part of creating the delocalized band structure commensurate with the onset of metallic properties. The electron transfer process can also be photoinduced under barrierless conditions by exciting a charge transfer band. The ensuing structural dynamics cast out the motions most strongly coupled to the electron transfer coordinate. These motions are expected to include both intramolecular bond length and bond angle changes as well as intermolecular motions

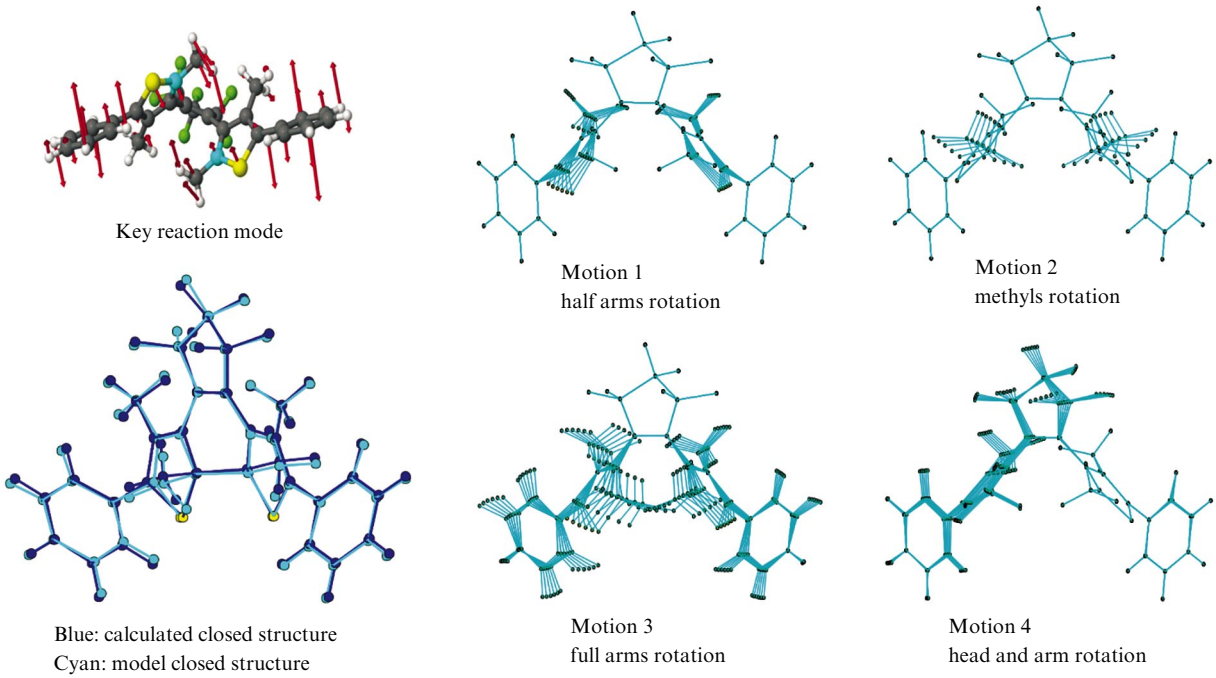


Figure 63. Modal analysis of the key reaction modes involved in electrocyclization with conserved stereochemistry for diarylethene. The main mode is shown in the upper left panel, which corresponds to motion 3 in the second row. These theoretically generated classes of motions were used in structure refinement to provide a converged fit to the data with hundreds of diffraction orders for constraints. These are the key reaction modes and the time ordering leading to ring closing. There are no long-lived intermediates that would allow torsional sampling and loss of stereochemistry, but rather a continual progression from a very fast inertial motion to bring the labile carbon atoms involved in bond formation to be within wave function overlap and torsions to click the bond formation into place to close the ring. (From Ref. 106 with minor revision).

as part of the intra- and intermolecular reorganizational energy defining the electron transfer reaction coordinate. No bonds are made or broken. Electron transfer processes are determined by the intra- and intermolecular reorganization or medium repolarization to both bring electronic states into resonance and to stabilize the change in charge distribution. The change in the structure of the EDO-TTF lattice with T is known from X-ray diffraction of the insulating and metallic phases. Using the traditional thinking in conceptualizing the transition state, one would expect the key reaction modes would be the flattening of the thio rings to increase the wave function overlap as part of the process of forming an electronic band. In keeping with the above discussion, it is not possible to project static structural end points to the motions involved in barrier crossing. As above for the diaryl case, there are always surprises from conventional expectations when the chemistry is observed at the atomic level.

This experimental study also exploited radiofrequency pulse compression to get the necessary number of electrons and source brightness to overcome the very low thermal conductivity and thermal accumulation artifacts. The experiment had to be conducted at sampling repetition rates of 10 Hz and it would not have been possible to obtain sufficient SNR before the onset of crystal degradation with low brightness sources. The diffraction quality was extraordinary with rms amplitude variation in diffraction intensities of the order of a few percent reflecting the high stability of the electron source. This crystal diffracted well beyond 0.1 Å (reciprocal space parlance) to enable very high spatial resolution (camera was cut off at 0.2 Å). This is an order of magnitude higher than typical X-ray studies where 2 Å is the cut off in the reciprocal space for atomic resolution. There were literally hundreds of diffraction peaks to constrain the diffraction analysis in the inversion to real space. The first major surprise that hits you immediately is the enormous reduction in dimensionality. Of all the myriad of possible nuclear configurations, the motions collapsed to just a few key motions. There are over 280 degrees of freedom in this problem including all possible molecular motions within the unit cell as part of the intermolecular reorganization. Using a new method for differential diffraction analyses to remove the background, and a Pearson correlation analysis of an exhaustive basis of possible atomic motions connecting the initially known structure to the final photoproduct state, it was found that the hundreds of diffraction orders over multiple time points could be described by just three key reduced reaction modes. The second major surprise was the specific mode most strongly modulating the electron transfer coordinate or medium reorganization. The dominant mode was the motion of PF_6^- counterion rather than the expected ring flattening. This observation could not have been guessed as we don't have enough information on how the counterion is coupled to the electronic states. The coupling of the PF_6^- anion to the electron transfer is obviously substantial from the magnitudes of the relative motions. Most important, the three dominant reaction modes were fully correlated. The trajectories appear to be shadow projections of each other. This observation means that the slowest mode of the three is dominating the overall medium repolarization in response to the change in electron distribution.

A slow mode would not be able to respond in lock step with a higher frequency mode and would necessarily appear to execute relaxation on separated time scales. This was not the case. The slowest mode is related to the motion of the PF_6^- counterion. In retrospect, the role of the counterion is obvious. The photoinduced electron transfer from one EDO-TTF to another creates a local electric field, which would electrostatically create the largest force on PF_6^-. This counterion is so large that its displacement driven by the reaction field leads to renormalization of the PES local to the EDO-TTF to assist ring flattening, lowering further energy for the new charge state, and also the intermolecular potential leading to the change in the centre of mass locations of the EDO-TTF rings. See the atomic movie of these correlated motions to get an impression of the significant effect of the counterion in stabilizing the electron transfer (**Supplement**:§ Molecular movie 2).

This observation is what inspired the above analogy of the hike in the Alps where your every step changes the landscape opening secret passages to hidden valleys. At the hazard of overdoing analogies, the very motion of PF_6^- is like an elephant going into a crowded room. Everyone would move out of the way, and if the floor was weak enough, it would bend under the weight to create new minima depending on the location of the elephant in the room, to which this many-body/person potential would involve movement to accommodate (the heavy slow mode correlates the lighter mass faster motions). This direct observation of the importance of the counterion helps rationalize previously inexplicable counterion dependence of material properties for this class of organic materials. The counterion in organic salts is not screened by the motions of other ions as it would be in a liquid. It is the nearest neighbor and dominant source term to the local electric field. Its motion strongly modulates the energetics, or barrier heights, of the electron transfer reaction coordinate and modifies the PES to slave other motions that lead to increased wave function overlap. The system is poised to interconvert from insulating to metallic through these motions over a collective coordinate. We now see the effect of the bath on electron transfer processes directly at the atomic level.

The most significant advance in ultrafast imaging of chemistry was the recent work on the metal-to-metal electron transfer in the organometallic system $Me_4P[Pt(dmit)_2]_2$ (Me_4P is tetramethylphosphonium, dmit is 1,3-dithiole-2-thione-4,5-dithiolate).[17] This system, as EDO-TTF, is a charge-separated ionic crystal that undergoes a structural phase transition in which formally an electron is transferred from one Pt atom to another within the $[Pt(dmit)_2]_2$ dimers. This process can also be photoinduced through a charge-transfer band. It is effectively a metal-to-metal electron transfer process. The motions most strongly coupled to the photoinduced excited state would be the same motions involved in intramolecular and intermolecular reorganization involved in the thermally accessed electron transfer process.

This reaction mechanism is specifically exploited in biological processes involving metal centres for mediating charge transfer and contains all the physics involved in classic metal-to-metal electron transfer in solution phase that we teach in first-year chemistry courses. The difference is that we have a well-defined solid-state lattice from which we can pull out the details of the reaction forces on the

§ iopscience.iop.org/journal/0036-021X

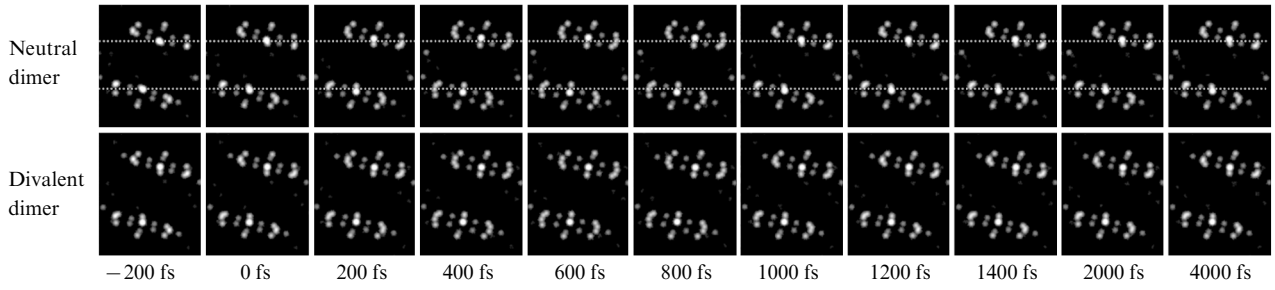


Figure 64. Molecular movie of organometallic system $Me_4P[Pt(dmit)_2]_2$.[106] Frame-by-frame movie of the atomic motions involved in metal-to-metal electron transfer. The atomic positions are indicated as white circles, the largest brightest circles as the Pt atoms, and the other atoms are the sulfur atoms in the rings. The dotted yellow line is given as a reference to enable observation of the motions. The change in Pt motions can be discerned by eye and the tilting of the rings can be seen by the change in the projections of the sulfur atoms along this viewing axis.

atomic motions, which would not be discernable in the ensemble average of disordered structures in solution phase. We effectively have well-defined initial atomic coordinates for the bath to directly image the medium repolarization effects. It is also important to note that $Pt(dmit)_2$ has a crystal structure with unit cell dimensions of 3.7 nm, which puts it on par with protein crystals for complexity. A compact electron gun was used for these studies. This simple robust design concept has now achieved the level of brightness needed to capture the atomic motions for such a high dimensional system. The results were stunning.

Figure 64 shows the femtosecond electron diffraction (FED) results for $Pt(dmit)_2$ using a new mathematical inversion method. To appreciate the space-time resolution achieved, some comments are warranted. In conventional diffraction analysis, it is not possible to uniquely invert the diffraction pattern to real space as the measurement only contains information on the intensity of the different diffraction orders or structure factors. The scattered wave amplitude also has a phase and interference effects between scattering centres that lead to ambiguity in the reconstruction. Simply put there is not enough information in the intensities to uniquely invert from reciprocal space to real space as there are two spatially dependent variables for which you only have the intensity. This problem cannot be solved for imaging unknown structures. The published atomic structures for molecules based on diffraction data are refined using constraints from either theory or molecular models based on other absolute structures for which some known scattering centre was exploited to phase the data. In time-resolved diffraction experiments, we are dealing with known initial structures and final structures. We are not trying to solve unknown structures. Here differential detection in combination with this additional information is sufficient to solve the phase problem. The work of Ishikawa *et al.*[17] introduced a new method in which the known initial structure, conserved bond lengths, bond angles and the causal constraint of continuous progression to the product state (no discontinuous jumps) were sufficient constraints to give unique convergence to structures (please, see SOM of Ref. 17). In effect, the known conserved features act mathematically as phasing centres to uniquely solve the phase ambiguity problem. The atomic motions you see in Fig. 64 are not the result of a fit to a model or computer simulations used for refinement. The results shown in Fig. 64 are the first full atom-resolved chemical reaction.

As you zoom in and focus on the details in this figure a number of features become apparent. In this respect, we are very good at discerning space-time correlations *i.e.*, how one event leads to another and over what length and time scales. We now can directly observe what we tried to imagine previously. For this reason, movies of causally connected events make a particularly powerful means to convey the operating physics of a phenomenon. This distinguishes the time series of connected actions from well separate intermediates, as observed in time lapse photography. You see the 'before' and 'after' structures but not the pathway. To not bias your eye with balls and sticks or van der Waals surfaces, Fig. 64 is shown with the atoms depicted as stars against a night sky. The brightest 'star' is the Pt atom, which is the largest scattering source term. You can see immediately that not all possible atomic motions are involved or there would be a blur and no well resolved motion. Instead you can make out by eye that there are at least two dominant motions involving primarily the Pt – Pt separation and direction of displacement. This system has over 1000 degrees of freedom including all intramolecular and intermolecular motions that could be involved in the reorganization to stabilize the photoinduced electron transfer. This effect is seen more dramatically than stills if you observe the time correlated motions as a movie to fully exploit our ability to see space-time correlations compare Fig. 63 to (**Supplement**:¶ Molecular movie 3). From the movie, there is much greater clarity of the causally connected events. You can now see directly the collapse of innumerable possible nuclear configurations to just a few key modes. The times scale is slower than that for IVR in this large molecule such that the condition of equipartition of energy (*vide supra*) is approximately correct, at least for individual excited sites. Even in this case, not all degrees of freedom are involved. The reaction forces are highly anistropic and drive specific modes. This enormous reduction in dimensionality during structural transitions is in keeping with study of reaction dynamics in diarylethenes, EDO-TTF, and other systems we are exploring. This reduction in dimensionality during structural transitions is a general phenomenon.

The degree of space-time resolution achieved in these experiments to light up the specific reaction modes can only

¶ iopscience.iop.ogr/journal/0036-021X

be fully appreciated by examining the key modes involved quantitatively. The time-resolved structural changes involving thousands of diffraction orders for constraints could be mapped on to 6 dominant reduced reaction modes, as show in Fig. 65. The change in electron density upon the photoinduced electron transfer affects largely the Pt metal centres. For this reason, the largest motions involve the Pt atoms. This aspect of the structural changes could have been expected based on the fact the electron transfer process involves the Pt metal centred, however, neither the magnitudes nor the anisotropic coupling to the other displacements could be *a priori* inferred. Also, this system is too large and involves high Z atoms that are difficult to properly treat with *ab initio* methods.

The level of detail from these experiments should provide rigorous benchmarks to explore different approximations to theoretically treat reactions on this scale, which is essential if we wish this level of understanding to be relevant to current synthetic objectives. From the inspection of the time dependent changes in the Pt – Pt distance, it is possible to observe the oscillations and damping of this mode on to the fully relaxed position corresponding to the high temperature charge distribution. The amplitude of the motion is only 0.1 Å but is clearly resolved. The rms noise can be used to estimate the resolution limit to be of the order of 0.01 – 0.02 Å. This spatial resolution limit is comparable to the zero point motions of bound states for 2nd row atoms in the periodic table. The resolution only depends on the diffraction efficiency such that the same resolution can be achieved for all systems. With high-brightness electron sources, we have effectively achieved the fundamental limit for space-time imaging of chemical reactions. We can now directly observe the far-from-equilibrium motions that direct chemistry with sufficient resolution to provide new experimental benchmarks for theory.

The overall message that jumps out of this data is that the simple bit of missing physics discussed above that makes chemical reaction mechanisms transferable is the enormous reduction in dimensionality that occurs in the barrier-crossing regions. The high degree of anharmonicity in this region of nuclear configuration space couples high-frequency modes with more spatially delocalized modes that are most strongly damped. It is the quantum aspect of this coupled state that leads to more localized motions through interference terms. One can readily see from the atomic motions for the photoinduced electron transfer for $Me_4P[Pt(dmit)_2]_2$ that there are spatially delocalized motions involving the entire $Me_4P[Pt(dmit)_2]_2$ moiety and these cascade to larger, more localized motions of the Pt atoms. The proposal here is that different reaction mechanisms involve a certain class of reaction modes that direct the chemistry and it is these conserved features that make chemical reaction mechanisms transferable from one molecule to another. It is the reduction of a high-dimensional many-body problem of order $3N$ to just a few key modes that is the 'magic'of chemistry. This is the key physics that we need to determine in systematic way by exploring different classes of reaction mechanisms.

In parallel, there has been tremendous progress in X-ray source development to enable imaging chemical reaction dynamics. The first work to achieve sufficient time resolution to follow chemical reaction dynamics with X-ray probes was based on table top laser driven X-ray plasma source.[520 – 522] The major new developments were the significantly improved optics for higher collection efficiency with respect to focusing the plasma-based X-rays on the sample and the use of very thin metal targets with rapid exchange to obtain X-ray pulses as short as 100 fs. The number of X-rays per pulse constitute a low brightness source such that fully reversible systems need to be studied. It should be mentioned, however, that taking into account

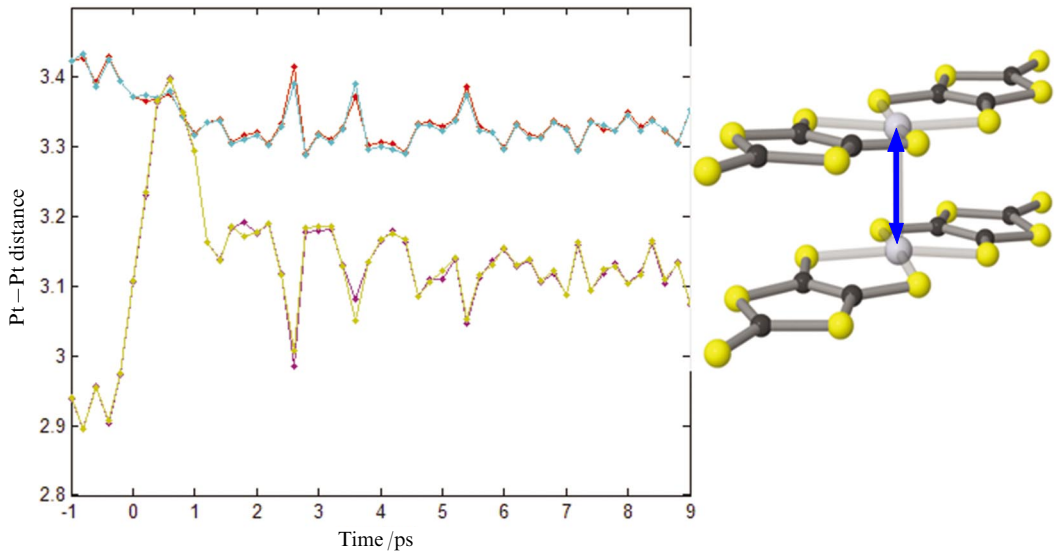


Figure 65. Quantifying the atomic motions: analysis of the Pt – Pt separation in $Me_4P[Pt(dmit)_2]_2$ with photoinduced electron transfer. There are two different Pt – Pt dimers in the crystal depending on the spatially ordered charge state. The motion is schematically shown for the ball and stick structure to the right showing the Pt atoms (large grey spheres), sulfur atoms in the ring (yellow spheres) and carbon atoms (black spheres). The upper curve curve is for the '–2' dimer and the lower curve is for the neutral dimer. The spatial resolution is sufficient to resolve minute changes in energetics as the system undergoes lattice reorganization, with the Pt – Pt distances being one the dominant terms. There are five other key modes involved (see Ref. 17).

the relatively high repetition rate of the laser (kHz) the net photon flux per second can approach X-ray fluxes from beam slicing sources at synchrotrons but with a table-top source. The work of the Elsaesser group and collaborators stands out in achieving the highest time resolution to date and the introduction of heterodyne detection strategies for certain symmetry classes to dramatically increase the signal detection and mitigate some of the disadvantages of a low brightness source.[520 – 523] The work to date has focused for the most part of ionic crystals, which appear to be the most capable of reversible charge transfer processes.

The most interesting finding is the discovery of a concerted electron-proton transfer and evidence for a highly collective reorganization of the lattice in the formation of high spin state of the classic iron bispyridine system. The low photon numbers of the source require the use of relatively thick crystals to get the maximum diffraction efficiency for a given excitation volume. Given the large mismatch between resonant excitation of the sample and the X-ray probed volume, these experiments have had to use two-photon excitation to get sufficient penetration into the required crystals thicknesses for optimal diffraction. In order to excite at least 10% of the lattice to observe the small signal changes, there will necessarily be higher order multiphoton excitation processes. Further excitation levels above two-photon are all resonant and would strongly compete with pure nonresonant two-photon state preparation. The observed structural dynamics are likely from ionization processes as opposed to photochemistry from well-defined excited-state surfaces. It is not clear what excited states or ionization processes may be contributing to the observed structural changes. This is the same limitation for all X-ray studies as there is a large mismatch between the needed X-ray probed volume for sufficient diffraction and resonant one-photon preparation of well-defined excited states. The very recent development of extremely high-power femtosecond IR lasers promises to push the X-ray flux several of orders of magnitude higher, which should be sufficient to enable resonant one-photon excitation to well-defined excited states. The experiments to date illustrate the structural capabilities. This approach will provide a new tool comparable to the high-brightness electron sources for the study of systems that are not readily amenable to electron probes such as solution phase and protein systems.

In the past year, XFELs have also achieved real time atomic movies of chemical reaction dynamics. These sources represent an increase of several orders of magnitude in X-ray source brightness over previous generations of major X-ray facilities.[524] The source is spatially coherent in the transverse plane like a conventional laser operating at visible wavelengths so it can be focused down to near transform limits of nanometre dimensions for imaging applications. The enormous X-ray flux is generated by self-amplified spontaneous emission (SASE process) that is subject to noise fluctuations in initiating the amplification cascade. As such, these sources undergo large stochastic variations in intensity. The accompanying reduced SNR for differential detection of structural dynamics and the longer wavelength intrinsically decrease the effective space-time resolution relative to electron sources, all other factors being constant. However, there are other variables at play that determine the overall imaging efficacy. Samples are a big issue.

Source brightness can also play a defining parameter in what systems can be studied. The importance of source brightness and XFELs, in particular, for X-ray diffraction studies has been amply demonstrated through the work of Minniti *et al.*[87] in the gas-phase study of the ring-opening reaction of the classic CHD problem. This system, as in the diarylethene study discussed above, serves as a model system for electrocyclization processes. Given the extremely low X-ray scattering cross-section and gas density, this experiment would have been impossible without an XFEL source. The diffracted signal went out to a couple of diffraction orders that allowed resolving the bond dissociation dynamics, which matched well optical studies. By using theoretical constraints, it was possible to project the resulting dynamics from bond breaking to the ring open structure and onset to the different conformational states of the photoproduct. With higher number of diffraction orders, it will be possible to directly map these motions onto specific modes. In the gas-phase studies, the sample limitations are not an issue and rapid sample exchange is a major advantage over solid-state studies. Here the excitation conditions match well those of nonperturbative all-optical studies such that the nature of the excited state leading to the observed chemistry is well defined.

As emphasized above, the highest spatial resolution is obtained with crystalline samples *via* the N^2 dependence in the diffraction process and reduced diffuse background scatter from disordered systems, *e.g.*, gas and solution phase. In this regard, the major advantage of X-ray sources over electrons is the ability to use conventional crystals or solution phase pathlengths by the very virtue of the much weaker scattering cross-section for X-rays. The use of X-ray probes has, however, its own sample limitations.

Conventional crystals giving high quality diffraction patterns are typically of the order of 10 μm or thicker. In order to excite 10% of the unit cells to get above background, the peak power typically used to get sufficient changes in diffraction intensities for this crystal thickness is of the order of TW/cm^2 for nearly every experiment performed to date. Peak powers of of the order of 100 GW cm^{-2} have led to significant nonresonant three-photon ionization of water for similar pathlengths.[525] The phototriggered optical processes for time-resolved X-ray diffraction are fully resonant processes, which are greatly amplified above the aforementioned problem with nonresonant two-photon excitation. The resonance condition creates amplification for all n-photon excitation pathways. Multiphoton processes could be the dominant source for the induced structural changes. This excitation mechanism changes significantly the chemistry from well-defined excited state surfaces undergoing isomerization, cyclization, *etc.* to ionization-driven structural changes from ill-defined states. The effect of multiphoton ionization has not been taken into account in terms of contributions to the observed structural changes.

With this caveat, XFELs are still the only source currently capable of studying biological systems, simply due to the problem of obtaining thin enough samples for electron structural probes. The main limitation for electron sources is the difficulty in obtaining sufficient protein crystals on the 100-nm scale for time-resolved studies. This problem of obtaining large numbers of protein crystals has been solved for serial crystallography applications. In this respect, XFELs enable probing the issue of reduced dimensionality for systems of increasing complexity. The ultimate

limit in scaling to larger systems is to observe the transduction of chemistry into biological functions. In the case of proteins, one is now dealing with highly associated glass-like systems (on long time scales) with $>10\,000$ atoms; yet the chemistry driving functions and biochemical pathways is highly robust.

The system does not get trapped in local minima along the chemically relevant reaction coordinate. In this context, the reduction of the structure – function relationship of biological systems to a few key modes is a truly profound observation of how highly optimized nature has become. In this regard, the most significant results have come from the study of the structural changes involved in ligand dissociation within carboxymyoglobin as a model system for the tertiary level structural changes involved in molecular cooperativity in hemoglobin.[526] This response forms the cornerstone of our understanding in general of molecular cooperativity in biological systems as one form of feedback in biochemical pathways of living systems. As discussed in the introduction in the context of Levinthal's paradox, this system is highly associated and involves chemistry at the extreme end of the complexity scale.

The Collective Mode Coupling Model was proposed as the mechanism by which such highly associated systems beat being trapped in local minima in executing their biological function.[527 – 532] This model was based initially on direct observation of collective motions of the protein driven by the ligand dissociation and exhaustive all optical studies of different length scales of motion and energetics to show that this is the dominant mechanism. It is the inherent spatial correlations in the fluctuations of biological systems that enables the effective reduction in dimensionality and escape from glass-like dynamics in dictating functional responses. This statement goes back to the initial discussion of correlated motions and reaction phase space. The issue in terms of making the connection between the evolutionarily optimized structure and function can only be solved by a direct observation of protein function at the atomic level.

The latest XFEL experiments have fully confirmed that the protein motions involved collective modes and these correlated motions are close to those based on molecular dynamics calculations.[526] The issue of ionization effects is still a problem. The motions involved may not be biologically relevant. However, it is clear from this work that there are correlated motions, which can be discussed in terms of collective modes bearing out the collective mode coupling model. These studies need to be redone at excitation levels for which the forces driving the protein motion originate from ligand dissociation. The other key experiment is the XFEL study of the light induced structural changes involved in the isomerization of the photoactive yellow protein.[533] Again, this work shows beautifully that there are highly localized changes directing the isomerization process. The excitation process in the sampled volume is ~ 1 TW cm^{-2}, which again raises issues of ionization in this interpretation. Power dependences are needed to sort out functionally relevant motions from possible ionization effects. The particular motions resolved at excitation levels above 100 GW cm^{-2} are likely dominated by ionization effects and forces from the created highly excited ion states rather than the potential related to the chemically relevant forces.

The main point in light of the above discussion is that even out to systems as large as proteins, the chemistry involved reduces to a few key modes. This reduction in dimensionality holds in general for chemical reactions and has been highly exploited by nature in scaling to ever more complex systems. At the extreme end of complexity as defined by proteins, the reaction forces of this reduced chemically active space are further coupled even out to mesoscale dimensions by the imposed structural constraints of the highly optimized protein structure to reduce the phase space and direct reaction forces to execute biological functions, often at the maximum possible efficiency.[527] It is an extraordinary feat in directing chemistry into action.

The above discussion has focused on direct atom-resolved chemical reaction dynamics — direct imaging of chemistry. As with any observation, as one looks closer and closer with great acuity, one finds surprises in how things work. Here we are talking about observing chemistry at the fundamental space-time limit, watching chemistry unfold at the atomic level of detail. Our previous conceptual models for chemical reaction mechanisms have been hard earned through the extensive use of molecular probes as in the case of synthetic chemistry or equally extensive spectroscopic and molecular beam studies. We have historically focused on details that were particular to a given molecule. In the process, we have failed to see that generalities of chemical processes. For each system, the concept of reaction modes has long been discussed. However, it is only now that we see directly the innumerable nuclear possibilities collapse to a few key reaction modes that the significance of the anharmonic coupling in the barrier-crossing region becomes fully apparent. We can now witness these far from equilibrium motions reduce the dimensionality of the possible nuclear rearrangements to a few key reaction modes for systems as small as a few atoms up to systems as complex as proteins. The first full atom-resolved chemical reactions have experimentally established that a general physical principle is indeed at work.

The many-body potential is so complex and the degree of nonadiabatic coupling between electronic and nuclear degrees of freedom is not known with the required accuracy to predict reaction pathways. The major advance made is that we can now observe these motions directly. What can we do with this information and new insight into reaction dynamics? This question will be addressed below in relation to developing a new conceptual basis for chemistry that will naturally arrive with the convergence of experimental and theoretical tools to study systems at every increasing levels of complexity — at the atomic level of detail.

XIV. Complementarity of spectroscopy and diffraction for studying structural dynamics

The preceding sections reviewed current research on the structural dynamics observed by TRED and TRXD with time resolution reaching from the nanosecond to the femtosecond regime.

The history of structural dynamics research goes back to pulsed photolysis (flash photolysis) proposed in the late 1940s and early 1950s,[15, 534 – 536] which found widespread acceptance and recognition (Nobel Prize in Chemistry 1967). Even using classical light sources (flash lamps), this method allowed the identification of intermediate products of photoinduced reactions with a time resolution at the submicrosecond level. The advent of lasers capable of generating very short light pulses made it possible to develop a large number of methods for laser spectroscopy and to investigate dynamical processes with femtosecond

time resolution. The description of these techniques and their applications is beyond the scope of this review, because they are covered in the voluminous literature (see, for example, Ref. 537). We confine ourselves to a brief discussion of problems closely related to the topic of the present work, such as relaxation processes and intramolecular dynamics associated with vibronic interactions in the ground electronic states of molecule and several examples of time-resolved diffraction studies of coherent nuclear dynamics in photoinduced processes.

The advent of pulsed tunable IR lasers made it possible to initiate research on the processes associated with excited vibronic states in molecules due to direct excitation of their nuclear subsystems. This promoted investigations into the collisional relaxation of vibrational excitation, including V – V exchange and V – T/R relaxation (see reviews [538, 539]). The use of IR multiphoton excitation (IR MPE) effect (see a monograph [540] for details) made possible the investigation of relaxation processes in highly excited molecules. Specifically, it was shown that the rate of vibrational-translational (V – T/R) relaxation is a nonlinear function of the level of vibronic excitation in the molecules.[541] The harnessing of the IR MPE effect made it possible to undertake an experimental study of intramolecular vibrational relaxation (IVR) that reflects stochastization of the vibrational motion of the nuclei in polyatomic molecules (see Refs 397 – 399). Subsequently, with the appearance of lasers generating ultrashort pulses it became possible to use the methods of IR and Raman spectroscopies to study the IVR dynamics with picosecond and femtosecond time resolutions. A detailed analysis of the results obtained in this field can be found in the review.[400]

For simple diatomic molecule, the time-varying spectroscopic signals can be easily related to the molecular structural dynamics and wave packet dynamics.[72] But the situation becomes rapidly more complicated when the number of atoms increases so that the retrieval of structural dynamics information becomes a difficult task. This can be accounted for by the fact that optical spectroscopy probes valence electron states affecting many parts of the molecular system. Therefore, they are only indirectly and ambiguously related to nuclear subsystem dynamics, with the exception of some favorable occasions that can be studied by IR and Raman spectroscopies.[542 – 550] Hence, the necessity of alternative or auxiliary methods directly providing information on the structural dynamics, such as X-ray absorption fine structure (XAFS) methods that probe the X-ray absorption spectrum in the vicinity of absorption jumps of elements contained in the sample.[551, 552]

X-ray absorption spectra are known to have sharp edges that relate to the ionization of inner electron shells of atoms or ions. The photoelectrons generated by radiation near the absorption edges are scattered by the electron density shells of nearby atoms/ions, which gives rise to interferences that are observed as modulations in the X-ray absorption cross-section. The spectral modulations cover a range of ~40 eV about the absorption edge that may be at about 1000 eV, giving rise to what is known as XAFS spectra.[551, 552] Taking advantage of the well-developed state of XAFS theory, the X-ray absorption spectra are widely applied to structural analysis. Synchrotrons, which became available for research in the early 1970s, proved to be the most suitable radiation sources for such measurements. Since then, the theory and instrumentation for XAFS have rapidly developed.[551 – 553] Although XAFS methods enable the study of only short-range order, *i.e.*, structural features at distances shorter than the mean free path of a photoelectron in a sample, they attract much attention from materials science. XAFS can be applied to study matter in any aggregate state, and the measuring systems are very simple, requiring neither sophisticated goniometers nor vacuum equipment

The distant shell structures around the X-ray absorbing atoms can be resolved from both XAFS and XANES regions. From a photochemistry standpoint, as a molecule absorbs a photon in the ultraviolet (UV) to near-IR region, its valence electrons undergo a redistribution instantaneously to form the Franck – Condon (F – C) excited state. The molecule in this state experiences a new field caused by redistributed electrons while retaining the same nuclear structure as the ground state (Fig. 66). The atomic displacements at this stage are deemed to be coherent for molecules described by wave packet motions on an APES. Subsequently, the excited state molecules either reach an equilibrium at the bottom of the initial excited state APES with a new structure (q_{ES_1}) or cross to a APES of another excited state, then reach another equilibrated structure (q_{ES_2}), and subsequently transform themselves to product molecules.[553]

The distribution of an EXAFS signal can be mathematically inverted to derive the distribution function $g_{\alpha\beta}(r)$ of a pair of atoms α and β of the system in the direct space. Once the distribution functions for all elements in a liquid are known, it is possible to determine interatomic distances, coordination numbers, and the degree of local order around the atom of interest. Analysis of the near-threshold region by the XANES method is sensitive to oxidation states.[551, 552, 554] We note that the scattering atoms should not necessarily be chemically bound to the absorbing atom.

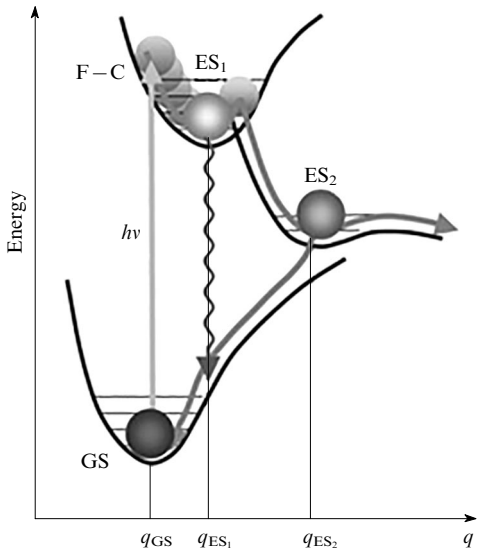


Figure 66. Generalized diagram showing typical excited state dynamics along reaction coordinates, where GS and ES stand for the ground and excited states, respectively, q is the reaction coordinate and F – C stands for the Franck – Condon excited state.[553] The impulsive excitation generates a coherent superposition of vibrational states that lead to coherent vibration wave packets weighted by the Franck – Condon factors and details of the excited-state surface. The excited state relaxes to the equilibrium at the bottom of the initial excited-state APES with a new structure (q_{ES_1}) or crosses to another excited state (q_{ES_2}), then as shown have a certain transition probability to the product channel.

The distance measurement error in this method is usually about ~1% within a 600 pm radius. However, the error in the measurement of the coordination number may be large and strongly depends on the system under study. Therefore, a comparison with other methods is highly desirable to aid the interpretation of EXAFS data. Because the fine structure being observed is related to the absorption edge of a concrete set of atoms and the absorption edge energy depends on the chemical element and the degree of its oxidation, the EXAFS method investigates the local structure around the element of interest in a given oxidation state. A study involving several absorbing elements of the sample provides more comprehensive and reliable structural information.[552] Because the EXAFS and XANES techniques yield local structural information,[551 – 553] they can be used to record a signal from local laser excitation. EXAFS provides quantitative structural information with subangstrom resolution with the aid of the so-called EXAFS equation,[555] whereas XANES brings quantitative information ('fingerprints') on the local geometry of a chemical bond, *i.e.*, orbital hybridization in the immediate proximity to the atom(s) of interest,[552] possibly facilitating the understanding of molecular dynamics in solutions where the solvent medium markedly affects the dynamics of the chemical reaction. Similar to TRXL,[463, 464, 556] X-ray absorption spectroscopy has been employed in time-resolved research.

A scheme with the use of a pump laser and an X-ray probe was applied in studies of charge transfer processes [410, 555, 557 – 560] and spin crossover [561, 562] in coordination compound chemistry, radical solvation dynamics [563] and the structural dynamics of intermediate photodissociation products in the liquid phase.[560, 564] The structural information obtained from X-ray absorption is limited to the local surroundings of a specific atom, unlike that obtained by diffraction methods that record signals of all the particles present in the scattering region. It is, however, an advantage of the EXAFS and XANES methods, since the locality of X-ray absorption ensures enhanced sensitivity. In other words, TRXL methods and time-resolved X-ray absorption spectroscopy are well complementary; their combination in the future may prove useful for obtaining more comprehensive and reliable information on the structural dynamics in solutions.

The time resolution in TRXL is currently limited by the length of X-ray pulses of synchrotron radiation (100 ps), but efforts are underway to extend it into the < 100 fs regime using FEL X-ray pulses.[565] This would make possible the study of atomic dynamics along the APES in real time, the formation and breaking of chemical bonds, and isomerization processes in the liquid phase. However, the employment of such short X-ray pulses is at variance with both the assumption of thermal equilibrium of a solute and the usage of hydrodynamic equations for a solvent.[464]

Suitable methods for detailed characterization of electronic excited states have been lacking until recent publication of Wernet *et al.*[346] as discussed above that combined the use of X-ray laser based femtosecond-resolution spectroscopy and advanced quantum chemical theory to probe the reaction dynamics.

The above discussion is given to simply point out the connection of other methods from optical, vibrational to variants of X-ray scattering provide additional information on structural dynamics. There is a whole suite of different variants to meet these ends. In addition to those discussed above, there are important emerging application for X-ray methods for probing chemical reaction dynamics [566] that take us from liquids to solid/liquid interfaces to chemical reactions and even gas phase reaction dynamics with sufficient brightness to follow even low scattering density systems.

XV. Theory: closing the loop

The main ideas in this section are an excerpt from Ref. 106. The experimental advances discussed above dictate the necessity of developing new theoretical methods for the analysis of structural data that is capable of treating observables derived from electron, optical, to X-ray sources. Each experimental method adds additional information to the problem in much the same way that additional information enables a solution of the inversion problem in image reconstruction or structural refinement. Here we are talking about additional information to reconstruct a many-body potential or dynamical refinement. The higher the information content the better we understand the reaction forces and can start to look for general features in the physics driving chemistry.

We need to further reinforce that there will only be a small subset of chemical reactions that are amenable to direct experimental observation of real time atomic motions for the reasons discussed above. There are precious few systems that can be prepared under barrrierless conditions. There are a much larger class of photochemical systems and one can expand the perturbative approach to T jump and fast mixing means to induce chemistry. The problem then reduces to trying to theoretically predict reaction intermediates. This approach is limited as the pathway to these transient structures is no better determined than it would be from static starting points.

Chemistry is all about controlling barrier heights to kinetically control the direction of chemical processes in competition with deleterious channels. It is therefore essential to directly observe the atomic motions or pathways over even a restricted set of reaction mechanisms. These experiments will serve as rigorous benchmarks to refine theoretical methods to ultimately enable extension to other areas of chemistry. The experimental observable is precisely the objective of the theoretical methods being developed for understanding reaction dynamics. It also interesting to note that theory is going through the same challenges as experiments to scale to higher levels of complexity to approach relevant timescales. While the experimentalists need a brighter source to atomically image reaction dynamics, the theoreticians need a 'brighter' code. The problem is to handle in a computationally efficient manner the electron correlation effects on reaction dynamics for larger and larger systems. The goal is to approach the scale of current interest in chemistry.

In this regard, there has been tremendous progress on the theory front that has enabled first principle calculations of excited state reaction dynamics without the Born – Oppenheimer approximation, which breaks down at CI's and other regions of avoided crossings. This important detail can be readily understood as the time scale for electronic redistribution within the two electronic surfaces depends inversely on the energy gap between the two surfaces coupled through nuclear fluctuations. The transmission probability is then given by the electronic coupling and the

relative time of nuclear passage or sampling of the critical point.

There is no longer a clear separation in time scales between the electronic and nuclear degrees of freedom such that the wave function can no longer be factored into electronic and nuclear terms, *i.e.*, the full time-dependent Schrödinger equation must be solved without the Born – Oppenheimer approximation. In order to keep computational costs for this level of theory reasonable, a reduced molecular model is used to approximate the system with the intramolecular and intermolecular generally treated classically in a quantum mechanics/molecular mechanics (QM/MM) formalism. As the truncated molecular model is an approach to simplify the problem, the bath coupling must also be approximated, normally at the lowest level, assuming linear vibrational coupling.

This approach has been used extensively for small-molecule systems ($N < 10$ atoms). The challenge lies in scaling this level of theory to larger systems that are relevant to the current level of synthetic chemistry ($N > 100$ atoms). Ideally, one would like to scale theoretical approaches up to the level of treating the photochemistry of biomolecules. The development of single-reference *ab initio* methods for the calculation of excited states, especially those that take advantage of the resolution-of-the-identity approximation is most notable.[567 – 569] This approach, also known as density fitting, increases the computation speed for calculating four-centre, two-electron integrals by an order-of-magnitude speed-up. This development has enabled quantitatively accurate excited-state calculations for systems as large as molecular clusters and nucleosides.[570, 571] The implementation of nonadiabatic coupling vectors and matrix elements between singlet excited states[572, 573] has enabled the application of some such methods to excited state to excited state internal conversion processes; however, the description of excited state to ground state crossings remains problematic.[574]

Even higher computational efficiency is possible by employing semiempirical electronic structure methods adapted to excited-state calculations,[575] such as the OM2/MRCI method.[576, 577] Though at the cost of parameterization against experimental and/or theoretical reference data. In particular, the OM2/MRCI method has been successfully applied to various photoinduced processes of large organic molecules (see, *e.g.*, Ref. 575 for an overview). It should be pointed out, however, that the range of applicability of this and other semiempirical methods is limited by inherent requirements of prior parametrization, and validation against suitable benchmarks for each specific system to be simulated. This limitation may no longer be so restricting if this approach can be bench marked against atomically resolved reaction dynamic, which is the main objective in all cases. We are seeing a great reduction in complexity to a few key modes in barrier-crossing regions. This simplification of the problem to a reduced modal basis should greatly favour the use of semiempirical methods with the establishment of a reaction mode basis for certain classes of chemical processes.

Another cornerstone of computational photochemistry is the use of QM/MM methods first introduced by Warshel and Levitt.[578] The idea is simple enough in that the main reaction site of the system is treated using a QM electronic structure method, while its surroundings is described using a classical MM calculation. The computational cost of an MM calculation is typically very low in comparison to a QM excited-state calculation. This difference enables the use of the QM/MM method for the simulation of photochemical reactions in large systems such as biomolecules and crystals. This approach will only be reasonable if the reaction can be considered as localized at a particular reaction site, defining a relatively small reaction volume — which as we have seen by the above discussion is the correct picture.

To date, the emphasis of theoretical treatments has been to obtain higher and higher levels of accuracy in the prediction of electronic states for comparison to spectroscopic variables. In this respect, each molecule has as unique electronic structure and excited state dynamics that reflects by definition the unique many-body potential of different molecules. The ultimate goal is to be able to accurately calculate the electronic structure and excited state dynamics for any given molecule. By extension, every molecule will have unique PESs requiring high dimensional analysis to get the reaction dynamics correct. The problem is that in the pursuit of rigour we have lost the prospect for unearthing generalities in reaction dynamics.[106] Based on the enormous success of the various name reactions in enabling the construction of virtually any imaginable molecule, one can deduce that there must be general relationships involved in directing chemistry. Further, these named reactions have been discovered over time using static structures and highly localized views of the minimal motions to connect reactant to product states.

The fact that chemistry reduces to a few key reaction modes has now been directly observed. More to the point, we now can directly observe the key motions and the amplitudes and relative correlations of these atomic motions. This information allows direct reconstruction of the barrier region, the near mythical region in nuclear configuration space (*i.e.*, the barrier) we wish to control. It is now absolutely clear now that this enormous reduction in dimensionality in the barrier-crossing region is what makes chemical concepts transferrable from one molecule to another.[106] There is a relatively simple bit of physics at play that we will miss if we don't focus on finding generalities in reaction dynamics as oppose to focusing on the uniqueness of each molecule. Again, given the enormous success again of synthetic probes and very simple pictures for the reaction pathway used by synthetic chemists, we don't need a high level of accuracy in terms of the reaction energetics. We just need to know what the key motions are to direct the chemistry at a given reaction site of interest. This information will allow synthetic means to lower the barrier height of this process. One only needs differential stabilization of the order of 0.05 eV to obtain an order of magnitude enhancement of reaction yields over competing processes. It is also equally important to realize that errors in the predicted electronic surfaces will affect the competing reaction pathways in equal measure. It is the relative difference in barrier heights that is most important not the absolute rate of crossing.

The new ability to directly observe the key reaction modes for even a limited number of reaction mechanisms will provide rigorous benchmarks for theory. The focus in this case should be on projecting out the modes that are most strongly coupled to the reaction coordinate rather than on absolute terms with respect to energetics or dynamics. This focus will likely enable the use of much more efficient coarse grain theories or semiempirical approaches to enable the formulation of a reaction mode basis for

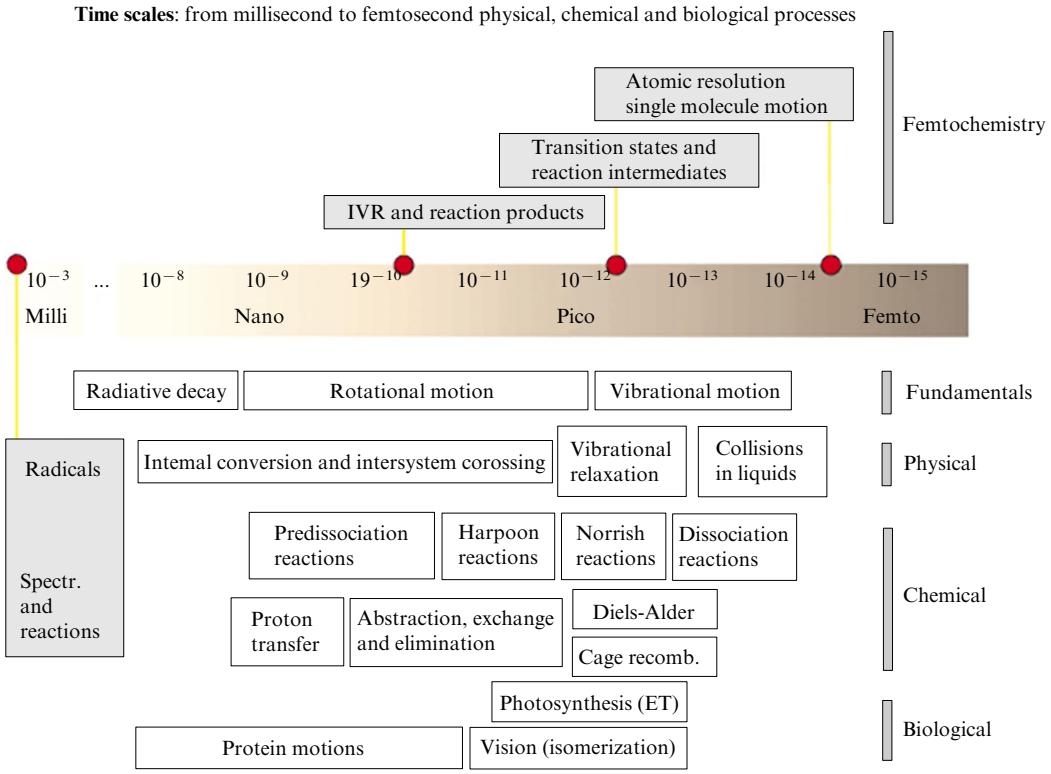


Figure 67. Time scales.[72, 115] The relevance to physical, chemical and biological changes. The fundamental limit of the vibrational motion defines the regime for femtochemistry. Examples are given for each change and scale. We note that the few femtosecond time scale demarcated for 'atomic resolution single molecule motion' needs to be revised to 'limit of sub-Å atomic motion of chemical bonds' not net rms single molecule motion, which is several orders of magnitude slower.

chemistry. This conceptual basis would represent a significant advance over current means of depicting the nuclear configuration of the barrier region and thereby significantly advance our ability to control barrier heights and associated chemistry. The few experimental cases where full atom-resolved chemical reactions are possible will provide the proving ground for developing these theoretical tools that can then be generalized to all chemistry. One can see a day in which theoretical tools will become available in which the key modes for a given class of molecules and chemical reaction mechanisms are used to construct the nuclear configuration of the barrier region and then rank order the proposed mechanism in relation to competing processes.[106] This approach will also afford a two-tier strategy in which the generalized motions per reaction class are used to predict a given reaction pathway which would then warrant higher level theoretical calculations to guide synthetic strategies in the event there was not sufficient contrast in the predicted barrier heights to give satisfactory yields.

The above strategy emphasizes reformulating chemistry in terms of a reaction mode basis to properly treat the far-from-equilibrium motions that lead to chemistry in much the same way we use normal (vibrational) modes to describe equilibrium fluctuations. In the case of thermal equilibrium fluctuations, we have vibrational spectroscopy to directly report on these motions. With the advent of ultrabright electron and X-ray sources, we now have similar direct observation of the highly anharmonic motions that lead to chemistry. The full breadth of chemical processes are shown in Fig. 67. The relevant time scales can all be interrelated through barrier distributions to the various processes with proper statistical weighting of the different interactions. The atomic view of chemistry that is now in hand will provide a grand unification of all these phenomena over all length and time scales. We are approaching a new way of thinking of chemistry in which the 'Structure – Dynamics – Function' triad is understood at the most fundamental level. It is this level of new insight that will ultimately allow us to create de nouvo molecular systems of greater complexity that will form the bridge from passive to active matter — at some point rivaling biological constructs.

XVI. Conclusions and future outlook

'Next, said I, compare our nature in respect of education and its lack to such an experience as this. Picture men dwelling in a sort of subterranean cavern with a long entrance open to the light on its entire width. Conceive them as having their legs and necks fettered from childhood, so that they remain in the same spot, able to look forward only, and prevented by the fetters from turning their heads. Picture further the light from a fire burning higher up and at a distance behind them, and between the fire and the prisoners and above them a road along which a low wall has been built, as the exhibitors of puppet shows have partitions before the men themselves, above which they show the puppets.'[225] (See Fig. 68).

Integration of electron optics and pulsed laser techniques into a single experimental layout provides an effective tool for research into the structural dynamics of matter with

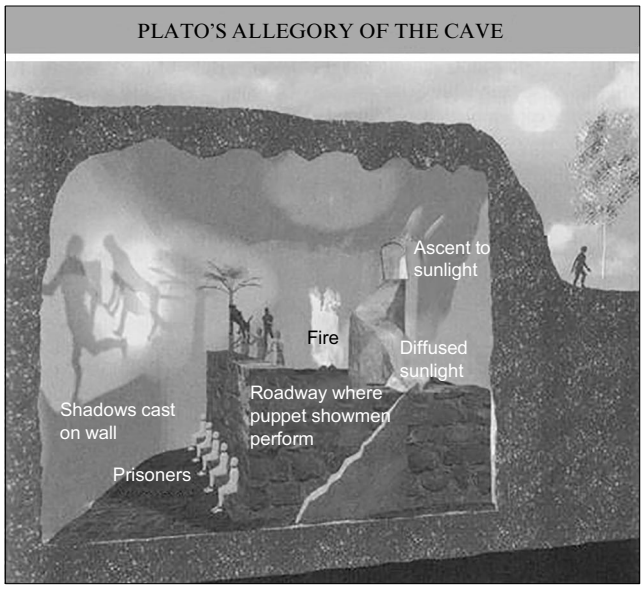


Figure 68. Plato's allegory of the Cave. Sun; Natural things; Shadows of natural things; Fire; Artificial objects; Shadows of artificial objects; Allegory level. 'Good' idea, Ideas, Light, Creatures and Objects, Image, Analogy of the Sun, and the Analogy of the Divided Line. (Picture from J.S. Fox 'Inside Plato's Cave', 2016: http://janetsfox.com/inside-platos-cave/).

high temporal and spatial resolution. The new techniques give rise to a very promising branch of modern physics and chemistry, advancing investigations in the 4D space-time continuum for a better understanding of both the dynamic properties of molecular systems with an intricate landscape of the PES and the mechanisms holds promise to provide a common understanding of diverse phenomena from chemical/biological process to larger length scales associated with phase transitions in condensed media, including full description of nanovolumes of solid particles.

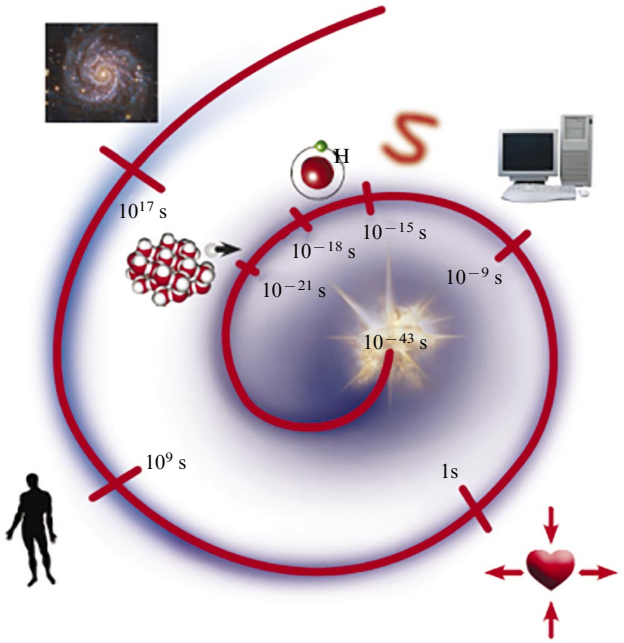


Figure 69. Characteristic time scales in nature and technology. The current age of the Universe is 14 billion years = 5×10^{17} s, the average human lifespan — 70 years = 2×10^{9} s, cardiac rhythm — 1 s, computer speed — 3×10^{-10} s, Terahertz pulse length — 10^{-12} s = 1 ps, light field oscillation period — 3×10^{-15} s = 3 fs, period of electron revolution about a proton in a hydrogen atom — 1.5×10^{-16} s = 150 as, strong nuclear interactions — 10^{-21} s = 1 zs, primeval fireball of the Big Bang (Planck time) — 10^{-43} s.[580]

A wide array of instruments is drawn into the study of natural and technological processes, depending on the characteristic time scales. By way of example, Fig. 69 shows typical time scales spanning an unprecedented 60 orders of magnitude, from the Big Bang (time scale corresponding to the strong nuclear interaction) to the period of electron revolutions about the nucleus (electron dynamics) to the age of the Universe.[579] We know at some level all these different length and time scales are interconnected. The problem is the sensitivity to initial conditions by which one may interconnect causally related events. In the molecular world, it is not possible to define a path from the big bang to the creation of any given molecule. In similar fashion, one can not connect the 'molecular big bang' or chemical reaction to the creation of a person or changes in the heavens. However, one can connect pathways and causal relationships from chemical events from femtoseconds onward as long as the reference length scales are of the mesoscale to microscale dimensions of living cells. This new ability to define the earliest possible moments in chemistry and biology allows a remarkable correlation of phenomena spanning over 15 decades in time and over 10 orders in length scales. We are seeing a convergence in which matter will be understood at the atomic level with sufficient information on the relevant length-times scales and fluctuating forces (PESs) governing atomic motions to predict material properties from first principles.

Much of what we have learned and expect to learn on this grand scale has been made possible with the extraordinary progress in the development of pulsed lasers. These pertubative approaches allow following nuclear to electron dynamics in real time. Today, a wide scope of research is being carried out on picosecond, femtosecond, and even subfemtosecond ranges: from registration of ultrafast processes of matter by spectroscopic techniques to primary processs of chemistry to electron transport characteristics of semiconductors to electron correlation effects responsible for collective phenomena and macroscopic material properties. One more application is the so-called Terahertz technology that gained new momentum with the advent of powerful commercial femtosecond lasers. This new pertubative source will enable direct excitation of bath modes to effectively achieve thermally driven chemistry on close to the primary timescales to open up all classes of chemistry, beyond photochemical processss.

Another important breakthrough with a high potential for practical application is the discovery of the possibility of controlling chemical reactions with femtochemical resolution, femtochemistry, with the involvement of ultrashort laser pulses tunable over a wide frequency range. This prospect will provide direct information on the quantumness of chemistry and will bring the wave-particle duality in describing atomic motions into sharp focus.

These advances are driven by the development of appropriate experimental facilities for ultrafast electron diffraction method and microscopy, which have made it possible to combine a spatial resolution of the order of 0.01 Å and

time resolution on the 100-fs time scale. We have now achieved the fundamental space-time resolution needed for following the primary processes directing chemical processes. There are still further gains to be made. Current machine physics concepts hold the potential to increase electron source brightness by a further two orders of magnitude with improved time resolution down to 10 fs and potentially attosecond time scale with electron bunch charges exceeding 10^6 electrons per pulse and transverse coherence lengths exceeding 10 nm. This level of source brightness with electrons is within reach and will allow quantum-limited mapping of atomic motions. In this limit, relative motions as small as 0.001 Å are possible, which would correspond to relative changes in energetics (force x distance) on the 10-meV range. This energy resolution is at the thermal limit for ambient conditions. These next-generation electron souces will enable space-time resolution, and energetics to be determined at the quantum limit for imaging chemistry. In the spirit that 'seeing is believing', Chemistry is about to go through a major revolution in conceptualization and a new level of mastery that will come with a truly atomic level understanding.

The reader may ask: Is it possible to extend ultrafast electron diffraction to the sub-atomic time scale (say, shorter than 1 as)? In principle, such studies can be conducted in the case of diffraction of isolated relativistic electrons scattered with a characteristic time of $\tau = D_{\mathrm{nucl}}/c = 10^{-22}-10^{-23}$ s. Under favorable conditions, the results may open up new possibilities for the investigation of the dynamics of extreme states of matter. This development will move us further up the time clock shown in Fig. 69. Naturally, the development of such new lines of research will require great efforts by both experimentalists and theorists, as well as considerable financial investments, let alone the proper experimental base. It can be expected that the success of these activities will depend on how effectively the methods and approaches from different fields of physics and technology are combined into a single experimental layout. We appear to be witnessing not only a new birth of electron microscopy but also its principally new achievements to come as it approaches a centenary of successful developments and wide practical applications.

Today, electron sources provide the principal possibility of studying the properties of matter in the space-time continuum exploiting short photoelectron beams. There are currently over 50 research laboratories all over the world experimenting or planning to experiment with ultrafast electron diffraction and a resurgence in the use of ultrabright electron beams in electron microscope platforms for single particle imaging as well as dynamics. The inherently short de Broglie wavelength of electrons at moderate to high energy electrons provides intrinsically the highest space-time resolution to bring our universe into sharp focus. We don't know what the future will bring — just that it will bright.

Acknowledgments

A.A.Ischenko acknowledges support by the RFBR Grant No. 16-29-1167 OFI_m and partial support by the Grant No. 14-22-02035 OFI_m. P.M.Weber acknowledges support by the National Science Foundation, Grant No. CBET-1336105, and the Army Research Office, Grant number W911NF-17-1-0256. A.A.Ischenko would like to the thank Dr. Yu.A.Zhabanov and A.A.Otlyotov for help in preparing this manuscript and providing figures and Dr. G.V.Fetisov for valuable discussions. R.J.Dwayne Miller would like to thank the Max Planck Society for support and Gastón Corthey, Stuart A.Hayes, Michał A.Kochmann, and María S.Grigera for help in preparing this manuscript and providing figures.

References

1. J C Polanyi, A H Zewail *Acc. Chem. Res.* **28** 119 (1995)
2. A H Zewail *Annu. Rev. Phys. Chem.* **57** 65 (2006)
3. A H Zewail *Science* **328** 187 (2010)
4. A H Zewail, J M Thomas *4D Electron Microscopy: Imaging in Space and Time* (London: Imperial College Press, 2010)
5. J D Ewbank, L Schäfer, A A Ischenko *J. Mol. Struct.* **524** 1 (2000)
6. A A Ischenko, G V Girichev, Y I Tarasov *Difraktsiya Elektronov: Struktura i Dinamika Svobodnykh Molekul i Kondensirovannogo Sostoyaniya Veshchestva* (Electron Diffraction: The Structure and Dynamics of Free Molecules and Condensed Matter) (Moscow: Fizmatlit, 2012)
7. A A Ischenko, S A Aseev, V N Bagratashvili, V Y Panchenko, E A Ryabov *Physics Uspehki* **57** 633 (2014)
8. A A Ischenko, S A Aseyev *Time Resolved Electron Diffraction: for Chemistry, Biology and Material Science* (San Diego, CA: Elsevier, 2014)
9. J R Dwyer, C T Hebeisen, R Ernstorfer, M Harb, V B Deyirmenjian, R E Jordan, R J Dwayne Miller *Philos. Trans. R. Soc. A* **364** 741 (2006)
10. R J Dwayne Miller *Annu. Rev. Phys. Chem.* **65** 583 (2014)
11. A A Ischenko, V V Golubkov, V P Spiridonov, A V Zgurskii, A S Akhmanov, M G Vabischevich, V N Bagratashvili *Appl. Phys. B* **32** 161 (1983)
12. A A Ischenko, V N Bagratashvili, V V Golubkov, V P Spiridonov, A V Zgurskii, A S Akhmanov *Moscow Univ. Chem. Bull., Ser 2, Chem.* **26** 140 (1985)
13. A A Ischenko, Y I Tarasov, V P Spiridonov, A V Zgurskii, in *The Structure and Properties of Molecules* (Ivanovo: Interuniversity Coolection of Scientific Papers, 1988) p. 63
14. M G Vabishchevich, A A Ischenko *Method of Studying the Kinetics of Fast Processes* USSR Certificate number 1679907. Registered in the State Register of Inventions of the USSR on May 22, 1991. Priority of invention October 14, 1988
15. R G W Norrish, G Porter *Nature (London)* **164** 658 (1949)
16. M P Minitti, J M Budarz, A Kirrander, J Robinson, T J Lane, D Ratner, K Saita, T Northey, B Stankus, V Cofer-Shabica, J Hastings, P M Weber *Faraday Discuss.* **171** 81 (2014)
17. T Ishikawa, S A Hayes, S Keskin, G Corthey, M Hada, K Pichugin, A Marx, J Hirscht, K Shionuma, K Onda, Y Okimoto, S-y Koshihara, T Yamamoto, H Cui, M Nomura, Y Oshima, M Abdel-Jawad, R Kato, R J Dwayne Miller *Science* **350** 1501 (2015)
18. A A Ischenko, V P Spiridonov, L Schäfer, J D Ewbank *J. Mol. Struct.* **300** 115 (1993)
19. C-Y Ruan, Y Murooka, R K Raman, R A Murdick, R J Worhatch, A Pell *Microsc. Microanal.* **15** 323 (2009)
20. P M Weber, S D Carpenter, T Lucza *Proc. SPIE* **2521** 23 (1995)
21. W E King, G H Campbell, A Frank, B Reed, J F Schmerge, B J Siwick, B C Stuart, P M Weber *J. Appl. Phys.* **97** 111101 (2005)
22. B J Siwick, J R Dwyer, R E Jordan, R J Dwayne Miller *Science* **302** 1382 (2003)
23. A A Ischenko, J D Ewbank, L Schafer *J. Phys. Chem.* **99** 15790 (1995)
24. G Sciaini, R J Dwayne Miller *Rep. Prog. Phys.* **74** 096101 (2011)
25. A A Ishchenko, V N Bagratashvili, A S Avilov *Crystallogr. Rep.* **56** 751 (2011)
26. D J Flannigan, A H Zewail *Acc. Chem. Res.* **45** 1828 (2012)

27. A A Ischenko, Yu I Tarasov, L Schäfer *Fine Chem. Technol.* **12** (2) 5 (2017)
28. S A Aseyev, P M Weber, A A Ischenko *JASMI* **3** 30 (2013)
29. A A Ischenko, Yu I Tarasov, L Schäfer *Fine Chem. Technol.* **12** (4) 5 (2017)
30. R J Dwayne Miller *Science* **343** 1108 (2014)
31. G H Campbell, J T McKeown, M K Santala *Appl. Phys. Rev.* **1** 041101 (2014)
32. K T Kim, D M Villeneuve, P B Corkum *Nat. Photon.* **8** 187 (2014)
33. A A Ischenko, L Schäfer, Yu I Tarasov, E A Ryabov, S A Aseyev *Fine Chem. Technol.* **12** (1) 5 (2017)
34. S Manz, A Casandruc, D Zhang, Y Zhong, R A Loch, A Marx, T Hasegawa, L C Liu, S Bayesteh, H Delsim-Hashemi, M Hoffmann, M Felber, M Hachmann, F Mayet, J Hirscht, S Keskin, M Hada, S W Epp, K Flottmann, R J Dwayne Miller *Faraday Discuss.* **177** 467 (2015)
35. M S Robinson, P D Lane, D A Wann *Rev. Sci. Instrum.* **86** 013109 (2015)
36. D A Plemmons, P K Suri, D J Flannigan *Chem. Mater.* **27** 3178 (2015)
37. P Zhu, Y Zhu, Y Hidaka, L Wu, J Cao, H Berger, J Geck, R Kraus, S Pjerov, Y Shen, R I Tobey, J P Hill, X J Wang *New J. Phys.* **17** 063004 (2015)
38. C Gerbig, A Senftleben, S Morgenstern, C Sarpe, T Baumert *New J. Phys.* **17** 043050 (2015)
39. M Centurion *J. Phys. B: At. Mol. Opt. Phys.* **49** 062002 (2016)
40. A L Buchachenko *Russ. Chem. Rev.* **68** 85 (1999)
41. A L Buchachenko, V L Berdinsky *Russ. Chem. Rev.* **73** 1033 (2004)
42. V A Nadtochenko, N N Denisov, V Y Gak, F E Gostev, A A Titov, O M Sarkisov, V V Nikandrov *Russ. Chem. Bull.* **51** 457 (2002)
43. I B Bersuker *Nouv. J. Chim.* **4** 139 (1980)
44. I B Bersuker *Teor. Eksp. Khim.* **16** 291 (1980)
45. A H Zewail *Faraday Discuss. Chem. Soc.* **91** 207 (1991)
46. S Pedersen, L Baåares, A H Zewail *J. Chem. Phys.* **97** 8801 (1992)
47. W H Miller *Annu. Rev. Phys. Chem.* **41** 245 (1990)
48. H J Foth, J C Polanyi, H H Telle *J. Phys. Chem.* **86** 5027 (1982)
49. A Aloi, R Tomass, in *Raman Spectroscopy and Applications* (Ed. K Maaz) (Rijeka: InTech, 2017) p. 269
50. D M Neumark *Annu. Rev. Phys. Chem.* **43** 153 (1992)
51. P R Brooks *Chem. Rev.* **88** 407 (1988)
52. E R Lovejoy, S K Kim, C B Moore *Science* **256** 1541 (1992)
53. R A Marcus *Science* **256** 1523 (1992)
54. M M Kreevoy, D Truhlar *Investigations of Rates and Mechanism of Reactions* (New York: Wiley, 1986)
55. P Pechukas *Annu. Rev. Phys. Chem.* **32** 159 (1981)
56. G Hose, H S Taylor, Y Y Bai *J. Chem. Phys.* **80** 4363 (1984)
57. B Hartke, J Manz, J Mathis *Chem. Phys.* **139** 123 (1989)
58. R M Hochstrasser *Pure Appl. Chem.* **52** 2683 (1980)
59. J Saltiel, Y-P Sun *Photochroism-Molecules and Systems* (Amsterdam: Elsevier, 1990)
60. E G Lewars *Computational Chemistry* (2nd Edn) (Dordrecht, Heidelberg: Springer, 2011)
61. T F George *J. Phys. Chem.* **86** 10 (1982)
62. B G Garrett, D G Truhlar, R S Grev, R B Walker *J. Chem. Phys.* **73** 235 (1980)
63. A M F Lau, in *Advances in Chemical Physics* (Eds K P Lawley) (Hoboken, NJ: Wiley, 1982) p. 191
64. J C Polanyi, A J McCaffery, J McCormack, A J Hynes, J H Brophy, P N Clough, J Johnston, P A Gorry, C V Nowikow, R Grice, D M Hirst, M F Jarrold, K Birkinshaw, M A D Fluendy, K P Lawley, D Sutton, G W Black, M S Child, J N L Connor, W Jakubetz, A Laganà, J Manz, J C Whitehead, J Allison, M A Johnson, R N Zare, D W Setser, H U Lee, R G Macdonald, J J Sloan, K F Freed, M Menzinger, A Tanin, J C Wong, A González Ureña, V J Herrero, F A Moleres, G C Schatz, M H Alexander, P J Dagdigian, D J Wren, P E Siska, D R Herschbach, K H Bowen, G W Liesegang *Faraday Discuss. Chem. Soc.* **67** 110 (1979)
65. A Gallagher, in *Physics of Electronic and Atomic Collisions* (Eds S Datz) (Amsterdam: North-Holland, 1982) p. 403
66. P R Brooks, R F Curl, T C Maguire *Ber. Bunsenges. Phys. Chem.* **86** 401 (1982)
67. J L Carlsten, A Szöke, M G Raymer *Phys. Rev. A* **15** 1029 (1977)
68. M C Castex *J. Chem. Phys.* **66** 3854 (1977)
69. M Dantus, M J Rosker, A H Zewail *J. Chem. Phys.* **87** 2395 (1987)
70. M J Rosker, M Dantus, A H Zewail *J. Chem. Phys.* **89** 6113 (1988)
71. M J Rosker, M Dantus, A H Zewail *Science* **241** 1200 (1988)
72. A H Zewail *The Nobel Prizes 1999 Les Prix Nobel: Nobel Prizes, Presentations, Biographies, and Lectures* (Stockholm: Almquiest & Wiksell Intl 2000)
73. N F Scherer, J L Knee, D D Smith, A H Zewail *J. Phys. Chem.* **89** 5141 (1985)
74. V V Eremin, I O Glebov *Theor. Math. Phys.* **153** 1463 (2007)
75. V V Poddubnyy, I O Glebov, V V Eremin *Theor. Math. Phys.* **178** 257 (2014)
76. E J Heller *Acc. Chem. Res.* **14** 368 (1981)
77. R L Sundberg, D Imre, M O Hale, J L Kinsey, R D Coalson *J. Phys. Chem.* **90** 5001 (1986)
78. M Shapiro, R Bersohn *J. Chem. Phys.* **73** 3810 (1980)
79. U Halavee, M Shapiro *Chem. Phys.* **21** 105 (1977)
80. A H Zewail *Femtochemistry: Ultrafast Dynamics of the Chemical Bond* (Teaneck, NJ, Singapore: World Scientific, 1994)
81. A A Ischenko, P M Weber, R J Dwayne Miller *Chem. Rev.* **117** 11066 (2017)
82. I O Glebov, V V Eremin *Russ. J. Phys. Chem. A* **82** 586 (2008)
83. G A Worth, L S Cederbaum *Annu. Rev. Phys. Chem.* **55** 127 (2004)
84. A H Zewail *Pure Appl. Chem.* **72** 2219 (2000)
85. C C Pemberton, Y Zhang, K Saita, A Kirrander, P M Weber *J. Phys. Chem. A* **119** 8832 (2015)
86. V I Prokhorenko, A Picchiotti, M Pola, A G Dijkstra, R J Dwayne Miller *J. Phys. Chem. Lett.* **7** 4445 (2016)
87. M P Minitti, J M Budarz, A Kirrander, J S Robinson, D Ratner, T J Lane, D Zhu, J M Glownia, M Kozina, H T Lemke, M Sikorski, Y Feng, S Nelson, K Saita, B Stankus, T Northey, J B Hastings, P M Weber *Phys. Rev. Lett.* **114** 255501 (2015)
88. R G McKinlay, J M Zurek, M J Paterson *Theoretical and Computational Inorganic Chemistry* (London, Amsterdam, Burlington, San Diego: Academic Press, 2010)
89. J von Neumann, E P Wigner *Phys. Zeitschr.* **30** 467 (1929)
90. E Teller *Isr. J. Chem.* **7** 227 (1969)
91. M A Robb, M Garavelli, M Olivucci, F Bernardi, in *Reviews in Computational Chemistry* (Eds K B Lipkowitz, D B Boyd) (New York: Wiley, 2000) p. 87
92. M J Paterson, M J Bearpark, M A Robb, L Blancafort, G A Worth *Phys. Chem. Chem. Phys.* **7** 2100 (2005)
93. N M S Almeida, R G McKinlay, M J Paterson, in *Computational Studies in Organometallic Chemistry (Structure and Bonding)* Vol. 167 (Eds S A Macgregor, O Eisenstein) (Cham: Springer Int. Publ., 2016) p. 107
94. I B Bersuker *The Jahn–Teller Effect: A Bibliographic Review* (New York: Plenum, 1984)
95. I B Bersuker *The Jahn-Teller Effect and Vibronic Interactions in Modern Chemsitry (Modern Inorganic Chemistry)* (Ed J P Fackler) (New York: Plenum, 1984)
96. I B Bersuker *Chem. Rev.* **101** 1067 (2001)
97. I B Bersuker *Chem. Rev.* **113** 1351 (2013)
98. D Zhong, E W-G Diau, T M Bernhardt, S De Feyter, J D Roberts, A H Zewail *Chem. Phys. Lett.* **298** 129 (1998)

99. M Chachisvilis, A H Zewail *J. Phys. Chem. A* **103** 7408 (1999)
100. E W-G Diau, S De Feyter, A H Zewail *J. Chem. Phys. A* **110** 9785 (1999)
101. S C Althorpe, G A Worth *Quantum Dynamics at Conical Intersections* [Daresbury: Daresbury Laboratory, Warrington: Collaborative Computational Project on Molecular Quantum Dynamics (CCP6), 2004]
102. H Köuppel, W Domcke, L S Cederbaum, in *Advances in Chemical Physics* (Eds I Prigogine, S A Rice) Vol. 57 (New York: Wiley, 1984) p. 59
103. D R Yarkony *Rev. Mod. Phys.* **68** 985 (1996)
104. M S Child, in *The Role of Degenerate States in Chemistry (Advances in Chemical Physics)* Vol.124 (Eds M Baer, G D Billing) (New York: Wiley, 2002) p. 1
105. W Domcke, D R Yarkony, H Köppel *Conical Intersections: Electronic Structure, Dynamics and Spectroscopy* (Singapore: World Scientific, 2004)
106. R J Dwayne Miller *Farad. Discuss.* **194** 777 (2016)
107. R A Bonham, M Fink *High Energy Electron Scattering* (New York: Van Nostrand Reinhold, 1974)
108. I Hargittai, M Hargittai *Stereochemical Applications of Gas-Phase Electron Diffraction* (New York: VCH, 1988)
109. A A Ischenko, L Schäfer, J D Ewbank *J. Mol. Struct.* **376** 157 (1996)
110. P Debye *J. Chem. Phys.* **9** 55 (1941)
111. C Cohen-Tannoudji, B Diu, F Laloe *Quantum Mechanics* (New York: Wiley-Interscience, 1987)
112. J D Ewbank, L Schäfer, A A Ischenko *J. Mol. Struct.* **321** 265 (1994)
113. A N Tikhonov, A V Goncharsky, V V Stepanov, A G Yagola *Numerical Methods for the Solution of Ill-Posed Problems* (Netherlands: Springer, 1995)
114. A N Tikhonov, A S Leonov, A G Yagola *Non-Linear Ill-Posed Problems* (Netherlands: Springer, 1998)
115. A H Zewail *J. Phys. Chem.* **100** 12701 (1996)
116. A H Zewail *J. Phys. Chem. A* **104** 5660 (2000)
117. J S Baskin, A H Zewail *ChemPhysChem* **6** 2261 (2005)
118. S Ryu, R M Stratt, P M Weber *J. Phys. Chem. A* **107** 6622 (2003)
119. S Ryu, R M Stratt, K K Baeck, P M Weber *J. Phys. Chem. A* **108** 1189 (2004)
120. S Ryu, P M Weber, R M Stratt *J. Chem. Phys.* **112** 1260 (2000)
121. J C Williamson, A H Zewail *J. Phys. Chem.* **98** 2766 (1994)
122. K Hoshina, K Yamanouchi, T Ohshima, Y Ose, H Todokoro *Chem. Phys. Lett.* **353** 27 (2002)
123. K Hoshina, K Yamanouchi, T Ohshima, Y Ose, H Todokoro *J. Chem. Phys.* **118** 6211 (2003)
124. J C H Spence, R B Doak *Phys. Rev. Lett.* **92** 198102 (2004)
125. J P Bergsma, M H Coladonato, P M Edelsten, J D Kahn, K R Wilson, D R Fredkin *J. Chem. Phys.* **84** 6151 (1986)
126. R N Zare *Angular Momentum: Understanding Spatial Aspects in Chemistry and Physics* (New York: Wiley, 1988)
127. S E Choi, R B Bernstein *J. Chem. Phys.* **85** 150 (1986)
128. I S Gradshtein, I M Ryzhik *Tables of Integrals, Series, and Products* (New York: Academic Press, 1965)
129. M Abramowitz, I A Stegun *Handbook of Mathematical Functions with Formulas, Graphs, and Mathematical Tables (Appl. Math. Ser. 55)* (Washington, DC: National Bureau of Standards, 1965)
130. S I Vetchinkin, A S Vetchinkin, V V Eryomin, I M Umanskii *Chem. Phys. Lett.* **215** 11 (1993)
131. V V Eryomin, N E Kuz'menko, I M Umanskii *Khim. Fiz.* **15** 5 (1996)
132. R Kosloff *J. Phys. Chem.* **92** 2087 (1988)
133. R Kosloff, S A Rice, P Gaspard, S Tersigni, D J Tannor *Chem. Phys.* **139** 201 (1989)
134. G G Balint-Kurti, R N Dixon, C Clay Marston *Int. Rev. Phys. Chem.* **11** 317 (1992)
135. C Clay Marston, G G Balint-Kurti *J. Chem. Phys.* **91** 3571 (1989)
136. A N Tikhonov, V Y Arsenin *Metody Resheniya Nekorrektnykh Zadach* (Methods of Solution of Ill-posed Problems) (Moscow: Nauka, 1979)
137. K Miller *SIAM J. Appl. Math.* **18** 346 (1970)
138. K Miller, G A Viano *J. Math. Phys.* **14** 1037 (1973)
139. M Bertero, C De Mol, G A Viano, in *Inverse Scattering Problems in Optics (Topics in Current Physics)* Vol. 20 (Eds H P Baltes) (Berlin, Heidelberg: Springer, 1980) p. 161
140. T Ho, H Rabitz *J. Chem. Phys.* **90** 1519 (1989)
141. T S Ho, H Rabitz *J. Phys. Chem.* **97** 13447 (1993)
142. X Zou, S Hovmöller, P Oleynikov *Electron Crystallography: Electron Microscopy and Electron Diffraction (International Union of Crystallography Texts on Crystallography)* Book 16 (Oxford, New York: Oxford University Press, 2011)
143. I I Vorontsov, P Coppens *J. Synchrotron Radiat.* **12** 488 (2005)
144. M Gao, PhD Thesis, University of Toronto, Toronto, 2014
145. E J Kirkland *Advanced Computing in Electron Microscopy* (2nd Edn) (New York: Springer 2010)
146. I I Vorontsov, T Graber, A Y Kovalevsky, I V Novozhilova, M Gembicky, Y-S Chen, P Coppens *J. Am. Chem. Soc.* **131** 6566 (2009)
147. M Walczak, H Grubmüller *Comput. Phys. Commun.* **201** 159 (2016)
148. I V Rubtsov, D V Khudiakov, V A Nadtochenko, A S Lobach, A P Moravskii *Chem. Phys. Lett.* **229** 517 (1994)
149. I V Rubtsov, D V Khudiakov, A P Moravskii, V A Nadtochenko *Chem. Phys. Lett.* **249** 101 (1996)
150. A M Shakhov, A A Astafiev, D O Plutenko, O M Sarkisov, A I Shushin, V A Nadtochenko *J. Phys. Chem. C* **119** 12562 (2015)
151. A Stolow, J G Underwood, in *Advances in Chemical Physics* Vol. 139 (Eds S A Rice) (Hoboken, NJ: Wiley, 2008) p. 497
152. S Schneider *Ber. Bunsenges. Phys. Chem.* **99** 1447A (1995)
153. P M Felker, A H Zewail, in *Advances in Chemical Physics: Evolution of Size Effects in Chemical Dynamics* Pt. 1, Vol. 70 (Eds I Prigogine, S A Rice) (New York: Wiley, 1988) p. 265
154. P M Felker, A H Zewail, in *Femtosecond Chemistry* (Eds J Manz, L Wöste) (Weinheim, New York: Wiley-VCH, 1995) p. 193
155. L R Khundkar, A H Zewail *Annu. Rev. Phys. Chem.* **41** 15 (1990)
156. Q Liu, A H Zewail *J. Phys. Chem.* **97** 2209 (1993)
157. M Dantus, M J Rosker, A H Zewail *J. Chem. Phys.* **89** 6128 (1988)
158. M Dantus, R M Bowman, A H Zewail *Nature (London)* **343** 737 (1990)
159. M Dantus, S B Kim, J C Williamson, A H Zewail *J. Phys. Chem.* **98** 2782 (1994)
160. M J Rosker, T S Rose, A H Zewail *Chem. Phys. Lett.* **146** 175 (1988)
161. T S Rose, M J Rosker, A H Zewail *J. Chem. Phys.* **88** 6672 (1988)
162. T S Rose, M J Rosker, A H Zewail *J. Chem. Phys.* **91** 7415 (1989)
163. P Cong, A Mokhtari, A H Zewail *Chem. Phys. Lett.* **172** 109 (1990)
164. D H Semmes, J S Baskin, A H Zewail *J. Chem. Phys.* **92** 3359 (1990)
165. D M Willberg, M Gutmann, J J Breen, A H Zewail *J. Chem. Phys.* **96** 198 (1992)
166. *Femtosecond Chemistry* (Eds J Manz, L Wöste) (Weinheim: Wiley-VCH, 1995)
167. A A Ischenko, J D Ewbank, L Schäfer *J. Phys. Chem.* **98** 4287 (1994)
168. A A Ischenko, L Schäfer, J Y Luo, J D Ewbank *J. Phys. Chem.* **98** 8673 (1994)
169. D Rapp, T Kassal *Chem. Rev.* **69** 61 (1969)
170. R D Levine, R B Bernstein *Molecular Reaction Dynamics* (New York: Oxford University Press, 1974)

171. G Herzberg *Electronic Spectra and Electronic Structure of Polyatomic Molecules* (New York: Van Nostrand, 1966)
172. H Bony, M Shapiro, A Yogev *Chem. Phys. Lett.* **107** 603 (1984)
173. I Levy, M B Shapiro, P Brumer *J. Chem. Phys.* **93** 2493 (1990)
174. M S Child, R B Bernstein *J. Chem. Phys.* **59** 5916 (1973)
175. I Bialynicki-Birula, M Cieplak, J Kaminski *Theory of Quanta* (New York: Oxford University Press, 1992)
176. B M Garraway, K A Suominen *Rep. Prog. Phys.* **58** 365 (1995)
177. E J Heller *J. Chem. Phys.* **62** 1544 (1975)
178. E J Heller, in *Potential Energy Surfaces and Dynamics Calculations for Chemical Reactions and Molecular Energy Transfer* (Ed. D Truhlar) (New York: Plenum, 1981) p. 103
179. E J Heller *Phys. Rev. A* **35** 1360 (1987)
180. A A Ischenko, J D Ewbank, L Schäfer *J. Mol. Struct.* **320** 147 (1994)
181. P Morse, H Feshbach *Methods of Theoretical Physics* (New York, Tokyo: McGraw-Hill, Kogakusha, 1953)
182. E C Kemble *The Fundamental Principles of Quantum Mechanics* (New York, London: McGraw-Hill, 1937)
183. R A Marcus *Chem. Phys. Lett.* **7** 525 (1970)
184. R B Shirts *J. Phys. Chem.* **91** 2258 (1987)
185. M Shapiro *J. Chem. Phys.* **56** 2582 (1972)
186. M Shapiro, G G Balint-Kurti *J. Chem. Phys.* **71** 1461 (1979)
187. R S Berry, in *Alkali Halide Vapors: Structure, Spectra, and Reaction Dynamics* (Eds P Davidovits, D L McFadden) (New York: Academic Press, 1979) p. 77
188. V Engel, H Metiu *J. Chem. Phys.* **91** 1596 (1989)
189. V Engel, H Metiu, R Almeida, R A Marcus, A H Zewail *Chem. Phys. Lett.* **152** 1 (1988)
190. S-Y Lee, W T Pollard, R A Mathies *J. Chem. Phys.* **90** 6146 (1989)
191. S E Choi, J C Light *J. Chem. Phys.* **90** 2593 (1989)
192. J Alvarellos, H Metiu *J. Chem. Phys.* **88** 4957 (1988)
193. J R Waldeck, M Shapiro, R Bersohn *J. Chem. Phys.* **99** 5924 (1993)
194. L Landau *Phys. Z. Sowjetunion* **2** 1 (1932)
195. C Zener *Proc. R. Soc. London Ser. A* **137** 696 (1932)
196. G G Balint-Kurti, M Shapiro *Chem. Phys.* **61** 137 (1981)
197. G G Balint-Kurti, R N Dixon, C Clay Marston *J. Chem. Soc. Faraday Trans.* **86** 1741 (1990)
198. G G Balint-Kurti, C L Ward, C Clay Marston *Comput. Phys. Commun.* **67** 285 (1991)
199. F Góğtas, G G Balint-Kurti, C Clay Marston *QCPE Bull.* **14** 19 (1994)
200. A Vibók, G G Balint-Kurti *J. Phys. Chem.* **96** 8712 (1992)
201. J D Geiser, P M Weber *J. Chem. Phys.* **108** 8004 (1998)
202. A A Ischenko, L Shäfer, J D Ewbank, in *Time-Resolved Diffraction* (Eds J R Helliwell, P M Rentzepis) (Oxford: Oxford University Press, 1997) p. 323
203. C Vallance *Phil. Trans. R. Soc. A* **362** 2591 (2004)
204. M N R Ashfold, N H Nahler, A J Orr-Ewing, O P J Vieuxmaire, R L Toomes, T N Kitsopoulos, I A Garcia, D A Chestakov, S-M Wu, D H Parker *Phys. Chem. Chem. Phys.* **8** 26 (2006)
205. R Neutze, R Wouts, D van der Spoel, E Weckert, J Hajdu *Nature (London)* **406** 752 (2000)
206. J M Budarz, M P Minitti, D V Cofer-Shabica, B Stankus, A Kirrander, J B Hastings, P M Weber *J. Phys. B: At. Mol. Opt. Phys.* **49** 034001 (2016)
207. L E Ballentine *Quantum Mechanics* (Englewood Cliffs, New Jersey: Prentice Hall, 1990)
208. E P Wigner *Perspectives in Quantum Theory* (Dover, New York, 1979)
209. M Hillery, R F O'Connell, M O Scully, E P Wigner *Phys. Rep.* **106** 121 (1984)
210. K E Cahill, R J Glauber *Phys. Rev.* **177** 1882 (1969)
211. E Freenberg, PhD Thesis, Harvard University, Cambridge, MA, 1933
212. S Weigert *Phys. Rev. A* **53** 2078 (1996)
213. J C Williamson, J Cao, H Ihee, H Frey, A H Zewail *Nature (London)* **386** 159 (1997)
214. H Ihee, V A Lobastov, U M Gomez, B M Goodson, R Srinivasan, C-Y Ruan, A H Zewail *Science* **291** 458 (2001)
215. H Ihee, J Cao, A H Zewail *Chem. Phys. Lett.* **281** 10 (1997)
216. D J Tannor, S A Rice *J. Chem. Phys.* **83** 5013 (1985)
217. Y J Yan, S Mukamel *Phys. Rev. A* **41** 6485 (1990)
218. Y J Yan, R E Gillilan, R M Whitnell, K R Wilson, S Mukamel *J. Phys. Chem.* **97** 2320 (1993)
219. J L Krause, R M Whitnell, K R Wilson, Y J Yan *J. Chem. Phys.* **99** 6562 (1993)
220. J L Krause, R M Whitnell, K R Wilson, Y Yan, in *Femtosecond Chemistry* (Eds J Manz, L Wöste) (Weinheim, New York: VCH, 1995) p. 743
221. J L Krause, K J Schafer, M Ben-Nun, K R Wilson *Phys. Rev. Lett.* **79** 4978 (1997)
222. V V Lozovoy, S A Antipin, F E Gostev, A A Titov, D G Tovbin, O M Sarkisov, A S Vetchinkin, S Yu Umanskii *Chem. Phys. Lett.* **284** 221 (1998)
223. V V Lozovoy, O M Sarkisov, A S Vetchinkin, S Yu Umanskii *Chem. Phys.* **243** 97 (1999)
224. O M Sarkisov, F E Gostev, V V Lozovoy, E A Sviridenkov, A A Titov, D G Tovbin, S Yu Umansky *Russ. Chem. Bull.* **45** 553 (1996)
225. Plato *Republic, Book VII* (Cambridge, MA: Harvard University Press, 1935)
226. U Leonhardt *Measuring the Quantum State of Light* (Cambridge, MA: Cambridge University Press, 1997)
227. A A Ischenko *Izv. Vyssh. Uchebn. Zaved., Khim. Khim. Tekhnol.* **52** 58 (2009)
228. F Natterer *The Mathematics of Computerized Tomography* (Chichester, New York: Wiley, 1986)
229. U Leonhardt *Phys. Rev. A* **53** 2998 (1996)
230. M Munroe, D Boggavarapu, M E Anderson, M G Raymer *Phys. Rev. A* **52** R924 (1995)
231. S R de Groot, L G Suttorp *Foundations of Electrodynamics* (Amsterdam: Norh-Holland, 1972)
232. Th Richter *Phys. Lett. A* **211** 327 (1996)
233. Th Richter *J. Opt. B Quantum Semiclassical Opt.* **1** 650 (1999)
234. Th Richter, A Wünsche *Acta Phys. Slovaca* **46** 487 (1996)
235. U Leonhardt, M Munroe, T Kiss, Th Richter, M G Raymer *Opt. Commun.* **127** 144 (1996)
236. U Leonhardt, M G Raymer *Phys. Rev. Lett.* **76** 1985 (1996)
237. U Leonhardt, S Schneider *Phys. Rev. A* **56** 2549 (1997)
238. U Leonhardt *Science* **312** 1777 (2006)
239. A Messiah *Quantum Mechanics* (Amsterdam: North-Holland Publ. Comp., 1965)
240. A A Ischenko, L Schäfer, J D Ewbank *Proc. SPIE* **3516** 580 (1999)
241. J D Ewbank, W L Faust, J Y Luo, J T English, D L Monts, D W Paul, Q Dou, L Schäfer *Rev. Sci. Instrum.* **63** 3352 (1992)
242. J C Williamson, M Dantus, S B Kim, A H Zewail *Chem. Phys. Lett.* **196** 529 (1992)
243. J D Ewbank, J Y Luo, J T English, R Liu, W L Faust, L Schäfer *J. Phys. Chem.* **97** 8745 (1993)
244. R R Sadeghi, S R Gwaltney, J L Krause, R T Skodje, P M Weber *J. Chem. Phys.* **107** 6570 (1997)
245. T R Todd, W B Olson *J. Mol. Spectrosc.* **74** 190 (1979)
246. W-B Tzeng, H-M Yin, W-Y Leung, J Y Luo, S Nourbakhsh, G D Flesch, C Y Ng *J. Chem. Phys.* **88** 1658 (1988)
247. Y-P Chang, D A Horke, S Trippel, J Küpper *Int. Rev. Phys. Chem.* **34** 557 (2015)
248. B A Zon, B G Katsnel'son *Sov. Phys. JETP* **42** 595 (1976)
249. B Friedrich, D Herschbach *Phys. Rev. Lett.* **74** 4623 (1995)
250. H Stapelfeldt, T Seideman *Rev. Mod. Phys.* **75** 543 (2003)
251. D M Villeneuve, S A Aseyev, P Dietrich, M Spanner, M Y Ivanov, P B Corkum *Phys. Rev. Lett.* **85** 542 (2000)
252. D M Villeneuve, S A Aseyev, A Avery, P B Corkum *Appl. Phys. B* **74** s157 (2002)

253. A Korobenko, A A Milner, V Milner *Phys. Rev. Lett.* **112** 113004 (2014)
254. C J Hensley, J Yang, M Centurion *Phys. Rev. Lett.* **109** 133202 (2012)
255. P-M Weber, R-C Dudek, S Ryu, R-M Stratt, in *Femtochemistry and Femtobiology: Ultrafast Events in Molecular Science* (Eds M M Martin, J T Hynes) (Amsterdam: Elsevier, 2004) p. 19
256. D Shorokhov, S T Park, A H Zewail *ChemPhysChem* **6** 2228 (2005)
257. C-Y Ruan, V A Lobastov, R Srinivasan, B M Goodson, H Ihee, A H Zewail *Proc. Natl. Acad. Sci. USA* **98** 7117 (2001)
258. R C Dudek, P M Weber *J. Phys. Chem. A* **105** 4167 (2001)
259. G Ravindra Kumar, C P Safvan, F A Rajgara, D Mathur *Chem. Phys. Lett.* **217** 626 (1994)
260. S Banerjee, G Ravindra Kumar, D Mathur *J. Phys. B: At. Mol. Opt. Phys.* **32** 4277 (1999)
261. D Mathur, V R Bhardwaj, P Gross, G Ravindra Kumar, F A Rajgara, C P Safvan, K Vijayalakshmi *Laser Phys.* **7** 829 (1997)
262. A Iwasaki, A Hishikawa, K Yamanouchi *Chem. Phys. Lett.* **346** 379 (2001)
263. D Townsend, H Satzger, T Ejdrup, A M D Lee, H Stapelfeldt, A Stolow *J. Chem. Phys.* **125** 234302 (2006)
264. V Kumarappan, L Holmegaard, C Martiny, C B Madsen, T K Kjeldsen, S S Viftrup, L B Madsen, H Stapelfeldt *Phys. Rev. Lett.* **100** 093006 (2008)
265. T Fuji, Y-I Suzuki, T Horio, T Suzuki *Chem. Asian J.* **6** 3028 (2011)
266. C Z Bisgaard, O J Clarkin, G Wu, A M D Lee, O Gessner, C C Hayden, A Stolow *Science* **323** 1464 (2009)
267. P Hockett, C Z Bisgaard, O J Clarkin, A Stolow *Nat. Phys.* **7** 612 (2011)
268. K Wang, V McKoy, P Hockett, M S Schuurman *Phys. Rev. Lett.* **112** 113007 (2014)
269. J Yang, V Makhija, V Kumarappan, M Centurion *Struct. Dyn.* **1** 044101 (2014)
270. J C H Spence, K Schmidt, J S Wu, G Hembree, U Weierstall, B Doak, P Fromme *Acta Crystallogr. Sect. A* **61** 237 (2005)
271. R Srinivasan, J S Feenstra, S T Park, S Xu, A H Zewail *Science* **307** 558 (2005)
272. P Reckenthaeler, M Centurion, W Fuß, S A Trushin, F Krausz, E E Fill *Phys. Rev. Lett.* **102** 213001 (2009)
273. M Centurion, P Reckenthaeler, F Krausz, E Fill *J. Mol. Struct.* **978** 141 (2010)
274. J Yang, J Beck, C J Uiterwaal, M Centurion *Nat. Commun.* **6** 8172 (2015)
275. M Kalal, K Nugent *Appl. Opt.* **27** 1956 (1988)
276. D M Dennison, N Wright *Phys. Rev.* **38** 2077 (1931)
277. D M Dennison *Phys. Rev.* **41** 304 (1932)
278. L Holmegaard, S S Viftrup, V Kumarappan, C Z Bisgaard, H Stapelfeldt, E Hamilton, T Seideman *Phys. Rev. A* **75** 051403 (2007)
279. T van Oudheusden, P L E M Pasmans, S B van der Geer, M J de Loos, M J van der Wiel, O J Luiten *Phys. Rev. Lett.* **105** 264801 (2010)
280. P Zhang, J Yang, M Centurion *New J. Phys.* **16** 083008 (2014)
281. F M Rudakov, J B Hastings, D H Dowell, J F Schmerge, P M Weber *AIP Conf. Proc.* **845** 1287 (2006)
282. J B Hastings, F M Rudakov, D H Dowell, J F Schmerge, J D Cardoza, J M Castro, S M Gierman, H Loos, P M Weber *Appl. Phys. Lett.* **89** 184109 (2006)
283. P Musumeci, J T Moody, C M Scoby *Ultramicroscopy* **108** 1450 (2008)
284. P Zhu, H Berger, J Cao, J Geck, Y Hidaka, R Kraus, S Pjerov, Y Shen, R I Tobey, Y Zhu, J P Hill, X J Wang *arXiv:1304.5176 [physics.ins-det]* (2013)
285. L Schäfer, A A Ischenko, Y A Zhabanov, A A Otlyotov, G V Girichev *Izv. Vyssh. Uchebn. Zaved., Khim. Khim. Tekhnol.* **60** 4 (2017)
286. S Deb, P M Weber *Annu. Rev. Phys. Chem.* **62** 19 (2011)
287. B C Arruda, R J Sension *Phys. Chem. Chem. Phys.* **16** 4439 (2014)
288. R B Woodward, R Hoffman *The Conservation of Orbital Symmetry* (Weinheim: Verlag Chemie, 1970)
289. D C Clary, A J H M Meijer *J. Chem. Phys.* **116** 9829 (2002)
290. G Dallinga, M L H Toneman *J. Mol. Struct.* **1** 11 (1967)
291. M Traetteberg *Acta Chem Scand.* **22** 2305 (1968)
292. H Oberhammer, S H Bauer *J. Am. Chem. Soc.* **91** 10 (1969)
293. D Autrey, J Choo, J Laane *J. Phys. Chem. A* **105** 10230 (2001)
294. M Merchán, L Serrano-Andrés, L S Slater, B O Roos, R McDiarmid, X Xing *J. Phys. Chem. A* **103** 5468 (1999)
295. T Mori, S Kato *Chem. Phys. Lett.* **476** 97 (2009)
296. A Li, S Yuan, Y Dou, Y Wang, Z Wen *Chem. Phys. Lett.* **478** 28 (2009)
297. H Ihee, J Cao, A H Zewail *Angew. Chem. Int. Ed.* **40** 1532 (2001)
298. H Ihee, J Cao, A H Zewail *Angew. Chem.* **113** 1580 (2001)
299. F Rudakov, P M Weber *Chem. Phys. Lett.* **470** 187 (2009)
300. A Nenov, P Kölle, M A Robb, R de Vivie-Riedle *J. Org. Chem.* **75** 123 (2010)
301. M Garavelli, C S Page, P Celani, M Olivucci, W E Schmid, S A Trushin, W Fuss *J. Phys. Chem. A* **105** 4458 (2001)
302. N Kuthirummal, F M Rudakov, C L Evans, P M Weber *J. Chem. Phys.* **125** 133307 (2006)
303. H T Philipp, M Hromalik, M Tate, L Koerner, S M Gruner *Nucl. Instr. Meth. Phys. Res. A* **649** 67 (2011)
304. M Ben-Nun, T J Martínez, P M Weber, K R Wilson *Chem. Phys. Lett.* **262** 405 (1996)
305. C P J Barty, M Ben-Nun, T Guo, F Ráksi, C Rose-Petruck, J Squier, K R Wilson, V V Yakovlev, P Weber, Z Jiang, A Ikhlef, in *Time-Resolved Diffraction* (Eds J R Helliwell, P M Rentzepis) (Oxford, MS: Oxford University Press, 1997) p. 44
306. M Ben-Nun, J Cao, K R Wilson *J. Phys. Chem. A* **101** 8743 (1997)
307. J Cao, K R Wilson *J. Phys. Chem. A* **102** 9523 (1998)
308. K B Møller, N E Henriksen, in *Molecular Electronic Structures of Transition Metal Complexes I (Structure and Bonding)* Vol. 142 (Eds D M P Mingos, P Day, J P Dahl) (Berlin, Heidelberg: Springer, 2012) p. 185
309. K Saita, D V Shalashilin *J. Chem. Phys.* **137** 22A506 (2012)
310. H-J Werner, P J Knowles, G Knizia, F R Manby, M Schütz *Wiley Interdiscip. Rev. Comput. Mol. Sci.* **2** 242 (2012)
311. T Northey, N Zotev, A Kirrander *J. Chem. Theory Comput.* **10** 4911 (2014)
312. R B Woodward, R Hoffmann *Angew. Chem., Int. Ed. Engl.* **8** 781 (1969)
313. W Fuß, W E Schmid, S A Trushin *J. Chem. Phys.* **112** 8347 (2000)
314. S A Trushin, K Kosma, W Fuß, W E Schmid *Opt. Lett.* **32** 2432 (2007)
315. K Kosma, S A Trushin, W Fuß, W E Schmid *J. Mod. Opt.* **55** 2141 (2008)
316. K Kosma, S A Trushin, W E Schmid, W Fuß *Opt. Lett.* **33** 723 (2008)
317. K Kosma, S A Trushin, W Fuß, W E Schmid *Phys. Chem. Chem. Phys.* **11** 172 (2009)
318. S Adachi, M Sato, T Suzuki *J. Phys. Chem. Lett.* **6** 343 (2015)
319. E Tapavicza, A M Meyer, F Furche *Phys. Chem. Chem. Phys.* **13** 20986 (2011)
320. J Hine *J. Org. Chem.* **31** 1236 (1966)
321. S H Pullen, N A Anderson, L A Walker II, R J Sension *J. Chem. Phys.* **107** 4985 (1997)
322. N A Anderson, S H Pullen, L A Walker II, J J Shiang, R J Sension *J. Phys. Chem. A* **102** 10588 (1998)
323. J D Cardoza, R C Dudek, R J Mawhorter, P M Weber *Chem. Phys.* **299** 307 (2004)
324. P Celani, F Bernardi, M A Robb, M Olivucci *J. Phys. Chem.* **100** 19364 (1996)

325. W Th A M Van der Lugt, L J Oosterhoff *J. Am. Chem. Soc.* **91** 6042 (1969)
326. E C Lim, in *Advances in Photochemistry* Vol. 23 (Eds D C Neckers, D H Volman, G von Bünau) (New York, Chichester: Wiley, 1997) p. 165
327. E C Friedberg *Nature (London)* **421** 436 (2003)
328. C E Crespo-Hernández, B Cohen, P M Hare, B Kohler *Chem. Rev.* **104** 1977 (2004)
329. B R Henry, M Kasha *Annu. Rev. Phys. Chem.* **19** 161 (1968)
330. G W Robinson, R P Frosch *J. Chem. Phys.* **38** 1187 (1963)
331. M Bixon, J Jortner *J. Chem. Phys.* **48** 715 (1968)
332. J Michl, in *Conical Intersections: Electronic Structure, Dynamics, and Spectroscopy (Advanced Series in Physical Chemistry)* (Eds W Domcke, D R Yarkony, H Köppel) (Singapore: World Scientific, 2004) p. ix
333. R Srinivasan, V A Lobastov, C-Y Ruan, A H Zewail *Helv. Chim. Acta* **86** 1761 (2003)
334. G B Kistiakowsky, C S Parmenter *J. Chem. Phys.* **42** 2942 (1965)
335. J H Callomon, J E Parkin, R Lopez-Delgado *Chem. Phys. Lett.* **13** 125 (1972)
336. G W Parshall *Science* **208** 1221 (1980)
337. H B Gray, A W Maverick *Science* **214** 1201 (1981)
338. P T Snee, C K Payne, S D Mebane, K T Kotz, C B Harris *J. Am. Chem. Soc.* **123** 6909 (2001)
339. M Besora, J-L Carreón-Macedo, A J Cowan, M W George, J N Harvey, P Portius, K L Ronayne, X-Z Sun, M Towrie *J. Am. Chem. Soc.* **131** 3583 (2009)
340. E A Juban, A L Smeigh, J E Monat, J K McCusker *Coord. Chem. Rev.* **250** 1783 (2006)
341. M Chergui *Dalton Trans.* **41** 13022 (2012)
342. A F Heyduk, D G Nocera *Science* **293** 1639 (2001)
343. B A Arndtsen, R G Bergman, T A Mobley, T H Peterson *Acc. Chem. Res.* **28** 154 (1995)
344. J A Labinger, J E Bercaw *Nature (London)* **417** 507 (2002)
345. S E Bromberg, H Yang, M C Asplund, T Lian, B K McNamara, K T Kotz, J S Yeston, M Wilkens, H Frei, R G Bergman, C B Harris *Science* **278** 260 (1997)
346. P Wernet, K Kunnus, I Josefsson, I Rajkovic, W Quevedo, M Beye, S Schreck, S Grübel, M Scholz, D Nordlund, W Zhang, R W Hartsock, W F Schlotter, J J Turner, B Kennedy, F Hennies, F M F de Groot, K J Gaffney, S Techert, M Odelius, A Föhlisch *Nature (London)* **520** 78 (2015)
347. M Wrighton *Chem. Rev.* **74** 401 (1974)
348. G L Geoffroy, M Wrighton *Organometallic Photochemistry* (New York: Academic Press, 1979)
349. W Fuß, S A Trushin, W E Schmid *Res. Chem. Intermediat.* **27** 447 (2001)
350. L Bañares, T Baumert, M Bergt, B Kiefer, G Gerber *Chem. Phys. Lett.* **267** 141 (1997)
351. M Poliakoff, J J Turner *Angew. Chem.* **113** 2889 (2001)
352. M Poliakoff, J J Turner *Angew. Chem., Int. Ed.* **40** 2809 (2001)
353. E S Apostolova, A P Tikhonov, O A Sendyurev *Russ. J. Coord. Chem.* **28** 38 (2002)
354. S A Trushin, W Fuss, W E Schmid, K L Kompa *J. Phys. Chem. A* **104** 1997 (2000)
355. P Portius, J Yang, X-Z Sun, D C Grills, P Matousek, A W Parker, M Towrie, M W George *J. Am. Chem. Soc.* **126** 10713 (2004)
356. R V G Ewens, M W Lister *Trans. Faraday Soc.* **35** 681 (1939)
357. J Donohue, A Caron *J. Phys. Chem.* **70** 603 (1966)
358. M I Davis, H P Hanson *J. Phys. Chem.* **71** 775 (1967)
359. B Beagley, D W J Cruickshank, P M Pinder, A G Robiette, G M Sheldrick *Acta Crystallogr., Sect. B* **25** 737 (1969)
360. B Beagley, D G Schmidling *J. Mol. Struct.* **22** 466 (1974)
361. B W McClelland, A G Robiette, L Hedberg, K Hedberg *Inorg. Chem.* **40** 1358 (2001)
362. J H Jang, J G Lee, H Lee, Y Xie, H F Schaefer III *J. Phys. Chem. A* **102** 5298 (1998)
363. K Pierloot *Mol. Phys.* **101** 2083 (2003)
364. U Radius, F M Bickelhaupt, A W Ehlers, N Goldberg, R Hoffmann *Inorg. Chem.* **37** 1080 (1998)
365. I L Rusakova, Y Y Rusakov, L B Krivdin *Russ. Chem. Rev.* **85** 356 (2016)
366. R G McKinlay, J M Żurek, M J Paterson, in *Theoretical and Computational Inorganic Chemistry* (*Advances in Inorganic Chemistry*) Vol. 62 (Eds R van Eldik, J Harvey) (Academic Press, 2010) p. 351
367. N J Turro, V Ramamurthy, J C Scaiano *Principles of Molecular Photochemistry: An Introduction* (Sausalito, CA: University Science Books, 2009)
368. S K Kim, S Pedersen, A H Zewail *Chem. Phys. Lett.* **233** 500 (1995)
369. S A Trushin, W Fuß, W E Schmid *Chem. Phys.* **259** 313 (2000)
370. S A Trushin, W Fuss, W E Schmid, K L Kompa *J. Phys. Chem. A* **102** 4129 (1998)
371. B O Roos, K Andersson, M P Fülscher, P-å Malmqvist, L Serrano-Andrés, K Pierloot, M Merchán, in *New Methods in Computational Quantum Mechanics (Advances in Chemical Physics)* Vol. 93 (Eds I Prigogine, S A Rice) (New York: Wiley, 1996) p. 219
372. B O Roos, in *Theory and Applications of Computational Chemistry: The First Forty Years* (Eds C E Dykstra, G Frenking, K S Kim, G E Scuseria) (Amsterdam: Elsevier, 2005) p. 725
373. Y Jean *Molecular Orbitals of Transition Metal Complexes* (Oxford: Oxford University Press, 2005)
374. R G McKinlay, M J Paterson, in *The Jahn-Teller Effect: Fundamentals and Implications for Physics and Chemistry* (*Springer Series in Chemical Physics*) Vol. 97 (Eds H Köppel, D R Yarkony, H Barentzen) (Berlin, Heidelberg: Springer-Verlag, 2009) p. 311
375. B J Persson, B O Roos, K Pierloot *J. Chem. Phys.* **101** 6810 (1994)
376. K Pierloot, E Tsokos, L G Vanquickenborne *J. Phys. Chem.* **100** 16545 (1996)
377. M J Paterson, P A Hunt, M A Robb, O Takahashi *J. Phys. Chem. A* **106** 10494 (2002)
378. G A Worth, G Welch, M J Paterson *Mol. Phys.* **104** 1095 (2006)
379. N Leadbeater *Coord. Chem. Rev.* **188** 35 (1999)
380. O Rubner, V Engel, M R Hachey, C Daniel *Chem. Phys. Lett.* **302** 489 (1999)
381. R L Jackson *Acc. Chem. Res.* **25** 581 (1992)
382. H C Longuet-Higgins *Proc. R. Soc. London, Ser. A* **344** 147 (1975)
383. U Manthe, H Köppel *J. Chem. Phys.* **93** 1658 (1990)
384. A Ceulemans, L G Vanquickenborne, in *Stereochemistry and Bonding* (*Structure and Bonding*) Vol. 71 (Berlin, Heidelberg: Springer-Verlag, 1989) p. 125
385. I B Bersuker, N B Balabanov, D Pekker, J E Boggs *J. Chem. Phys.* **117** 10478 (2002)
386. M Poliakoff, A Ceulemans *J. Am. Chem. Soc.* **106** 50 (1984)
387. M Poliakoff, E Weitz *Acc. Chem. Res.* **20** 408 (1987)
388. Yu N Demkov, P B Kurasov *Theor. Math. Phys.* **153** 1407 (2007)
389. D Guillaumont, A Vlček, C Daniel *J. Phys. Chem. A* **105** 1107 (2001)
390. P J Costa, M J Calhorda, J Bossert, C Daniel, C C Romão *Organometallics* **25** 5235 (2006)
391. N Ben Amor, D Ambrosek, C Daniel, R Marquardt *Chem. Phys.* **338** 81 (2007)
392. R J Ryther, E Weitz *J. Phys. Chem.* **95** 9841 (1991)
393. R J Ryther, E Weitz *J. Phys. Chem.* **96** 2561 (1992)
394. K Ossipov, I F Seregina, M A Bolshov *Russ. Chem. Rev.* **85** 335 (2016)
395. I I Yurkov, V V Eremin, N E Kuz'menko *Russ. J. Phys. Chem. A* **79** 2029 (2005)
396. I O Glebov, V V Eremin *Theor. Math. Phys.* **162** 201 (2010)

397. V S Letokhov *Laser Spectroscopy of Highly Vibrational Excited Molecules* (Bristol: Adam Hilger, 1989)
398. K K Lehmann, G Scoles, B H Pate *Annu. Rev. Phys. Chem.* **45** 241 (1994)
399. D J Nesbitt, R W Field *J. Phys. Chem.* **100** 12735 (1996)
400. A A Makarov, A L Malinovsky, E A Ryabov *Physics Uspekhi* **55** 977 (2012)
401. D G Poydashev, V N Lokhman, V O Kompanets, S V Chekalin, E A Ryabov *J. Phys. Chem. A* **118** 11177 (2014)
402. V O Kompanets, V N Lokhman, D G Poydashev, S V Chekalin, E A Ryabov *JETP* **122** 621 (2016)
403. M S Wrighton, D S Ginley, M A Schroeder, D L Morse *Pure Appl. Chem.* **41** 671 (1975)
404. R L Whetten, K J Fu, E R Grant *J. Am. Chem. Soc.* **104** 4270 (1982)
405. I Langmuir *Science* **54** 59 (1921)
406. R Hoffmann *Angew. Chem., Int. Ed. Engl.* **21** 711 (1982)
407. S K Nayak, G J Farrell, T J Burkey *Inorg. Chem.* **33** 2236 (1994)
408. P T Snee, C K Payne, K T Kotz, H Yang, C B Harris *J. Am. Chem. Soc.* **123** 2255 (2001)
409. W Zhang, R Alonso-Mori, U Bergmann, C Bressler, M Chollet, A Galler, W Gawelda, R G Hadt, R W Hartsock, T Kroll, K S Kjaer, K Kubicek, H T Lemke, H W Liang, D A Meyer, M M Nielsen, C Purser, J S Robinson, E I Solomon, Z Sun, D Sokaras, T B van Driel, G Vankó, T-C Weng, D Zhu, K J Gaffney *Nature (London)* **509** 345 (2014)
410. Ch Bressler, C Milne, V-T Pham, A ElNahhas, R M van der Veen, W Gawelda, S Johnson, P Beaud, D Grolimund, M Kaiser, C N Borca, G Ingold, R Abela, M Chergui *Science* **323** 489 (2009)
411. N Huse, H Cho, K Hong, L Jamula, F M F de Groot, T K Kim, J K McCusker, R W Schoenlein *J. Phys. Chem. Lett.* **2** 880 (2011)
412. A A Bengali, R G Bergman, C B Moore *J. Am. Chem. Soc.* **117** 3879 (1995)
413. A G Joly, K A Nelson *Chem. Phys.* **152** 69 (1991)
414. B Ahr, M Chollet, B Adams, E M Lunny, C M Laperle, C Rose-Petruck *Phys. Chem. Chem. Phys.* **13** 5590 (2011)
415. K Fukui *Angew. Chem., Int. Ed. Engl.* **21** 801 (1982)
416. A L Buchachenko *Russ. Chem. Rev.* **59** 307 (1990)
417. A L Buchachenko *J. Phys. Chem. A* **105** 9995 (2001)
418. K M Salikhov, R Z Sagdeev, A L Buchachenko, Y N Molin *Spin Polarization and Magnetic Effects in Radical Reactions* Vol. 22 (Studies in Physical and Theoretical Chemistry) (Amsterdam: Elsevier, 1984)
419. M Lim, T A Jackson, P A Anfinrud *Science* **269** 962 (1995)
420. E T J Nibbering, H Fidder, E Pines *Annu. Rev. Phys. Chem.* **56** 337 (2005)
421. S J Greaves, R A Rose, Th A A Oliver, D R Glowacki, M N R Ashfold, J N Harvey, I P Clark, G M Greetham, A W Parker, M Towrie, A J Orr-Ewing *Science* **331** 1423 (2011)
422. R G Hicks *Org. Biomol. Chem.* **5** 1321 (2007)
423. D Griller, K U Ingold *Acc. Chem. Res.* **9** 13 (1976)
424. L Schafer *J. Am. Chem. Soc.* **90** 3919 (1968)
425. J F Southern, L Schäfer, K Brendhaugen, H M Seip *J. Chem. Phys.* **55** 2418 (1971)
426. V N Bagratashvili, V S Doljikov, V S Letokhov, E A Ryabov *Appl. Phys.* **20** 231 (1979)
427. V V Golubkov, A A Ischenko, A V Zgursky, V I Petrov, in *The XIIth All-Union Conference on Electron Microscopy, Sumy, 1982* p. 62
428. V V Golubkov, A V Zgursky, A A Ischenko, V I Petrov *Bull. Acad. Sci. USSR, Phys. Ser.* **47** 1115 (1983)
429. W T Borden, E R Davidson *J. Am. Chem. Soc.* **101** 3771 (1979)
430. T-K Ha, R Meyer, H H Günthard *Chem. Phys. Lett.* **69** 510 (1980)
431. K Pierloot, B J Persson, B O Roos *J. Phys. Chem.* **99** 3465 (1995)
432. H Wang, K Brezinsky *J. Phys. Chem. A* **102** 1530 (1998)
433. M J Bearpark, M A Robb, N Yamamoto *Spectrochim. Acta, Part A: Mol. Biomol. Spectrosc.* **55** 639 (1999)
434. X Zhou, D A Hrovat, W T Borden *J. Am. Chem. Soc.* **129** 10785 (2007)
435. T Zeng, D G Fedorov, M W Schmidt, M Klobukowski *J. Chem. Theory Comput.* **7** 2864 (2011)
436. W Zou, M Filatov, D Cremer *Int. J. Quantum Chem.* **112** 3277 (2012)
437. P-K Lo, K-C Lau *J. Phys. Chem. A* **118** 2498 (2014)
438. G R Liebling, H M McConnell *J. Chem. Phys.* **42** 3931 (1965)
439. L Yu, S C Foster, J M Williamson, M C Heaven, T A Miller *J. Phys. Chem.* **92** 4263 (1988)
440. L Yu, D W Cullin, J M Williamson, T A Miller *J. Chem. Phys.* **98** 2682 (1993)
441. V A Korolev, O M Nefedov *Russ. Chem. Bull.* **42** 1436 (1993)
442. A A Ganeev, A R Gubal, S V Potapov, N N Agafonova, V M Nemets *Russ. Chem. Rev.* **85** 427 (2016)
443. H Ihee, J S Feenstra, J Cao, A H Zewail *Chem. Phys. Lett.* **353** 325 (2002)
444. H A Jahn, E Teller *Phys. Rev.* **49** 874 (1936)
445. H A Jahn, E Teller *Proc. R. Soc. London, Ser. A* **161** 220 (1937)
446. L Salem *The Molecular Orbital Theory of Conjugated Systems* (New York: Benjamin, 1966)
447. S-i Ohnishi, I Nitta *J. Chem. Phys.* **39** 2848 (1963)
448. A D Liehr *J. Phys. Chem.* **67** 389 (1963)
449. A Carrington, H C Longuet-Higgins, R E Moss, P F Todd *Mol. Phys.* **9** 187 (1965)
450. M Kira, M Watanabe, H Sakurai *J. Am. Chem. Soc.* **102** 5202 (1980)
451. P J Barker, A G Davies, M-W Tse *J. Chem. Soc., Perkin Trans. 2* 941 (1980)
452. L Yu, J M Williamson, T A Miller *Chem. Phys. Lett.* **162** 431 (1989)
453. D W Cullin, L Yu, J M Williamson, T A Miller *J. Phys. Chem.* **96** 89 (1992)
454. R Meyer, F Graf, T-K Ha, H H Günthard *Chem. Phys. Lett.* **66** 65 (1979)
455. R Engleman Jr, D A Ramsay *Can. J. Phys.* **48** 964 (1970)
456. S Sun, E R Bernstein *J. Chem. Phys.* **103** 4447 (1995)
457. J Fossey, D Lefort, J Sorba *Free Radicals in Organic Chemistry* (Chichester: Wiley, 1995)
458. P S Skell, D L Tuleen, P D Readio *J. Am. Chem. Soc.* **85** 2849 (1963)
459. H Ihee, J Kua, W A Goddard III, A H Zewail *J. Phys. Chem. A* **105** 3623 (2001)
460. H Ihee, B M Goodson, R Srinivasan, V A Lobastov, A H Zewail *J. Phys. Chem. A* **106** 4087 (2002)
461. D Shorokhov, A H Zewail *Phys. Chem. Chem. Phys.* **10** 2879 (2008)
462. H Ihee, A H Zewail, W A Goddard III *J. Phys. Chem. A* **103** 6638 (1999)
463. T K Kim, J H Lee, M Wulff, Q Kong, H Ihee *ChemPhysChem* **10** 1958 (2009)
464. H Ihee, M Wulff, J Kim, S-i Adachi *Int. Rev. Phys. Chem.* **29** 453 (2010)
465. H Mark, R Wierl *Naturwiss.* **18** 205 (1930)
466. H Mark, R Wierl *Die Experimentellen und Theoretischen Grundlagen der Electronenbeugung* (Berlin: Verlag von Gebruder Borntraeger, 1931)
467. T Zuo, A D Bandrauk, P B Corkum *Chem. Phys. Lett.* **259** 313 (1996)
468. M Lein, J P Marangos, P L Knight *Phys. Rev. A* **66** 051404 (2002)
469. S N Yurchenko, S Patchkovskii, I V Litvinyuk, P B Corkum, G L Yudin *Phys. Rev. Lett.* **93** 223003 (2004)
470. M Spanner, O Smirnova, P B Corkum, M Yu Ivanov *J. Phys. B: At. Mol. Opt. Phys.* **37** L243 (2004)

471. D Gabor *Nature (London)* **161** 777 (1948)
472. M Meckel, D Comtois, D Zeidler, A Staudte, D Pavičić, H C Bandulet, H Pépin, J C Kieffer, R Dörner, D M Villeneuve, P B Corkum *Science* **320** 1478 (2008)
473. L V Keldysh *Russian JETP* **20** 1945 (1965)
474. V S Popov *Physics Uspekhi* **47** 855 (2004)
475. P B Corkum, F Krausz *Nat. Phys.* **3** 381 (2007)
476. B Wolter, M G Pullen, A T Le, M Baudisch, K Doblhoff-Dier, A Senftleben, M Hemmer, C D Schröter, J Ullrich, T Pfeifer, R Moshammer, S Gräfe, O Vendrell, C D Lin, J Biegert *Science* **354** 308 (2016)
477. E M-L Ohrendorf, F Tarantelli, L S Cederbaum *J. Chem. Phys.* **92** 2984 (1990)
478. R Thissen, J Delwiche, J M Robbe, D Duflot, J P Flament, J H D Eland *J. Chem. Phys.* **99** 6590 (1993)
479. J Biegert, P K Bates, O Chalus *IEEE J. Sel. Top. Quantum Electron.* **18** 531 (2012)
480. M Baudisch, H Pires, H Ishizuki, T Taira, M Hemmer, J Biegert *J. Opt.* **17** 094002 (2015)
481. B Gaire, S Y Lee, D J Haxton, P M Pelz, I Bocharova, F P Sturm, N Gehrken, M Honig, M Pitzer, D Metz, H K Kim, M Schöffler, R Dörner, H Gassert, S Zeller, J Voigtsberger, W Cao, M Zohrabi, J Williams, A Gatton, D Reedy, C Nook, Th Müller, A L Landers, C L Cocke, I Ben-Itzhak, T Jahnke, A Belkacem, Th Weber *Phys. Rev. A* **89** 013403 (2014)
482. K Doblhoff-Dier, M Kitzler, S Gräfe *Phys. Rev. A* **94** 013405 (2016)
483. M Alagia, C Callegari, P Candori, S Falcinelli, F Pirani, R Richter, S Stranges, F Vecchiocattivi *J. Chem. Phys.* **136** 204302 (2012)
484. X Xie, K Doblhoff-Dier, H Xu, S Roither, M S Schöffler, D Kartashov, S Erattupuzha, T Rathje, G G Paulus, K Yamanouchi, A Baltuška, S Gräfe, M Kitzler *Phys. Rev. Lett.* **112** 163003 (2014)
485. M G Pullen, B Wolter, A-T Le, M Baudisch, M Hemmer, A Senftleben, C D Schröter, J Ullrich, R Moshammer, C D Lin, J Biegert *Nat. Commun.* **6** 7262 (2015)
486. P B Corkum *Phys. Rev. Lett.* **71** 1994 (1993)
487. J L Krause, K J Schafer, K C Kulander *Phys. Rev. Lett.* **68** 3535 (1992)
488. J Itatani, J Levesque, D Zeidler, H Niikura, H Pépin, J C Kieffer, P B Corkum, D M Villeneuve *Nature (London)* **432** 867 (2004)
489. E Fill, L Veisz, A Apolonski, F Krausz *New J. Phys.* **8** 272 (2006)
490. P Baum, A H Zewail *Proc. Natl. Acad. Sci. USA* **103** 16105 (2006)
491. P Baum, A H Zewail *Proc. Natl. Acad. Sci. USA* **104** 18409 (2007)
492. S A Hilbert, C Uiterwaal, B Barwick, H Batelaan, A H Zewail *Proc. Natl. Acad. Sci. USA* **106** 10558 (2009)
493. P Baum, J Manz, A Schild *Sci. China Physics, Mechanics and Astronomy* **53** 987 (2010)
494. M Aidelsburger, F O Kirchner, F Krausz, P Baum *Proc. Natl. Acad. Sci. USA* **107** 19714 (2010)
495. A R Bainbridge, C W Barlow Myers, W A Bryan *Struct. Dyn.* **3** 023612 (2016)
496. H-C Shao, A F Starace *Phys. Rev. Lett.* **105** 263201 (2010)
497. B J Siwick, J R Dwyer, R E Jordan, R J Dwayne Miller *J. Appl. Phys.* **92** 1643 (2002)
498. T van Oudheusden, E F de Jong, S B van den Geer, W P E M Op't Root, O J Luiten, B J Siwick *J. Appl. Phys.* **102** 093501 (2007)
499. G J H Brussaard, A Lassise, P L E M Pasmans, P H A Mutsaers, M J Van der Wiel, O J Luiten *Appl. Phys. Lett.* **103** 141105 (2013)
500. C T Hebeisen, R Ernstorfer, M Harb, T Dartigalongue, R E Jordan, R J Dwayne Miller *Opt. Lett.* **31** 3517 (2006)
501. M Hada, D Zhang, K Pichugin, J Hirscht, M A Kochman, S A Hayes, S Manz, R Y N Gengler, D A Wann, T Seki, G Moriena, C A Morrison, J Matsuo, G Sciaini, R J Dwayne Miller *Nat. Commun.* **5** 3863 (2014)
502. J Hirscht, PhD Thesis, Universität Hamburg, 2015
503. M Gao, Y Jiang, G H Kassier, R J Dwayne Miller *Appl. Phys. Lett.* **103** 033503 (2013)
504. J Cao, Z Hao, H Park, C Tao, D Kau, L Blaszczyk *Appl. Phys. Lett.* **83** 1044 (2003)
505. S Williamson, G Mourou, J C M Li *Phys. Rev. Lett.* **52** 2364 (1984)
506. C Guo, A J Taylor *Phys. Rev. B* **62** R11921 (2000)
507. M Kandyla, T Shih, E Mazur *Phys. Rev. B* **75** 214107 (2007)
508. K Franjic, M L Cowan, D Kraemer, R J Dwayne Miller *Opt. Express* **17** 22937 (2009)
509. S Amini-Nik, D Kraemer, M L Cowan, K Gunaratne, P Nadesan, B A Alman, R J Dwayne Miller *PLoS ONE* **5** e13053 (2010)
510. H Petersen, F Tavakoli, S Kruber, A Münscher, A Gliese, N-O Hansen, S Uschold, D Eggert, W D Robertson, T Gosau, S Sehner, M Kwiatkowski, H Schlüter, U Schumacher, R Knecht, R J Dwayne Miller *Lasers Surg. Med.* **48** 385 (2016)
511. R Ernstorfer, M Harb, C T Hebeisen, G Sciaini, T Dartigalongue, R J Dwayne Miller *Science* **323** 1033 (2009)
512. G Sciaini, M Harb, S G Kruglik, Th Payer, C T Hebeisen, F-J M zu Heringdorf, M Yamaguchi, M H-v Hoegen, R Ernstorfer, R J Dwayne Miller *Nature (London)* **458** 56 (2009)
513. M Eichberger, H Schäfer, M Krumova, M Beyer, J Demsar, H Berger, G Moriena, G Sciaini, R J Dwayne Miller *Nature (London)* **468** 799 (2010)
514. N Erasmus, M Eichberger, K Haupt, I Boshoff, G Kassier, R Birmurske, H Berger, J Demsar, H Schwoerer *Phys. Rev. Lett.* **109** 167402 (2012)
515. B J Siwick, J R Dwyer, R E Jordan, R J Dwayne Miller *Chem. Phys.* **299** 285 (2004)
516. M Gao, C Lu, H Jean-Ruel, L C Liu, A Marx, K Onda, S-y Koshihara, Y Nakano, X Shao, T Hiramatsu, G Saito, H Yamochi, R R Cooney, G Moriena, G Sciaini, R J Dwayne Miller *Nature (London)* **496** 343 (2013)
517. H Jean-Ruel, M Gao, M A Kochman, C Lu, L C Liu, R R Cooney, C A Morrison, R J Dwayne Miller *J. Phys. Chem. B* **117** 15894 (2013)
518. M Irie, T Fukaminato, K Matsuda, S Kobatake *Chem. Rev.* **114** 12174 (2014)
519. H Jean-Ruel, R R Cooney, M Gao, C Lu, M A Kochman, C A Morrison, R J Dwayne Miller *J. Phys. Chem. A* **115** 13158 (2011)
520. M Woerner, F Zamponi, Z Ansari, J Dreyer, B Freyer, M Prémont-Schwarz, Th Elsaesser *J. Chem. Phys.* **133** 064509 (2010)
521. Th Elsaesser, M Woerner *Acta Crystallogr., Sect. A* **66** 168 (2010)
522. V Juvé, M Holtz, F Zamponi, M Woerner, Th Elsaesser, A Borgschulte *Phys. Rev. Lett.* **111** 217401 (2013)
523. F Zamponi, P Rothhardt, J Stingl, M Woerner, Th Elsaesser *Proc. Natl. Acad. Sci. U. S. A.* **109** 5207 (2012)
524. P Emma, R Akre, J Arthur, R Bionta, C Bostedt, J Bozek, A Brachmann, P Bucksbaum, R Coffee, F-J Decker, Y Ding, D Dowell, S Edstrom, A Fisher, J Frisch, S Gilevich, J Hastings, G Hays, Ph Hering, Z Huang, R Iverson, H Loos, M Messerschmidt, A Miahnahri, S Moeller, H-D Nuhn, G Pile, D Ratner, J Rzepiela, D Schultz, T Smith, P Stefan, H Tompkins, J Turner, J Welch, W White, J Wu, G Yocky, J Galayda *Nat. Photon.* **4** 641 (2010)
525. V I Prokhorenko, A Halpin, P J M Johnson, R J Dwayne Miller, L S Brown *J. Chem. Phys.* **134** 085105 (2011)

526. Th R M Barends, L Foucar, A Ardevol, K Nass, A Aquila, S Botha, R B Doak, K Falahati, E Hartmann, M Hilpert, M Heinz, M C Hoffmann, J Köfinger, J E Koglin, G Kovacsova, M Liang, D Milathianaki, H Lemke, J Reinstein, C M Roome, R L Shoeman, G J Williams, I Burghardt, G Hummer, S Boutet, I Schlichting *Science* **350** 445 (2015)
527. R J Dwayne Miller *Acc. Chem. Res.* **27** 145 (1994)
528. R J Dwayne Miller *Can. J. Chem.* **80** 1 (2002)
529. M R Armstrong, J P Ogilvie, M L Cowan, A M Nagy, R J D Miller *Proc. Natl. Acad. Sci. USA* **100** 4990 (2003)
530. M Walther, V Raicu, J P Ogilvie, R Phillips, R Kluger, R J Dwayne Miller *J. Phys. Chem. B* **109** 20605 (2005)
531. R J Dwayne Miller *Annu. Rev. Phys. Chem.* **42** 581 (1991)
532. G D Goodno, V Astinov, R J Dwayne Miller *J. Phys. Chem. A* **103** 10630 (1999)
533. K Pande, C D M Hutchison, G Groenhof, A Aquila, J S Robinson, J Tenboer, S Basu, S Boutet, D P DePonte, M Liang, T A White, N A Zatsepin, O Yefanov, D Morozov, D Oberthuer, C Gati, G Subramanian, D James, Y Zhao, J Koralek, J Brayshaw, C Kupitz, C Conrad, S Roy-Chowdhury, J D Coe, M Metz, P L Xavier, T D Grant, J E Koglin, G Ketawala, R Fromme, V Šrajer, R Henning, J C H Spence, A Ourmazd, P Schwander, U Weierstall, M Frank, P Fromme, A Barty, H N Chapman, K Moffat, J J van Thor, M Schmidt *Science* **352** 725 (2016)
534. G Porter *Science* **160** 1299 (1968)
535. G Porter, M R Topp *Nature (London)* **220** 1228 (1968)
536. G Porter, M R Topp *Proc. R. Soc. London, Ser. A* **315** 163 (1970)
537. W Demtröder *Laser Spectroscopy* (4th Edn) (Berlin: Springer, 2008)
538. J T Yardley *Introduction to Molecular Energy Transfer* (New York: Academic Press, 1980)
539. G W Flynn, C S Parmenter, A M Wodtke *J. Phys. Chem.* **100** 12817 (1996)
540. V N Bagratashvili, V S Letokhov, A A Makarov, E A Ryabov *Multiple Photon Infrared Laser Photophysics and Photochemistry* (London, Paris, New York, Chur: Harwood Acad. Publ., 1985)
541. S A Akhmanov, V M Gordienko, A V Mikheenko, V Y Panchenko *JETP Lett., Engl. Transl.* **26** 453 (1977)
542. Y-L Li, D M Chen, D Wang, D L Phillips *J. Org. Chem.* **67** 4228 (2002)
543. N Biswas, S Umapathy *J. Chem. Phys.* **107** 7849 (1997)
544. P Kukura, D W McCamant, S Yoon, D B Wandschneider, R A Mathies *Science* **310** 1006 (2005)
545. Y Mizutani, T Kitagawa *Science* **278** 443 (1997)
546. W J Schreier, T E Schrader, F O Koller, P Gilch, C E Crespo-Hernández, V N Swaminathan, T Carell, W Zinth, B Kohler *Science* **315** 625 (2007)
547. S O Williams, D G Imre *J. Phys. Chem.* **92** 3363 (1988)
548. M C Asplund, M T Zanni, R M Hochstrasser *Proc. Natl. Acad. Sci. USA* **97** 8219 (2000)
549. J Zheng, K Kwak, J Xie, M D Fayer *Science* **313** 1951 (2006)
550. M Cho *Chem. Rev.* **108** 1331 (2008)
551. V L Aksenov, M V Koval'chuk, A Yu Kuz'min, Yu Purans, S I Tyutyunnikov *Crystallogr. Rep.* **51** 908 (2006)
552. G V Fetisov *Synchrotron Radiation: Investigation Methods for the Structure of Matter* (Moscow: Fizmatlit, 2007)
553. L X Chen *Annu. Rev. Phys. Chem.* **56** 221 (2005)
554. S Tokita, M Hashida, S Inoue, T Nishoji, K Otani, S Sakabe *Phys. Rev. Lett.* **105** 215004 (2010)
555. C Bressler, M Chergui *Chem. Rev.* **104** 1781 (2004)
556. J H Lee, H Ihee *Struct. Chem.* **21** 37 (2010)
557. L X Chen *Angew. Chem.* **116** 2946 (2004)
558. L X Chen *Angew. Chem. Int. Ed.* **43** 2886 (2004)
559. L X Chen, X Zhang, E C Wasinger, K Attenkofer, G Jennings, A Z Muresan, J S Lindsey *J. Am. Chem. Soc.* **129** 9616 (2007)
560. W Gawelda, V-T Pham, M Benfatto, Y Zaushitsyn, M Kaiser, D Grolimund, S L Johnson, R Abela, A Hauser, C Bressler, M Chergui *Phys. Rev. Lett.* **98** 057401 (2007)
561. M Khalil, M A Marcus, A L Smeigh, J K McCusker, H H W Chong, R W Schoenlein *J. Phys. Chem. A* **110** 38 (2006)
562. W Gawelda, M Johnson, F M F de Groot, R Abela, C Bressler, M Chergui *J. Am. Chem. Soc.* **128** 5001 (2006)
563. V-T Pham, W Gawelda, Y Zaushitsyn, M Kaiser, D Grolimund, S L Johnson, R Abela, C Bressler, M Chergui *J. Am. Chem. Soc.* **129** 1530 (2007)
564. L X Chen, W J H Jäger, G Jennings, D J Gosztola, A Munkholm, J P Hessler *Science* **292** 262 (2001)
565. *European X-Ray Free-Electron Laser: Annual Report* (Ed. M Altarelli) (Hamburg: 2012)
566. *X-ray Free Electron Lasers: Applications in Materials, Chemistry and Biology* (Eds J Yano, V Yachandra, U Bergmann) (London: Royal Society of Chemistry, 2017)
567. M Feyereisen, G Fitzgerald, A Komornicki *Chem. Phys. Lett.* **208** 359 (1993)
568. B I Dunlap *Phys. Chem. Chem. Phys.* **2** 2113 (2000)
569. Y Jung, A Sodt, P M W Gill, M Head-Gordon *Proc. Natl. Acad. Sci. USA* **102** 6692 (2005)
570. P G Szalay, T Watson, A Perera, V F Lotrich, R J Bartlett *J. Phys. Chem. A* **116** 6702 (2012)
571. P G Szalay, T Watson, A Perera, V Lotrich, G Fogarasi, R J Bartlett *J. Phys. Chem. A* **116** 8851 (2012)
572. A Tajti, P G Szalay, *J. Chem. Phys.* **131** 124104 (2009)
573. F Plasser, R Crespo-Otero, M Pederzoli, J Pittner, H Lischka, M Barbatti *J. Chem. Theory Comput.* **10** 1395 (2014)
574. D Tuna, D Lefrancois, Ł Wolański, S Gozem, I Schapiro, T Andruniów, A Dreuw, M Olivucci *J. Chem. Theory Comput.* **11** 5758 (2015)
575. W Thiel. *Wiley Interdiscip. Rev. Comput. Mol. Sci.* **4** 145 (2014)
576. W Weber, W Thiel *Theor. Chem. Acc.* **103** 495 (2000).
577. A Koslowski, M E Beck, W Thiel *J. Comput. Chem.* **24** 714 (2003)
578. A Warshel, M Levitt *J. Mol. Biol.* **103** 227 (1976)
579. A E Kaplan *Opt. Photon. News* **17** 28 (2006)
580. A E Kaplan *Nature (London)* **431** 633 (2004)